Pulsar Scattering and the Ionized Interstellar Medium

Marisa Geyer
Lady Margaret Hall
University of Oxford

A thesis submitted for the degree of
Doctor of Philosophy

Trinity 2017

Aan my pa, vir al die etenstafel-fisika waar appels om papbakkies wentel.

Acknowledgements

An astronomical thank you to Aris, my supervisor, without whom this study was impossible. For routinely making time for my project and for sharing his insights and enthusiasm for pulsars with me. I am grateful for his kindness and his continuous encouragement, during the lulls and the triumphs, and for ensuring the progress and quality of this study.

My gratitude to the Commonwealth Scholarship Commission, whose financial support granted me this opportunity. Thank you for investing in me.

To Jocelyn Bell-Burnell, the humble hero of the pulsar world, and an inspiration to all women in science. It has been an immeasurable privilege to share Oxford's corridors with you.

To the members of the LOFAR Pulsar Working Group, for their advice and their feedback on my work. To my collaborator Mark Walker, from Manly Astrophysics in Sydney, for sharing his ideas and his understanding of the interstellar medium with me, for his meticulous correspondence and for all the catch-up coffees in Oxford.

To my pulsar comrades in Oxford over these years, Elmarie van Heerden, Paul Brook and Jayanth Chennamangalam who patiently watched me draw "if this is the pulsar and that is the screen..." countless times. For those moments that we thought we had stumbled ourselves into *Nature*-worthy results, just to be humbled again. To the alien hunter, Griffin Foster, for showing me that writing-up is about running faster. To all the attendees of pulsar coffee, that made Tuesdays the best day of the week.

To my office mates, first in 512, and then in 650, who endured my craziness, who organised the pub trips and who made Oxford Astrophysics a home. To Laura Prichard for the everyday babble, the dreadful puns, the scrutiny of academia's quirks and troubles and her sincerest friendship and support. You made my experience of Oxford and DPhil-life so much richer.

To Ashling Morris, Humaira Ahmed-Erfan and Richard Smith, the wizards that made my admin and IT worries go away.

To Garret Cotter and Will Potter for helping me through the official check-points towards submission, reminding me that "it's all just electrons underneath". My gratitude to John Miller and Gemma Janssen, the examiners of this thesis, for their dedicated preparation and suggested improvements to this manuscript.

And thank goodness for the Stable Closers, my housemates Maggie, Domi and Sam. For a life of diversions, for preparing the merriments and the brunches too.

My deepest thanks to my mom, dad and sister for showing me the beauty in the fine-print of the world. For their endless love and support. I have missed you all.

To JM, my confidant, for always listening, always advising *en al jou liefde*.

Statement of Originality

I declare that no part of this thesis has been, or is being, submitted for any qualification other than the degree of Doctor of Philosophy at the University of Oxford.

This thesis is the result of my own work unless otherwise stated.

Chapters of this work have been published in part as papers in the journals below. The projects are fully my own. I wrote the relevant pulsar scattering analysis code and conducted the data analysis. I am the main author of the manuscripts. Dr. Karastergiou contributed through his supervision and advice. The remaining authors on the second paper either provided me with data or, as members of the LOFAR Pulsar Working Group, provided comments to an advanced version of the manuscript.

Chapter 4:

The frequency dependence of scattering imprints on pulsar observations, M. Geyer and A. Karastergiou. Monthly Notices of the Royal Astronomical Society, July 2016, volume: 462 (3), pages: 2587–2602.

Chapter 5 and 6:

Scattering analysis of LOFAR pulsar observations, M. Geyer, A. Karastergiou et al. Monthly Notices of the Royal Astronomical Society, September 2017, volume: 470 (3), pages: 2659–2679.

Chapter 7 contains applications and ongoing projects, some of which are collaborative work. Sec. 7.2 describes my involvement with Mr. Scott England's MPhil project. I adapted my code for the project and assisted Mr. England with the data analysis. Sec. 7.3 describes an ongoing project with Dr. Mark Walker. Dr. Walker is conducting the theoretical modelling for this project, whereas I am conducting the numerical analysis.

Marisa Geyer, July 2017

Abstract

Fifty years after the discovery of the first pulsating neutron star, the field of pulsar science has grown into a multidisciplinary research field, working to address a wide range of problems in astrophysics – from stellar evolution models to high precision tests of General Relativity to analysing the detailed structure of the Interstellar Medium in the Milky Way. Over 2500 Galactic pulsars have been discovered. The next generation telescopes, such as the Square Kilometre Array, promise to discover the complete observable Milky Way population, of several tens of thousands, over the next decade.

These point sources in the sky have extreme properties, with matter densities comparable to that of an atomic nucleus, and surface magnetic fields a trillion times stronger than Earth's magnetic field. Observationally, the most valuable property is their rotational stability – allowing us to anticipate and sum their beamed radio emission, as the pulsar spins around its axis, on millisecond to second timescales.

The detected radio wave signals carry with them information of the ionised interstellar medium (IISM) paths they traveled along. The imprints reveal that the pulsar signals we detect travel along multiple paths. While the bulk of the emitted signal propagates along a straight line, we also receive delayed emission scattered through small angles, back into our line of sight. This scattering is caused by fluctuations in the free electron densities of the IISM. The impact of these inhomogeneities is exaggerated at low observing frequencies, where averaged pulsar profiles are observed to be broadened, and showcase exponential scattering tails characterised by a scattering timescale τ.

Simple theoretical models predict a power law dependence of τ on frequency, with a spectral index $\alpha = 4$. Despite these predictions, my analysis of pulsar data in this thesis, reveal a more complex frequency dependence on τ.

I investigate the scattering characteristics of a set of pulsars observed by the Low Frequency Array (LOFAR), at 110 MHz to 190 MHz. These data are ideal datasets for accurate studies of pulsar scattering, providing broad frequency bands at low frequencies.

I find anomalously low power law spectral indices, α, describing the frequency dependence of τ. These indices are likely due to anisotropic scattering mechanisms or small scattering clouds in the IISM.

To conduct effective data analysis, I develop scattering fitting techniques by first analysing IISM effects on simulated pulsar data. I investigate the effects of two different types of scattering mechanisms, isotropic and anisotropic scattering, and consider each of their particular frequency-dependent impacts on pulsar data.

The work on simulated data provides a robust fitting technique for extracting scattering parameters and a framework for the interpretation of the LOFAR data used in this study. The fitting technique simultaneously models scattering effects and standard frequency-dependent pulse profile evolution.

I present results for 13 pulsars with simple pulse shapes, and find that τ, associated with scattering by a single thin screen, has a power law dependence on frequency with α ranging from 1.50 to 4.0. My results show that extremely anisotropic scattering can cause low α measurements. The anomalous scattering properties can also be caused by the presence of small scattering clumps in the IISM, as opposed to the conventionally modelled large scattering screens.

Evidence for both anisotropic scattering and small scattering clouds with high electron densities come from other areas of research. Indications of the anisotropic nature of the local IISM mostly come from high resolution pulsar scintillation analyses, while evidence for high density scattering clouds is often based on extreme scattering events measured through quasar observations.

My results suggest that these anomalous scattering properties are more prevalent than formerly thought, prompting us to reconsider the physical conditions of the IISM, where traditionally high electron densities are reserved for HII regions and anisotropy is not modelled.

High quality, low frequency pulsar data, where anomalous propagation effects become measurable, are a valuable addition in assisting us to distinguish between the different physical mechanisims that can be at play. The more complex these IISM characteristics reveal themselves to be, the harder it will be to disentangle intrinsic profile emission from IISM propagation imprints. Successfully separating these effects, however, promises to improve our understanding of the intrinsic pulsar radio emission – a process that is still poorly understood.

die sterre vat jou hart
want die sterre is vir jou nie bietjie honger nie!
die sterre verruil jou hart vir 'n ster se hart
die sterre vat jou hart en voer jou 'n ster se hart
dan word jy nooit weer honger nie

Uit Wat die sterre sê deur Antjie Krog

You ride astride the imaginary in order to hunt down the real

Breyten Breytenbach

Contents

List of Figures

List of Tables

Chapter 1

Pulsars and the ionized Interstellar Medium

This year, 2017, marks the 50th anniversary of the discovery of CP1919, the original pulsating neutron star, by Dame Jocelyn Bell-Burnell (Hewish et al., 1968). Since then, the astronomy community has discovered more than 2500 such pulsating objects. Half a century has not only revealed an ever growing number of radio pulsars and their extreme properties, but has also allowed us to become increasingly adept at utilising pulsars as tools to probe other problems in astrophysics.

In this thesis, I employ pulsars to examine the characteristics of the ionized interstellar medium (IISM) that infuses the space through which the pulsar signal travels before being detected at Earth. Investigating the imprints of the IISM on pulsar signals, will firstly lead to an improved understanding of the IISM, and in turn allow us to disentangle propagation effects from the intrinsic pulsar radio emission – an emission process which is still poorly understood.

I start by presenting an introduction of pulsar characteristics that are relevant to studying propagation effects through the IISM. These properties form by no means an exhaustive list of pulsar phenomena. Thereafter, I discuss the nature of the ionized interstellar medium, and in the last section of this chapter illustrate how pulsars are suited to studying the composition of the IISM.

1.1 An Introduction to Pulsars

Pulsars are fast-spinning, highly magnetic neutron stars that emit radio beams along their magnetic axis, as depicted in Fig. 1.1. A misalignment between the rotational axis and magnetic axis allows for these beams to sweep through our line of sight as the star rotates, leading to the observation of periodic radio pulses. Single pulses are

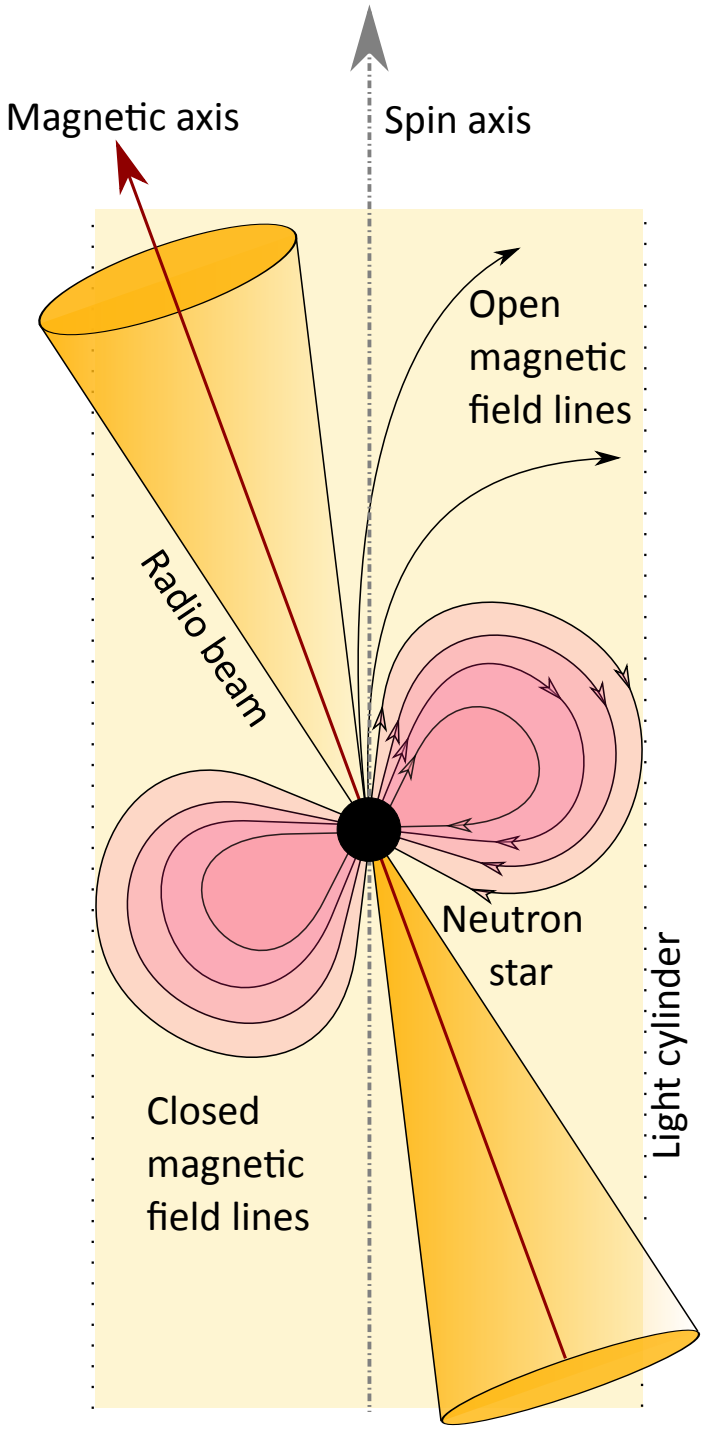

Figure 1.1: An artist's impression of the standard pulsar model. As the neutron star spins around its own axis, the misalignment between the spin and magnetic axes, combined with a favourable orientation of the pulsar in the sky, causes the emitted radio beam to pass through our line of sight. This periodic illumination of the line of sight leads to observed radio pulses in the time domain. Credit: M. Geyer.

typically faint and have highly variable shapes, but the periodic nature of the signal permits a build-up of signal-to-noise (S/N) over many ($\sim$ 1000) rotational periods, leading to an observed pulse profile shape that exhibits surprising stability (Helfand et al., 1975).

1.1.1 Pulsars are compact

Pulsars are one of several long-lived end-states of massive stars. The most extreme of these end-states are black holes, formed through the complete chain collapse of stars with masses exceeding 60 to 100 $M_\odot$ (Teukolsky & Shapiro, 1983). Somewhat less massive progenitors, with masses between 8 and 20 M $_\odot$, end their lives as neutron stars (Stairs, 2004). The progenitor star, typically an OB star, (Blaauw, 1985) burns through a lifetime supply of nuclear fuel over more than 10 million years, until finally the matter's inward gravitational pull overwhelms the star's remaining thermal pressure. Within milliseconds the massive star is crushed to a compact core, while its outer gas shells are expelled in a supernova explosion. Around 60 young pulsars are observed to be associated with their supernova remnants (Yao et al., 2017). A spectacular example of this is the Crab pulsar (PSR B0531+21) embedded in the Crab Nebula, the remnant of a supernova explosion (SN 1054) documented by Chinese astronomers as a *guest star* in the year 1054 (Duyvendak, 1942).

Following the supernova explosion, the resulting neutron star is expected to have a mass of approximately 1.4 $M_\odot$ (Chandrasekhar, 1931). Studies of the orbital parameters in binary systems, in which either two neutron stars, or a white dwarf and neutron star, orbit each other, have led to a mass distribution of neutron stars ranging from 1.2 $M_\odot$ to 2.1 $M_\odot$ (Kiziltan et al., 2013).

Measurements of the radii of neutron stars are harder to obtain, with most theoretical models predicting a value of around 10 km (Lattimer & Prakash, 2001), leading to average matter densities as high as $\rho = 1 \times 10^{15}$ g cm^{-3} (Teukolsky & Shapiro, 1983). The neutron star is supported against further collapse through outward neutron degeneracy pressure. At this canonical density, the neutron star is an order of magnitude more dense than nuclear matter, providing a highly exotic environment beyond the scope of laboratory experiments on Earth. An exact model for the equation of state, that relates the density, mass and radius of neutron stars, remains an area of ongoing investigation (Özel & Freire, 2016).

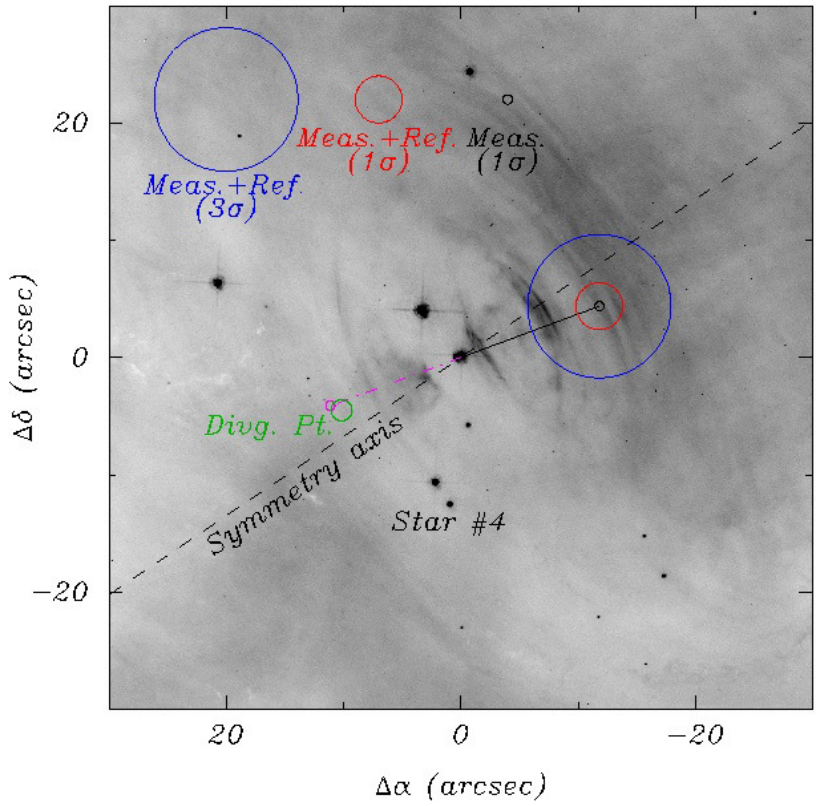

Figure 1.2: Figure taken from Kaplan et al. (2008). It shows the proper motion of the Crab pulsar on a drizzled image (Koekemoer et al., 2003). The vector indicated by the solid line shows the proper motion of the pulsar and its position 1000 years from now. The inner-most circle is the 1σ statistical uncertainty. The middle circle is the 1σ error that includes the uncertainty of the progenitor's motion w.r.t. the rest frame, and the outer circle is a 3σ combined uncertainty. More details in Kaplan et al. (2008).

1.1.2 Pulsars are high velocity objects

Early on, in 1970 when only 41 pulsars had been discovered, researchers already noted that many of these were moving much faster than what is typical for their presumed progenitor OB stars (Gunn & Ostriker, 1970). Their high velocities are thought to originate from asymmetric supernova explosions that impart a strong kick velocity on the new born pulsar.

Massive stars are typically observed to be close to the Galactic plane (Sun & Han, 2004). A similar distribution is expected for progenitor stars of pulsars, such that a kick velocity imparted to the pulsar at birth would likely make it move away from the Galactic plane. Theoretical models that can lead to such supernova kicks are discussed in detail in Lai et al. (2001) and references therein.

Pulsar velocities are determined from measurements of their proper motion and distance. One of the first pulsars for which a high proper motion was observed, is the Crab pulsar. A recent estimation of the proper motion of this pulsar within the Crab nebula is given in Kaplan et al. (2008), and shown in Fig. 1.2. From their proper motion measurements the authors calculated a transverse velocity of approximately 120 km s^{-1}. The projected motion of the pulsar over the next 1000 years is shown as a black line in Fig. 1.2.

Hobbs et al. (2005) studied the proper motions of 233 pulsars. From a subset of young pulsars in their study, the authors compute an average birth velocity of around 400 km s^{-1}. The fastest pulsar for which they have an accurate (parallax) distance measurement (PSR B1133+16) has a speed of 640 km s^{-1}, whereas some pulsars with less accurate distance measurements (e.g. inferred from electron density models, see Sec. 1.2.2) have speeds greater than 1500 km s^{-1}.

1.1.3 The pulsar period P and its derivative $\dot{P}$

The most accurately measured properties of pulsars are their spin periods (P) and their period derivatives ($\dot{P}$), i.e. the rate at which they are spinning down. An updated P-$\dot{P}$ diagram (plotting P against $\dot{P}$ on a logarithmic scale) for over 2500 radio pulsars is shown in Fig. 1.3. The bulk of the pulsar population has periods between 0.1 and 3.0 sec. These are the so-called normal or isolated pulsars, born through a single core-collapse supernova as described in Sec. 1.1.1. In Sec. 1.1.3.2, I

[1]http://www.atnf.csiro.au/research/pulsar/psrcat
[2]http://www.physics.mcgill.ca/ pulsar/magnetar/main.html

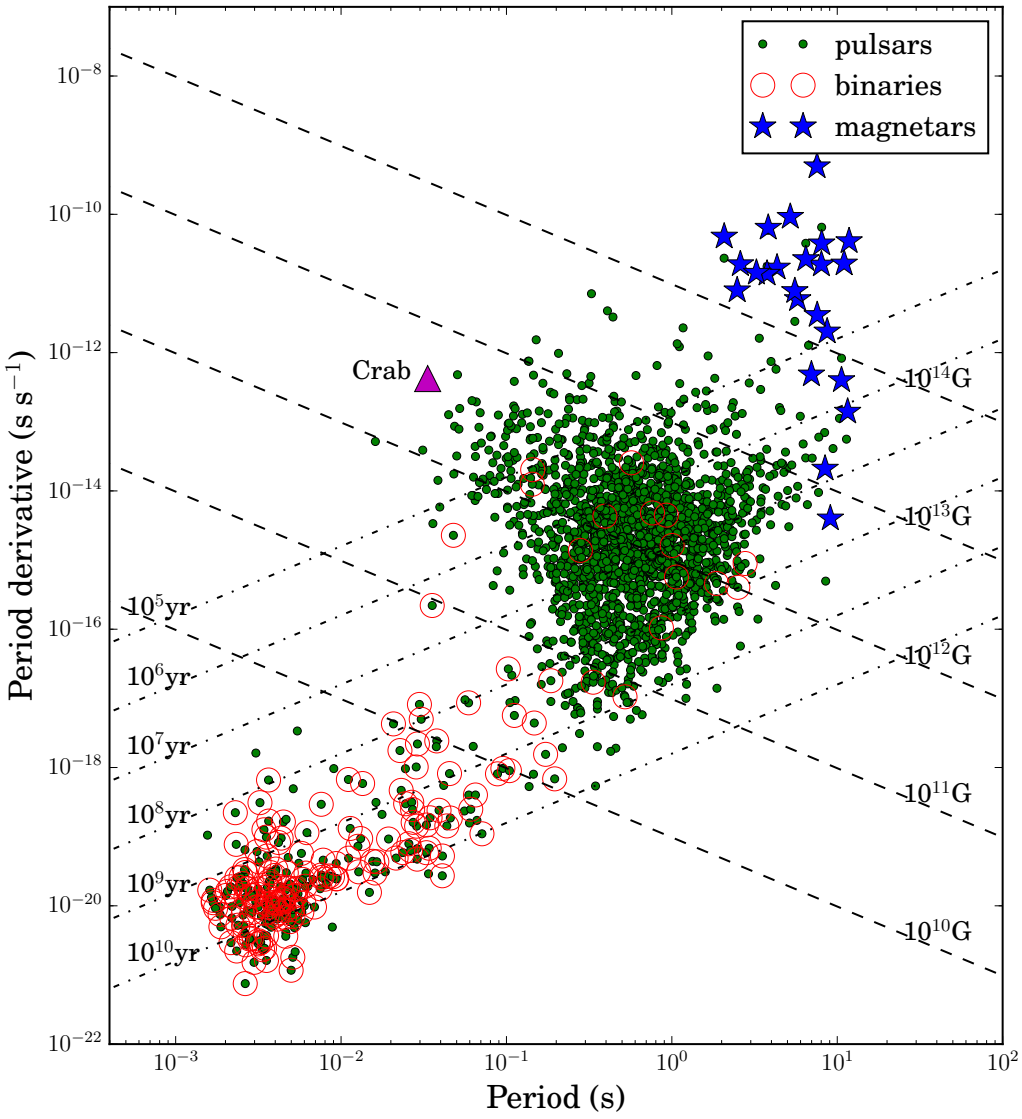

Figure 1.3: A P-$\dot{P}$ diagram showing the pulsar population as a function of their rotational periods and period derivatives. Binary systems are circled in red, and magnetars shown as blue stars. The young Crab pulsar is labelled with a magenta triangle. This P-$\dot{P}$ diagram was produced using data from the online ATNF pulsar catalogue[1] (version 1.56, as on 11 April 2017; Manchester et al. 2005). Magnetar data points were added using the McGill online magnetar catalogue (Olausen & Kaspi, 2014)[2].

will present an overview of two more classes of pulsars, the millisecond pulsars (circled in red) and magnetars (blue stars).

1.1.3.1 Derived pulsar parameters

The P-$\dot{P}$ diagram of Fig. 1.3 also contains lines of constant *characteristic magnetic field* strength (dashed lines, in units of Gauss) and lines of constant *characteristic age* (dotted lines, in years). These indirect properties can be derived from the measured P and $\dot{P}$ values of a pulsar, using a simple pulsar model as follows.

In the canonical model, shown in Fig. 1.1, the surface magnetic field of the pulsar is modelled as a dipole, with closed and open field lines. The radio beam is associated with the open field lines, separated from the closed field lines that are contained within the *light cylinder* radius. At this distance from the neutron star surface, the co-rotation speed is equal to the speed of light, such that no plasma co-rotates with the neutron star beyond the light cylinder radius.

The rotating magnetic dipole radiates electromagnetic waves, causing the spinning dipole to slow down. The evolution of the rotational frequency, ν, of the pulsar is given by,

$$\dot{\nu} = -C\nu^n, \qquad \text{or similarly,} \tag{1.1}$$

$$\dot{P} = CP^{2-n}, \tag{1.2}$$

in terms of the rotational period, where n is the braking index and C a constant. For a pure magnetic dipole we expect $n = 3$ (Lorimer & Kramer, 2004). Note however that many deviations from $n = 3$ have been measured, as shown in e.g. Espinoza et al. (2011), Archibald et al. (2015).

From this simplified model a *characteristic age* (τ_c) can be defined, that is the time over which the pulsar has been spinning down due to the above magnetic braking, to reach its current P and $\dot{P}$ values. Assuming that its birth period was much shorter than the current P,

$$\tau_c = \frac{P}{2\dot{P}}\,. \tag{1.3}$$

The strength of a *characteristic magnetic field* (B) can be estimated too, based on the pure dipole model, and by additionally assuming that the pulsar is an orthogonal

rotator (i.e. the angle between the spin axis and rotational axis is 90°) with typical canonical values for its radius and moment of inertia. Under these assumptions,

$$B = 3.2 \times 10^{19}\ \mathrm{G}\sqrt{\mathrm{P}\dot{\mathrm{P}}}. \tag{1.4}$$

For a more detailed derivation please refer to a standard pulsar textbook, such as the *Handbook of Pulsar Astronomy* by Lorimer & Kramer (2004). Fig. 1.3 shows that typical characteristic ages for canonical pulsars range from 100 kyr to 10 Gyr. The characteristic magnetic field strength, of the bulk of the canonical pulsars, lies between 10^{11} and 10^{13} G. These large magnetic fields may be formed through the conservation of the progenitor star's magnetic field, although the process is poorly understood (e.g. Spruit 2009). A massive main sequence star has a magnetic field typically of the order of 100 G. During the gravitational collapse the radius of the star shrinks by a factor of approximately 10^5, or equally the surface area shrinks by a factor of 10^{10}, leading to an increase of the surface magnetic field by a factor of 10^{10} to reach a field size of approximately 10^{12} G (Teukolsky & Shapiro, 1983).

1.1.3.2 Pulsar populations

The pulsar parameters computed above and displayed on the P-$\dot{P}$ diagram, provide insight into two other pulsar populations, besides normal isolated pulsars, namely millisecond pulsars and magnetars.

Millisecond pulsars

The concentration of pulsars in Fig. 1.3 with periods below 10 ms, most of which are marked as binaries (red circles) is the group of millisecond pulsars (MSPs), often also called *recycled pulsars*. They represent an older population of pulsars, with characteristic ages lying between 10^8 and 10^{10} years.

The majority of MSPs are in binary orbits, with their binary companions ranging from white dwarfs to main sequence (MS) stars or other neutron stars. These systems are thought to have evolved from progenitor MS star binaries. The more massive MS star in the original binary system will undergo a supernova explosion (as discussed in Sec. 1.1.1) leading to the formation of a neutron star or pulsar. Most often the impact of the supernova will completely disrupt the binary. However, if the newly formed neutron star remains bound to its companion, it can evolve into a MSP. Over the next few million years, the companion star evolves, expanding into a red giant star. Due to the strong gravitational attraction of the neutron star, matter from the

atmosphere of the red giant can be accreted onto the neutron star. This accretion process spins up the neutron star to reach millisecond periods. It also dramatically weakens the magnetic field of the neutron stars (Shibazaki et al., 1989), such that MSPs end up with magnetic field strengths below 10^{10} G, as seen on the P-$\dot{P}$ diagram.

The fast spin rates of MSPs leads them to have narrower light cylinders than normal pulsars. This means that a larger fraction of the magnetic field lines will be unbounded, leading to broader associated radio beams. As such, the observed MSP profile covers a larger fraction of the pulse period, and is said to have a higher *duty cycle* than normal pulsars.

In Chapter 4, when I create simulated pulsar data, I do so for both a canonical pulsar, with a period of 1.0 s and duty cycle 2.5%, and for a typical millisecond pulsar with a period of 20 ms, and duty cycle of 10%.

Magnetars

Magnetars are indicated in the top right corner of Fig. 1.3 (blue stars). From their large P and $\dot{P}$ values, they are inferred to have magnetic fields much larger than ordinary pulsars. Magnetars are observed to produce both X-ray and γ-ray flares, and have highly variable radio emission. The high energy flares are believed to be powered through the decay of the magnetar's strong magnetic field.

To date, 29 magnetars are known (Olausen & Kaspi, 2014), of which only four are observed to emit in the radio spectrum. They share many properties with young pulsars, and are therefore anticipated to provide insight into the evolutionary history of pulsars. A recent review of magnetars and their properties can be found in Kaspi & Beloborodov (2017). Only one magnetar features in this thesis, in Sec. 7.1, when I consider the pulsar population and the scattering properties around the Galactic Centre.

1.1.4 Pulsar radio emission is strongly frequency dependent

A comprehensive understanding of the radio emission mechanisms in pulsars, is still lacking (see e.g. Graham-Smith 2003, Melrose & Yuen 2016). However, the simplified theoretical models described here have observational consequences, that in many ways match what we do see. More involved theoretical studies of the pulsar radio emission mechanism can be found in the recent works by P. B. Jones (2014, 2015).

I start with the same simplified picture of the previous section, in which the pulsar is modelled as a rapidly rotating magnetic dipole. The rapidly rotating magnetic

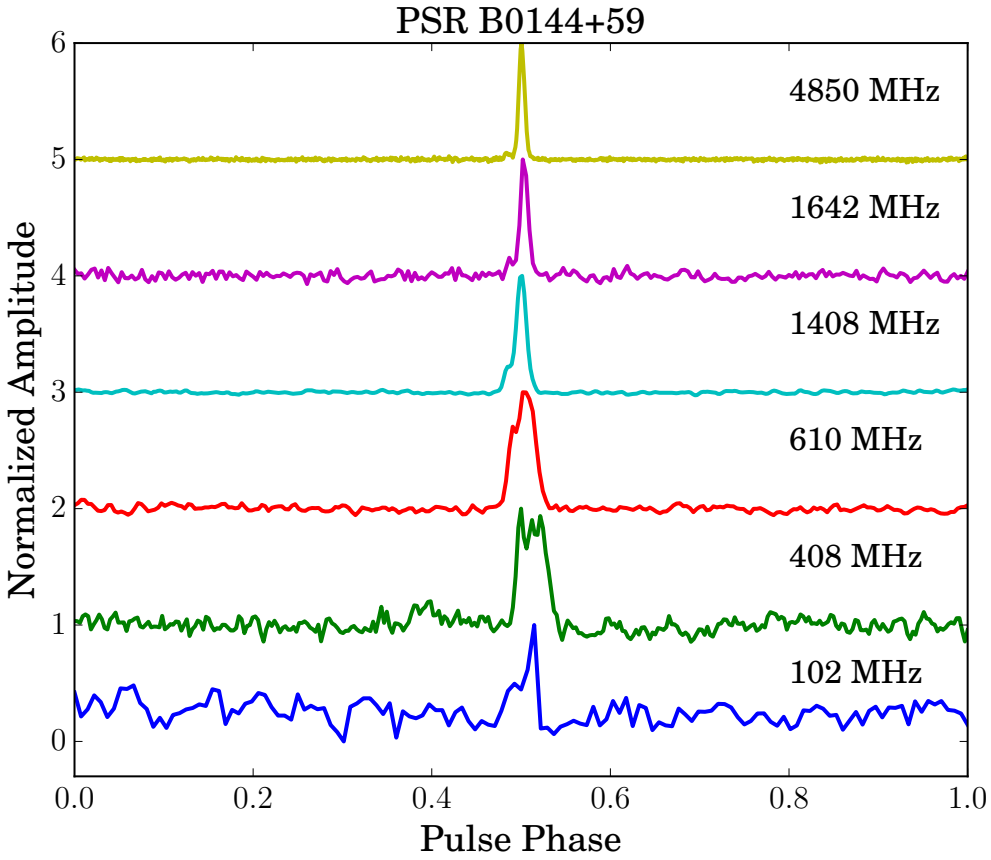

Figure 1.4: Average profile shapes of PSR B0144+59 at different frequencies. This figure was created using profiles from the European Pulsar Network (EPN) database[3] (Lorimer et al., 1998).

dipole induces an electric field (somewhat similar to a disk dynamo) that accelerates charged particles from the neutron star surface along the open field lines. This particle beam accelerated along the magnetic field lines, emits high-energy γ-rays through curvature radiation. Subsequently, the γ-rays interact with the background magnetic field causing a runaway production of electron-positron pairs (Sturrock, 1971). These pairs form the coherent plasma responsible for the beamed emission observed along the magnetic axis. The emitted radio beams are broad band, with pulsars having been observed across the radio spectrum from $\sim$ 30 MHz to 300 GHz.

1.1.4.1 Frequency dependence of average pulsar profiles

The simplest model of the radio beam is a cone-shaped beam framed by the arrangement of the dipole magnetic field lines (Radhakrishnan & Cooke, 1969). The observed radio pulse represents a trajectory through the pulse beam when it cuts

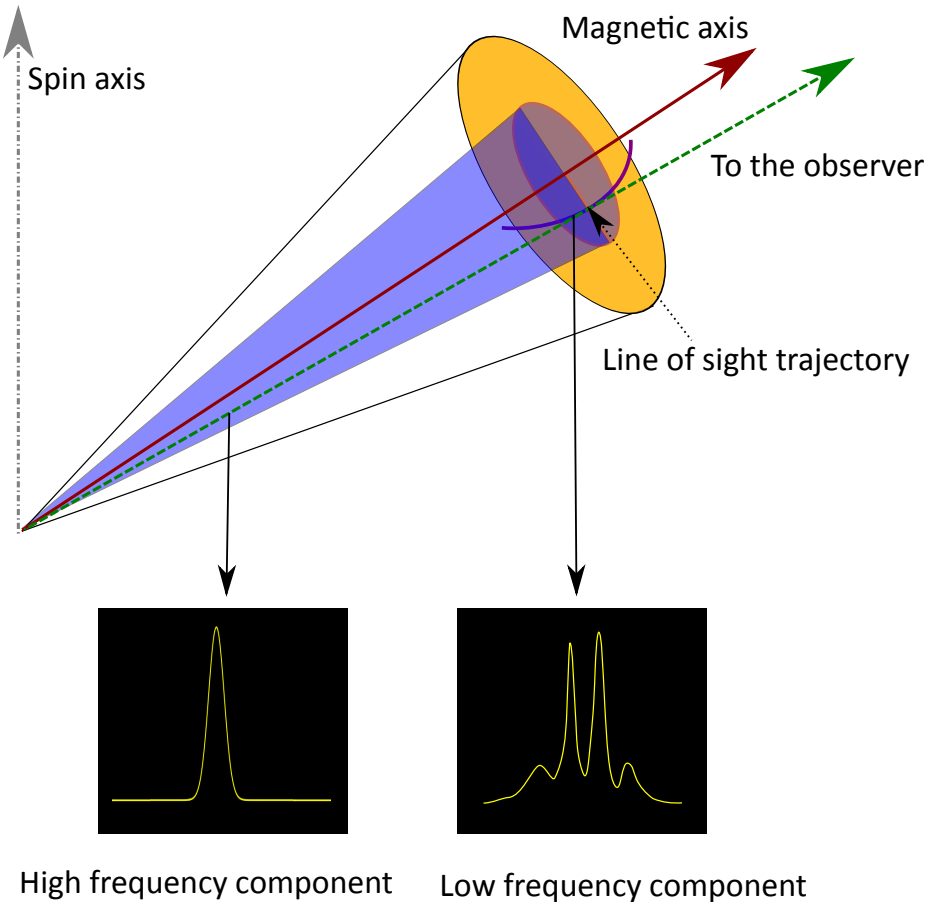

Figure 1.5: A diagram of a simple pulsar beam model. The cone-shaped beam is broader further away from the neutron star surface. The *radius-to-frequency mapping* (RFM) model suggests that higher frequencies are emitted closer the surface leading to narrower pulse shapes, whereas the emission heights for lower frequency radiation increases creating broader pulse shapes. A complex beam interior (here simply modelled as a secondary cone imbedded in the beam) can also lead to varying pulse shapes (with a varying number of components) at independent observing frequencies. Credit: M. Geyer

our line of sight. Pulsar observations show a strong dependence of profile shapes with frequency. Observational evidence mostly points to broader pulse profiles at low frequencies, and a decrease in multi-component separation with frequency (Gupta & Gangadhara, 2003, Rankin & Rosen, 2014). Fig. 1.4 shows these trends for the average profile shapes of PSR B0144+59 at various observing frequencies.

The simple cone-shaped model can account for this frequency dependence, by assuming that higher frequencies are emitted closer to the neutron star surface leading to narrower pulse profiles, while lower frequencies are emitted at higher emission heights, leading to broader profiles, as illustrated in Fig. 1.5 (Thorsett, 1991). This is known as *radius-to-frequency mapping* (RFM, Cordes 1978), since the radii of different sections of the cone are associated with different emission frequencies.

A recent study of the profile evolution of a small set of pulsars (Hassall et al., 2012), across the same low frequency range as used in this thesis, found frequency evolution features that are not well explained by a RFM model. The authors found that in some cases the radio emission originates from a small range of heights in the magnetosphere, in contradiction to the RFM picture which predicts a range of emission heights. Additionally, for some targets the profile width or component separation was found to increase with increasing frequency – the inverse of what is expected from a RFM model.

Ongoing research aims to address our understanding of such intrinsic changes through improved modelling of the pulsar magnetosphere and the beam interior. This includes for e.g. modelling beam structures with a patchy nature and a finite number of emission regions (Kijak & Gil, 2002).

1.1.4.2 Frequency dependence of pulsar flux

Pulsar flux measurements are observed to be strongly frequency dependent. Pulsars have steep flux density spectra, such that they are brighter at low frequencies than at higher frequencies. The pulsar observations used in this thesis are conducted at frequencies between 110 MHz and 190 MHz where pulsars are typically bright.

Pulsar flux spectra are mostly modelled using a power law $S_\nu \propto \nu^{-\gamma}$, with ν the observing frequency. Observed spectral indices have a mean value of $\gamma = -1.8 \pm 0.2$ (Maron et al., 2000), or more recently $\gamma = -1.4 \pm 1.0$ (Bates et al., 2013). Spectral indices in these ranges are used in Chapter 4 to accurately simulate pulsar data.

Deviations from a simple power law flux spectrum have been observed. Most notably some pulsar spectra appear to turn over at low frequencies, typically around

[3]http://www.epta.eu.org/epndb/

100 MHz (Lorimer et al., 1995), similar to the frequencies studied in this thesis. Thermal absorption by dense surrounding environments may be partially responsible for spectral turnovers (Rajwade et al., 2016). Some evidence suggests that the efficiency of the radio emission shuts off at lower frequencies (Malofeev et al., 2000). Alternatively, extrapolating from the RFM model discussed in the previous section, the intersection of the line of sight with the radio emitting regions will also be frequency dependent, with the possibility of the line of sight gradually missing the emitting regions altogether at low frequencies. In contrast, a small group of pulsars show turnovers at much higher frequencies. These are known as the gigahertz peaked spectrum (GPS) pulsars. The GPS turnovers are also attributed to either the radio emission process becoming inefficient above a threshold frequency, or dense IISM environments (Kijak et al., 2007, 2011).

In this thesis I will study the effects of pulsar scattering at low frequencies on observed flux spectra, and investigate how scattering effects could cause spectral turnovers too.

In contrast to this picture for ordinary pulsars, radio magnetars are mostly observed to have flat spectra, as revisited in Sec. 7.1 (Camilo et al., 2007, Levin et al., 2010).

1.1.5 Modern Science with Pulsars

The extreme compact nature of pulsars, together with their large spin rates and associated angular momentum make them highly stable objects. The periods of the best timed millisecond pulsars are known to within 1 part in 10^{13} (e.g. Desvignes et al. 2016).

This impressive tick-rate precision has led to a research field in pulsar astronomy known as *pulsar timing*. Pulsar timing experiments conduct long-term monitoring programmes of millisecond pulsars, that aim to model the time of arrival (ToA) of pulsar signals with supreme accuracy, by accounting for as many of the physical processes as possible that impact upon the observed pulse arrival times. These include modelling intrinsic rotational parameters, P and $\dot{P}$, as well as external effects, such as pulsar proper motion, binary orbital motion (if the pulsar has a binary companion) and IISM signal propagation.

Formally, there are three dedicated pulsar timing efforts, known as the European Pulsar Timing Array (EPTA), the Parkes Pulsar Timing Array (PPTA) in Australia and the North American Nanohertz Observatory for Gravitational Waves (NANOGrav). Each of these three pulsar timing arrays (PTAs) regularly times a set

of millisecond pulsars. Their combined datasets form the International Pulsar Timing Array (IPTA, Verbiest et al. 2016) collaboration. The main aim of this timing programme is to detect low frequency (nanohertz) gravitational waves (GWs), based on the idea that a GW passing between Earth and a field of pulsars, will alter the observed ToAs in a predictable and correlated way (Hobbs et al., 2010, Ravi et al., 2015). More precisely, the correlation in the timing residuals of any pair of pulsars will be a function of their angular separation as described by the Hellings and Downs (1983) curve. The most prominent sources of GWs in the nanohertz band, are expected to be the mergers of supermassive black holes ($\gtrsim 10^6$ $M_\odot$, e.g. Manchester 2010).

While the detection of GWs is the ultimate goal of many pulsar timing experiments, accurate timing models and timing datasets address a variety of interesting pulsar science. This includes conducting high precision tests of General Relativity, improving pulsar evolutionary models, investigating the intrinsic variability of pulsars as well as their magnetospheric and interior compositions.

To date, the most precise test of Einstein's theory of General Relativity, relies on measurements of the relativistic corrections to the Keplerian orbits of the double pulsar system, obtained through timing analysis (Kramer et al., 2006). These include measurements of the binary orbital decay, due to the emission of GWs. GWs are predicted to be fundamentally quadrupolar by GR (e.g. Hartle 2003). Particular tests of alternative *scalar-tensor* field theories can be conducted with relativistic binary systems where one object is more compact than its companion. Under these conditions scalar-tensor theories predict both dipolar and quadrupolar GW emission, and consequently a faster orbital period decay. The relativistic binary containing PSR J0348+0432, with a record mass of $\sim 2M_\odot$, and a low mass white dwarf, is currently used to conduct such tests (Antoniadis et al., 2013). Furthermore, improved constraints of the Strong Equivalence Principle, are expected to come from a recently discovered triple system, consisting of a MSP and two white dwarfs in close hierarchical orbits around the pulsar (Ransom et al., 2014, Shao, 2016).

The regular monitoring of pulsar periods, period derivatives and the associated braking index (Eq. 1.1) can improve our understanding of pulsar evolution and consequently their birth rates. A variety of models describing the evolutionary tracks of pulsars (from birth to death) across the P-$\dot{P}$-diagram, have been suggested (e.g. Johnston & Karastergiou 2017). An understanding of pulsar evolution and pulsar birth rates, in turn, helps address questions of how the observed pulsar population relates to the population of massive stars, their conventional progenitors. A study by

Keane & Kramer (2008) suggested that current estimates of the birth rate of isolated neutron stars are not consistent with the Galactic core-collapse supernova rate.

Evolutionary studies also enable us to form connections between different subclasses of the pulsar population, namely normal pulsars, millisecond pulsars, magnetars and high energy emitters (see Fig. 1.3). Of the current population of confirmed magnetars, about a third are found to be associated with supernova remnants, similar to young neutron stars (Kaspi & Beloborodov, 2017). Both high magnetic field neutron stars and magnetars have been found to exhibit similar behaviour, such as dramatic X-ray outbursts and intermittency in their radio emission, suggesting an evolutionary path between the two classes (Archibald et al., 2008, Ng & Kaspi, 2011). Investigations of a recent subclass of *transitional MSPs* are also revealing evolutionary links between a radio MSP state and an accreting X-ray pulsar state. These sources, as e.g. PSR J1023+0038, are observed to switch between a low-mass X-ray binary state where an accretion-disk is present, and an eclipsing radio pulsar state over timescales of several years (Archibald et al., 2009, Papitto et al., 2013, Deller et al., 2015).

The long term timing of pulsars also advances our analyses of a range of time-varying effects observed in pulsars. These include *nulling* and *state switching*, whereby the pulsar's radio emission is observed to switch off and then on, or to oscillate between different emission states. The timescales of these changes can range from a few pulse periods to hours or days (e.g. Wang et al. 2007, Lyne et al. 2010, Lorimer et al. 2012). Pulsars are also observed to switch off over longer timescales such as months and years, at which point they are called *intermittent* pulsars (e.g. Lyne et al. 2017).

Some sources are observed to emit giant pulses. The Crab pulsar discussed above, (and in more detail in Sec. 7.2) is a particularly extreme example, regularly emitting giant pulses with intensities a thousand times higher than its typical emission. Individual bright bursts with mega-Jansky intensities have been observed to last for only 0.4 nanoseconds Hankins & Eilek (2007), implying an emission region at most a metre in diameter. The current understanding of the mechanisms underpinning these dramatic types of pulsar variability is still far from complete.

Insight into the pulsar's magnetospheric composition can be gained from monitoring correlations between radio emission and high energy (e.g. X-ray or γ-ray) emission, leading to improvements in the plasma emission models of pulsars (Espinoza et al., 2013, Philippov et al., 2015).

Furthermore, a phenomenon known as *glitching* leads to sudden period changes in pulsars. Typically, glitches cause a spin-up in the pulsar period after which the spin-

down rate is found to increase (e.g. Radhakrishnan & Manchester 1969, Espinoza et al. 2011). Glitches are thought to be caused either by quakes in the crystalline crust of the neutron star surface or to be a consequence of the superfluidity of the neutron star interior (Anderson & Itoh, 1975). The rotating superfluid leads to the creation of superfluid vortices that weakly *pin* to the neutron star surface. As long as these vortices remain pinned to the crust, the superfluid does not spin down, thereby storing angular momentum in the interior (Haskell & Melatos, 2015). This reservoir of angular momentum is believed to periodically be released in the form of glitches. As such, continuous monitoring of pulsars can lead to an improved understanding of the complex neutron star interior and its equation of state (Anderson et al., 2012).

Lastly, as described in more detail in Sec. 1.3 and Chapter 2, long term monitoring of high velocity pulsars can improve our understanding of the detailed structure of the IISM. As the pulsars move across the sky, and the Earth around the Sun, our line of sight through the IISM to them changes continuously, allowing us to probe electron densities and density variations in the IISM.

1.2 An Overview of the ionized ISM

All the stars and objects in the Galaxy are embedded in a diffuse medium referred to as the *interstellar medium* (ISM). The ISM contains gas (made of atoms, molecules, ions and electrons), magnetic fields, and dust (tiny solid particles), all of which acts as a reservoir for stellar components.

Stellar matter is believed to cycle from the densest colder molecular parts of the ISM, where star formation can be catalysed, into new stars. Eventually a fraction of this material will be injected back into the ISM through stellar winds and supernova explosions that generate turbulent flows in the ISM, which can, in turn, lead to the birth of new molecular regions prone to star formation, completing the cycle (Ferrière, 2001).

1.2.1 The IISM through optical emission lines

The component of the interstellar medium that is relevant to studies at radio frequencies, is the magneto-ionic component of the ISM, most often just called the ionized ISM (IISM). The IISM was first detected 30 years before the discovery of pulsars through Hα and other optical emission lines (Struve & Elvey, 1938). An Hα transition is the Balmer transition of hydrogen from the second excited energy level ($n = 3$) to the first ($n = 2$). These emission lines can be used to estimate electron densities,

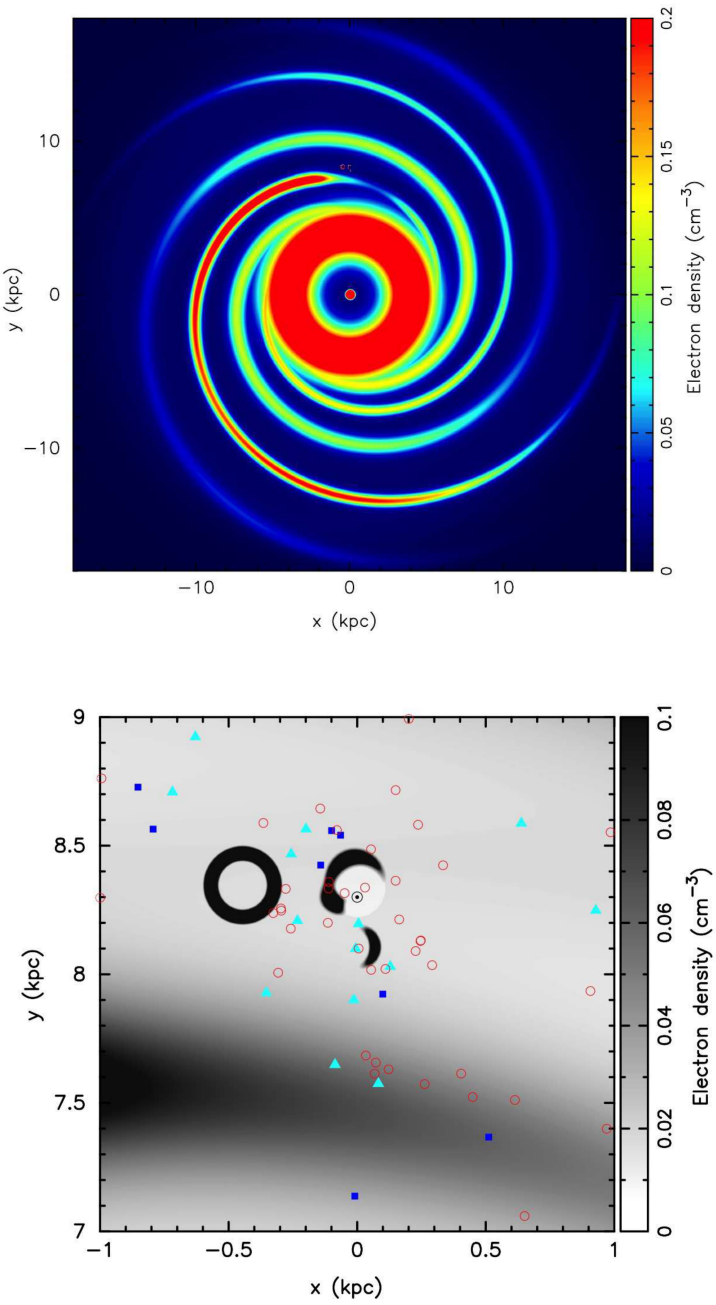

Figure 1.6: Taken from Yao et al. (2017). *Top:* The YMW16 electron density model in the Galactic plane. The Galactic Centre is at the origin and the Sun is at $x, y = 0.0, 8.5$ kpc. The dense annulus of central radius 4 kpc is the Galactic molecular ring. Spiral arms have a pre-determined logarithmic spiral form and generally decay exponentially at large Galactocentric radii. Exceptions are in the Carina-Sagittarius arm where there are over-dense and under-dense regions. Some local features are faintly visible near the position of the Sun. *Bottom:* Close-up of the local electron density model. The position of the Sun is marked with $\odot$. Identifiable features are the Carina enhancement and Carina-Sagittarius spiral arm, the Gum Nebula, the Local Bubble and Loop I (at $x, y = 0.1, 8.1$ kpc).

since the rate at which hydrogen ions combine with free electrons to form excited hydrogen atoms that emit Hα lines, is proportional to

$$n_{H+} n_e \propto n_e^2, \tag{1.5}$$

(Ferrière, 2001), with n_{H+} the density of hydrogen ions (free protons) and n_e the free electron density.

The temperature of the IISM, inferred from the width of the observed optical emission lines, is approximately 8000 K (Ferrière, 2001). The emission measures of these optical lines originally lead to computed average electron densities between 0.06 and 0.1 cm^{-3} (Reynolds, 1983, 1985, Ferrière, 2001). At the turn of the century, high resolution Hα maps by the Wisconsin H Mapper (WHAM) survey (Reynolds et al., 1999) displayed 'patches, filaments and loops' (Ferrière, 2001), revealing the complex patterns of enhanced Hα emission in the Galaxy,

The main components of a Galactic electron density (n_e) model, such as the Galactic spiral arms, can in general be inferred from our knowledge gained through Hα surveys, together with studies of the distribution of molecular gas and star-forming regions. However, electron densities measured through optical emission lines suffer from obscuration effects due to interstellar dust, leading to large uncertainties in the measured values. Optical emission lines alone can therefore not describe IISM structures in detail.

1.2.2 Current electron density models

To improve on the picture described above, pulsar observations, which are unaffected by dust, need to be included. In the next section, I will briefly discuss how pulsar signals interact with the free electron content of the IISM, leading to independent measurements of the n_e along a given line of sight in the Galaxy. The theory of these interactions is discussed in more detail in Chapter 2. Pulsars for which independent distances are known, through e.g. parallax measurements and associations with supernova remnants or globular clusters, are especially indispensable for building up an extensive model of the free electron content of our Galaxy.

Fig. 1.6 shows the most recent electron density distribution model, known as the YMW16 model, published in Yao et al. (2017). This model represents an improvement to the previous NE2001 (Cordes & Lazio, 2002), that has been the standard in use for the last 15 years. The YMW16 model has the same basic structure as its predecessors (Taylor & Cordes, 1993, Cordes & Lazio, 2002). It uses independent

distance measurements to 189 pulsars. The most prominent local features in this model include the Local Bubble, the Gum Nebula and Loop I as seen in Fig. 1.6 and described in Yao et al. (2017).

1.3 Pulsars and the IISM

Sec. 1.1 discussed intrinsic properties of pulsars and pulsar observations that are relevant to how pulsars are used as probes of the IISM. The compactness of pulsars allows us to treat them as point sources at the distances at which they are observed. This simplifies the modelling of how pulsar signals travel through the IISM, described in more detail in Sec. 2.2.1.1. Moreover, their high velocities mean that the line of sight to a pulsar, and therefore the IISM environment along the line of sight, changes with time, especially if they are embedded in complex environments such as nebulae. In particular, as discussed in Sec. 2.2.2, the relative motion between the IISM and the pulsar can cause interference patterns of the radio waves. Studying these patterns allows us to probe small scale characteristics within the IISM.

An overview of some of the chief interactions between the propagating pulsar signals and the IISM is given below, the details of which are the topic of the next chapter. Understanding these interactions leads to, amongst other things, estimates of n_e values along a given line of sight, which in turn can be used to refine the electron density models of Sec. 1.2.2.

1.3.1 Frequency dependent delays

The radio waves emitted by pulsars are perturbed by the charged particles in the IISM along their travel path. These interactions slow the radio waves down. The delays are dominated by the free electrons in the IISM and exaggerated at lower frequencies. By measuring the delay between pulse arrival times at a higher frequency compared to a lower frequency, during a pulsar observation, an estimate for the integrated electron density along the line of sight can be computed. These delay measurements (Dispersion Measure, Sec. 2.1.1) have led to an estimate of the mean Galactic electron density, $\langle n_e \rangle \sim 0.03$ cm^{-3}, for a smooth IISM density distribution (Ables & Manchester, 1976, Gómez et al., 2001).

1.3.2 Frequency dependent scattering

Inhomogeneities in the electron densities (Δn_e) along the line of sight, scatter radio emission, leading to the multipath propagation of pulsar signals. This scattering

induced by the IISM has a strong frequency dependence, causing both a characteristic broadening of received pulse shapes, as well as exponential *scattering tails* at low frequencies (Sec 2.2.1). The scattering tails of the broadened profiles are routinely modelled with exponential functions that take the form $e^{-t/\tau}$, where τ is referred to as the *characteristic scattering time*. Simple theoretical models, as discussed in Chapter 2, predict $\tau \propto \nu^{-4}$, with ν the observing frequency.

The analysis of the scattering of pulsar signals is pointing to an ever more inhomogeneous view of the Galactic electron density distribution. Studies have for example shown that the interstellar scattering of pulsar observations is often dominated by a single, or at most a few, regions of strong electron density fluctuations along the line of sight (Stinebring 2006, Trang & Rickett 2007, Sec. 2.2.3). Further evidence for clumpiness in the IISM, comes from dramatic flux variations in pulsar observations (Extreme Scattering Events, Sec. 2.2.3). These events are believed to be caused by small AU-sized ionized gas clumps (Walker, 2007). Pulsar scattering observations have also revealed an anisotropic nature of the IISM along certain lines of sight, leading to an elongated image of the pulsar (Brisken et al., 2010) and other structured features, such as parabolic arcs (Sec. 2.2.3) in pulsar observations.
Pulsars are effective probes of the IISM. The improvements of our understanding of the IISM characteristics has greatly been due to enhanced data quality from pulsar studies. However, higher quality pulsar observations are simultaneously revealing an increasing complexity of the frequency dependence of intrinsic pulsar signals. Intrinsic frequency dependent profile and flux evolution, as discussed in Sec. 1.1.4, complicates the task of separating IISM effects from intrinsic pulsar profile effects, since the profile shape cannot be treated as frequency independent, and accurate models of the intrinsic profile evolution are lacking.

1.4 Open Questions

Studies of the interactions of pulsar radio emission with the IISM, have unveiled many characteristics of the IISM structure, allowing us to construct increasingly sophisticated electron density models as shown in Sec. 1.2.2. However, as discussed above and revealed in more detail towards the end of Chapter 2, observations of pulsar propagation in the IISM have also lead to many unexpected results, pointing to an ever more anomalous and complex IISM, in need of further investigation.

With the aim of making progress towards a more comprehensive understanding of pulsar-IISM interactions, I pose the following *Open Questions*. Throughout this

thesis, I will return to these questions and consider how the analysis and results in this work, help address each of them.

I **How are pulsar profile shapes affected by the IISM at different frequencies?** Theoretical scattering models describe particular changes in observed pulse shapes at low frequencies. Are these the shapes we observe, and if any deviations are seen what could be the cause?

II **Does the frequency dependence of pulsar scattering spectra change with frequency?** Simple theoretical models expect scattering timescales to be described by a power law in frequency with a predicted spectral index. Do we observe the same power law spectral index at all frequency ranges? Or can the spectral index change with frequency? If so, what underlying IISM characteristic is causing such a change?

III **What temporal broadening functions effectively describe the scattering of pulsar signals by the IISM?** An accurate model of the temporal broadening function associated with the IISM along a given line of sight will greatly improve our ability to correct for the scattering effects - unveiling the intrinsic pulsar shape. Do we have the correct models for temporal broadening functions?

IV **Is there evidence in pulsar profile observations for clumpiness in the IISM?** From the observed profile shapes to the derived IISM broadening functions, is there evidence for finite scattering surfaces in the IISM? And if so, how can we design observations to reveal the presence of small scattering clouds? How does a clumpy IISM change our electron density distribution models?

V **Is there evidence in pulsar profile observations for anisotropic scattering?** Several authors and observations have suggested that the IISM can scatter pulsar signals anisotropically. Is there evidence for this in the pulsar profile shapes used in this thesis?

VI **Do we observe IISM effects on pulsar flux spectra at low frequencies?** The extreme scattering of pulsar pulses can smear out the periodicity of the signal. Do these effects impact the flux densities calculated from low frequency pulsar observations? Can we correct for such effects through effective modelling?

VII **How can we best disentangle intrinsic pulsar effects from IISM propagation effects?** An improved understanding of pulsar scattering will allow us to better decouple intrinsic variability from ISM effects. However if a more complex picture of the frequency dependence of pulsar scattering emerges (as seen in e.g. Löhmer et al. 2004, Lewandowski et al. 2015), then this will become less straightforward.

1.5 This Thesis

This thesis investigates the nature of pulsar scattering at low frequencies using data from the Low Frequency Array (LOFAR). In doing so, I consider how my findings at these low frequencies help address the questions posed above.

The thesis is organised as follows. In the next chapter, Chapter 2, I present the theory of the propagation of pulsar signals through the IISM. In Chapter 3, I discuss how pulsar observations are conducted and describe the data used in this study. Thereafter in Chapter 4, I provide a detailed analysis of numerical pulsar scattering fitting techniques. I propose a robust fitting technique that is effective at obtaining scattering properties from pulsar profiles in the presence of high levels of scattering, using both isotropic and anisotropic broadening functions. In Chapter 5, I analyse the scattering properties of a subset of 13 LOFAR pulsars that exhibit strong scattering and have simple profile shapes, commenting on the measured scattering timescales (τ) and scattering spectral indices (α), as well as the intrinsic pulsar properties and the calculated flux spectra. In Chapter 6, I discuss the results of the LOFAR data analysis extensively. I present continued applications of my scattering techniques and additional ongoing projects in Chapter 7. This includes a brief scattering analysis of the Galactic Centre environment, as well a study of the scattering timescales of the giant pulses of the Crab pulsar. I also describe a tangential project which investigates the nature of the diffuse IISM by comparing results from pulsar scattering to Far-Infrared (FIR) spectroscopy results. I end with my conclusions in Chapter 8 and future work and suggested proposals in Chapter 9.

Chapter 2

Pulsar IISM Theory

As pulsar signals travel towards Earth, they interact with the IISM in several ways. These effects can be grouped into imprints resulting from the *homogenous* component of the interstellar medium described by an average electron density (*dispersion* and *Faraday rotation*), and imprints resulting from the *inhomogeneous* component of the interstellar medium described by fluctuating electron density values (*scattering* and *scintillation*).

2.1 Pulsar propagation in a homogenous medium

2.1.1 Dispersion

In February 1968 the discovery of the first pulsar CP1919 (later renamed to PSR B1921+21) was published in *Nature*. The observations were made using the large radio telescope at the Mullard Radio Observatory in Cambridge. In this original publication, the authors showed that the pulsar signal at 80.5 MHz was detected 0.2 s later compared to the 81.5 MHz signal (Hewish et al., 1968).

This pulse delay with frequency is due to interstellar *dispersion*. Fig. 2 shows the dispersed pulse of PSR B1919+21, observed at 146 MHz. The frequency dependence of these delays (Δt) is inversely quadratic,

$$\Delta t \ \propto \ \mathrm{DM} \times (\nu_{\mathrm{L}}^{-2} - \nu_{\mathrm{H}}^{-2}), \tag{2.1}$$

where the frequencies ν_L and ν_H are the lower and higher observing frequencies, measured in MHz, between which the delay is estimated, and DM is the *dispersion measure* expressed in units of pc cm^{-3}.

The observed delays are due to the radio waves interacting with charged particles in the IISM along their travel path. The magnitude of the delay depends on the

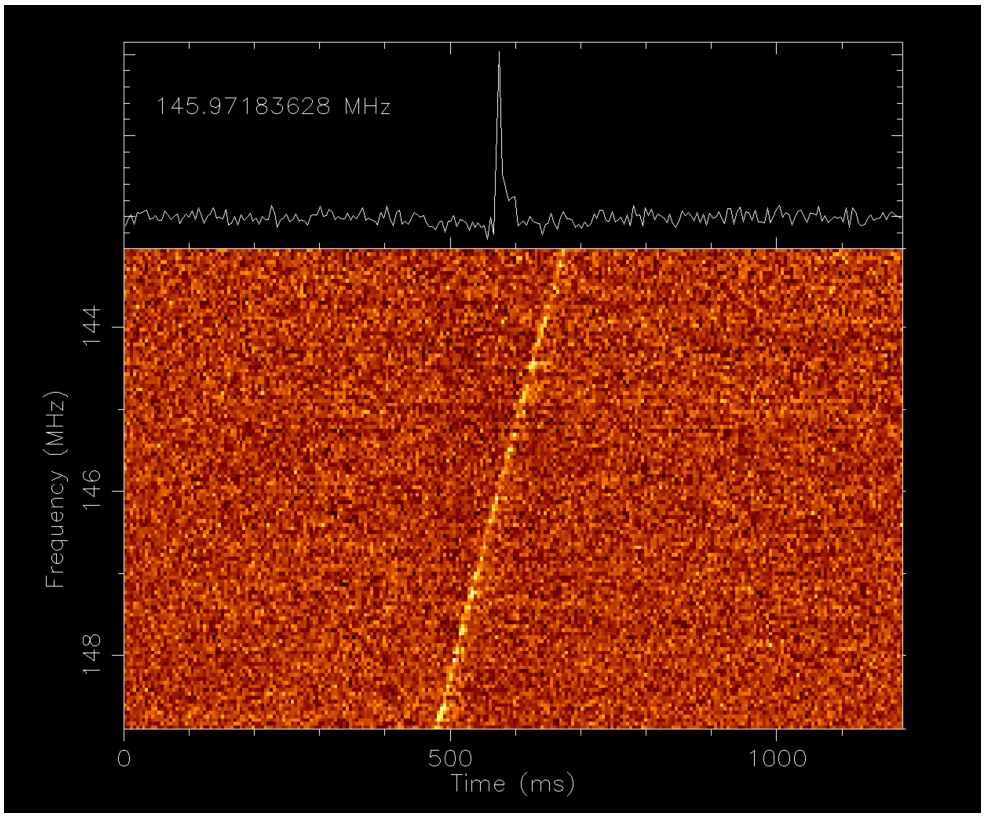

Figure 2.1: An observation of PSR B1919+21 at $\sim$ 146 MHz, showing the dispersed nature of the pulse. The pulse in the highest observing frequency channel arrives approximately 150 ms before the pulse in the lowest frequency channel. The observation was taken with the Rawlings Array at the Chilbolton Observatory in the UK, one of the Low Frequency Array (LOFAR) international stations. More details on the LOFAR observatory, are given in Chapter 3.

frequency of the radio wave and the mass and charge of the particles. Since the delay is proportional to the inverse of the charged particle's mass, it is dominated by the presence of free electrons along the line of sight. As such, the DM can be defined as the integral over the electron column density (n_e) from the observer to the pulsar,

$$\mathrm{DM} = \int_{\mathrm{obs}}^{\mathrm{pulsar}} \mathrm{n_e}\ \mathrm{dl}. \tag{2.2}$$

The free electrons of the diffuse Galactic IISM are typically characterised as an ionized plasma of around 8000 K, as described in Sec. 1.2. At these temperatures the plasma is not fully ionized, and thus often referred to as a *cold* plasma. The natural frequency of this IISM plasma (ν_p) is given by,

$$\nu_p = \sqrt{\frac{e^2\, n_e}{\pi\, m_e}}, \tag{2.3}$$

which is a function of the electron column density of the plasma, and the electron charge (e) and mass (m_e). To the propagating radio waves of frequency ν, the IISM (ignoring the Galactic magnetic field for now) will have a refractive index μ,

$$\mu = \sqrt{1 - \left(\frac{\nu_p}{\nu}\right)^2}. \tag{2.4}$$

Typical values in Eq. (2.3) lead to plasma frequencies of the order 1 kHz, much lower than the frequencies at which most pulsar observations are conducted (100 MHz – 10 GHz). Under the assumption $\nu_p \ll \nu$, I can express the group velocity ν_g of the radio wave as

$$\nu_g = c\,\mu = c\,\left(1 - \frac{\nu_p^2}{2\nu^2}\right), \tag{2.5}$$

where the expression for ν_p has been replaced with the first two terms of its Taylor series approximation.

The observed dependence of Eq. (2.1) is derived by computing the difference in integral values $\int_{\mathrm{obs}}^{\mathrm{pulsar}} (1/\nu_g)\,\mathrm{dl}$ at frequencies ν_L and ν_H, using Eqs. (2.5) and (2.3), and substituting the definition for DM from Eq. (2.2). This leads to,

$$\Delta t = \mathcal{D} \times \mathrm{DM} \times (\nu_{\mathrm{L}}^{-2} - \nu_{\mathrm{H}}^{-2}), \tag{2.6}$$

with the dispersion constant,

$$\mathcal{D} = \frac{e^2}{2\pi\, m_e\, c} \approx 4.15 \times 10^3 \mathrm{s\ pc^{-1}\ cm^3}. \tag{2.7}$$

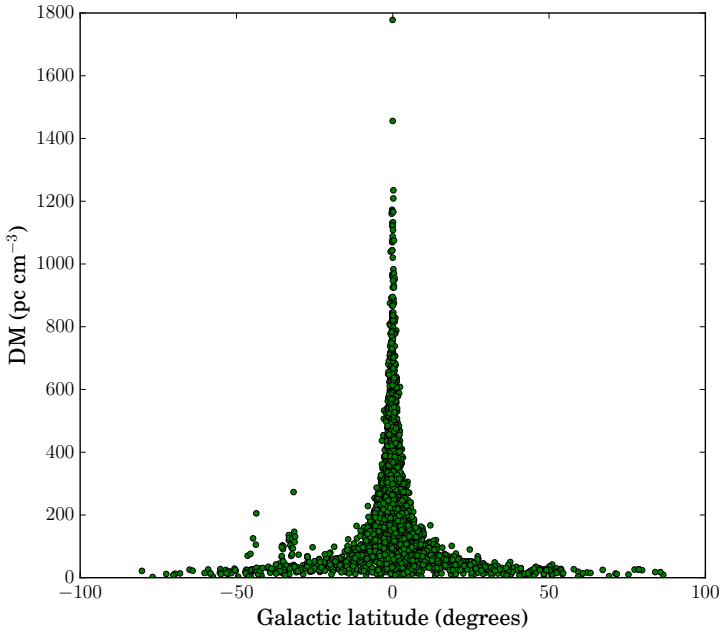

Figure 2.2: The distribution of pulsar DM values with Galactic latitude. This plot was created using data from the online ATNF pulsar catalogue[1](version 1.56, as on 11 April 2017, Manchester et al. 2005).

This set of equations illustrates the physical origin of the inverse square dependence of pulse time delays on radio wave frequency. An independent measurement of the distance to the pulsar through, for example, parallax measurements or associations with objects such as supernova remnants to which the distance is known, provides a means by which to estimate the mean electron density. In other words, if the distance D is known and the DM value measured, then by Eq. 2.2 the mean electron density can be calculated,

$$\langle n_e \rangle = \frac{\mathrm{DM}}{D}. \tag{2.8}$$

Conversely, without an independent distance measurement, an estimate for the distance to the pulsar can be obtained based on its observed DM and an assumption of the average Galactic electron density distribution along the line of sight. Approximations for n_e are obtained from electron density models, such as the NE2001 or YMW16 model, described in Sec. 1.2.2. A mean Galactic electron density value of $n_e \sim 0.03$ g cm^{-3} can be used as a zeroth order approximation (Ables & Manchester, 1976, Gómez et al., 2001).

Since the majority of observed pulsars lie within our Galaxy, pulsar DM values follow a distribution that corresponds to the free electron content of the Milky Way. Pulsars that lie within the Galactic disk, have a much higher DM value, as can be seen in Fig. 2.2, whereas pulsars outside of the Galactic disk are restricted to DM values below ~ 250 pc cm^{-3}. When in 2007, a single bright pulsar-like burst, the so-called *Lorimer burst*, was discovered with a DM of 375 pc cm^{-3} at a Galactic latitude of $-41.2°$, astronomers suspected that the signal must be extragalactic and debated its origin (Lorimer et al., 2007). The phenomenon is now known as Fast Radio Bursts (FRBs). At the time of writing, 22 such events have been discovered, see e.g. Spitler et al. (2016) and Tendulkar et al. (2017). The discovery of pulsar-like signals at distances beyond our Galaxy, holds the promise of uncovering the properties of the intergalactic medium through which these signals travel, as well as the IISM of other galaxies if the FRB signal is associated with a host galaxy.

In Chapter 3, I discuss pulsar observation techniques in more detail. This includes a description of how DM corrections to pulsar data are implemented. The techniques used for *dedispersing* pulsar data have improved significantly over the last decades. These improvements have permitted the studies of small DM variations toward specific pulsars (Cordes et al., 2016). Such DM variations can provide further insight into variations in the IISM environment. They are mostly considered to be due to the scattering of pulsar signals in the IISM, as described in Sec. 2.2.1. In Sec. 7.3, as part of an ongoing project, I show in more detail how the measured time evolution of DM values, can provide insights into the small-scale gas structure of the IISM.

2.1.2 Faraday Rotation

The IISM is weakly magnetised, such that a radio wave interacting with the magnetic field, can undergo phase changes in its plane of polarisation. The cyclotron frequency (ν_B) associated with the IISM is equal to,

$$\nu_B = \frac{e\,B}{2\pi\,m_e\,c}, \tag{2.9}$$

with the Galactic magnetic field (B) typically equal to a micro-Gauss. This leads to ν_B of the order of a few Hz, such that $\nu_B \ll \nu_p$. The correction to the refraction index of Eq. (2.4) due to ν_B and consequently on the delay between waves of different polarisation, is therefore neglible. However, the change in phase due to the presence

of ν_B is measurable. This rotation, known as *Faraday Rotation*, in units of radians is given by,

$$\phi = \mathrm{RM}\,\lambda^2, \tag{2.10}$$

where λ is the radio wavelength and RM is known as the *rotation measure*. The RM is proportional to n_e and to the component of the IISM magnetic field along the line of sight ($B_{||}$),

$$\mathrm{RM} = \frac{\mathrm{e}^3}{2\pi\,\mathrm{m_e^2\,c^4}} \int_{\mathrm{obs}}^{\mathrm{pulsar}} \mathrm{n_e\,B_{||}\ dl}. \tag{2.11}$$

2.2 Pulsar propagation in an inhomogeneous medium

2.2.1 Scattering

Inhomogeneities in the electron densities (Δn_e) of the IISM cause radio waves to scatter. This interstellar scattering leads to pulsar signals travelling along different paths with varying path lengths, before reaching the observer. The multipath propagation is strongly frequency dependent, leading to the temporal broadening of received radio pulses at low frequencies. Combining the multipath propagation of the pulsar signal with the relative motion between the pulsar and the IISM also induces flux density variations, or *scintillation*, as discussed in the Sec. 2.2.2.

2.2.1.1 Thin Screen Approximation

Since the earliest pulsar discoveries, changes of average profile shapes with frequency have been characterised, by partially attributing the changes to scattering and scintillation effects (Lyne & Rickett, 1968, Scheuer, 1968). At the start of the 1970's, Williamson published a series of papers describing pulse broadening due to scattering in the IISM (Williamson, 1972, 1973). He discusses the analytic solutions to two setups: a *thin screen* setup, where the scattering medium is modelled to be thin in the direction of propagation and at a single location along the line of sight, and an *extended medium* setup in which the scattering medium extends along the line of sight.

The thin screen approximation has gained popularity since, not only because of its simplicity, but also due to its successes in describing observed phenomena. It is considered a good approximation to a more realistic extended medium (Bramley, 1954, Rickett, 1970, Lang, 1971), since the line of sight can be dominated by the

presence of specific dense environments, such as an intersection with a Galactic spiral arm (Bower et al., 2014). The analyses of pulsar secondary spectra have also revealed thin parabolic arc structures, described in more detail in Sec. 2.2.3, which are considered evidence for a single dominating scattering surface along the line of sight (e.g. Walker et al. 2004, Stinebring 2006, Trang & Rickett 2007, Wucknitz 2015).

The scattering geometry for the thin screen model is shown in Fig. 2.3. The compactness of pulsars allows us to treat them as point sources. Fig. 2.3 shows a plane wave of radiation emitted by a pulsar at a distance D from the observer, hitting a scattering screen at a distance D_s from the pulsar. The photons are scattered through small angles by the screen, such that those diffracted back to the detector travel along paths of different lengths. The delays caused by the increase in travel time will result in the observation of radio pulses with characteristic scatter broadened profiles, as shown at the bottom of Fig. 2.3.

The relationship between the scattering angle (a) and the angle of observation (θ) is found by considering equivalent expressions for X, the transverse distance between the straight line path to the observer and the point of scattering. In one dimension,

$$X = D_s \tan(a - \theta) = (D - D_s) \tan\theta. \tag{2.12}$$

Given that the distance D is large (∼kpc) compared to the size of the pulsar, $D \gg X$, I can use the small angle approximation by which, $\tan x \approx x$, such that

$$\boldsymbol{\theta} \approx \boldsymbol{a}(D_s/D), \tag{2.13}$$

where I have generalised to two dimensional angles.

The relationship between temporal delay and angular broadening is equally trivial for this setup. Let R_i be the incident ray, R_s the scattered ray and $D_{obs} = D - D_s$. In one dimension it follows that,

$$\begin{aligned} R_s &= D_{obs}(1 + \tan^2\theta)^{1/2} \\ &\approx D_{obs}(1 + \theta^2)^{1/2} \approx D_{obs}(1 + \theta^2/2), \end{aligned} \tag{2.14}$$

where the first approximation is a small angle approximation and the second a Taylor expansion approximation. The extra path length travelled after the ray is scattered, in comparison to the shortest direct travel path, is $d = R_s - D_{obs} = D_{obs}\,\theta^2/2$. A similar calculation for the incident ray followed by substituting θ for a, leads to a total extra path length of,

$$d_{tot} = D_s\Big(1 - \frac{D_s}{D}\Big)\frac{a^2}{2} = D'_s\frac{a^2}{2}, \tag{2.15}$$

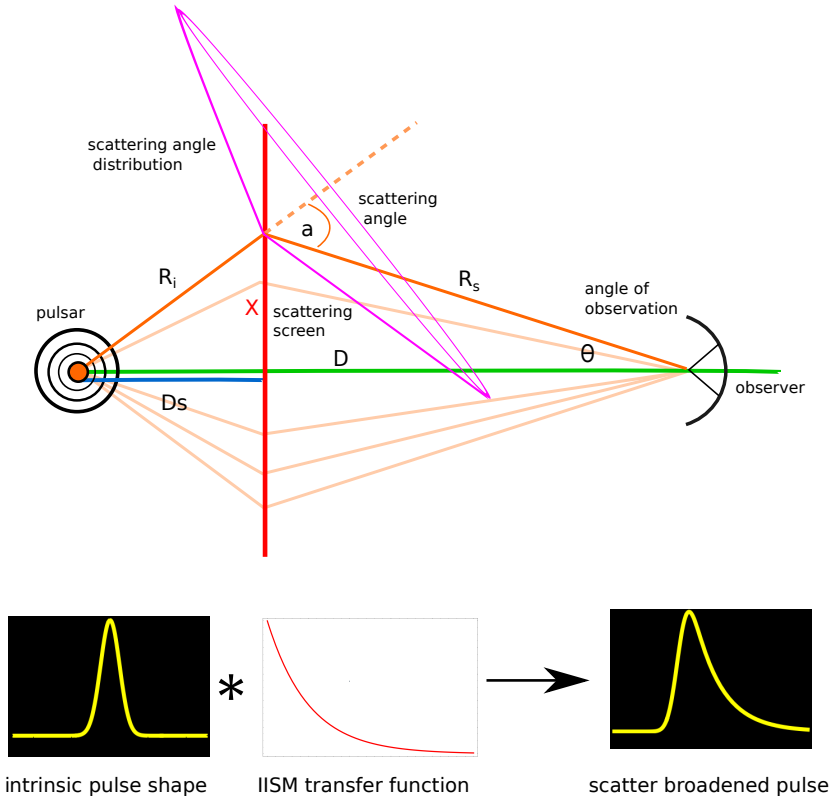

Figure 2.3: *Top:* A schematic representation of radio waves scattered by a thin scattering screen, with D_s the distance from the pulsar to the screen and D the overall distance from the pulsar to the observer. The scattering screen is assumed to be infinite transverse to the line of sight. The scattering angle a, is the angle by which the ray is scattered away from its straight line trajectory and θ the angle at which the scattered ray is observed. Note that these angles are small (θ, α ∼mas), and the distances large (D ∼kpc), such that the diagram is not to scale. *Bottom:* Pulsar scattering in the time domain. An intrinsic pulse shape, here portrayed as a Gaussian pulse, is convolved with a broadening function representative of pulsar scattering by the IISM, which results in a broadened profile with an exponential scattering tail. Credit: M. Geyer

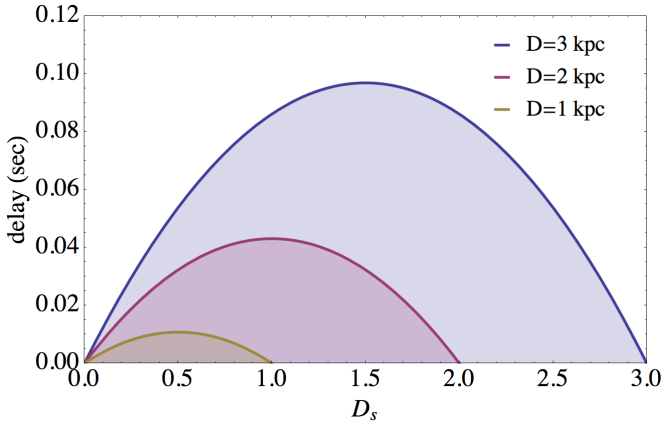

Figure 2.4: The scattering time delay depends geometrically on the distance to the modelled scattering screen. The delay is maximised for a screen at a midway distance to the pulsar. The dependencies for a pulsar at a distance 1, 2 and 3 kpc are shown. A scattering angle (a) of a few milliarcseconds at 1 GHz is used, to obtain the delay times observed at 150 MHz in seconds. Details on the frequency dependence of the delay are provided in Sec. 2.2.1.2.

which implies a time delay compared to an unscattered light ray of,

$$t_{\boldsymbol{a}} = D'_s \frac{|\boldsymbol{a}|^2}{2c}, \tag{2.16}$$

where I have generalised to two dimensional angles and with c the speed of light. The expression for $t_{\boldsymbol{a}}$ is maximised for a midway scattering screen, when $D'_s = D_s/2$, as shown in Fig. 2.4. In the following sections, I present the frequency dependence of the root mean square (rms) of the scattering angle a, to obtain the frequency dependence of the time delay. Thereafter I consider two scattering mechanisms, namely isotropic and anisotropic scattering, and give an example of a temporal broadening function associated with each.

2.2.1.2 Frequency dependence of the scattering angle

The frequency dependence of the distribution of scattering angles (a) will determine the frequency dependence of scattering imprints on pulsar profiles. For a simple model the dependence can be calculated as follows, making use of derivations in Salpeter (1967) and Lang (1971).

I start by supposing that the interstellar scattering discussed in the previous section, is caused by a collection of inhomogeneities in the IISM with a size scale d distributed uniformly through space. A plane wave of frequency ν that passes through a region of inhomogeneity of size d will undergo a phase change ($\Delta\phi$) determined by

the fluctuations in the plasma electron number density (Δn_e). In one dimension, this phase change is proportional to the size of Δn_e and d, and inversely proportional to the frequency of the wave,

$$\Delta\phi = r_e \, \Delta n_e \, d \, c/\nu, \tag{2.17}$$

where r_e is the classical electron radius. The pulsar is at a distance D, such that the radio waves will cross D/d inhomogeneities travelling to the observer. The root mean square (rms) of the phase fluctuation is then,

$$\phi_{\rm rms} = (D/d)^{1/2} \, \langle \Delta\phi^2 \rangle^{1/2} \propto \nu^{-1} \, (Dd)^{1/2} \, \langle \Delta n_e^2 \rangle^{1/2}, \tag{2.18}$$

which leads to an rms in scattering angle of

$$a_{\rm rms} = \frac{\phi_{\rm rms} \, c}{2\pi \, d \, \nu} \propto \left(\frac{D}{d}\right)^{1/2} \frac{\langle \Delta n_e^2 \rangle^{1/2}}{\nu^2}. \tag{2.19}$$

A given distribution in a with rms, $a_{\rm rms}$, will lead to a distribution in time delays with predicted frequency dependencies. In the next section I describe the frequency dependent temporal broadening functions for thin scattering screens that scatter radio waves isotropically or anisotropically.

2.2.1.3 Diffractive versus Refractive Scattering

The multipath IISM scattering introduced above, is strictly known as strong *diffractive scattering*. Diffractive scattering leads to rapidly varying phase changes of the propagating waves, as described in Eq. (2.17). The imparted phase changes have length scales (L_D) below the Fresnel radius (L_F),

$$L_D \ll L_F = (D/k)^{1/2}, \tag{2.20}$$

(Smith & Thompson, 1988), where D is, as before, the distance to the source, and k the wavenumber ($2\pi/\lambda$) of the propagating radio wave with wavelength λ. A useful quantity to define is the field coherence scale, $s_0 = 1/(k\theta_0)$, which describes the circular image on the thin screen (θ_0), within which the phase differences are less than 1 radian. In the far field, as is the case for distant pulsar observations, diffractive scattering occurs when, $s_0 \ll L_F$. The effects associated with diffractive scattering are as described above, temporal pulse broadening, or similarly angular broadening in the image domain, and strong intensity scintillations (Cordes et al., 1986), discussed in Sec. 2.2.2.

However, a scattering timescale much longer than this multipath timescale, associated with slow varying phase changes, has been observed as well (Sieber, 1982). This is known as *refractive scattering*, and leads to the angular wandering of source positions on the sky, as well as weaker intensity variations of the observed source over days or months (Rickett et al., 1984). In the image domain refractive scattering corresponds to angular sizes $> \theta_0$, which implies a refractive length scale of,

$$L_R = D\theta_0 = \frac{D}{ks_0} = \frac{L_F^2}{s_0}. \tag{2.21}$$

The scattering analysed in this thesis all fall into the category of strong diffractive scattering, caused by multipath propagation of the pulsar signals.

2.2.1.4 Scattering broadening functions

A temporal broadening function (f_t) describes the probability that a given light ray from the pulsar will be delayed by a time t. To obtain such a broadening function, I start by defining an electron column density distribution that leads to a probability density function (PDF) $f_{\boldsymbol{a}}$ in the scattering angle ($\boldsymbol{a}$). With the relationships given in Eqs. (2.13), (2.16) and (2.19) (between $\boldsymbol{a}$, $\boldsymbol{\theta}$ and t, as well as $a_{\rm rms}$ and ν), $f_{\boldsymbol{a}}$ can be rewritten in terms of time delays to produce f_t as a function of frequency.

I present two analytic forms of temporal broadening functions: one example associated with an isotropic infinite scattering screen and one for an anisotropic infinite scattering screen. For more detailed calculations, read Cordes & Lazio (2001).

Isotropic Broadening function

A Gaussian distribution in electron column densities leads to a Gaussian distribution in scattering angles (Salpeter, 1967, Lee & Jokipii, 1975). Here, I consider the screen to be infinite transverse to the direction of propagation, and the distribution in $\boldsymbol{a}$ to be a circularly symmetric Gaussian with standard deviation σ_a in each coordinate direction,

$$f_{\boldsymbol{a}} = \frac{1}{2\pi\sigma_{\boldsymbol{a}}}\, e^{-\boldsymbol{a}^2/2\sigma_{\boldsymbol{a}}^2}. \tag{2.22}$$

Following the procedure described in Cordes & Lazio (2001), I define the unit vector $\hat{a}_\phi$ such that,

$$\boldsymbol{a} = a_t\, \hat{a}_\phi = \left(\frac{2\,c\,t}{D_s'}\right)^{1/2} (\cos\phi\hat{x} + \sin\phi\hat{y}), \tag{2.23}$$

where ${a_t}^2 = |\boldsymbol{a}|^2 = 2ct/D'_s$ as in Eq. (2.16). The temporal broadening function is obtained by considering only the scattering angles that reach the observer, that is

$$f_t = \int d\boldsymbol{a}\ f_{\boldsymbol{a}}\ \delta[|\boldsymbol{a}| - a_t] \tag{2.24}$$

$$= \left(\frac{c}{D'_s}\right)\ \int_0^{2\pi} d\phi\ \frac{1}{2\pi\sigma_a^2}\ e^{-a_t^2/2\sigma_a^2} \tag{2.25}$$

$$= \frac{c}{D'_s\,\sigma_a^2}\ e^{-c\,t/D'_s\,\sigma_a^2}, \tag{2.26}$$

such that the temporal broadening function takes the form,

$$f_t = \tau^{-1}\, e^{-t/\tau}\, U(t) \quad \text{with} \tag{2.27}$$

$$\tau = D'_s\,\sigma_a^2/c, \tag{2.28}$$

and $D'_s = D_s\,(1 - D_s/D)$ as in Eq. (2.15). The unit step function, $U(t)$, ensures that time $t > 0$. Such a broadening function convolved with a pulsar profile shape, will clearly lead to an exponential tail. Using the frequency dependence of Eq. (2.19), $\sigma_a \propto \nu^{-2}$, leads to $\tau \propto \nu^{-4}$.

Modelling the inhomogeneities of electron densities in the IISM as Kolmogorov turbulence in a cold plasma, instead of a Gaussian distribution, would lead to a dependence of scattering timescales $\tau \propto \nu^{-4.4}$. I do not provide the derivation here, but point interested readers to e.g. Lee & Jokipii (1976) and Rickett (1977).

Eq. (2.27) describes the temporal broadening function for a scattering screen that is infinite transverse to the line of sight. An infinite screen will conserve the observed flux of the pulsar, since every ray scattered out of the line of sight is compensated by another ray hitting the infinite screen and being scattered back into the line of sight. Later, in Sec. 2.2.3 and in Chapters 4 and 6, I discuss the impacts of having finite scattering screens in detail.

Anisotropic Broadening function

I also consider a scenario where the scattering mechanism is anisotropic, and can be modelled by an asymmetric Gaussian distribution in scattered angles. This would lead to the observation of elongated images of point sources behind such screens. These effects have, for example, been observed for the pulsar B0834+06 at 322.5 MHz (Brisken et al., 2010), as shown in Fig. 2.5 and described in more detail in Sec. 2.2.3.

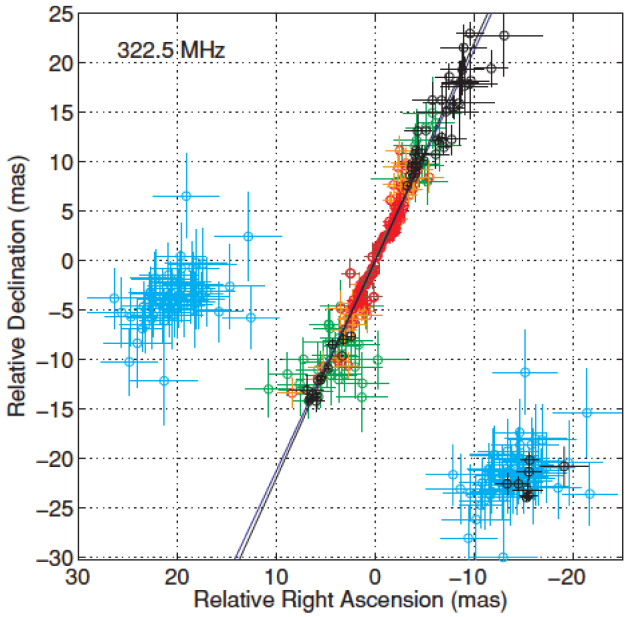

Figure 2.5: The VLBI constructed image of PSR B0834+06, taken from Brisken et al. (2010), clearly shows the point source (centered at a relative right ascension and declination of $(0, 0)$) broadened into an elongated image (red, orange and green points), due to a scattering surface estimated to be 420 pc from Earth. The cyan data points correspond to an image created by a possible secondary scattering surface, as discussed in Brisken et al. (2010).

I consider a Gaussian distribution in $\boldsymbol{a}$ such that the standard deviations, $\sigma_{\boldsymbol{a}}$, are different for each dimension ($\sigma_{a_x} \neq \sigma_{a_y}$). Using a similar transformation as before I find that,

$$f_t = \left(\frac{c}{D'_s}\right)\left(\frac{1}{2\pi\sigma_{a_x}\sigma_{a_y}}\right)\int_0^{2\pi} d\phi\; e^{-a_t^2\,\cos^2\phi/2\,\sigma_{a_x}^2}\; e^{-a_t^2\,\sin^2\phi/2\,\sigma_{a_y}^2}. \tag{2.29}$$

The derived temporal broadening function is dependent on two different characteristic scattering times, τ_x and τ_y, and has the form,

$$f_t = \frac{1}{\sqrt{\tau_x\tau_y}}\, e^{-\frac{t}{2}\left(\frac{1}{\tau_x}+\frac{1}{\tau_y}\right)}\, I\Big(0, \frac{t}{2}\Big(\frac{1}{\tau_x}-\frac{1}{\tau_y}\Big)\Big), \tag{2.30}$$

(Geyer & Karastergiou, 2016) where I is the modified Bessel function of the first kind. The scattering times are defined as in Eq. (2.28) with $\tau_{x,y} = D'_s\,\sigma^2_{a_{x,y}}/c$, which reduces to the isotropic case for $\tau_x = \tau_y$. In general, a more complex frequency dependence could be at play, since different observing frequencies will interact with anisotropic scattering ellipses of varying sizes. Sampling different regions of the scattering screen in this way, can lead to additional frequency dependencies not included in this description.
In the limiting case of extreme anisotropy, $\tau_x \gg \tau_y$ and the broadening function reduces to,

$$f_{t_{1D}} = \frac{e^{-t/\tau}}{\sqrt{\pi t\tau}}\, U(t). \tag{2.31}$$

In Fig. 2.6, the different shapes of the transfer functions associated with Eqs. (2.27), (2.30) and (2.31) are compared. In modelling pulsar scattering, these transfer functions are convolved with an intrinsic profile shape to produce a scatter broadened pulse profile, as shown at the bottom of Fig. 2.3.

2.2.2 Scintillation

2.2.2.1 Scintillation bandwidth measurements

The effects of n_e fluctuations in the IISM observed as pulsar scattering, can also be measured through a phenomena known as *scintillation*. Due do the phase changes imparted on the pulsar radio emission by the IISM, as described in Eq. 2.17, the radio

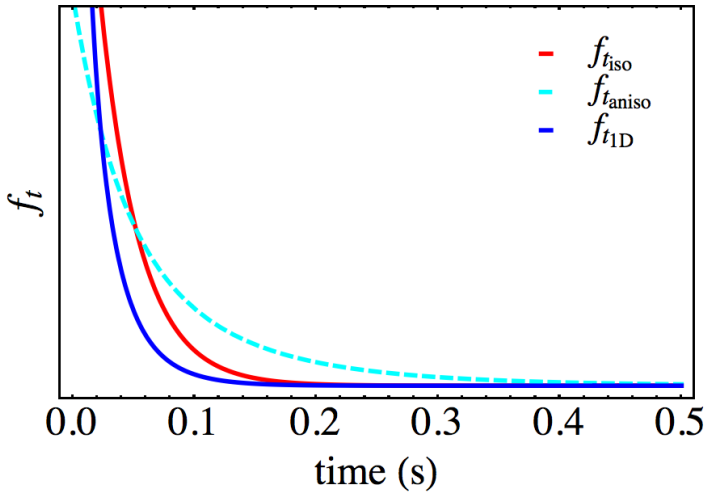

Figure 2.6: A comparison of the temporal broadening functions for an isotropic scattering screen (red), an anisotropic scattering screen (cyan, dashed) and an extreme anisotropic screen (blue). The broadening functions were all calculated for thin screens at a midway distance of $D_s = 1.5$ kpc. For the isotropic and extremely anisotropic (1D) broadening functions $\sigma_a = 3\,\mathrm{mas}\,\nu^{-2}$, and for the anisotropic $\sigma_{ax} = 3\,\mathrm{mas}\,\nu^{-2}$ and $\sigma_{ay} = 6\,\mathrm{mas}\,\nu^{-2}$. For all the broadening functions the observing frequency is $\nu = 150$ MHz.

waves will form an interference pattern at the observer. These interference patterns emerge for phase changes of the order,

$$2\pi\,\delta f\,\tau \approx 1 \quad \text{radian}, \tag{2.32}$$

where δf is known as the *scintillation bandwidth* (Cordes, 1986, Lyne & Rickett, 1968). The interference patterns can be seen in the *dynamic spectra* of pulsar observations. Dynamic spectra are two dimensional pulsar observations that show the intensity of a pulsar measurement as a function of both frequency channels and time. The pulse intensity variations due to multipath interference, show up as constructive and destructive (brighter and dimmer) speckles on these spectra. The scintillation bandwidth is an estimate of the typical size of such a speckle along the frequency axis of the dynamic spectrum. It is obtained by calculating the autocorrelation function of the dynamic spectrum, and defining δf equal to the half-width at half-maximum of the autocorrelation. Once δf is calculated, τ can be estimated from Eq. (2.32).

Fig. 2.7 shows an example of three dynamic spectra for PSR B0329+54, and the corresponding autocorrelation functions, as obtained in Gupta et al. (1994). Brighter and dimmer speckles, corresponding to the constructive and destructive interference of the radio waves are visible in the top panel.

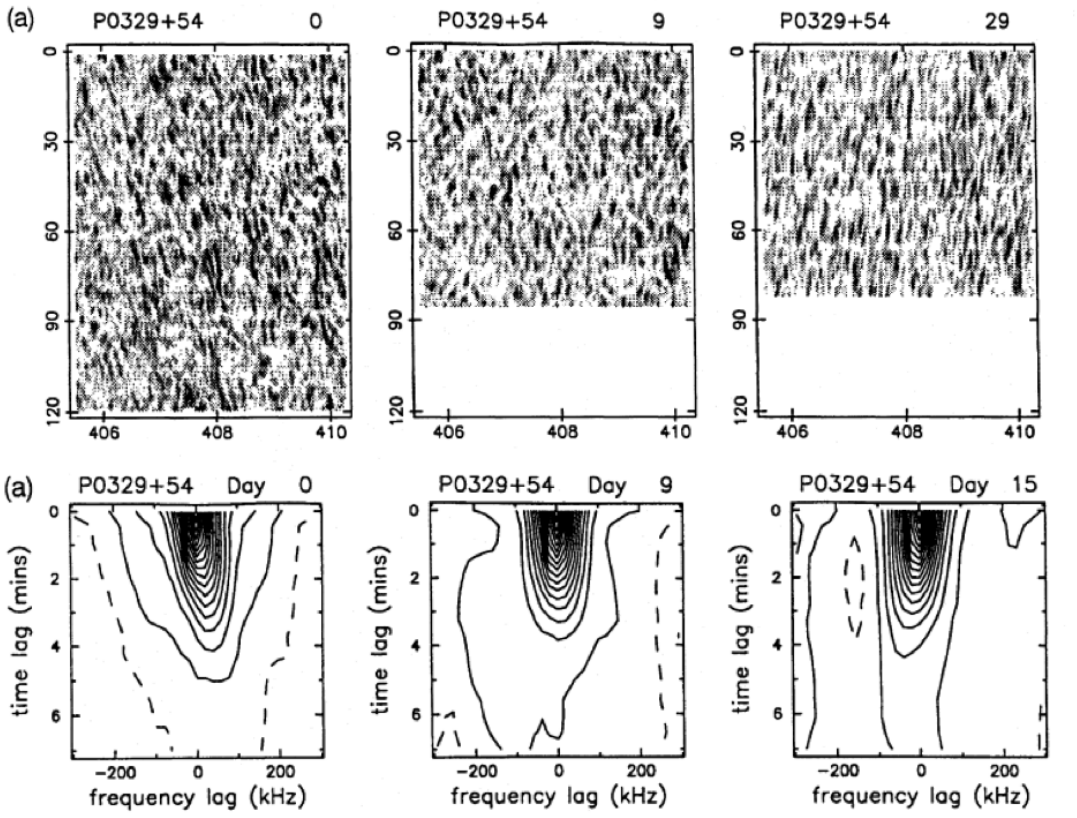

Figure 2.7: Dynamic spectra (top) and their autocorrelation functions (bottom) for PSR B0329+54. The images are taken from a study by Gupta et al. (1994), that investigates the interstellar scintillation of eight pulsars using the Lovell telescope at Jodrell Bank at 408 MHz. The top panels have x-axes frequency (MHz) and y-axes time (minutes).

Scintillation provides a valuable way for obtaining scattering τ estimates at higher frequencies where the effects of scattering on average pulse profiles become less visible. Under these circumstances it is difficult to tell the scattering tail and the intrinsic profile apart, such that measurements of τ from fitting the profile shape return large uncertainties.

2.2.2.2 Evidence for anisotropy

The first hints of anisotropic pulsar scattering by the IISM came from studies of dynamic spectra. These studies, such as by Rickett et al. (1997) and Gupta et al. (1999), revealed that the obtained dynamic spectra for some pulsars exhibited highly organised patterns, different from the more typical randomly distributed scintillation patterns shown in Fig. 2.7.

More compelling evidence for anisotropic scattering was later found by Stinebring et al. (2001), who noted that the complex patterns in the dynamic spectrum manifest themselves in the form of parabolic arcs in the *secondary (power) spectra* of pulsar observations.

The secondary spectrum of a pulsar observation is obtained by taking the 2D Fourier transform of the dynamic spectrum. This converts the original frequency axis to a delay axis and the time axis of the dynamic spectrum into a fringe-frequency axis. The fringe-frequency can be considered a proxy for the proper motion of the pulsar or the scattering screen. Such that, in the simplest terms, the parabolic arc is an indirect result of the $\tau \propto \theta^2$ relationship of Eqs. (2.13) and (2.16), where due to the proper motion different observing angles θ are sampled (Wucknitz, 2013). The appearance of parabolic arcs is enhanced for elongated scattered images. In this way they are valuable tools for probing the anisotropic structure in the IISM. More details on power spectra analysis and the interpretation of parabolic arcs are provided in Walker et al. (2004) and Cordes et al. (2006).

Fig. 2.8 shows the parabolic arc associated with the secondary spectrum[4] of the VLBI observation of PSR B0834+06 (Brisken et al., 2010). The VLBI image constructed from this spectrum is presented in the previous section in Fig. 2.5. The elongated image provides direct evidence of a filamentary scattering surface responsible for anisotropic scattering at low frequencies.

[4]since this is an interferometric observation, the relevant analogous spectrum is actually the *secondary cross spectrum*. A *dynamic cross spectrum* containing interferometric visibilities as a function of frequency and time is created first. The secondary cross spectrum is obtained by taking its complex 2D Fourier transform. For more details, see Brisken et al. (2010).

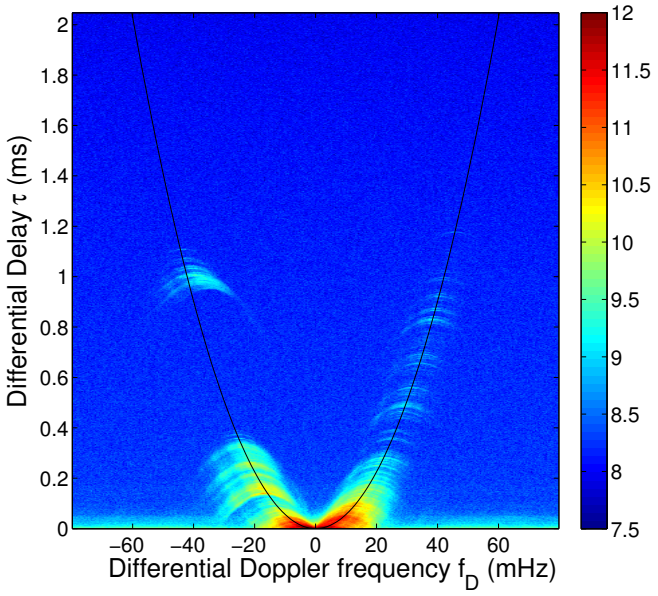

Figure 2.8: The parabolic arc structure visible in the computed secondary spectrum of PSR B0834+06 is an indirect result of the $\tau \propto \theta^2$ relationship, as explained in the text of Sec. 2.2.3. Enhanced parabolic arc features are considered evidence for anisotropy, and its thinness can indicate a single localised scattering surface. For more details, refer to Brisken et al. (2010) and Cordes et al. (2006).

Beyond being a diagnostic for anisotropy, the thinness of the parabolic arc also suggests that a sampled scattering angle corresponds to a single time delay, such that the line of sight to the pulsar ($D = 640$ pc) is dominated by a single scattering surface. In Brisken et al. (2010) the scattering surface toward PSR B0834+06 (at 327 MHz) was estimated to be 16 AU by 0.5 AU in size, and at a distance of 420 pc from Earth. In this way, the analysis of secondary pulsar spectra provides insight into the sizes and distribution of scattering surfaces in the Galaxy. The presence of small scattering screens in particular, can lead to anomalous scattering measurements as discussed in the next section.

2.2.3 Anomalous scattering

Sec. 2.2.1 provides theoretical motivation for expecting certain frequency dependencies of τ. Specifically, $\tau \propto \nu^{-4}$ for a Gaussian distribution in electron density fluctuations or $\tau \propto \nu^{-4.4}$ for electron density fluctuations described by Kolmogorov turbulence.

Many early studies provided observational support for these theoretical models, e.g. Slee et al. (1980), Wolszczan (1983) and Cordes et al. (1985). However, more

recently, deviations to these theoretical values have both been proposed and observed. These especially include spectral index values (α) smaller than the predicted values (Bhat et al., 2004, Löhmer et al., 2001, Lewandowski et al., 2013, 2015), but also some α values larger than expected (Rickett, 1990, Lambert & Rickett, 1999, Tuntsov et al., 2012). These deviations have been considered as evidence for anomalous scattering mechanisms and geometries.

2.2.3.1 Finite scattering screens

Weaker dependencies of τ on frequency than $\alpha = 4$, have, for example, been modelled as truncated screens as discussed in Cordes & Lazio (2001), in contrast to most theoretical models that assume the screen to be infinite transverse to the line of sight. At low enough frequencies (or long enough wavelengths), the finite screen can no longer conserve flux, since not all the light scattered out of the line of sight can be compensated by light scattered back into the line of sight at large angles, where there is no screen. This leads to an upper limit on the observing angle ($\theta_{\rm max}$) and a corresponding limit to the time delay ($t_{\rm max}$). Under these circumstances observed pulse profiles show no further scatter broadening with a decrease in frequency. This leads to a flattening of the scattering power law at low frequencies. The low frequency observations of PSR B0834+06 (Sec. 2.2.2.2, Figs. 2.5 and 2.8) have already suggested the existence finite AU-sized scattering screens. In Chapter 4, I construct numerical broadening functions representative of a truncated screen along the line of sight to the pulsar, and study the impact of this alternative broadening function on profile shapes, τ spectra, and flux spectra (investigating Open Questions I, IV, VI). In Chapter 5, when I study pulsar data, I also investigate whether evidence for truncated scattering screens are observed (Open Question IV).

Additional evidence for small dense scattering surfaces come from so-called extreme scattering events (ESEs). ESEs were first observed in quasars by Fiedler et al. (1987). More recently, similar extreme scattering events have been observed in pulsars and are thought to be associated with the same IISM structures (Cognard et al., 1993, Coles et al., 2015, Bannister et al., 2016). ESEs are characterised by dramatic flux variations over a period of several weeks. These variations are thought to be caused by the lensing of ISM ionized gas clouds with free electron densities as high as 10^3 cm^3 (Bannister et al., 2016). These extreme densities imply pressures that are unlikely to be long-lived, adding to the mysteries of the formation and existence of these structures. It is generally believed (e.g. Rickett et al. 1997) that Kolmogorov turbulence in the IISM is unlikely to produce such over densities. Physical models to

explain the phenomenon include *plasma sheets* and *self-gravitating clouds*. For more details on these respective models, see Walker (2007) and Pen & King (2012). Most recently, it has also been suggested that ESEs are associated with plasma filaments surrounding hot stars in the solar neighbourhood, as discussed in Walker et al. (2017).

In Chapter 7, I describe additional ongoing projects that I am involved with. One of these projects (Sec. 7.3), in collaboration with Dr. Mark Walker, investigates evidence for high density IISM clouds through combining Far-Infrared spectroscopy measurements and pulsar propagation effects.

2.2.3.2 The turbulence inner scale

Apart from finite scattering structures, it has been suggested that scatter broadening of pulsar profiles can be limited, at low frequencies, by a physical inner scale (cut-off scale) in the Kolmogorov distributions (Coles et al., 1987, Rickett, 1990). In other words, at length scales smaller than this inner scale, turbulence in the IISM is not supported. Such a cut-off will restrict diffraction to a maximum scattering angle (θ_{max}), leading to less power observed at large angles (Rickett et al., 2009), or alternatively flatter τ spectra with lower power law indices at low frequencies. In the case of an inner cut-off scale, however, there is expected to be no loss in observed flux at low frequencies (Open Question VI).

2.2.3.3 The effects of anisotropy

Anisotropic scattering by the IISM, as seen in Fig. 2.5, has also been considered a cause for measuring deviating scattering spectra (Tuntsov et al., 2012). In this thesis, in Chapter 4, when I discuss the methodology of conducting scattering fits, I show that incorrectly fitting anisotropic data with scattering models indeed leads to power law fits of τ with spectral index values lower than theoretically expected. In Chapter 5, I analyse low frequency pulsar profiles using different scattering models, and investigate whether I find evidence for anisotropic scattering (Open Question V).

2.2.3.4 The Galactic Centre anomaly

The Galactic Centre (GC) has produced mysterious scattering observations. Ongoing pulsar searches have long been hoping to unveil a pulsar population in the inner parsec of the Galaxy, where the presence of pulsars around the central supermassive black hole will be invaluable for tests of General Relativity (e.g. Liu et al. 2012). When searches at L-band (1.4 GHz) were unsuccessful in finding pulsars (Johnston et al., 1995), the lack of detected pulsars was thought to be due to extreme scattering by the

dense GC environment. Searches at ever higher frequencies however still did not find pulsars (Kramer et al., 2000, Deneva et al., 2010, Macquart et al., 2010). Finally, in 2013 a single magnetar was discovered close to the GC (Mori et al., 2013). Much to the observers' surprise, the τ value associated with the observed pulse was significantly lower than predicted by electron density models (Spitler et al., 2014, Bower et al., 2014). This discovery has perplexed the pulsar community, with some suggesting that the line of sight to the GC magnetar is along a serendipitous corridor of low electron column density (Roy, 2013). If this is true, it would provide substantiating evidence for the more patchy IISM as discussed above. In Sec. 7.1, as part of my chapter on ongoing projects, I describe a scattering model that I have constructed, which aims to reproduce the observed scattering characteristics of the GC magnetar, while accounting for the lack of pulsar discoveries to date.

Chapter 3

Pulsar Observations at Low Frequencies

The effects of the IISM on average pulsar profiles are highly frequency dependent, with simple theoretical models predicting scatter broadening for which $\tau \propto \nu^{-4}$, as discussed in Sec. 2.2.1.4. I am interested in investigating the imprints of the IISM at low frequencies where these effects are exaggerated. In order to study the frequency dependence of scattering parameters, I require observations for which the bandwidths ($\Delta\nu$) are large. The Low Frequency Array (LOFAR, van Haarlem et al. 2013) provides large $\Delta\nu$ relative to ν values at low frequencies. In this thesis I present pulsar observations conducted with LOFAR at observing frequencies below 200 MHz.

3.1 The LOFAR telescope

LOFAR is a radio interferometer, consisting of multiple antennas of which the signals are combined coherently. It has no moving parts, as would be the case for a traditional steerable radio dish, but 'points' to a target source by digitally combining the relevant signals to form a beam on the sky.

The telescope operates at frequencies between 10 MHz and 250 MHz and is made up of different configurations of dipole antennas, the core of which is located near Exloo in the Netherlands. Beyond the core, the telescope extends to 40 remote stations and 8 international stations creating interferometric baselines of up to 1500 km. Since all the data in this study were recorded using only the core stations, I limit the discussion of the telescope to the core. For more details, please refer to Stappers et al. (2011).

The inner core of the array, also known as the *Superterp* is shown in Fig. 3.1. It is made up of High Band Antennas (HBA) that operate at 110 – 250 MHz. A set

Figure 3.1: Image and caption taken from Stappers et al. (2011). Three successive zoom-outs showing the stations in the LOFAR core. The different scales of the hierarchically organised HBA elements are highlighted and their respective beam sizes are shown. The large circular area marks the edge of the Superterp, which contains the inner-most 6 stations (i.e. 12 HBA sub-stations: where there are 2 sub-stations, each of 24 tiles, in each HBA core station); other core stations can be seen highlighted beyond the Superterp in the third panel. *Left:* a single HBA tile and associated beam. *Middle:* A single HBA sub-station with three simultaneous station beams. *Right:* The 6 stations of the Superterp plus 3 core stations in the background are highlighted. Four independent beams formed from the coherent combination of all 24 core HBA stations, most of which are outside this photo, are shown.

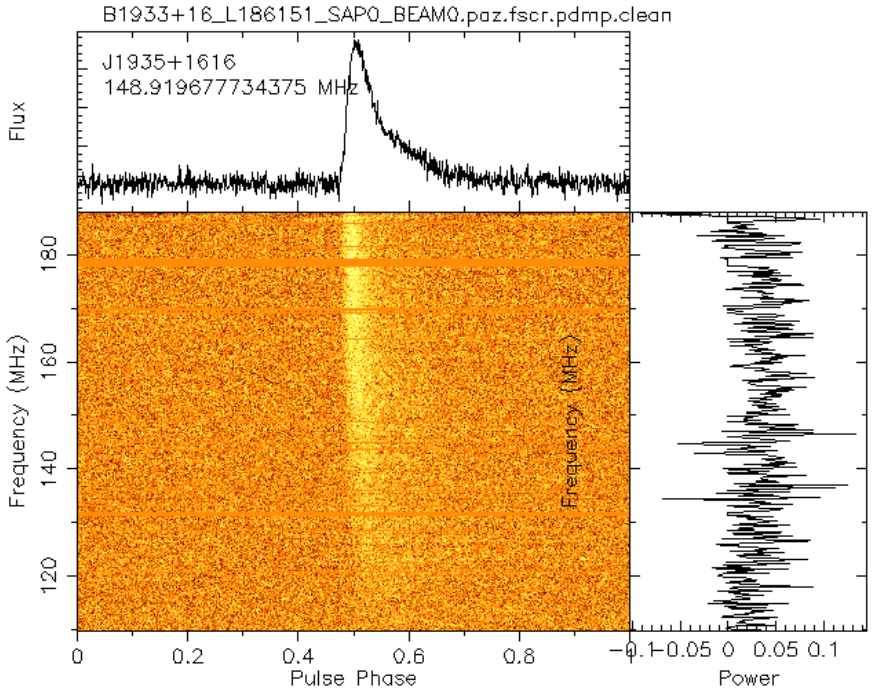

Figure 3.2: The dynamic spectrum of a LOFAR observation of PSR B1933+16. The data have already been dedispersed and folded at the pulse period. The plot was produced using `psrplot` in PSRCHIVE (van Straten et al., 2012). Narrow band RFI that has been removed from these data can be seen as solid orange lines running across the spectrum.

of 16 of these dipole antennas are combined to form a tile, and tiles are grouped to form stations. The core consists of 24 stations in total. For the pulsar data used in this thesis, the 24 station beams are combined coherently to form a tied-array beam on the sky.

3.2 Data Reduction

In order to study the frequency dependence of IISM scattering on average pulse profiles at low frequencies, I firstly require high signal-to-noise (S/N) pulse profiles. High S/N average pulse profiles ensure that the shape of the scattered profile can be fit accurately with the scattering methods described in the next chapter. These scattering methods incorporate the temporal broadening functions described in Sec. 2.2.1.4. Fitting scatter broadened profiles accurately therefore allows me to extract scattering parameters (e.g. τ values) that are well constrained. Secondly, I require sufficient frequency resolution to study the frequency evolution of profile shapes over the observed

bandwidth.

3.2.1 Average Pulse Profiles

Fig. 3.2 contains a LOFAR observation of PSR B1933+16 as an example of the required data quality. The S/N ratio of an observed pulse profile can be increased by adding a high number of single pulse profiles together to form an average profile. In Fig. 3.2 the plotted dynamic spectrum contains a 420 s observation that has been folded to the pulsar period of $P = 0.36$ s, revealing the pulse as a bright yellow band across the frequency channels. All of the pulsars studied in this thesis were observed for more than 1000 rotations or at least 20 min using the full LOFAR HBA Core, to ensure that a stable profile shape (unaffected by the variability of single pulses) is formed.

Summing all of the 400 frequency channels in Fig. 3.2 leads to the frequency-averaged pulse profile seen at the top of the figure. To study the frequency dependence of scattering, I do not add all the frequency channels. Rather, I split the band into typically 8 or 16 sections and then add the frequency channels within a section to form an associated average profile. In this way 8 or 16 average profiles are formed across the observing band.

3.2.2 Dedispersion

Before I can form average pulse profiles, the dispersion delay described in Sec 2.1.1, has to be corrected for. These corrections are typically done in one of two ways, both of which have been used on the LOFAR data in this thesis.

The simplest dedispersion technique is *incoherent dedispersion*. In this method the received voltage signal is detected first. That means, the voltage signal associated with each frequency channel is squared to obtain the power of the signal. The power as a function of frequency and time (known as filterbank data) is subsequently saved to disk.

Thereafter, as shown schematically in Fig. 3.3, a time delay correction (as computed by Eq. 2.6) is applied to each frequency channel. Fig. 3.3 shows that after incoherent dedispersion is applied, individual frequency channels still exhibit a small delay in the signal. Since DM delays are large at low frequencies, low frequency observations, especially, require high frequency resolution to ensure that the per channel *DM smearing* is negligible. To obtain average profiles, with shapes unaffected by these per channel delays, I use data for which the per channel smearing is of the

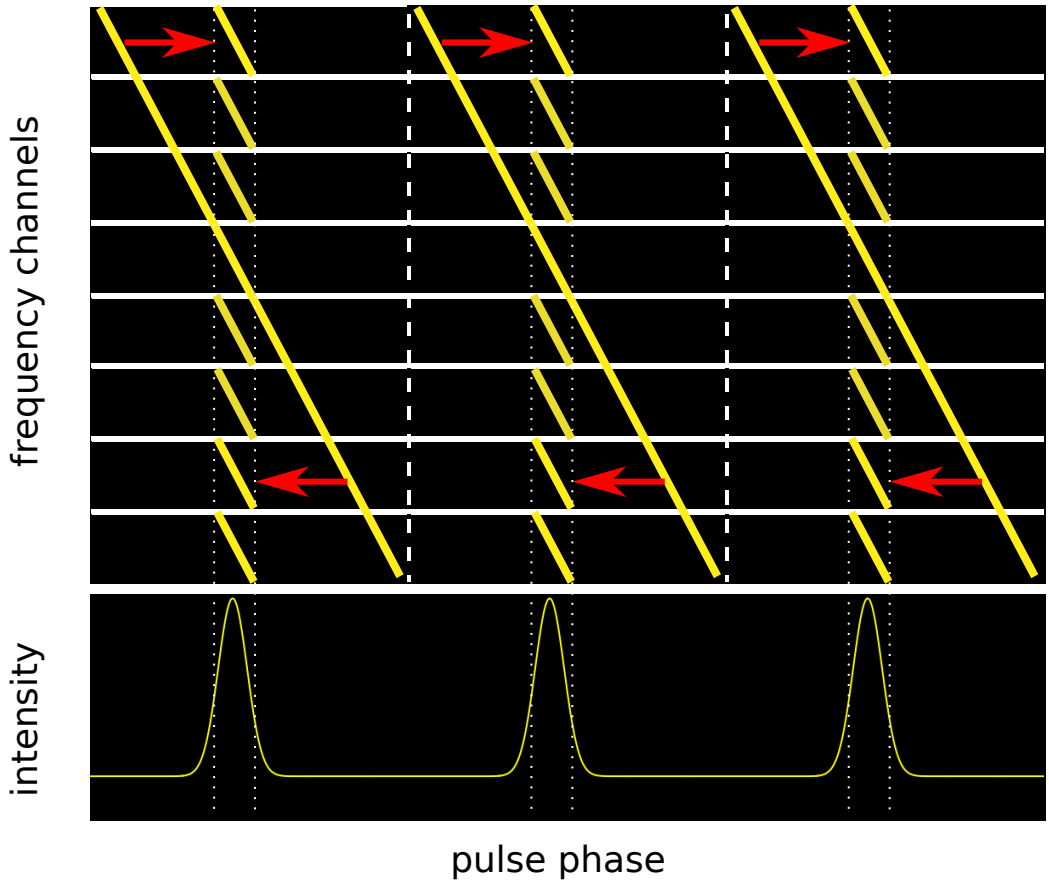

Figure 3.3: A diagrammatic illustration of the incoherent dedispersion procedure. A time correction is applied to each of the 8 frequency channels (relative to a reference frequency), before adding adding the signal to produce the pulse shape as shown at the bottom. Credit: M. Geyer

order a few phase bins. The absolute DM smearing values associated with different LOFAR data sets are given in Sec. 3.3.

A more sophisticated technique that circumvents this issue of inter-channel DM delays, is *coherent dedispersion*. A coherent dedispersion correction is applied directly to the raw voltage signals. In the Fourier domain, the dispersion effect of the IISM can be expressed as a phase change to the electric field of the measured signal,

$$E_m(\nu) = E_i(\nu)\ e^{ik(\nu)\phi}, \tag{3.1}$$

with E_m the measured electric field and E_i the field originally emitted, k the wavenumber (all of which are dependent on the observing frequency) and ϕ the imparted phase change. The dispersion can therefore be removed completely by multiplying E_m with an inverse phase correcting function, $e^{-ik\phi}$. After this correction has been applied, the dedispersed signal is obtained by transforming back to the time domain.

Once the dedispersion procedure (incoherent or coherent) is complete, the obtained intensities (as a function of time and frequency) can be folded at the pulsar period and frequency combined to obtain average pulse profiles as described in Sec. 3.2.1.

All the LOFAR data in this thesis were preprocessed using the standard LOFAR PULsar Pipeline (PulP), a PYTHON-based suite that conducts the dedispersion and folding of the observations. The details of PULP are described in Kondratiev et al. (2016).

3.2.3 Radio Frequency Interference Mitigation

Many terrestrial technologies emit radio waves in frequency bands within the observing frequencies of radio telescopes.

If interfering signals are not correctly flagged and removed, they lead to artificial changes in the obtained average pulse shapes. I am interested in both fitting scattering models to average pulse shapes, and in studying the frequency dependence of average profiles. It is therefore important to ensure that these are unaffected by terrestrial signals.

Radio Frequency Interference (RFI) occurs as either narrow band RFI (local in frequency) or broad band RFI (local in time) (Offringa et al., 2010). The former includes telecommunication signals such as radio and television stations, satellite transmission and air traffic control systems, while broad band RFI is caused by amongst other sources, lightning and high-voltage power cables.

Even though LOFAR is located in an area that is not densely populated, there are villages and technologies in its surroundings, which together with overhead interference from statellites, lead to RFI.

I make use of the `clean.py` tool from the CoastGuard[5] package (Lazarus et al., 2016) to remove both narrow band and broad band RFI. Specifically, I use the `surgical` cleaner within this script. The `surgical` cleaner identifies profiles affected by RFI by analysing folded profile data, and sets the weights of these profiles to zero. This way of masking allows the cleaning process to be reversible (since the data have not been altered).

To isolate the RFI of an affected profile, a model of a detected profile (unaffected by RFI, with a high S/N) is subtracted, and the residuals analysed. The analysis includes computing the standard deviation, the mean, the range, and the maximum amplitude of the Fourier transform, of the (mean-subtracted) residuals associated with each frequency channel. Based on the outcomes of these statistics, profiles that are considered outliers according to the results of at least 2 of the 4 indicators are zero-weighted, as described in more detail in Lazarus et al. (2016). For readers interested in using the tool, I specifically use the `surgical` cleaner as follows,

```
clean.py -F surgical -c "chan_numpieces=1, chanthresh=3,
subint_numpieces=1, subintthresh=3" -o <outputfile.clean> <inputfile.ar>
```

where

```
chan_numpieces -- The number of equally sized pieces to use for
   defining piecewise segments of each channel when detrending.

chanthresh -- The threshold (in number of sigmas) a profile needs to
   stand out compared to others in the same channel for it to be removed.

subint_numpieces -- The number of equally sized pieces to use for
   defining piecewise segments of each sub-int when detrending.

subintthresh -- The threshold (in number of sigmas) a profile needs to
   stand out compared to others in the same sub-int for it to be removed.
```

[5]https://github.com/plazar/coast_guard

3.2.4 Flux Calibration

The aim of flux calibrating the intensities associated with average pulse profile observations in this thesis, is to convert the intensity from arbitrary units associated with the received radio signal, to absolute units of flux density, such as milli-Jansky (mJy, where 1 Jy = 10^{-26} W m^{-2} Hz^{-}1 s^{-1}), associated with the astrophysical source. This allows me to compare the obtained LOFAR flux density values with flux density values in the literature, especially with values at higher frequencies to investigate whether flux spectra and flux spectral indices change with frequency (Open Question 6).

Flux calibration is typically achieved by using the telescope gain (G) to convert between temperature (T) and flux density (S), with the peak flux density, $S_{peak} = T_{peak}/G$. The gain is a measure of the telescope aperture efficiency and scales as,

$$G \sim \frac{4\pi\, d^2}{\lambda^2}, \tag{3.2}$$

where d is the aperture size and λ the observing wavelength.

For a simplified top hat signal of width W and period P, the mean flux density can be calculated by computing the product,

$$S_{mean} = S_{peak}\frac{W}{P} = \frac{T_{peak}\,W}{GP}. \tag{3.3}$$

In turn, the peak temperature T_{peak} can be expressed through the radiometer equation, as a function of the system noise temperature (T_{sys}), the pulse signal to noise (S/N), the observing bandwidth and integration time ($\Delta\nu$, t_{int}) and the number of measured polarisations (n_p), and W and P,

$$T_{peak} = \frac{\frac{S}{N}\,T_{sys}\,P}{\sqrt{n_p\,t_{int}\,\Delta\nu\;W(P-W)}}. \tag{3.4}$$

For more details on the radiometer equation, see a standard pulsar textbook such as Lorimer & Kramer (2004). These expressions provide a means by which to conduct a simple flux calibration, converting measurable and known quantities of Eq. (3.4) into flux density.

The flux calibration of beamformed LOFAR data is more complicated than the simple picture above. The main complication has to do with uncertainties in the characteristic beam shape. The sensitivity of dipole antennas varies strongly across the sky. This means that the sensitivity of the tied array beams varies strongly with

the observed source location. Furthermore, because LOFAR has large $\Delta\nu/\nu$ values, the beam size and sky temperature (both of which are frequency dependent) vary across the observing band. A detailed consideration of how to take these effects into account is discussed in Kondratiev et al. (2016).

In this thesis I apply the flux calibration strategy described in Kondratiev et al. (2016). This involves calculating the antenna responses[6] for each HBA station (as a function of observing frequency and sky direction) by making use of a suitable beam model (Hamaker, 2006). The computed antenna gain is scaled with the number of stations used for the observation (after having excluded any faulty dipoles), and the antenna temperature (T_{sys}) and sky temperature are calculated *in situ* as described in Wijnholds & van Cappellen (2011).

I use the `lofar_fluxcal.py` script[7] to conduct the flux calibration of the folded and frequency averaged profiles.

```
lofar_fluxcal.py -v --snrmethod Off --off-left 150 --off-right 250
--flagged <fraction of faulty dipoles> <profile.clean>
```

When the `snrmethod` flag is set to `Off`, the user has to specify an off-pulse window by defining the left (`off-left`) and right (`off-right`) boundaries in bin numbers. I typically use an off-pulse window of around 10% of the pulse period, since the scatter broadened pulse occupies a large fraction of the pulse period. The standard deviation of this off-pulse window (i.e. of the noise) is used to convert the arbitrary intensity of observed profile into physical units of Jansky. In this way the error on flux density measurements is associated with the noise of the observed profile. However, as discussed in detail in Kondratiev et al. (2016), the effective uncertainty of a given measurement is much larger. This has mostly to do with additional effects, such as the source's intrinsic variability, as well as IISM and ionospheric effects that impact on the antenna response and which are not accounted for. In Bilous et al. (2016), a review of LOFAR Census observations, a conservative error of 50% on flux density measurements is used. I adopt a similar flux density error margin in this thesis.

3.3 The LOFAR Data in this Thesis

Three different LOFAR datasets are used in this work, all of which were recorded using the LOFAR Core with the HBA antennas operating at 110-190 MHz. The

[6] using `mscorpol` by T. Carozzi at http://github.com/2baOrNot2ba/mscorol
[7] https://github.com/vkond/LOFAR-BF-pulsar-scripts

datasets are LOFAR Commissioning Data, Census Data (Bilous et al., 2016) and Cycle 5 timing data (project code: LT5_003; PI: Verbiest), discussed in more detail below. From the datasets I use sources that exhibit clear exponential scattering and that appear to have simple single component profiles and minimal intrinsic profile evolution. I check the profiles for multi component structure by eye and review the higher frequency shapes of these pulsars on the EPN database to estimate whether high levels of intrinsic profile evolution is expected.

3.3.1 Commissioning data

Data recorded using the LOFAR HBA Core (19–23 stations, depending on the observation) during the pre-Cycle 0 and Cycle 0 period (ending in November 2013), are here collectively called Commissioning data. The data are of similar quality as the data presented in Pilia et al. (2016).

The Commissioning data are typically split into 6400 frequency channels across the HBA band providing a frequency resolution of 12.2 kHz. The data are incoherently dedispersed, with the exception of PSR J1913−0440, for which the data are coherently dedispersed. The Commissioning data has coarser frequency resolution than the Census or Cycle 5 data, leading to a maximum per channel DM smearing at 110 MHz of 15 to 30 phase bins. However, the τ values at these 110 MHz are typically large compared to the DM smearing, with the per channel DM smearing maximally equal to 21% of the estimated τ value.

The folded average profiles have a phase bin resolution of 1024 bins across the pulse period. From the Commissioning data I present 9 sources that exhibit clear scatter broadening. I form 4, 8 or 16 average profiles across the observing bandwidth, to which the scattering methods of Chapter 4 are fit independently.

3.3.2 Census data

The original LOFAR HBA Census dataset (Bilous et al., 2016) includes 194 pulsars, observed from February to May 2014, at declinations $\delta > 8°$, and Galactic latitudes $|b| > 3°$. These specifications were chosen to maximise the telescope sensitivity (which decreases with increasing zenith angle) and to avoid higher background sky temperatures towards the Galactic plane, and are as such not necessarily highly scattered pulsars. From this set of pulsars, I picked the ones that have a high peak S/N, exhibit clear exponential scattering and appear to have simple single component profiles and minimal intrinsic profile evolution. All of the pulsars were observed for more than

1000 rotations or at least 20 min using the full LOFAR HBA Core to form stable average profile shapes.

The recorded bandwidth was split into 400 sub-bands, with either 64 or 128 channels per sub-band, leading to frequency channel resolutions of 3.05 or 1.53 kHz. The per channel DM smearing lies between 0.4 and 1.2 bins. The phase bin resolution varies from 128 to 1024 bins per pulse period. I present the Census data as 16 average profiles across the HBA band. More detail on the Census observing strategy and data acquisition can be found in Bilous et al. (2016).

3.3.3 Cycle 5 data

As part of an ongoing pulsar timing programme with LOFAR (Cycle 5, project code: LT5_003), two of the pulsars that overlap with the Commissioning data subset are continuously monitored at HBA frequencies. The data are recorded using the LOFAR Core (23 stations), in 10 min observations with 400 frequency channels, and coherently dedispersed, which means the dispersion effects are removed completely. I use Cycle 5 timing data for the two overlapping pulsars, and pick the observations with the highest S/N for each pulsar (ObsIDs L424139 and L423987). The data are averaged to form 16 profiles across the band.

Chapter 4

Scattering Methods on Simulated Data

The first step towards analysing pulsar scattering properties at LOFAR frequencies, and ultimately answering the Open Questions posed in Chapter 1, is to ensure that I extract accurate scattering parameters from the dataset described in the previous section. For this I develop effective scattering fitting methods. I test the performance of my fitting techniques on simulated average pulse profiles. The simulated pulsar profiles are both scatter broadened as described in detail in Chapter 2, and modelled after real pulsar observations, at frequencies below 200 MHz, as described in Chapter 3.

Once I have converged on a robust fitting method, I study the effects of simulated scattering on pulse shapes, characteristic scattering time (τ) spectra and flux spectra.

A large subset of this work has been publised in Geyer & Karastergiou (2016).

4.1 Simulated Data

To simulate scatter broadened pulse profiles, I firstly simulate an intrinsic pulse shape with an intrinsic flux spectrum, and thereafter convolve the simulated pulse with a frequency dependent temporal broadening function f_t associated with the scattering mechanism of choice, as presented in Sec. 2.2.1.4. Once a series of scatter broadened pulse profiles at different frequencies has been simulated, I fit the data with a set of methods and test how accurately they recover the simulated scattering parameters.

4.1.1 Simulated Intrinsic Pulse

The intrinsic pulse profile is described by a single Gaussian component with a given duty cycle and pulse period (P). The duty cycle describes the fraction of the pulse

period containing the pulse, in other words it is a proxy for the width of the pulse profile,

$$w_{50} = \text{duty cycle} \times \text{P} \tag{4.1}$$

$$\sigma = w_{50}/\, 2\sqrt{2\ln 2}, \tag{4.2}$$

with w_{50} the full width at half maximum, and σ the standard deviation of the Gaussian pulse profile.

When necessary, multiple pulse periods are stitched together to form a series of incoming pulses that I call a *pulse train*. I choose to simulate two types of pulsars, a typical slow pulsar with $P = 1$ s and a duty cycle of 2.5% (i.e. from the main isolated pulsars distribution in Fig. 1.3, green dots) and a fast pulsar with $P = 20$ ms with a duty cycle of 10% (i.e. from the main binary distribution in Fig. 1.3, red circles).

The mean flux spectral index for all the simulations is $\gamma = 1.6$, where the mean flux is $S_{mean} = S_m = \nu^{-\gamma}$, as described in Sec. 1.1.4. Hereafter, I always use γ to refer to a flux spectral index, and α to refer to the spectral index of the characteristic scattering time (τ), to avoid confusion. The mean flux of the pulsar is normalised such that it has a maximum value of $S_m = 1.0$ for the lowest studied frequency.

The use of a Gaussian template pulse shape is motivated by the fact that a large fraction of pulsar profiles are relatively well approximated by this shape (e.g Karastergiou & Johnston 2007, Johnston & Weisberg 2006). The drawback is that a single Gaussian shape is not representative of all pulsar profiles, especially not of older, slower pulsars. In Sec. 4.3.3, I simulate scattering impacts on a more complex profile shape based on the average profile of a specific pulsar, namely PSR B1237+25.

4.1.2 Simulated Scattering Screen

The simulated scattering screen is modelled after the thin screen setup presented in Fig. 2.3. I consider nearby Galactic sources by choosing a standard distance of $D = 3.0$ kpc from the observer to the pulsar, with a midway scattering screen at $D_s = 1.5$ kpc.

I make use of two scattering models for screens that are infinite transverse to the line of sight. Firstly the *isotropic scattering* model described by the temporal broadening function presented in Eq. (2.27), and secondly the *anisotropic scattering* model associated with the broadening function of Eq. (2.30).

In all cases the standard deviation of the distribution in scattering angles associated with the screen follows the relation, $\sigma_{\boldsymbol{a}} \propto \nu^{-2}$ (Eq. 2.19). I define what I call

a *scattering strength*, by choosing a proportionality constant in this relation. I use $\sigma_{\boldsymbol{a}} = 3$ mas at 1 GHz, such that $\sigma_\theta = 1$ mas at distances $D = 1$ kpc and $D_s = 1/3$ kpc, as suggested in Cordes & Lazio (2001).

Apart from the broadening functions associated with infinite scattering screens, I also include broadening functions in my analysis associated with truncated screens. For this simulation the shape of the associated broadening function is built up numerically.

In Cordes & Lazio (2001), it was shown that the broadening function for a disk-shaped isotropic scattering screen centered on the line of sight can be created by amending Eq. (2.27) with a unit step function, such that the broadening function becomes

$$f_{t_{\text{disk}}} = f_t \; U(t_{max} - t), \tag{4.3}$$

with f_t as given in Eq. (2.27). This means that beyond a maximum observation angle θ_{max}, no photons are scattered back into the observer's line of sight. The maximum angle has a geometric path length correspondence to a maximum time delay t_{max}, as measured with respect to the direct line of sight, and given by the relations in Eqs. (2.13) and (2.16).

I expand on this idea in Cordes & Lazio (2001) by creating a ray-tracing code that allows me to place a screen of any size between the source and the observer. I simulate a rectangular screen as a toy model: by specifying a screen's width and height, its position along the line of sight (D_s) and its two-dimensional offset with respect to the line of sight, the complete scattering setup is defined. The associated temporal broadening function is constructed by calculating the probability that a given photon hitting the truncated screen will reach the detector. Binning these probabilities according to the associated arrival times for each photon allows me to build up the broadening function with a required time resolution.

In Sec. 4.3, I discuss the outcomes for infinite (Sec. 4.3.2) and truncated screens (Sec. 4.3.3) independently.

4.1.3 Scattered Profiles

Fig. 4.1 gives a schematic overview of my two methods for producing scattered profiles. The method shown in the top panel represents the most intuitive way of creating folded scattered pulse profiles: a train of Gaussian pulses are convolved with a broadening function resulting in a train of broadened pulse shapes. A broadened pulse

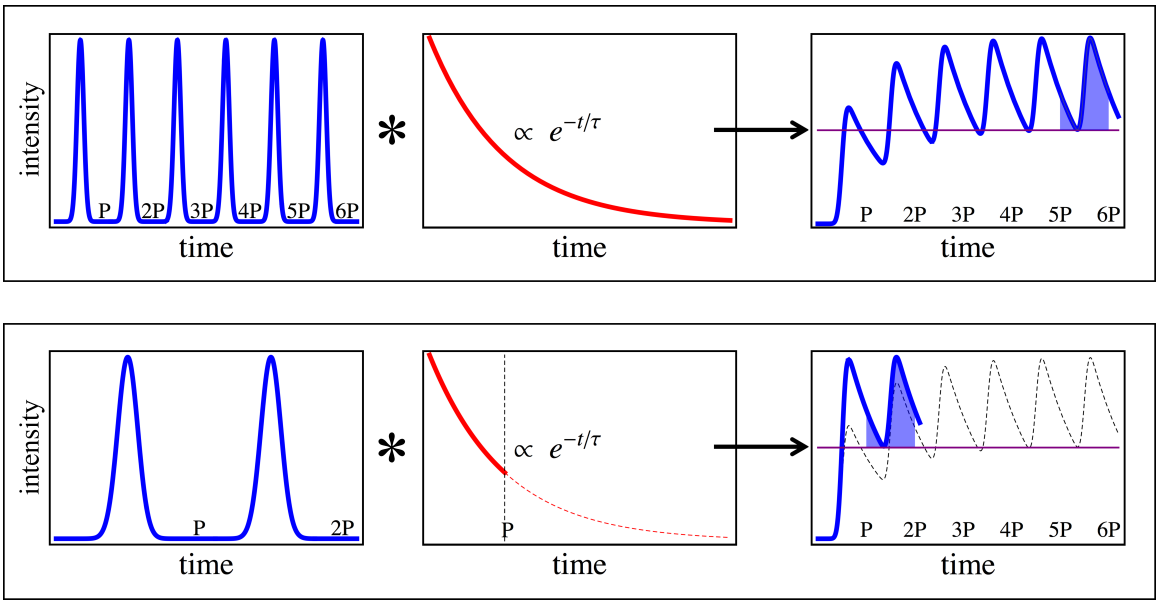

Figure 4.1: A schematic of the different methods for generating noiseless scattered profiles, for simulations or forward fitting. The top panel shows the *long train* method, and the bottom panel the preferred *train* method.

towards the end of the train (shaded) models the average pulse profile. I call this method the *long train* method, in reference to the long train of pulses used.

An alternative method is shown in the bottom panel of Fig. 4.1. This method, which I simply call the *train* method, convolves a Gaussian pulse train of two pulses with a truncated temporal broadening function defined over a single pulse period (solid line). The second broadened pulse is then extracted as the averaged pulse profile (shaded).

The outcome of the *long train* method (scaled by a constant factor and overplotted in dashed lines in the right-most frame) converges to the same average profile shape after a sufficient period of time. Fig. 4.2 shows the definitive convergence of the two methods. The residuals between the last broadened pulse resulting from the *train* method and the *long train* method are shown to decrease as the pulse train length (N) in the *long train* method is increased.

Note that the *long train* method requires care in the choice in the length of both the pulse train and the exponential function, to ensure that the convolution converges to a constant set of pulses. Typically, the required pulse train length increases with an increase in scattering, thereby also increasing the computation time. The advantage of the more simple *train* method is that it is both computationally less expensive and its accuracy is not dependent on the length of the broadening function or the pulse

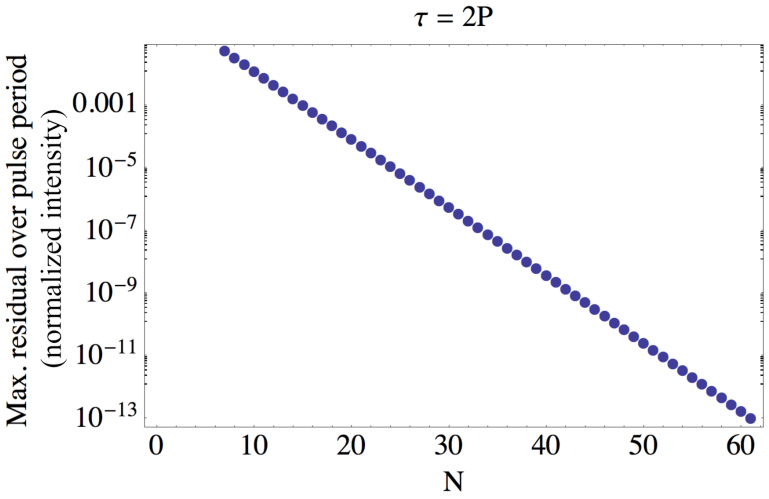

Figure 4.2: The residual intensity differences of the last broadened pulses, as calculated from the analytic expressions for the convolutions in the *train* method and the *long train* method respectively, after having corrected for a constant scaling factor equal to the integral of the broadening function up to $t = P$ (viz. $1 - e^{-P/\tau}$). The residuals are normalised to the area of the pulse and expressed as a function of the number of pulses (N) used in the pulse train of the *long train* method. The broadening function for the long train method is defined for all t, whereas for the train method the broadening function is truncated at the pulse period. In this example $P = 0.4$ s and $\tau = 2P$. The residual can be made arbitrarily small for larger scattering values, but requires ever larger N values.

train (beyond 2 pulses). This motivates me to make use of the *train* method in the subsequent analyses.

After generating the noiseless scattered profiles, Gaussian noise is added to simulate an observation with a chosen peak S/N. Starting from an intrinsic (unscattered) pulse with an off-pulse baseline defined at zero, all methods described above will, in the case of high levels of scattering (large τ compared to the period P), result in profiles with scattering tails that wrap around the full rotational phase and with a raised off-pulse baseline, as is evident from the right-hand side of Fig. 4.1. In order to estimate this baseline level, I use a Gaussian kernel to smooth the noisy simulated scattered profiles. From the smoothed profile I calculate its minimum to determine the raised baseline value to subtract. I monitor the impact of this step on the overall fitting technique and discuss the outcomes in Sec. 4.3.1.

I pick the frequency range over which to simulate the scattered profiles to agree with the LOFAR HBA frequencies, and the profile duty cycles to be such that severe scattering imprints are created at the lower end of the chosen frequency band. That means, at the lowest frequencies considered, τ is a substantial fraction or even larger than the pulse period. This choice is based on an expectation that LOFAR pulsar data will for some target sources be highly scattered within the HBA band.

Note that in modelling the intrinsic pulse to have a centroid (μ) independent of frequency, I have assumed that the scattered pulses have already been correctly dedispersed. The only IISM effect measurable from the simulated pulses is therefore interstellar scattering.

4.2 Fitting techniques

4.2.1 Forward fitting

In this thesis I make use of forward fitting techniques which create models to fit the data by convolving an estimated intrinsic pulse shape with a parameterised broadening kernel that describes the response of the ISM (Ramachandran et al., 1997). An alternative approach would be to perform a deconvolution of the broadened pulse shape as is done for example by the CLEAN algorithm (Bhat et al., 2003). Such inverse processes are complicated by the fact that they can be highly sensitive to e.g. the noise of the signal.

I focus on the forward fitting techniques. One of the main difficulties with this method is to obtain a model that accurately represents the intrinsic pulse shape since pulsars often exhibit intrinsic frequency evolution as described in Sec. 1.1.4. Here I

approximate the intrinsic pulse shape with a Gaussian function, with the caveats as stated in Sec. 4.1.1. Many other studies have opted to use a high frequency profile as an initial approximation of the intrinsic profile, such as Löhmer et al. (2001) and Krishnakumar et al. (2015), in which a high frequency pulsar is used to estimate and then fix the width of the Gaussian template used in the fitting method. Such a method does not allow for any width changes discrepant from ISM effects, such as intrinsic profile evolution.

An example of a forward fitting method is an Exponentially Modified Gaussian (EMG) method. In its most basic form this gives the analytic expression for a single Gaussian pulse convolved with a one-sided exponential function,

$$\mathrm{EMG}(\tau, \mu, \sigma, \mathrm{t}) = \frac{\mathcal{N}}{2\tau} \mathrm{e}^{\frac{2\mu\tau - 2\tau\mathrm{t} + \sigma^2}{2\tau^2}} \mathrm{erfc}\Big(\frac{\mu\tau - \tau\mathrm{t} + \sigma^2}{\sqrt{2}\tau\sigma}\Big), \tag{4.4}$$

with $\mathcal{N}$ the required normalisation factor and μ and σ the mean and standard deviation of the underlying Gaussian. Such a simplistic implementation would not work well for large scattering times compared to the pulse period, when the scattering tail wraps around the full rotational phase of the average pulse profile.

To construct a more efficient technique, I use the methods for generating noiseless scattered profiles, described in Sec. 4.1.3 and Fig. 4.1, as the fitting functions. The method fitting parameters are the underlying Gaussian intrinsic pulse components, i.e. the width (σ), mean (μ) and amplitude (A), as well as the characteristic scattering time (τ) and finally a DC offset, as discussed in more detail in the next section. I use the `lmfit` package in PYTHON, which is a standard least-squares minimiser, to compute the fits (Newville et al., 2014). Scripted, the basic structure of the fitting function is,

```
def GxETrain(x,mu,sigma,A,tau,dc,nbins):
    bins, profile = makeprofile(nbins,ncomps=1,A,mu,sigma)
    scat = psrscatter(broadfunc(nbins,tau),pulsetrain(2,nbins,profile))
    raisedpulse, observedpulse, flux = extractpulse(scat,1,nbins)
    return observedpulse + dc
```

where `makeprofile` creates a single component Gaussian shape which is turned into a series of two pulses by `pulsetrain`. The function `psrscatter` convolves the pulsetrain with a (truncated) broadening function as defined by `broadfunc`, and `extractpulse` extracts the single pulse, representative of the scatter broadened pulse,

```
import numpy as np

def psrscatter(brfunc,profile):
    scattered = np.convolve(profile,brfunc)
    bins = profile.shape[0]
    scatteredprofile = scattered[0:bins]
    return scatteredprofile

def extractpulse(train,pulsesfromend,binsperpulse):
        binstart = -pulsesfromend*binsperpulse
        binend = binstart + binsperpulse
        zerobpulse = train[binstart:binend]-np.min(train[binstart:binend])
        fluxlost = np.min(train[binstart:binend])*binsperpulse
        flux = np.sum(train[start:end]) - fluxlost
        return train[binstart:binend], zerobpulse, flux
```

The use of the *DC* offset parameter will become clear in Sec 4.3.1. The basic framework of the fitting function, that makes use of the above model is as follows:

```
from lmfit import Model

def tau_fitter(data,nbins):
    model = Model(GxETrain)
```

set initial values for all the fitting parameters, only 2 shown here

```
    model.set_param_hint('nbins',value=nbins,vary=False)
    model.set_param_hint('sigma',value=15,vary=True,min=0,max=nbins)
    ...
    pars = model.make_params()
    result = model.fit(data,pars,x=np.linspace(1,nbins,nbins))
    print(result.fit_report(show_correl = True))
    # best fit model
    noiselessmodel = result.best_fit
    # best fit value and error of tau
```

similarly for the other parameters, not shown here

```
besttau = result.best_values['tau']
taustd = result.params['tau'].stderr
...
#reduced chi square
rchi = result.redchi
return result, noiselessmodel, besttau, taustd, ... , rchi
```

A complete version of the code used to produce the results in this thesis can be found online at https://github.com/marisageyer/Scattering.

4.2.2 Monochromatic vs. Broadband frequency

Part of the aim of the study, is to investigate the shape of obtained τ spectra. This involves fitting the simulated scattered pulse profiles over a range of frequencies to obtain the frequency dependence of τ measurements. In doing so, I have to bear in mind that when dealing with real pulsar data, I will typically create observed scattered broadened profiles by adding a set of frequency channels, as described in Sec. 3.2.1. The τ value that I obtain from fitting a monochromatic simulated scattered profile at frequency f_m corresponds to the τ value associated with the central observing frequency f_c of the combined bandwidth Δf by,

$$\log f_c = \frac{1}{2}\Big(\log_{10}(f_m + \Delta f/2) + \log_{10}(f_m - \Delta f/2)\Big) \tag{4.5}$$

or inversely,

$$f_m = \frac{1}{2}\sqrt{\Delta f^2 + 4{f_c}^2}. \tag{4.6}$$

This equation provides the relevant frequency that should be associated with a fitted τ measurement, given any f_c and Δf, and assuming a power law spectrum. This means that computed τ values should be plotted against calculated f_m values to obtain meaningful spectral fits. I revisit the impact of this in the next section, when I start conducting trial experiments.

Lastly, I note the proposed methodology here fits all frequency bands independently, whereas more constraints could be placed by simultaneously fitting for τ and the pulse parameters across a broad bandwidth, if that were available.

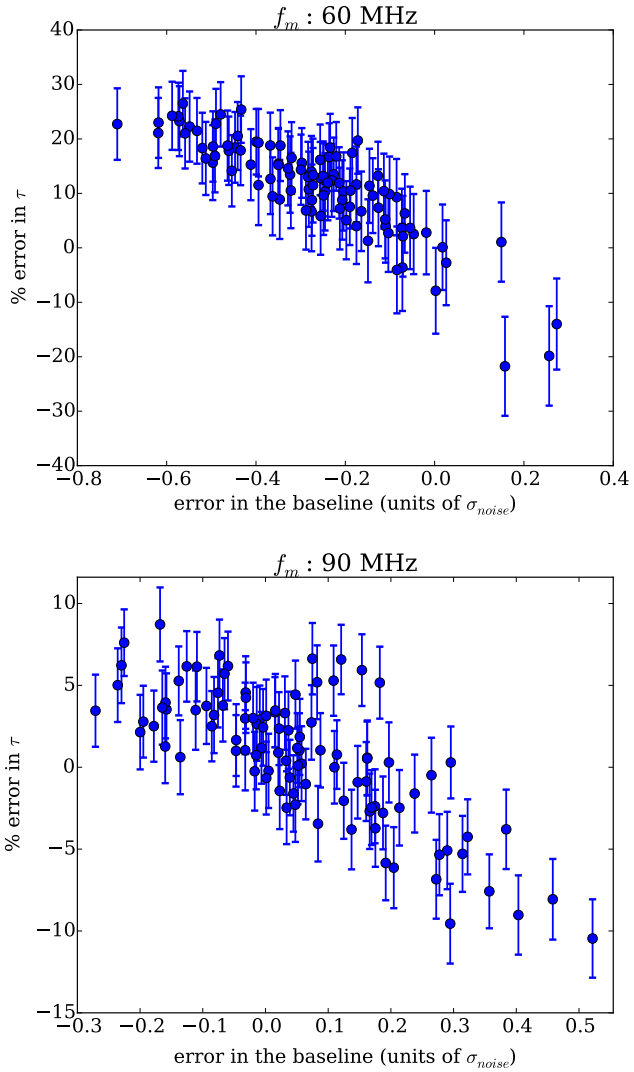

Figure 4.3: Uncertainties in the obtained τ values as a function of the error in estimating the baseline of the scattered profile, shown for two distinct frequency values. Each panel represents 100 independent realisations of Gaussian noise. The data are simulated as described in the text.

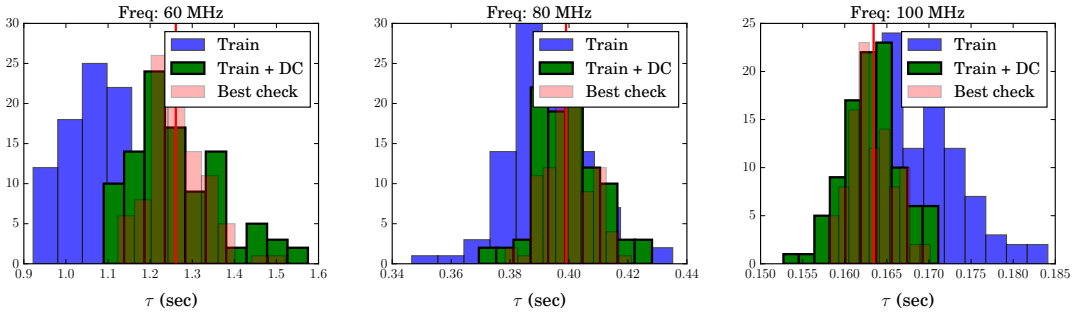

Figure 4.4: Histograms showing the obtained distributions in τ values at three sample frequencies, using different methods. The red line indicates the true value of τ. The *best check* histogram shows the distribution obtained from fits where the noiseless minimum of the profile is known exactly, and is therefore an idealised reference case. The *train* and *train + DC* methods show the spreads in τ using the train method with or without fitting for a DC-offset. In the case where the method does not fit for a DC-offset, a Gaussian smoothing kernel is used to estimate and subtract the raised off-pulse baselines.

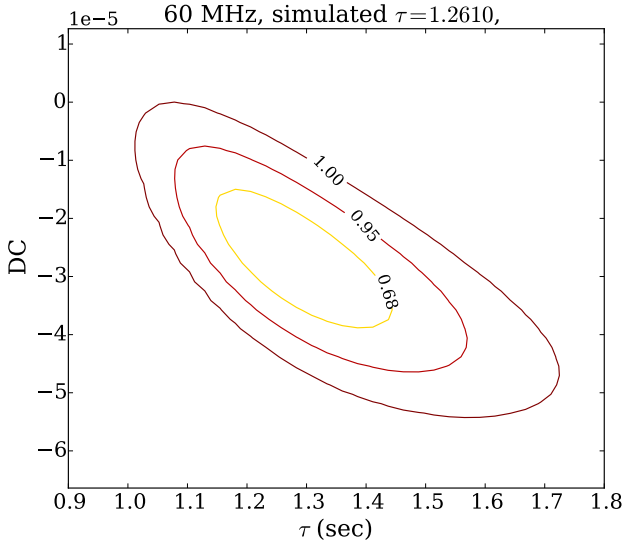

Figure 4.5: The confidence intervals (1σ - 3σ) associated with the obtained fits for the vertical offset parameter, DC, and characteristic scattering time, τ.

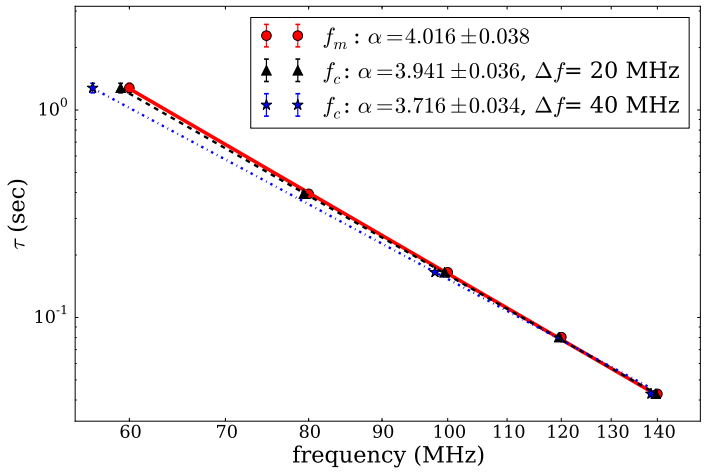

Figure 4.6: Deviations from the theoretical characteristic τ spectrum are observed as the bandwidth of the simulated data increases. The obtained τ associated with a central frequency f_c and bandwidth Δf, relate to the simulated result produced by a monochromatic frequency input f_m through Eq. (4.5).

4.3 Analyses of Simulated Data

4.3.1 A simple end-to-end experiment

Before moving onto detailed results, I describe a simple end-to-end experiment to test the basic efficiency of the fitting method. For this test, I choose to use a simulated isotropic infinite scattering screen, and the frequency range over which I conduct simulations is 60 – 140 MHz. Within this frequency range, the pulse profiles of the slow simulated pulsar, with $P = 1.0$ s and a duty cycle of 2.5 %, are notably scattered and, in the severest of cases (lowest frequencies), the scattering tail wraps around.

Initially, I generate profiles monochromatically at 60 and 90 MHz with a peak S/N of 20. I fit the noisy profiles using the *train* method discussed in Sec. 4.1.3. I find that the determination of the off-pulse baseline of the noisy data has an important effect on the outcome of the fit parameter values.

As mentioned in Sec. 4.1.3, the way in which I estimate the off-pulse baseline is by using a Gaussian kernel to smooth the simulated data after which I compute the minimum of this smoothed profile. I denote the minimum as b here. The effect of the error in accurately determining the baseline (b), on the subsequently fitted τ value, is displayed in Fig. 4.3. In the plots I compare the fitted τ values to the outcome when

the off-pulse baseline is known exactly. The plots show a percentage error in τ,

$$\tau_{\rm err} = 100\frac{\tau_{\rm known} - \tau_{\rm fit}}{\tau_{\rm known}}, \tag{4.7}$$

plotted against the error in the determined baseline in units of the simulated noise,

$$b_{\rm err} = \frac{b_{\rm known} - b_{\rm est.}}{\sigma_{\rm noise}}, \tag{4.8}$$

for 100 realisations of the noise at 60 and 90 MHz.

The error in the τ value increases systematically as the error in the baseline value grows, and is greater at the lower of the two frequencies. At 60 MHz, an error of 10 – 20% in the τ value is already possible for baseline errors below 1σ of the noise. As the frequency increases, the error in τ for a given error in the baseline drops significantly. I also note that at lower frequencies the τ value is more likely to be underestimated, whereas at higher frequencies τ is more likely to be overestimated.

This result prompts me to investigate an improved method. In Fig. 4.4, I present the impact of adding a DC-offset to the parameter set for which the method fits. In the *train + DC* model, I therefore no longer estimate the off-pulse baseline in order to subtract it from the profile before fitting the data, but allow the method to fit for a best off-pulse baseline value. The spread in τ values in Fig. 4.4 represents 100 noise realisations, and the data are simulated as for Fig. 4.3. Introducing a DC offset to the *train* method, ensures that the estimated τ values are centered on the true value (red line). The histogram labeled *best check* gives the spread in obtained τ values when the noiseless off-pulse baseline of the simulated data is known exactly. The *train + DC* model approximates this idealised distribution well. However, at both the low and high end of the frequency range shown, the *train + DC* distributions are more asymmetric than this reference case. The function `GxETrain` shown in the code sample of the method (page 62), includes a fit of the DC parameter.

Fig. 4.5 shows the correlation between DC and τ and the associated confidence intervals, at 60 MHz. The parameters are anti-correlated, with a correlation coefficient of $C(DC, \tau) = -0.73$ at this frequency. This correlation allows an improved accuracy of the obtained τ value, when including a DC value as a fitting parameter.

For the remainder of this chapter I make use of the *train + DC* method. The obtained τ values are therefore subject to uncertainties as inferred from the distributions in Fig. 4.4. This method is considered here the best match for real observational data, where the baseline determination is always affected by instrumental noise.

In this end-to-end experiment I also investigate the typical impact of the bandwidth of an observation on the determined τ spectrum. As described in Sec. 4.2.2 and Eq. (4.5) the τ value associated with a fit of an integrated profile must be remapped to the corresponding frequency f_m, before the spectrum is computed.

Fig. 4.6 shows the impact on the τ spectrum fit when the central frequency values f_c are used instead of f_m. Simulating the data monochromatically at 20 MHz intervals from 60 to 140 MHz leads to a measured spectral index of $\alpha = 4.00 \pm 0.04$, reproducing the theoretical spectrum, for which $\alpha = 4.0$, well. In contrast a bandwidth of 20 MHz at 20 MHz intervals leads to a spectral index of $\alpha = 3.94 \pm 0.04$, when plotted against f_c. An even larger bandwidth of 40 MHz gives $\alpha = 3.72 \pm 0.03$. To produce this figure, I subtracted the correct baseline value before adding noise and fitting the data with the *train* method. In this way I ensure that the effects of the baseline errors described above are not present, and that any deviations from the simulated α values are simply due to the bandwidth effects.

The LOFAR HBA data analysed in the next chapter has a full bandwidth of 80 MHz (ranging from 110 to 190 MHz). I typically split the full band into eight or 16 frequency channels, such that each channel has a bandwidth of $\Delta f = 10$ MHz or 5 MHz, smaller than the examples of Fig. 4.6. These will therefore not lead to severe deviations in α.

4.3.2 Findings for Infinite Screens

Having established the extent of the impact of the baseline, as well as the observing bandwidth effects, I move to testing the outcomes of infinite scattering screen setups on more intrinsic profiles over different frequency ranges. In each case I consider the two scattering mechanisms discussed (isotropic and anisotropic) and present the obtained τ and flux spectra.

4.3.2.1 Tau Spectra

Isotropic Scattering Tau-spectra

Isotropically scatter broadened profiles of the two simulated pulsars described in Sec. 4.1.1 are shown in Fig. 4.7 (1.0 s pulsar) and Fig. 4.9 (20 ms pulsar). The data are simulated to have peak S/N values of 20 across the band. A range of observing frequencies is chosen such that the scattering tail wraps around at the lower end of the frequency range and a typical exponential scattering tail is observed at the higher end.

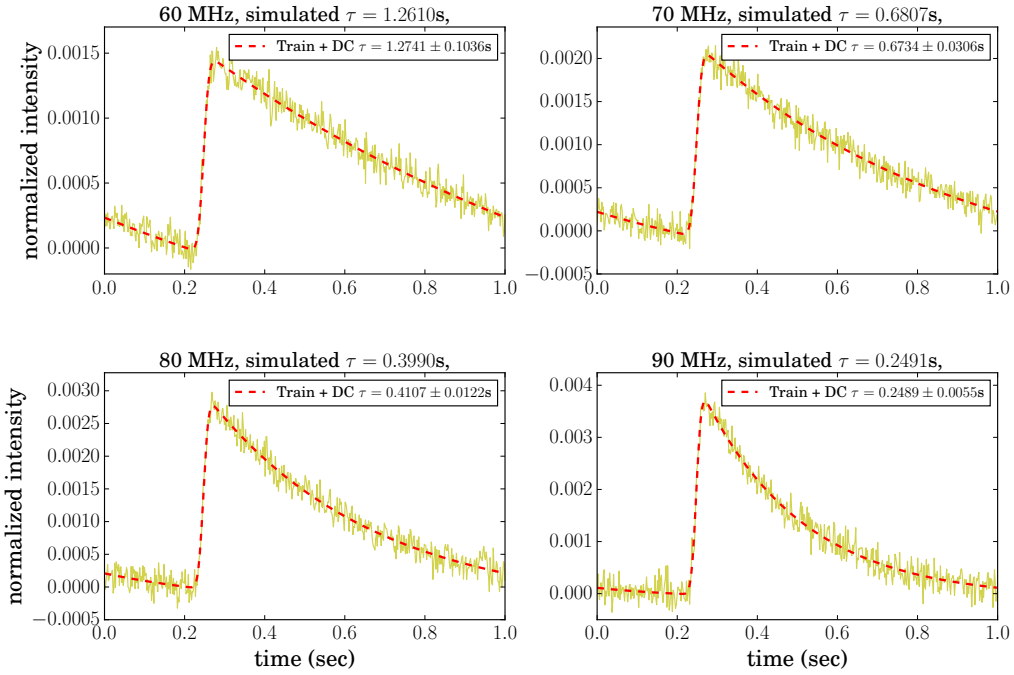

Figure 4.7: Best-fits as produced by the *train + DC* method for simulated scattered pulse profiles of a $P = 1.0$ s pulsar. Fits without the DC-offset parameter (i.e the *train* method in which the off-pulse baseline is determined using a smoothing kernel) look similar to the DC fits by eye, but produces skewed values for τ, as was shown in Fig. 4.4. The impacts of these offsets on the power law fit to the τ spectra can be seen in Table 4.1. Profiles are plotted normalised to the area under the pulse - such that at the lowest frequency (viz. 60 MHz) in the absence of a non-zero off-pulse baseline, the area under the pulse is equal to one.

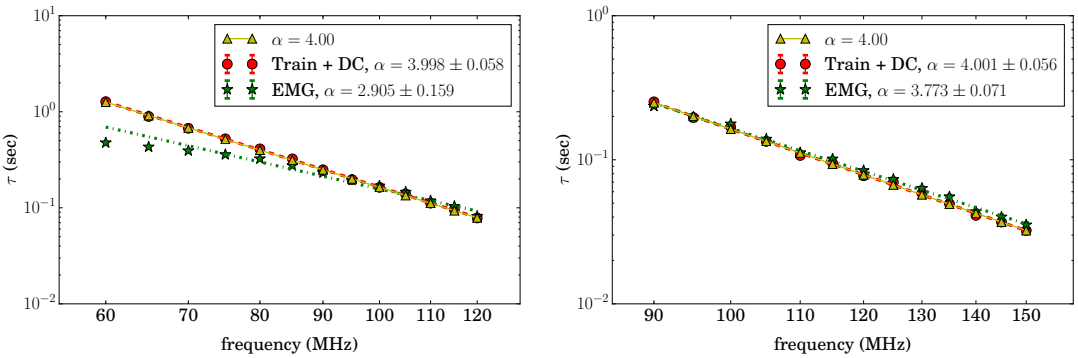

Figure 4.8: The τ spectra for the 1.0 s pulsar as obtained by the *train + DC* method. The left-hand panel shows the spectrum at lower frequency values (high scattering), and the right-hand panel at higher frequency values. Even at the levels of scattering associated with the left hand panel, the *train + DC* method is able to accurately reproduce the theoretical τ spectrum with a spectral index close to 4. The obtained 1σ error bars are of the same order as the marker size and therefore not clearly visible. The EMG method is included as an example of a method that does not model wrap around scattering tails and can therefore not accurately reproduce spectral index values in data where high levels of scattering are present. Table 4.1 gives additional information about the standard deviations in the α values when rerunning the experiment multiple times and fitting with various methods.

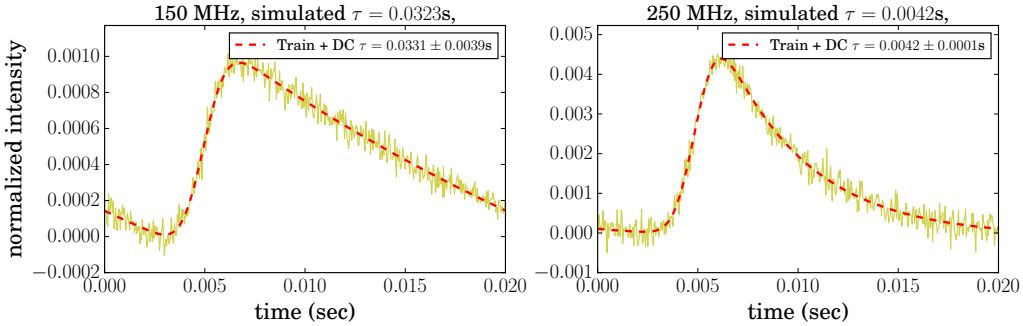

Figure 4.9: Similar to Fig. 4.7, but for a pulsar with period $P = 20$ ms and a duty cycle of 10%.

Table 4.1: The mean spectral indices (α) and standard deviations as obtained from 1000 fitted τ values and associated spectra fits. Two pulsars are investigated: a slow pulsar and a millisecond pulsar. For each pulsar the spectral index is determined over two sets of frequencies. The fits and their associated standard deviations improve with a decrease (increase) in scattering (frequency). The different methods are as described in the text.

Slow pulsar: 1.0 sec, 2.5% duty cycle, SNR: 20

Frequency Range: 60 – 120 MHz				
	EMG	Train	Train + DC	Train + DC asymm errors
Mean Spectral Index	2.90	3.80	4.00	4.01
Standard deviation	0.05	0.09	0.09	0.09
Error (%)	-27.60	-4.90	-0.10	0.20
Frequency Range: 90 – 150 MHz				
Mean Spectral Index	3.78	3.89	4.00	4.00
Standard deviation	0.06	0.06	0.06	0.03
Error (%)	-5.40	-2.80	0.00	0.00

Fast pulsar: 20 ms, 10% duty cycle, SNR: 20

Frequency Range: 150 – 210 MHz				
Mean Spectral Index	1.11	3.71	3.87	4.01
Standard deviation	0.06	0.42	0.32	0.17
Error (%)	-72.20	-7.20	-3.10	0.20
Frequency Range: 200 – 260 MHz				
Mean Spectral Index	2.38	3.85	3.98	3.99
Standard deviation	0.09	0.18	0.14	0.07
Error (%)	-40.40	-3.70	-0.50	-0.30

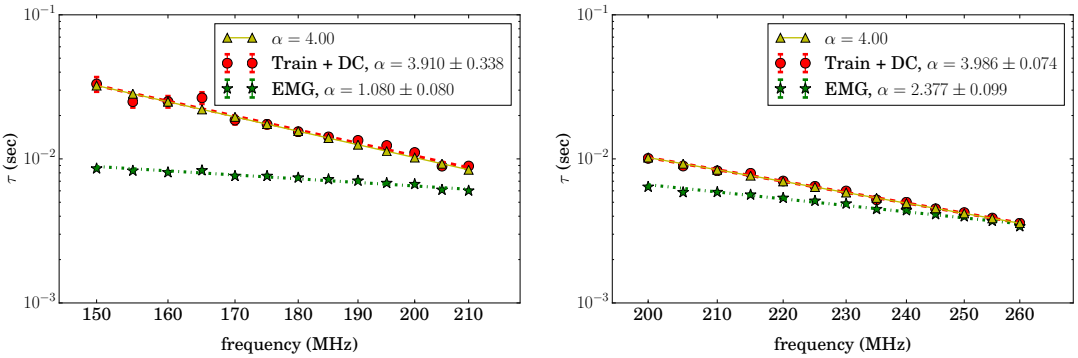

Figure 4.10: The τ spectra of the modelled millisecond pulsar. The uncertainty in the spectral index obtained by the *train + DC* method grows as the frequency range is lowered. At these lower frequencies the EMG method deviates most severely from the theoretical spectrum, and continues to underestimate the value of α even for the higher frequency range. The frequency at which the choice of method matters is much higher for the simulated millisecond pulsar than for the slow pulsar in Fig. 4.8.

The profiles are fitted with the *train + DC* method. Fits without the DC-offset parameter (i.e the *train* method in which the off-pulse baseline is determined using a smoothing kernel) look very similar to the DC fits by eye, but produce skewed values for τ as was shown in Fig. 4.4. The impacts of these offsets on the power law fit to the τ spectra can be seen in Table 4.1.

As described in Sec. 4.1.3, the *train* and the *long train* methods, with added DC offsets, can perform equally well for all the simulations. A *long train* method with a too short pulse train however, leads to an underestimation of τ.

In the case of severely scattered profiles it is vital to use an accurate fitting method as the outcome becomes increasingly sensitive to the model parameters. The *train + DC* method presents the simplest (and computationally fastest) way to obtain accurate τ values.

The τ spectra for the simulated pulsars are shown over two frequency ranges in Figs. 4.8 and 4.10. As the frequency increases, the obtained spectral index value more accurately approaches the simulated index of $\alpha = 4.0$. I also include a basic implementation of the EMG model not accounting for the pulse period P and the possible wrap around scattering tails. This method underestimates τ significantly at high levels of scattering. I make this failure explicit to encourage the revision of fits in the literature where wrap around scattering tails have not been modelled, e.g. Fig. 1 in Lewandowski et al. (2013). At higher frequencies where the scattering tail no longer wraps around, the choice of method becomes less important.

Table 4.1 contains the results of generating 1000 datasets of simulated scattered profiles at intervals of 5 MHz within our frequency ranges, for both the slow and millisecond pulsar, and running the fits for τ and α. The profile and τ-spectra plots (such as Figs. 4.7 and 4.8) represent 1 of these 1000 simulations, and are chosen to reflect the mean outcome as presented in this table. The table compares the outcomes achieved by different methods. For each realisation of the experiment, the *train + DC* method performs best, and in the case of the millisecond pulsar (for which the scattering compared to the pulse period is more severe overall) has a lower standard deviation in its estimation of α, than the standard *train* method. The average spectral index is calculated over two sets of frequencies for both the slow and millisecond pulsar. At higher frequencies (lower scattering) α approaches the simulated value of 4.0 more accurately. This can, for example, be seen in the tabulated error values, which represent the error of the mean spectral index with respect to the true value of 4.0 expressed as a percentage.

Fig. 4.4 shows the spread of τ values obtained by the *train* methods and by a *best check* reference case. As noted even the *train + DC* model shows a skewed distribution of τ, especially at low frequencies. To take this skewness into account, I update the power law fit as follows. I create a distribution of τ values by running many fits (using the *train + DC* method) on scattered pulses, each with the same S/N level but with noise generated for each independently. From this obtained distribution of τ, I subtract 16% of the values from both the lower and upper end of the distribution to be left with the 1σ (68%) central distribution. I now use the values within this range along with their corresponding frequency values to update the τ spectrum, shown in Fig. 4.11. As stated in Table 4.1 under the column heading *train + DC, asymm errors*, this process mainly provides a small improvement at extreme levels of scattering, such as for the simulated millisecond pulsar at 150 – 210 MHz. For the most part of my research I do not require these corrections.

The success of the τ spectra fits and the associated uncertainties are also impacted by the peak S/N value, and improve as the S/N increases. In Table 4.2, I show the achieved spectral index values after repeating the experiment of Table 4.1 at S/N values of 10 and 50. At a S/N value of 50 the theoretical spectrum is best reproduced and the standard deviation in the spread of individual measurements has decreased significantly.

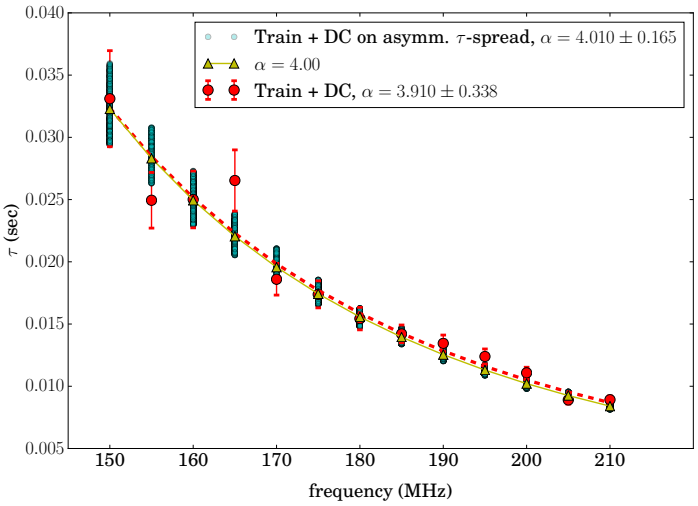

Figure 4.11: The power law fit of the millisecond pulsar is improved when taking the skewness of the τ distribution (resulting from 1000 noise realisations and subsequent fits) into account at each frequency. The τ values that fall within the 1σ uncertainty of this distribution are shown as cyan circles at each frequency. The *train + DC* fit (red) is an example of a single noise realisation and subsequent fit. Data are plotted on a linear scale for the τ spread values to be visible.

Anisotropic Scattering Tau-spectra

In the case of the discussed anisotropic scatterer, the broadened profile is dependent on two characteristic scattering times, each with a frequency dependence $\tau_{x,y} \propto \nu^{-4}$, as described in Sec. 2.2.1.4. I simulate a scattering screen with scattering strengths $\sigma_{ax} = 3$ mas and $\sigma_{ay} = 1$ mas at 1 GHz, as an example. That is to say the screen scatters 3 times more weakly in the chosen y-dimension than in the x-dimension. Since τ scales quadratically with σ_a, this leads to a ratio of $\tau_x/\tau_y = 9$. Setting $\sigma_{ay} = 3$ mas reproduces the isotropic scattering considered before. The scattering geometries are as before and the pulsar is the 1 s Gaussian profile (slow pulsar) from the previous section.

I again fit the simulated data with the *train + DC* method. The resultant profile fits for a selection of frequencies are shown in Fig. 4.12. I fit the data using both the isotropic scattering function (Eq. 2.27) and the extreme anisotropic (1D) scattering function (Eq. 2.31). At the lowest frequency here (60 MHz), the extreme anisotropic profile shape is clearly a mismatch to the simulated data. However, at higher frequencies the extreme anisotropic model is able to fit the simulated data well.

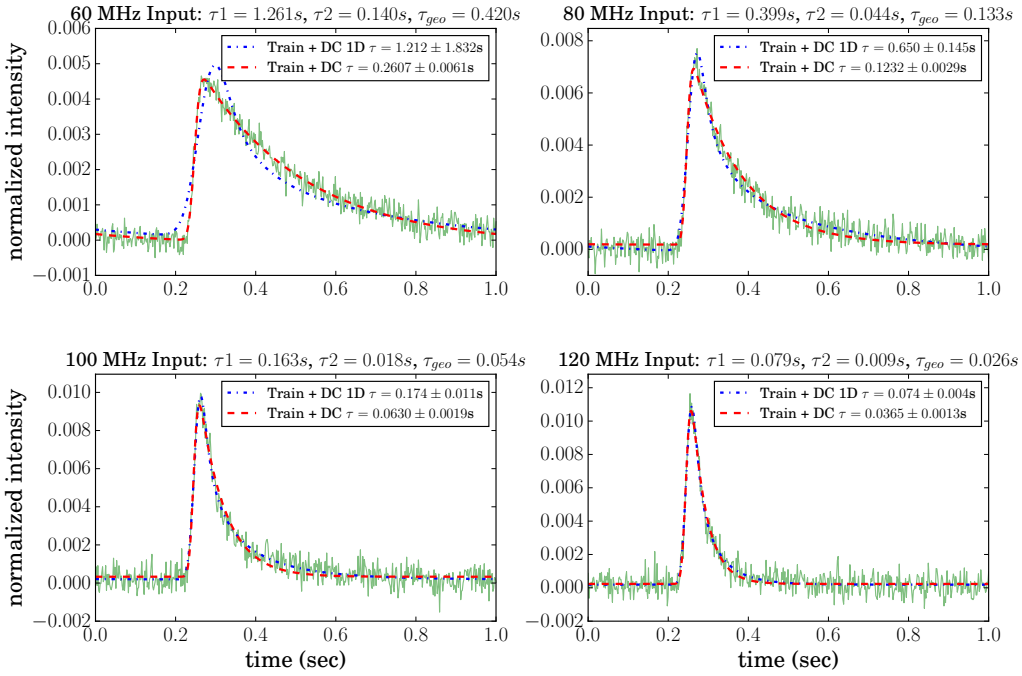

Figure 4.12: Profile fits as obtained by applying the isotropic *train + DC* method (red, dashed lines) and the extremely anisotropic *train + DC* method (blue, dot-dash lines) to anisotropically simulated pulse profiles of a $P = 1.0$ s pulsar (green). The anisotropy is created by choosing a thin screen that scatters three times more strongly in one dimension than in the other. At higher frequencies the isotropic fit to anisotropic data leads to a rough estimation of the geometric mean scattering time (τ_{geo}). At low frequencies τ_{geo} is significantly underestimated. Profiles are plotted normalised to the area under the pulse, such that at the lowest frequency (viz. 60 MHz) in the absence of a non-zero off-pulse baseline, the area under the pulse is equal to one.

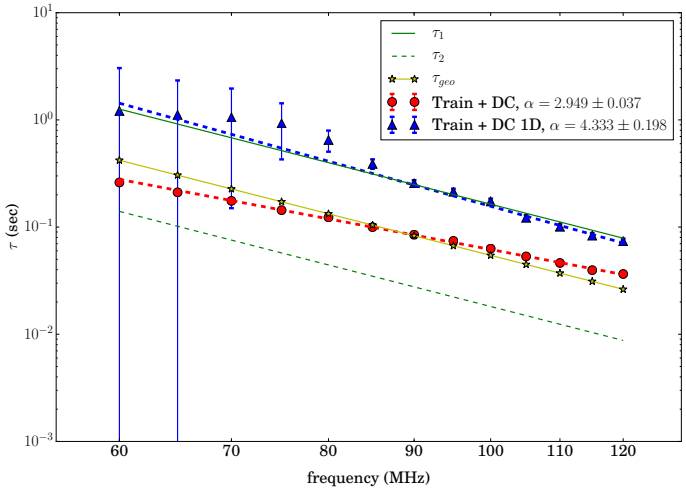

Figure 4.13: The τ spectrum for an anisotropic scattering event fitted with a single power law is shown in red (thick dashed line, circles). I also show the fit resulting from the extreme anisotropic (1D) model in blue (thick dashed line, triangles). The green lines (solid and dotted without markers) show the simulated values for τ_1 and τ_2. The geometric mean for each of these values, $\tau_{\rm geo} = \sqrt{\tau_1 \tau_2}$ is shown in yellow (stars). The τ_1, τ_2 and $\tau_{\rm geo}$ values have a modelled frequency dependence $\tau \propto \nu^{-4}$, with $\tau_1 = 1.26$ s and $\tau_2 = 0.14$ s at 60 MHz. At mid frequencies the isotropic fit leads to an estimate of the $\tau_{\rm geo}$ values, while the extremely anisotropic fit leads to an estimate of the largest τ value (τ_1).

Table 4.2: Spectral indices similarly obtained as for Table 4.1. The simulated data have S/N values of 10 and 50, and show the expected improvements in fits as the S/N values increases. The tabulated values represent a mean α and associated standard deviation after 1000 executions of the experiment.

Slow pulsar: 1.0 sec, 2.5% duty cycle, SNR: 20		
Frequency Range: 60 – 120 MHz		
	S/N = 10	S/N = 50
Mean Spectral Index	4.00	4.00
Standard deviation	0.18	0.04
Error (%)	-0.5	-0.1

Table 4.3: The mean spectral indices as obtained by fits to profiles produced through an anisotropic scattering process. The tabled spectral indices represent the average index as obtained from 1000 fitting procedures, for both the *train+DC* model using the isotropic broadening function and the extremely anistropic broadening function.

Anisotropic Scattering

Slow pulsar: 1.0 sec, 2.5% duty cycle, SNR: 20		
Frequency Range: 60 – 120 MHz		
	Train + DC Isotropic	Train + DC 1D
Mean Spectral Index	2.95	4.29
Standard deviation	0.05	0.27
Error (%)	-26.3	7.3

The corresponding τ spectra are shown in Fig. 4.13. I have chosen the figures, as before, to represent the mean profiles and spectrum after repeating the experiment with Gaussian noise with a peak S/N of 20, multiple times. The mean and standard deviation of the spectral index, as calculated after 1000 repetitions, are given in Table 4.3.

The τ spectrum is shown in Fig. 4.13, along with the input values of τ_1 and τ_2 (green solid and dashed lines). Both have a frequency dependence with spectral index $\alpha = 4.0$. The fit using the extreme anisotropic model (blue triangles) leads to a good approximation of the largest τ value at higher frequencies. Consequently the obtained α value is closer to the simulated value of 4.0. At the lowest frequency value however, the extreme anisotropic profile shape leads to large error bars on τ.

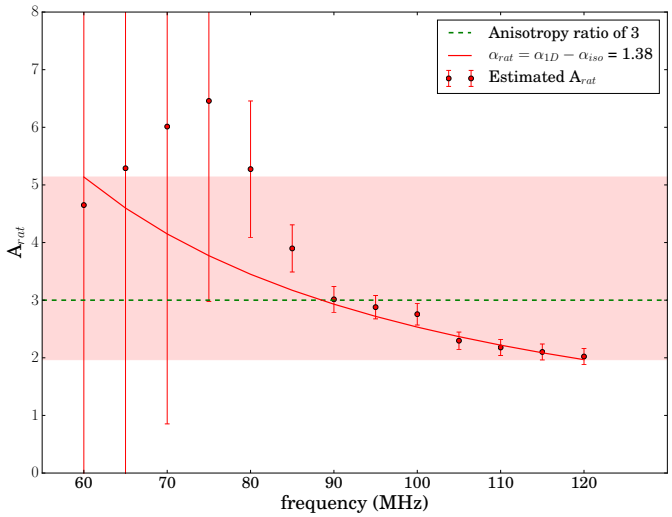

Figure 4.14: Anisotropic ratio associated with Fig. 4.13 as calculated by Eq. (4.10).

The geometric mean of the two input τ values,

$$\tau_{geo} = \sqrt{\tau_1 \tau_2} \tag{4.9}$$

which would reduce the anisotropic scattering to isotropic scattering for $\tau_1 = \tau_2 = \tau_{\rm geo}$, is computed from the input τ_1 and τ_2 and shown in yellow (stars). The single isotropic τ fit, shown in red, provides an estimate of the $\tau_{\rm geo}$ value at mid frequencies. At low frequencies however the method fits deviate from $\tau_{\rm geo}$ significantly. Such an estimate of $\tau_{\rm geo}$ will worsen as the degree of anisotropy increases.

Assuming that the values associated with the isotropic fit ($\tau_{\rm iso}$) are approximations to $\tau_{\rm geo}$, and the τ values associated with the 1D model ($\tau_{\rm 1D}$) are approximations to the largest τ value (where $\tau_1 > \tau_2$), then the degree of anisotropy ($A_{\rm rat}$) can be estimated ($\tilde{A}_{\rm rat}$) through,

$$A_{\rm rat} = \sqrt{\frac{\tau_1}{\tau_2}} = \frac{\tau_1}{\tau_{\rm geo}} \sim \frac{\tau_{\rm 1D}}{\tau_{\rm iso}} = \tilde{A}_{\rm rat}. \tag{4.10}$$

The anisotropic ratio estimated from the best fit τ values of Fig. 4.13 is shown in Fig. 4.14. The boundaries of the plotted function, leads to an approximation of $1.9 < A_{\rm rat} < 5.2$, with the values associated with the mid-frequencies leading to the estimates closest to the true value of 3.0.

These results show that scatter broadened profiles that have been produced by anisotropic scattering mechanisms require more sophisticated fitting models that can account for the degree of anisotropy. Such a model would make explicit use of

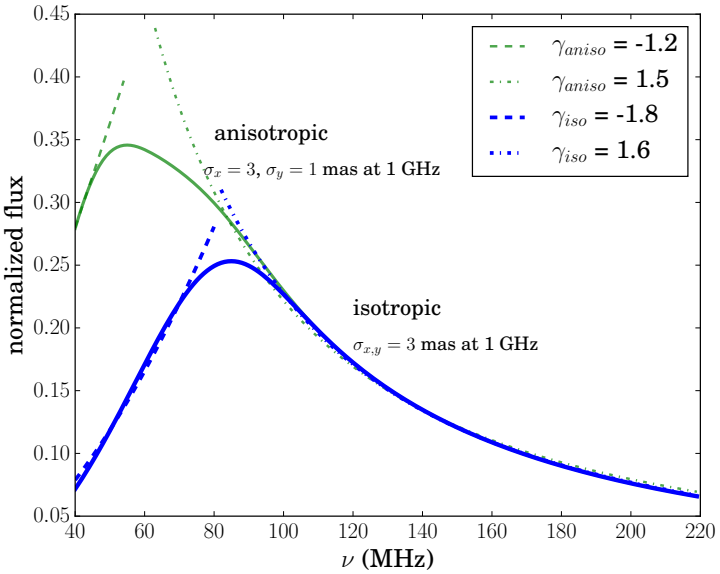

Figure 4.15: Spectral turnovers in the flux spectra of the $P = 1.0$ s pulsar associated with an infinite isotropic and an infinite anisotropic scattering screen. The turnovers at low frequencies are due to the raise in off-pulse baselines, which lead to a loss in observable flux. These effects cause positive spectral slopes over the associated low frequency ranges. The spectrum related to the anisotropic scattering screen, has a turnover at a lower frequency than the isotropic case. This is because the mean scattering strength, of the modelled anisotropic screen, is weaker.

Eq. (2.30) in its description. Fitting with Eq. (2.30) proved to be difficult, mainly because the covariance of the two τ parameters often lead to large uncertainties in at least one τ value. The fitting method was also found to be sensitive to the initial parameter guesses of the τ values.

For individual pulsars, screen anisotropy might be revealed through elongated images (Brisken et al., 2010) or features of the secondary spectra as discussed in Sec. 2.2.3, which will be instructive in determining the choice of fitting function, and in improving the accuracy of the fit.

4.3.2.2 Flux-spectra

The mean flux (S_m) of a pulse profile is calculated by integrating the intensity of the profile averaged over the pulse period. This is illustrated schematically on the right-hand side of Fig. 4.1, where the mean observable flux is shaded in blue. Scatter broadening that causes the power of pulses to be smeared into succeeding pulses will lower the observable flux, since the intrinsic flux contained in the raised baseline, can

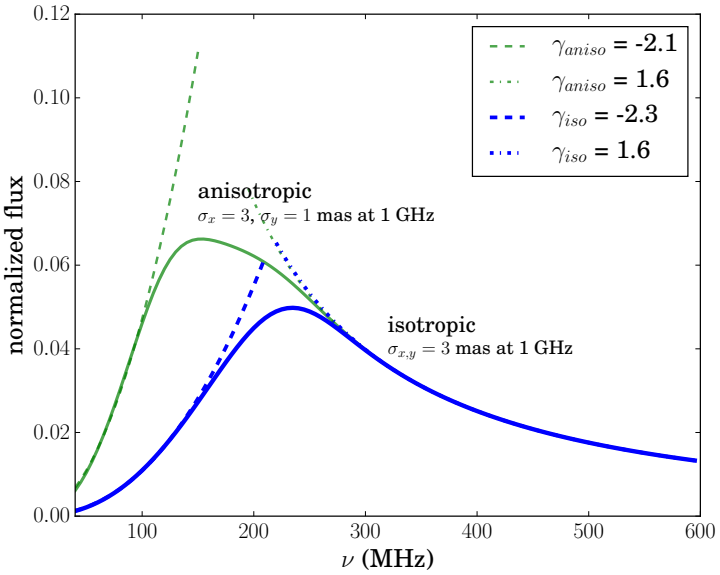

Figure 4.16: Spectral turnovers in the flux spectra of the simulated millisecond pulsar. The turnovers occur at higher frequencies than for Fig. 4.15, due to higher τ/P values for the fast spinnning spulsar.

not be measured. This loss in observable flux is an artifact of the temporal domain, such that one way to, in principle, circumvent it would be by imaging pulsars directly (e.g. Dembska et al. 2015, more details in Chapter 9).

I compute the flux for the slow and fast pulsar described in Sec. 4.3.2.1. Fig. 4.15 shows a turnover in the flux spectrum due to scattering effects at low frequencies. The mean flux values quoted here are calculated from the noiseless scatter broadened pulse shapes. It is normalised such that in the absence of the baseline being raised, the lowest considered frequency (viz. 40 MHz) has a mean flux equal to 1.0.

Fig. 4.15 shows the turnovers in flux spectra for both the isotropic and anisotropic scattering setup. The turnover for the isotropic model occurs at $\sim$ 90 MHz. The turnover for the anisotropic scattering model, occurs at a lower frequency ($\sim$ 55 MHz) and causes a smaller loss in flux since the mean scattering is weaker. The turnover also has an asymmetric shape. Turnover frequencies associated with the isotropic and anisotropic model are related by $\sqrt{\sigma_{a_x}\sigma_{a_y}}/\sqrt{\sigma_i^2}$, where the subscript i refers to the isotropic case and a to the anisotropic case, with (x, y) the two dimensions defining the thin screen ($\sigma_i = \sigma_{a_x} = 3$ and $\sigma_{a_y} = 1$ mas at 1 GHz).

Fits to the high-frequency end of these spectra approximate the intrinsic spectral index of $\gamma = 1.6$. For low frequencies, however, the spectral turnover leads to a positive slope such that (using the convention $S_\gamma = \nu^{-\gamma}$) the spectral index is estimated

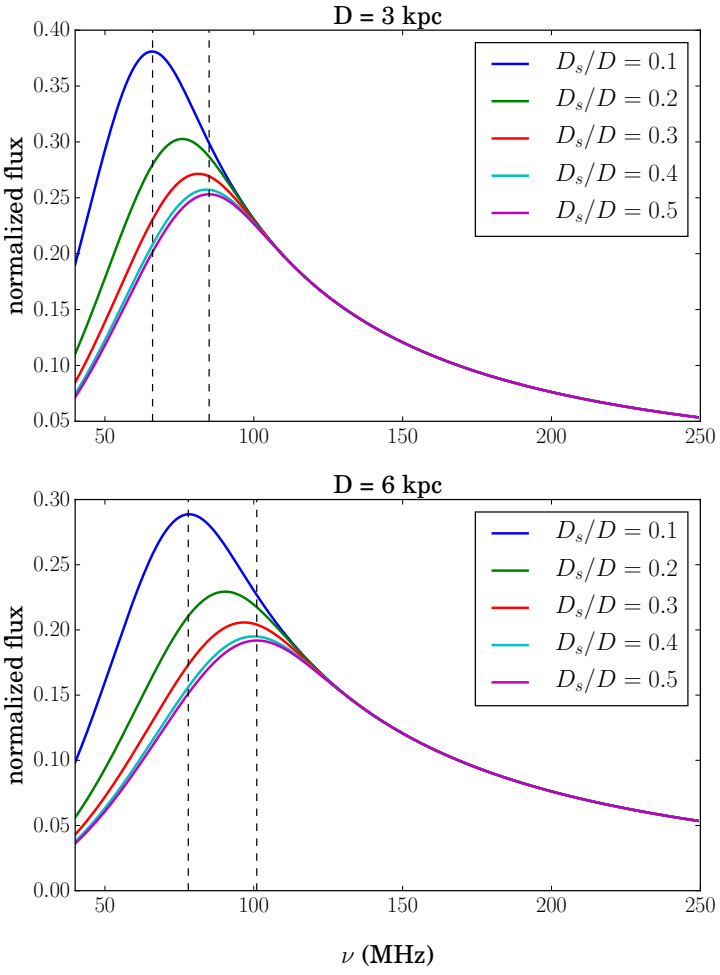

Figure 4.17: Flux spectra plotted for different ratios of D_s/D and overall distances, D. The highest frequency at which a spectral turnover occurs, increases from 86 MHz to 102 MHz as D is increased from 3 to 6 kpc. Ever higher values of D do not increase the turnover frequency significantly ($D = 12$ kpc has a turnover at $\sim$120 MHz).

to be $\gamma = -1.8$ for the isotropic case and $\gamma = -1.2$ for the anisotropic case.

In Fig. 4.16, I show the flux spectrum associated with the millisecond pulsar. As expected from the scattering analysis in the previous section, the turnovers in this flux spectrum occur at higher frequencies than for the slow pulsar. For the isotropic model the turnover occurs at 235 MHz and for the anisotropic model at 155 MHz, i.e. in both cases at an almost three times higher frequency value.

The fractional flux loss is also highly increased for the fast pulsar. At the lowest frequency of 40 MHz less than 2% of the expected intrinsic flux is measurable, whereas for the slow pulsar around 7% of the intrinsic flux remains measurable for the isotropic case, and 28% for the anisotropic case.

In Fig. 4.17, I investigate how changing the scattering geometry impacts on the flux spectra. As the position of the screen (D_s) is moved for a fixed overall distance (D), the frequency at which a spectral turnover due to baseline effects is expected to be observed, will change. This phenomenon is symmetric about the mid-point ($D_s/D = 0.5$) such that for example the spectra for $D_s/D = 0.8$ and 0.2 are equal. The observed scattering effects are maximized for $D_s/D = 0.5$ and therefore the frequency at which flux loss is first observed will be highest for a midway screen.

The overall distance D is increased from 3 kpc to 6 kpc from the top panel to the bottom panel of Fig. 4.17. This overall increase in distance increases the scattering and subsequently the frequency at which spectral turnover appears. Simultaneously, as D is increased the frequency window within which spectral turnover takes place for all plotted ratios of D_s/D (indicated with dashed lines), grows slowly. This result shows that for distances within our Galaxy and a scattering strength of $\sigma_\theta = 3$ mas at 1 GHz, as taken from Cordes & Lazio (2001), turnovers in mean flux spectra occur below 100 MHz. Spectral turnovers at higher frequencies are either due to different scattering mechanisms (deviations from isotropically Gaussian scattering) or different scattering strengths than the typical value used here. However since a wide range of scattering strengths are likely expected, it is unclear whether or not a coherent picture is expected throughout the population of pulsars with measured spectra. At very large distances, $D > 200$ kpc, (while still using the above scattering strength) the simulated pulse is completely scattered out and a turnover in the flux spectrum no longer detectable in this way.

4.3.3 Findings for Truncated Screens

In Sec. 4.1.2, I discussed computing the temporal broadening functions (f_t) of truncated screens by means of a ray-tracing code. I expect these finite screens to cause

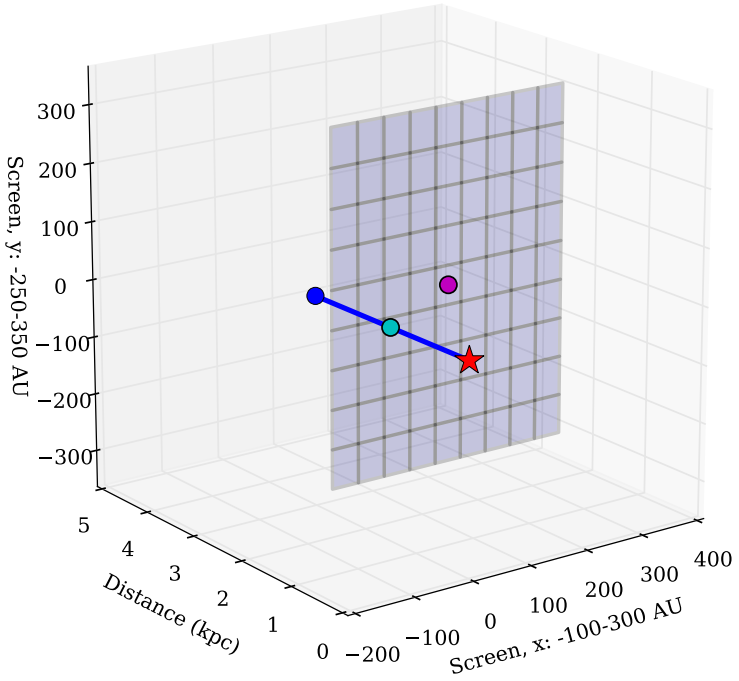

Figure 4.18: A cartoon of the toy model truncated screen. The simluated screen here has a size 400 AU by 600 AU placed at a midway distance between the observer (blue dot) and the pulsar (red star) that are 3 kpc apart. The pulsar is offset w.r.t. to the centre of the screen (magenta) by 100 AU horizontally and 50 AU vertically (cyan dot). On this coordinate grid the width of the screen is defined between −100 AU and 300 AU and the height from −250 AU to 350 AU. Note that the cartoon is not to scale, with the axis describing the direct line of sight in kpc while the other axes are in AU.

a loss in the observable flux of the pulsar. I also investigate how the shape of an average pulse profile, and consequently the τ spectrum, is impacted by the presence of such a screen.

By defining the screen in terms of its height and width I can create both square screens that have an impact comparable to that of a circular screen (as described in Cordes & Lazio 2001) or rectangular (elongated) screens. In the theoretical limit where screens become infinitely more long than wide (i.e. 1D filaments) the broadening function tends to Eq. (2.31).

4.3.3.1 Profile effects

The numerically created broadening function for a source at a distance of $D = 3$ kpc with a finite isotropic scattering screen halfway between the source and the observer

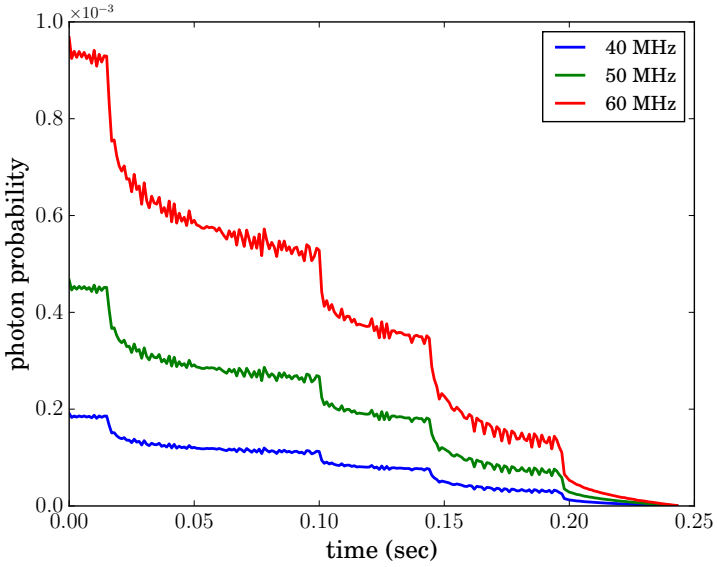

Figure 4.19: The broadening functions associated with a truncated scattering screen of size 400 AU by 600 AU, with the pulsar offset to the centre of the screen as discussed in the text. The functions are generated numerically by means of a ray tracing code that calculates the probability of photons arriving at the observer at a given time.

is presented in Fig. 4.19. The screen is modelled to have a size 400 AU by 600 AU, with the pulsar offset to the middle of the screen by 100 AU horizontally and 50 AU vertically, as shown in cartoon style in Fig. 4.18. The scattering strength is as before, $\sigma_a = 3$ mas at 1GHz.

The dips in the broadening function are associated with the four edges of the screen and show the associated loss in flux at different frequencies. In this instance there are dips at $0.02, 0.10, 0.15$ and 0.20 s associated with distances to the edge of $100, 250, 300$ and 350 AU.

The numerical broadening functions are convolved with the same $P = 1.0$ s pulsar as used for the infinite scattering screens in Sec. 4.3.2. A selection of the resulting broadened profiles are shown on the left-hand side of Fig. 4.20.

The observed profile broadening effects can be split into three regimes. At high frequencies (above 210 MHz, not shown) the effect of scattering is negligible and the observed pulse resembles the intrinsic Gaussian pulse. At mid-frequencies (here 120 – 210 MHz) the pulse shapes have the typical exponential tail as would be associated with an infinite scattering screen. At low frequencies (below 120 MHz) the finite nature of the scatterer becomes visible in the form of bumps associated with the loss in flux at various path lengths (or times). These pulse shapes have a much steeper

trailing edge than normally associated with a scatter broadened pulse shape.

To test these effects on a more complicated profile shape, I use a high frequency profile of PSR B1237+25 as a multi-component template and scatter the signal with a simulated truncated screen. In the simulations I use the pulsar's period ($P = 1.38$ s) and distance ($D = 0.85$ kpc). Note that this pulsar is a high Galactic latitude source, and not an ideal candidate for scattering studies, but provides an interesting profile shape to experiment with. I model the impact of an isotropic screen, size 200 by 200 AU, placed midway along the line of sight. The scattering strength is as before. The resulting broadened pulse shapes at several frequencies are shown on the right-hand side of Fig. 4.20. The truncation effect of the screen causes the height of the two profile peaks to change relative to each other with frequency. Between 110 and 130 MHz the left peak is lower than the right one, at 140 MHz the peaks are roughly equal, and beyond 140 MHz the left peak is the higher peak. Changes like these are similar to typical intrinsic variations observed in pulsars, and could as such be misinterpreted as features of the intrinsic pulse shape, when it is really the ISM causing the variation.

The above scattering setups are somewhat contrived theoretical constructs, however by investigating the impact of truncated screens on both the τ and flux spectra, I can build a more complete picture of all the possible sources of deviations to the otherwise theoretically predicted spectral trends for infinite screens.

4.3.3.2 Effects on τ spectra

To estimate the τ spectra I add Gaussian noise to the simulated profiles, after which I fit them with the *train* method. (Since the truncation prevents wrap around profiles here I do not have to include a DC offset parameter.) The S/N value is modelled to scale with the mean flux of the profile, and is therefore notably smaller at low frequencies for which the flux loss is greater. I discuss the flux spectrum in more detail in the next section. The resulting profile fits for a selection of frequencies are shown in Fig. 4.21.

The corresponding τ spectrum is shown in Fig. 4.22. From the τ spectrum it is clear that a model based on the assumption of an infinite screen, greatly underestimates the true value of τ. A weighted power law fit to all the obtained τ-values produces a spectral index of $\alpha = 3.17$. If I identify a single frequency at which the observations appear to become sensitive to the edges of the screen, I can fit the spectrum with two power laws instead. Using 100 MHz as this breakpoint, I find that

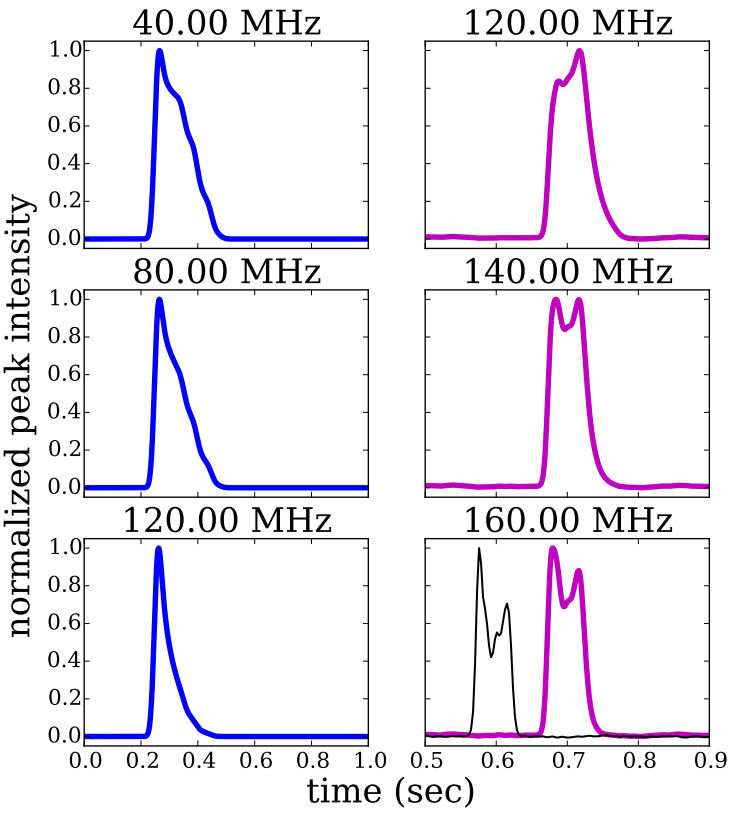

Figure 4.20: *Left:* Convolutions of an intrinsic Gaussian pulsar profile with the temporal broadening functions shown in Fig. 4.19. The scattering screen has size 400 AU by 600 AU, offset with respect to the line of sight as described in the text. The distances are $D = 3$ kpc and $D_s = D/2$ kpc. At 40 MHz and 80 MHz the effect of a truncated screen is seen as bumps and an overall steepening of the profile shape. At 120 MHz the profile starts to resemble the typical exponential scattering tail. *Right:* Broadened pulses using PSR B1237+25 as a profile template and a screen of size 200 AU by 200 AU, centered on the line of sight, with $D = 0.85$ kpc and $D_s = D/2$. The relative heights between the two peaks change as the observing frequency changes. All profiles are plotted normalised to their height. The unscattered intrinsic profile shape is shown in black in the last frame.

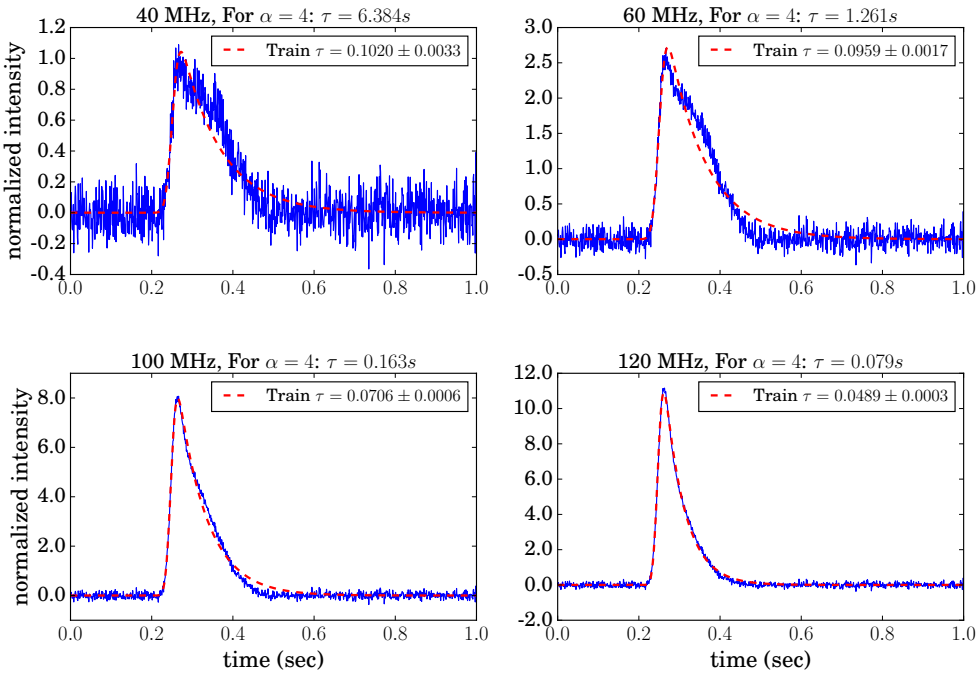

Figure 4.21: Profiles as generated by the truncated broadening function of Fig. 4.19 with added Gaussian noise. The profiles plotted here are normalised relative to the peak of the profile at 40 MHz (which has suffered the greatest flux loss). The input τ values at different frequencies are given, along with the values obtained from the fits with the *train* method. In all instances the τ values are underestimated by more than 45%.

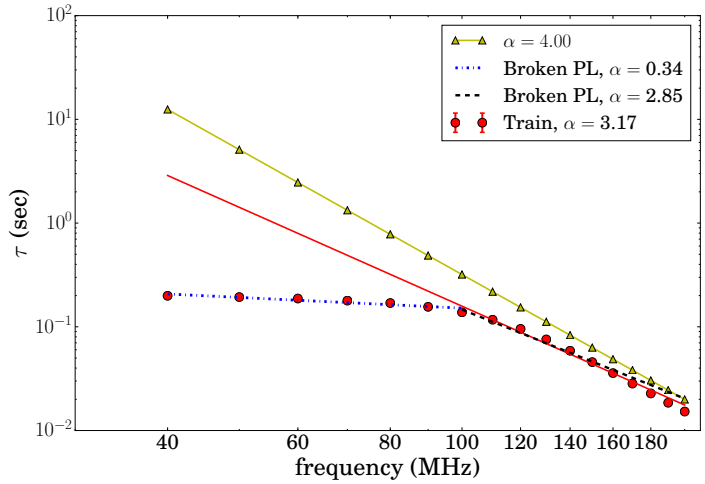

Figure 4.22: The τ spectrum associated with a truncated screen. At low frequencies (high scattering) the τ values as obtained by the *train* method (red circles, with error bars smaller than the marker) greatly underestimates the input scattering (yellow triangles). This is due to the fact that at large wavelengths the scattering model becomes sensitive to the edges of the screen leading to imprints in the temporally broadened pulse profiles for which our method does not account. The short black (dashed) and blue (dot-dash) lines show a broken power law fit with spectral indices as indicated in the legend, and the long red (dashed) line is the weighted power law fit of all the obtained τ values.

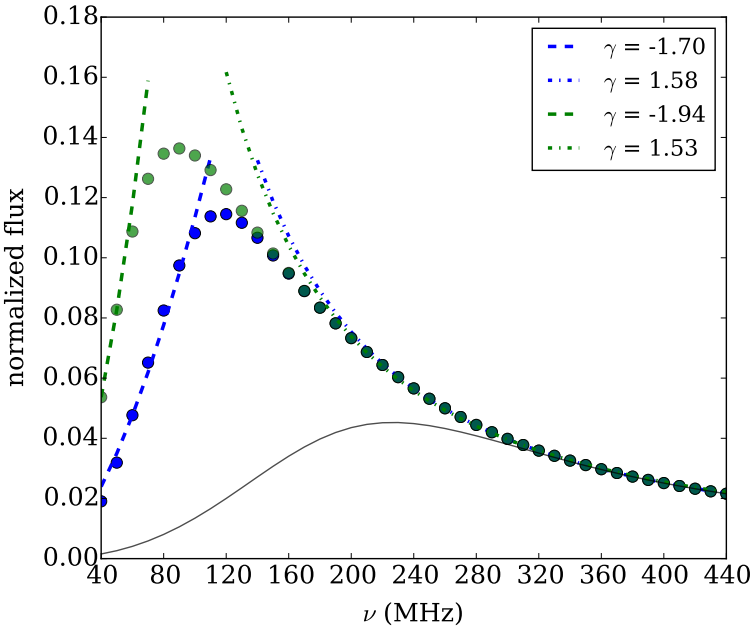

Figure 4.23: The flux spectrum of the truncated scattering screen setup discussed in the text is shown in blue. The turnover in the spectrum is due to the longer wavelengths being emitted beyond the boundaries of the screen such that not all of the pulsar's flux fill be received back at the detector. The equivalent anisotropic case for a screen that scatters 3 time more weakly in one dimension is presented in green. The turnover in this case occurs at a lower frequency compared to the stronger isotropic scatterer. The grey line shows the flux spectrum for a smaller screen (100 by 200 AU). Decreasing the screen size leads to turnovers at higher frequencies.

$\alpha = 2.85$ above this frequency. Below 100 MHz I see a flattening of the τ spectrum, such that the obtained spectral index is $\alpha = 0.34$.

4.3.3.3 Effects on flux-spectra

I expect to measure a loss in the observable flux for a pulsar behind a truncated scattering screen, of such size that at low frequencies not all the photons from the pulsar are refracted back to our line of sight. To model this loss I, calculate the probability that a photon hitting the truncated screen at some angle and location on the screen is scattered to reach the observer. I then compare this to the probability associated with a sufficiently infinite screen. I define *sufficiently infinite* in terms of the width of the Gaussian distribution from which the scattering angle is drawn. A distribution that is defined between $-5\ \sigma_\theta$ and $5\ \sigma_\theta$ is considered to be an approximation of an infinite screen distribution.

The ray-tracing code is normalised such that the temporal broadening function of a sufficiently infinite screen at the lowest studied frequency produces an impulse flux of unity. This means, when convolving a simulated pulse with an infinite screen, the resulting flux spectrum will equal the intrinsic flux spectrum of the pulsar with $S_m = 1.0$ at the lowest observed frequency (provided that no flux is lost due to high levels of scattering that have lead to wrap around scattering tails).

The flux spectrum in Fig. 4.23, associated with isotropic scattering, shows a turnover close to 120 MHz. Above this frequency the screen is effectively infinite such that the flux of the pulsar behind it is conserved, and the intrinsic pulsar spectrum with $\gamma = 1.6$ becomes visible. Below 120 MHz, the spectral index changes sign as more flux is lost towards lower frequencies (longer wavelengths) when the scattering model becomes sensitive to the edges of the scattering screen.

Fig. 4.23 also contains the flux spectrum for a truncated anisotropic scatterer of the same size and location. The anisotropy is created by again choosing that the screen scatters 3 times more weakly in one dimension. Since this leads to an altogether weaker scatterer, the loss in flux is less severe and the onset of flux loss is seen to be at a lower frequency that for the isotropic example.

The turnovers in both Figs. 4.15 and 4.23 occur at frequencies below 150 MHz for the current scattering setup. Pushing the overall distance (D) to 6 kpc in Fig. 4.17 did not greatly increase the frequency at which the spectral turnover due to baseline effects occur. An alternative way to produce turnovers at higher frequencies, while keeping the scattering strength, is by means of ever smaller scattering clouds. Fig. 4.23 includes an example (grey line) of a smaller screen with a higher turnover frequency.

4.4 Summary of the Simulated Data Findings

I summarise the findings of this methodology chapter as follows.

- Introducing a DC offset parameter is key to ensure that the estimated τ value distribution is centered on the true simulated value, especially at high levels of scattering where wrap around scattering tails occur.

- To obtain accurate τ-spectral fits, the measured τ values should be associated with the monochromatic frequency (f_m), computed from the central frequency (f_c), for bandwidths larger than 20 MHz at frequencies below 200 MHz.

- For the most extreme level of scattering modelled here (fast pulsar at low frequencies), the simulations show an underlying asymmetry in the measurement

uncertainties of τ. Correctly accounting for the asymmetry results in a more accurate measurement of α.

- Having introduced the above techniques and corrections, the α values for all the isotropically simulated data have a mean value within 0.3% of the true value, and a standard deviation below 0.2.

- Fitting anisotropically scattered profiles (simulated with an asymmetric Gaussian distribution), with isotropic models leads to systematic errors in τ. Improvements to such fits rely on using more appropriate broadening functions, such as Eqs. (2.30) or (2.31), in the fitting model.

- Truncated scattering screens, (here of size 400 AU by 600 AU, at a midway distance of 1.5 kpc), change the shape of the pulse profile with frequency and leads to a flattened τ spectrum at low frequencies (here below 200 MHz).

- Complex pulse profile shapes can exhibit frequency evolution due to scattering by a truncated screen, seemingly similar to intrinsic profile variation. In principle the effects can be disentangled, as it is unlikely that both will have the same dependence on frequency.

- Fig. 4.24 provides a cartoon style summary of deviations from the theoretical τ spectrum (modelled to have $\alpha = 4$) and the underlying causes.

- Apparent low frequency turnovers in flux spectra can be caused by high levels of scattering by infinite screens, due to a loss in measurable integrated flux to the baseline. For the simulated slow and fast pulsar this leads to spectral turnovers below 100 MHz and 250 MHz respectively.

- The turnover frequencies in the flux spectra associated with simulated anisotropic scattering, which represents weaker scattering along one dimension, occurs at lower frequencies.

- Flux spectral turnovers can also be caused by actual flux loss associated with truncated scattering screens. The simulated scattering screen (400 AU by 600 AU) placed at the same location as the infinite screen, leads to spectral turnovers at frequencies (125 MHz and 90 MHz for the isotropic and anisotropic case respectively), similar to the modelled inifinite case. Smaller screens lead to higher turnover frequencies.

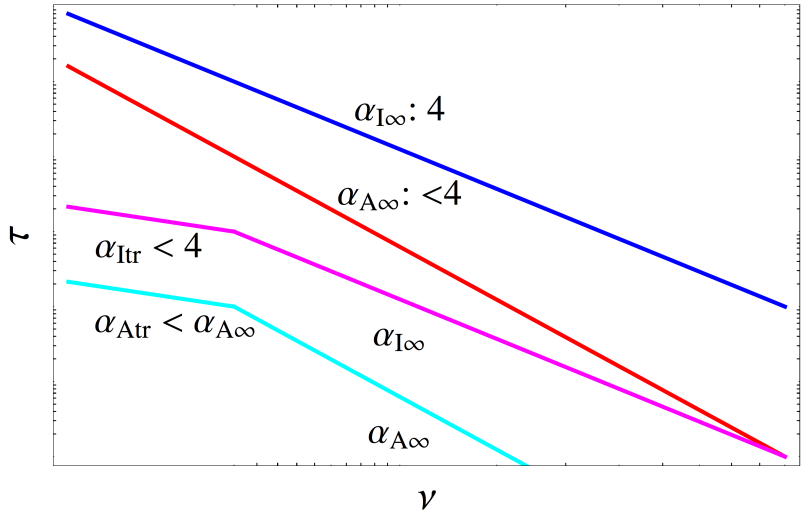

Figure 4.24: A cartoon summary of the deviations from the theoretical τ spectrum and their underlying causes. Subscripts I and A refer to isotropic and anisotropic scattering mechanisms, and ∞ or tr to either infinite or truncated thin screens. The anisotropic scatterer shown here scatters more weakly in one dimension than what is considered a typical isotropic scattering strength.

Chapter 5

Results of Pulsar scattering in LOFAR data

In this chapter I analyse the scatter broadening of the average pulse profiles of 13 pulsars, using data recorded by the HBA antennas (110 MHz - 190 MHz) of the LOFAR Core (Chapter 3). The data are analysed using the fitting methods described in detail in Chapter 4. The investigation aims to answer the Open Questions posed at the end of Chapter 1. The bulk of the results presented here have been published in Geyer et al. (2017).

5.1 Data Summary

5.1.1 Target sources

An overview of the 13 chosen sources and their associated parameters, is given in Table 5.1. It contains pulsars from the three datasets, as described in Sec. 3.3. Datasets are abbreviated as Co, Ce and Cy for Commissioning, Census and Cycle 5 data, respectively. All of the pulsars in the set are slow pulsars, with periods ranging from 0.1 s to 1.58 s. They are mostly nearby sources (1.56 kpc $< D <$ 5.00 kpc, with one exception) and have measured DM values ranging between $49 - 217$ pc cm^{-3}. Flux values at $\sim$ 400 MHz for the set show that the pulsars are bright at low frequencies, with the highest flux value at this frequency equal to 296 mJy (PSR J0742−2822).

The target sources were chosen from an original sample of about 200 pulsars that were observed during the Commissioning or Census LOFAR observing cycles. Pulsars were picked from this set based on:

- Having significant S/N values (> 3 for the lowest frequency profile)

Pulsar J-name	Pulsar B-name	P (s)	DM (pc cm^{-3})	D (kpc)	$S_\nu^\dagger$ (mJy)	$\eta^\dagger$	Data	MJD
J0040+5716	B0037+56	1.12	92.5146	2.42 (2.99)	5.00*	1.8	Ce	56753
J0117+5914	B0114+58	0.10	49.4210	1.77 (2.22)	43.40*	2.4	Co	56518
			49.4207				Ce	56781
J0543+2329	B0540+23	0.25	77.7026	1.56 (2.06)	29.00	0.7	Ce	56780
J0614+2229[k]	B0611+22	0.33	96.9100	1.74 (2.08)	29.00	2.1	Cy	57391
			96.9030				Co	56384
J0742−2822[k,l]	B0740-28	0.17	73.7950	2.00‡	296.00	2.0	Co	56603
J1851+1259	B1848+12	1.21	70.6333	2.64 (3.50)	8.00	1.8	Ce	56687
J1909+1102[k,l]	B1907+10	0.28	150.0050	4.80‡	50.00	2.5	Co	56388
J1913−0440[k,l]	B1911-04	0.83	89.3700	4.04 (2.79)	118.00	2.6	Co	56259
			89.3850				Cy	57391
J1917+1353[k,l]	B1915+13	0.19	94.6580	5.00‡	43.00	1.8	Co	56525
J1922+2110[k,l]	B1920+21	1.08	217.0220	4.00‡	30.00	2.4	Co	56388
J1935+1616[k,l]	B1933+16	0.36	158.6210	3.70‡	242.00	1.4	Co	56607
J2257+5909	B2255+58	0.37	151.1330	3.00‡	251.90*	0.8	Co	56518
J2305+3100[l]	B2303+30	1.58	49.5845	25.00 (3.76)	24.00	2.3	Ce	56773

Table 5.1: The list of sources analysed in this study. The periods are given to two decimal values. The DM values, to four decimals, are the values with which the data files are dedispersed. The quoted distance values (D) are obtained from the ATNF pulsar catalogue[1] (Manchester et al., 2005), and are mostly computed using the updated YMW16 electron density distribution model (Yao et al., 2017). Bracketed values are older estimates based on the NE2001 (Cordes & Lazio, 2002) electron density model. The superscripts indicate, ‡distances derived independently from DM values, e.g. from parallax measurements or the association with objects, such as supernova remnants. These are typically more reliable than values calculated from electron density distribution models; [k]sources appearing in Krishnakumar et al. (2015); [l]sources in Lewandowski et al. (2015); *flux density values (at 350 MHz) from Stovall et al. (2014); †flux density values (at 408 MHz) and flux density spectral indices, η, taken from Lorimer et al. (1995), where $S_\nu \propto \nu^{-\eta}$, with S_ν the flux density and ν the frequency.

- Exhibiting clear scattering
- Having seemingly simple single component profile shapes
- Showing minimal profile evolution with frequency

The majority of the sample sources were rejected for not showing measurable scatter broadening. This is mainly due to the fact that the Census survey was conducted out of the Galactic plane (see Sec. 3.3), where scattering effects are significantly decreased.

5.1.2 Data reduction

The data were processed using standard LOFAR reduction methods as described in Sec. 3.2. The number of frequency channels ranges from 4 to 16, with 8 or 16 used most often. Typically, the number of frequency channels are reduced if average pulse profiles have S/N values below 3. Omitted profiles are discussed in detail on a pulsar-by-pulsar basis in Sec. 5.2.

5.1.3 Data fitting

Once the data processing is complete, I write the data files out to ascii format (using `pdv` in PSRCHIVE; van Straten et al. 2012). These ascii files are subsequently analysed by the PYTHON *train + DC* scattering method of Secs. 4.2.1 and 4.3.1, which fits each channelised profile. I make use of two IISM broadening functions within this method, namely the isotropic broadening function of Eq. (2.27) and the extreme anisotropic (1D) broadening function of Eq. (2.31). I also account for the frequency integration of the channelised data as described in Sec. 4.2.2 and Eq. (4.6) to extract the monochromatic frequency associated with an obtained τ value. For the LOFAR data used here, the corrections in α due to the channelized bandwidth size, is less than 0.5%.

A fit to an average profile of PSR J0614+2229 in Fig. 5.1 shows the typical impact of τ errors on the modelled scatter broadened shape. The dark grey shaded region around the best-fit τ value (red solid line) represents a 2σ error, and the dashed line shows the 5σ error margin. Quoted errors in this chapter are 1σ errors.

To evaluate the goodness of the model fits, I make use of two standard metrics, the reduced Chi-squared ($\chi^2_{\rm red}$) value and the Kolmogorov–Smirnov (KS) test. The KS test is applied to the residuals (data − model) of the fit to test the Gaussianity of the residuals. This test provides a probability value that the residuals follow a Gaussian

distribution. The main objective is to identify examples where the residuals are severely non-Gaussian. The quality of the data do not warrant more sophisticated goodness of fit tests. I compare the outcomes of these metrics for two scattering mechanisms (isotropic and extremely anisotropic) for all the sources. This enables me to address Open Questions III and V, which aim to test the appropriate form of the IISM temporal broadening function and investigate whether anisotropic scattering is present.

For each pulsar I produce a series of diagnostic plots, which includes the profile fits, τ and scatter-corrected flux density spectra, as well as plots of the underlying Gaussian parameters (σ, μ, A) and a DC offset.

Different from the simulated data in Chapter 4 (which was assumed to have been correctly dedispersed), I can also obtain a DM correction value (ΔDM), from the fitted μ (centroid) values,

$$\Delta\mu = \Delta\mathrm{DM}\left(\frac{1}{\nu_{\mathrm{i}}^2} - \frac{1}{\nu_{\mathrm{H}}^2}\right), \tag{5.1}$$

where $\Delta\mu = \mu_H - \mu_i$ is the shift in the intrinsic pulse centroid value between a given frequency channel (ν_i) and the highest frequency channel (ν_H), similar to in Eq. (2.2). I label the proportionality constant as ΔDM, since it represents a change in the DM value, compared to the value used to dedisperse the observation during the initial PulP analysis (Sec. 3.2.2).

5.2 Scattering results for 13 LOFAR pulsars

I discuss the results for each pulsar individually. For convenience, I provide subheadings for each pulsar, summarising the period, scattering time and DM, with no errors, as well as the time and frequency resolution of the data (δt and $\delta\nu$).

Thereafter, I show the outcomes of the fitting models and consider the goodness of the fits. A complete set of the diagnostic plots produced by the fitting procedure, can be found in Appendix A. I present the τ spectra, providing comparisons to values from the literature, as well as a subset of flux density spectra and ΔDM plots here. A summary of the obtained τ, α and ΔDM values are also presented in Table 6.2 in Chapter 6, where I discuss my results in detail. As a shorthand, I refer to the isotropic scattering model as IM, and the extreme anisotropic model as $\mathrm{AM_{1D}}$.

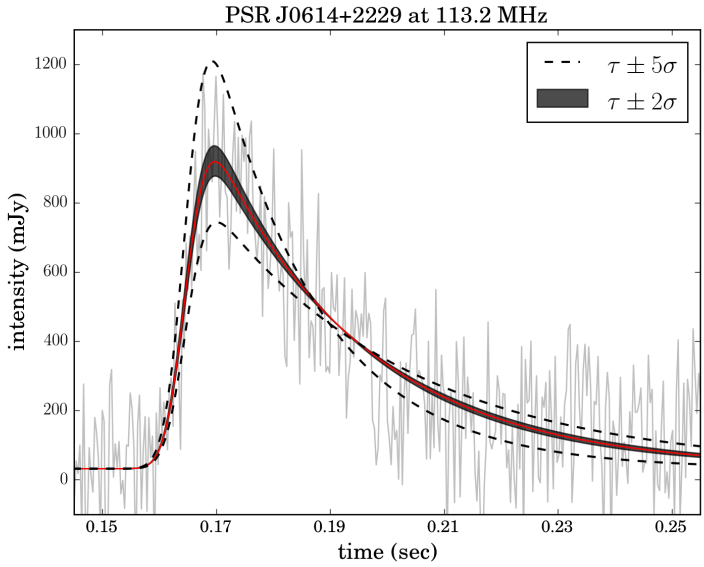

Figure 5.1: The range of pulse shapes for PSR J0614+2229 resulting from the best-fit τ value (solid red line) and the best-fit value with an added 2σ (shaded region) or 5σ error range (dashed lines). To ensure that the error ranges are visible, only 10 s of the pulse period is shown.

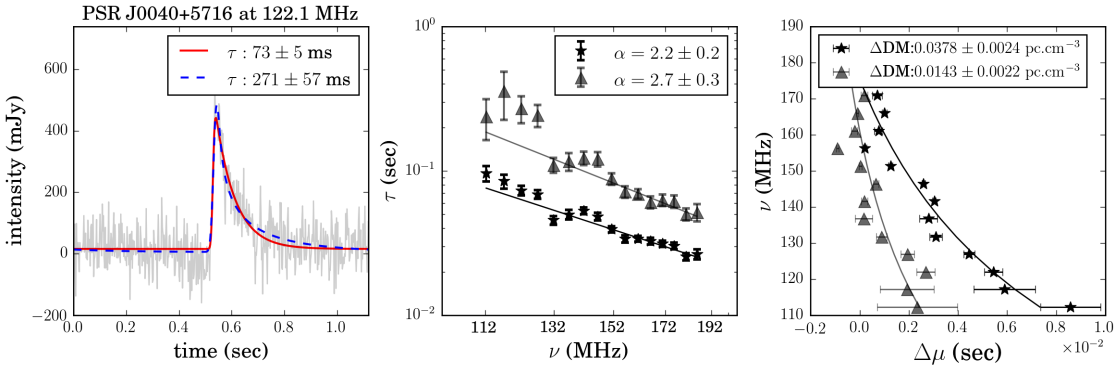

Figure 5.2: *Left:* The scattering fits to a profile shape of PSR J0040+5716 at 122.1 MHz (IM, red solid line; AM_{1D}, blue dashed line). *Middle:* The associated τ spectra, IM fits are shown in black (stars) and AM_{1D} fits in grey (triangles). *Right:* The obtained ΔDM fits for both models (as before, IM as stars and AM_{1D} as triangles).

5.2.1 PSR J0040+5716

P = 1.12 s, τ_{150} = 40 ms, DM = 92.5 pc cm^{-3}, δt = 2.2 ms, $\delta\nu$ = 1.5 kHz

PSR J0040+5716 was discovered in a search for low-luminosity pulsars at 390 MHz using the 92-m transit telescope at Green Bank (92m-GBT) in West Virginia, US (Dewey et al., 1985), and has the lowest tabulated flux density for the list of sources (Table 5.1). The distance estimate of this pulsar has changed from 4.48 kpc (Taylor & Cordes, 1993) to 2.99 kpc (NE2001 model, Cordes & Lazio 2002) to more recently 2.42 kpc (Yao et al., 2017). Its DM value of 92.5 pc cm^{-3} is close to the average DM of the set DM values.

I use LOFAR HBA Census data for this pulsar. Using the European Pulsar Network (EPN) database[3] (Lorimer et al., 1998), I find that it is a single-component pulsar at 408 MHz (Gould & Lyne, 1998) and, as it exhibits no clear secondary components in my dataset, it is likely a single component pulsar down to low frequencies. There are currently no scattering measurements published for this pulsar.

A sample profile at 122.1 MHz is shown in the left-hand panel of Fig. 5.2, with the fit by the IM model in red (solid line) and the AM_{1D} model in blue (dashed line). The τ value associated with the AM_{1D} at this frequency, is almost 4 times that of the IM value.

The profile fits over all 16 channels (for which the lowest peak S/N is equal to 4.4) produce a τ spectrum with spectral index $\alpha = 2.2 \pm 0.2$ for the IM, and $\alpha = 2.7 \pm 0.3$ for the AM_{1D} fits (Fig. 5.2, middle panel). The error bars on τ and the spread in τ values obtained from the IM (black, stars) are typically smaller than for the AM_{1D} (grey, triangles). The goodness of fit parameters for the whole dataset is presented in Chapter 6, Table 6.1. For PSR J0040+5716 they do not favour a particular scattering model.

The τ spectrum appears to have three segments with breaks around 130 MHz and 150 MHz. The residuals of the profile at 136 MHz are less Gaussian in their distribution than the other frequency channels.

Splitting the bandwidth into only 4 channels, to increase the S/N, and refitting, leads to a similar α value of 2.1 ± 0.3. I also find that the σ (the unscattered pulse width) versus frequency relationship for this pulsar follows a rough power law dependence (see Fig. 6.6 in Chapter 6). Fixing the σ values to this power law dependence and refitting, increases the α value to 2.3, which lies within the errors of the original

value. I conclude that the obtained α value is robust, and not critically sensitive to these tested changes in the fitting method.

The ΔDM values obtained from Eq. (5.1), are shown in the right-hand panel of Fig. 5.2 and presented in Table 6.2.

The flux density values inferred from the fitting models show no clear dependence on frequency (and therefore on scattering). Bilous et al. (2016) measured a mean flux density at HBA frequencies of 33 ± 17 mJy. Similarly, I find a frequency-averaged (scattering corrected) mean flux density of 31.4 mJy (IM), and 35.8 mJy (AM_{1D}). At 151.3 MHz, I measure flux density values of 34 ± 30 mJy and 37 ± 22 mJy (IM and AM_{1D}). Stovall et al. (2014) published a value of $4.7 - 5.0$ mJy at 350 MHz. Using a simple power law spectrum and the spectral index (η) from Table 5.1, the Stovall et al. (2014) result implies a flux density of 21.9 ± 0.7 mJy at 151.3 MHz, well within the LOFAR flux density error margins.

5.2.2 PSR J0117+5914

P = 0.10 s, τ_{150} = 7 ms (Ce) 8 ms (Co), DM = 49.4 pc cm^{-3}, δt = 0.8 ms (Ce) 0.1 ms (Co), $\delta\nu$ = 3.1 kHz (Ce) 12.2 kHz (Co)

PSR J0117+5914 is the fastest spinning pulsar in the set and was discovered in a 92m-GBT survey for short-period pulsars (Stokes et al., 1985). It is one of the closest pulsars in the set ($D = 1.77$ kpc) and has the lowest DM value (49.4 pc cm^{-3}) of the studied sources. This is the only pulsar for which I have both Commissioning and Census data. I use eight frequency channels across the band for the Commissioning data, and 16 for the Census data.

Fig. 5.3 shows the results from both datasets jointly. The left-hand panel shows the average pulse profile of the Census data at 112.3 MHz, with the IM fit to the data in red (solid), and the AM_{1D} fit in blue (dashed). These profiles have lower phase resolution than the other datasets, with only 128 bins across the pulse profile. I note that the τ value obtained using the AM_{1D} is more than four times that obtained using the IM. The AM_{1D} fits higher into the pulse peak.

The middle panel shows the τ spectra for both datasets and models, with Census data as solid lines (stars for the IM, and triangles for the AM_{1D} data points) and Commissioning data in dotted (IM) and dash-dotted (AM_{1D}) lines.

The datasets show similarities, and in the case of the IM, the α values agree within a 1σ error. The IM fit produces one of the lowest α values of the set, $\alpha = 1.9 \pm 0.2$

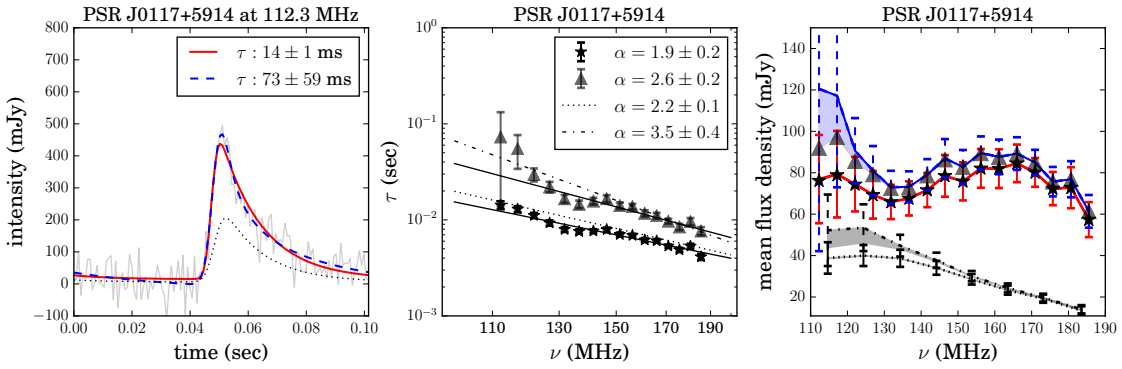

Figure 5.3: PSR J0117+5914. *Left:* Average Census profile with the IM fit in red (solid line) and the AM_{1D} fit in blue (dashed line). An IM fit to the Commissioning profile at 114.6 MHz is also shown (dotted line). *Middle:* The associated τ spectra. It shows τ values obtained from the IM (Census data: stars with solid line fit, Commissioning data: dotted line) and from the AM_{1D} (Census data: triangles with solid line fit, Commissioning data: dash-dotted line). *Right:* Flux spectra calculated from scattered profiles. Uncorrected flux density values are shown as stars (IM) and triangles (AM_{1D}) for the Census data, with corrected flux density values as red and blue solid lines, respectively. For the IM the uncorrected and corrected values are near equal, for the AM_{1D} the shaded region represents the increase in flux density when applying a scattering correction. The error bars associated with the corrected flux density values are shown in red (solid, IM) and blue (dashed, AM_{1D}). The flux density spectrum for the Commissioning data appears at lower mean flux density values (dotted line for corrected IM flux density and dash-dotted line for corrected AM_{1D} flux density).

Table 5.2: The original DM values used to dedisperse the different observations, along with the DM corrections as suggested by both the IM and the AM_{1D}, all in units of pc cm^{-3}. The last column shows how the change in DM values between epochs is impacted by the choice of model.

	Comm. data	Census data	Change in DM
Original DM	49.4210	49.4207	0.0003
Isotropic correction	49.4128 ± 0.0009	49.4143 ± 0.0006	-0.0015 ± 0.0015
Anisotropic correction	49.4169 ± 0.0011	49.4169 ± 0.0006	0.0000 ± 0.0017

for the Census and $\alpha = 2.2 \pm 0.1$ for the Commissioning data. The high S/N of the Census data constrains the goodness of fit of the two models well (Table 6.1).

The right-hand side of Fig. 5.3 shows the flux density measurements from the scattering fits. The shaded regions towards low frequencies indicate the flux density corrections that account for scattering effects. Corrected flux density values with error bars, range from approximately 50 to 100 mJy (IM) or 40 to 200 mJy (AM_{1D}) for the Census data. In contrast, the Commissioning data flux density values are much lower. Stovall et al. (2014) recently measured the flux density to be 43.4 mJy at 350 MHz. Using the spectral index from Table 5.1, this flux density is translated to approximately 330 mJy at 150 MHz – higher than the measured values between 30 and 90 mJy (Co & Ce) at 150 MHz here, even with an additional 50% error range. However, the flux densities obtained from the Census data, do agree well with the mean flux density value of $S_{\rm HBA} = 79 \pm 39$ mJy, published in Bilous et al. (2016), where flux density values were not corrected for scattering as I have done.

For both datasets, the flux density values obtained from the AM_{1D} are higher than the corresponding IM values. Both the Commissioning and Census data for this pulsar are shown in Appendix A, Figs. A.2 and A.3. Below 135 MHz, the Census data suggest that scattering tails are wrapping around, i.e. the scattering tail stretches beyond the pulse period. This could be correlated with a turnover in the flux density spectrum. However, a turnover in the flux density spectrum is seen more clearly for the Commissioning data than for the Census data.

In Table 5.2, I compare DM corrections for pulsars for which I have more than one dataset. I start by assuming that the diffuse component of the IISM leads to an average free electron density that is mostly constant over time, along the line of sight (producing a constant underlying DM value) and that the measured ΔDM effects are primarily due to scattering effects. Under these assumptions, I expect an accurate

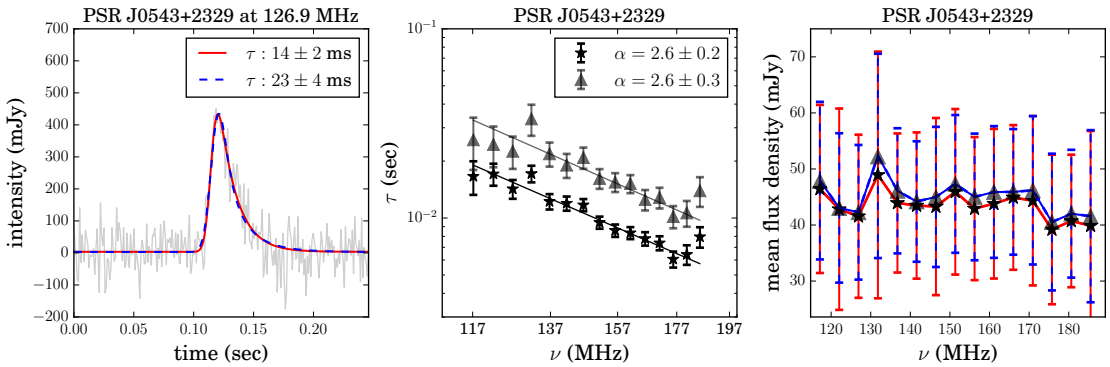

Figure 5.4: PSR J0543+2329. *Left:* Average Census profile with the IM fit in red (solid line) and the AM_{1D} fit in blue (dashed line). *Middle:* The associated τ spectra. It shows τ values obtained from the IM (Census data: stars with solid line fit) and from the AM_{1D} (Census data: triangles with solid line fit). *Right:* Flux spectra calculated from scattered profiles. Uncorrected flux density values are shown as stars (IM) and triangles (AM_{1D}) for the Census data, with corrected flux density values as red and blue solid lines, respectively. For both the IM and AM_{1D} the uncorrected and corrected values are near equal.

scattering model to lead to DM corrections (measured ΔDM values), such that, once applied, similar DM values at different epochs are obtained. For PSR J0117+5914, I note that applying the ΔDM correction from the AM_{1D} model results in DM values that remain more similar between the two observing epochs.

5.2.3 PSR J0543+2329

P = 0.25 s, τ_{150} = 10 ms, DM = 77.7 pc cm^{-3}, δt = 1.0 ms, $\delta\nu$ = 1.5 kHz

This pulsar is associated with the Supernova Remnant IC 443. It was discovered in one of the earliest pulsar searches with the Lovell telescope at Jodrell Bank, at 408 MHz (Davies et al., 1972). The Census data are channelised to 16 average pulse profiles, of which the lowest channel is excluded from the analysis for having a low peak S/N value. As seen in Fig. 5.4, the τ spectra for both scattering models have similar power law indices. The profile fits (left panel) also have indistinguishable shapes at 126.9 MHz.

Cordes (1986) gives τ = 2.69 μs at 1 GHz. Our measurement of τ = 0.01 s at 150 MHz and α = 2.61, would translate to τ = 66 μs at 1 GHz. The required spectral index to link the 186 MHz observation to the 1 GHz measurement, is α = 4.6, close to the Kolmogorov value of 4.4. Kuzmin & Losovsky (2007) published $\tau = 15 \pm 5$ ms

Table 5.3: Low frequency characteristic scattering time values (τ, in ms) from the literature for pulsars with two or more of these values quoted in text. *Values at 102 MHz, the rest of the Kuzmin & Losovsky (2007) values are at 111 MHz. See text for full references.

Reference	*Kuzmin 2007*	*This work*	*Slee 1980*	*Alurkar 1986*	*Löhmer 2004*	*K15*
Freq (MHz)	102 /111	150	160	160	243	327
J0614+2229	40 ± 10	15 ± 0				1.74 ± 0.03
J0724−2822	$22 \pm 5.3^*$	20 ± 2		24.5 ± 2.8		0.71 ± 0.01
J1909+1102		42 ± 3	27 ± 7	26.5 ± 8.1		1.35 ± 0.02
J1913−0440	$35 \pm 15^*$	7 ± 0	32 ± 5	16.7 ± 1.8		0.19 ± 0.01
J1917+1353	$40 \pm 20^*$	11 ± 1	12 ± 3	11.7 ± 1.9		0.36 ± 0.01
J1922+2110		42 ± 2		96.8 ± 50	4.4 ± 1.5	2.3 ± 0.1
J1935+1616	50 ± 15	20 ± 1	25 ± 4	21.7 ± 1.6	4.6 ± 0.2	3.21 ± 0.02
J2303+3100	13 ± 3	9 ± 0		9.9 ± 3.6		

at 111 MHz, using data from the Large Phased Array Radio Telescope (BSA) at the Pushchino Radio Astronomy Observatory in Russia. Again using the obtained IM power law index I find $\tau = 22 \pm 6$ ms at 111 MHz, which lies just outside their error bounds.

The flux density measurements (right panel of Fig. 5.4) show no clear frequency dependence. At 151.4 MHz the computed flux density values are 46 ± 15 mJy (IM) and 47 ± 12 mJy (AM_{1D}). To incorporate the uncertainty in the initial flux calibration (of 50%) during the data reduction stage, I augment these values to 46 ± 23 mJy (IM) and 47 ± 24 mJy (AM_{1D}). Bilous et al. (2016) published a similar mean flux density of 36 ± 18 mJy. The measured flux density of $S_{408} = 28.9 \pm 1.3$ mJy at 408 MHz (Lorimer et al., 1995) leads to an expected flux density of around 58 mJy at 150 MHz, using a simple power law spectrum with spectral index 0.7 (Table 5.1). This value lies within 50% of my best-fit HBA flux density measurement at 150 MHz.

5.2.4 PSR J0614+2229

P = 0.33 s, $\tau_{150} = 15$ ms (Co & Cy) , DM = 96.9 pc cm^{-3}, $\delta t = 0.3$ ms (Co & Cy), $\delta\nu = 195$ kHz, coherently dedispersed (Cy), 12.2 kHz (Co)

PSR J0614+2229 was discovered in the same survey as PSR J0543+2329. For this pulsar I have LOFAR Commissioning and Cycle 5 data. The Cycle 5 data lead to a τ spectrum for which $\alpha = 2.1 \pm 0.1$ (IM), and $\alpha = 3.1 \pm 0.3$ (AM_{1D}), as shown

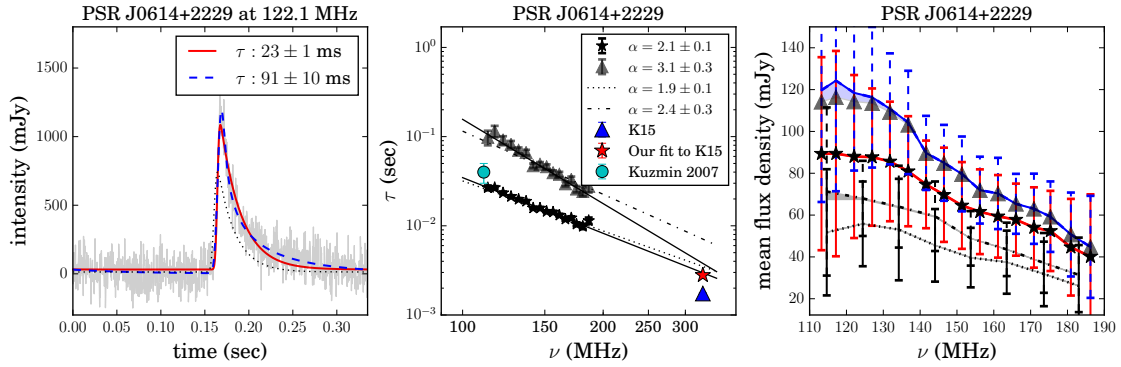

Figure 5.5: *Left:* The average profile of PSR J0614+2229 at 122.1 MHz (grey), and the IM (red, solid line) and AM_{1D} fits (blue, dashed line). The dotted line shows the Commissioning data average profile at 124.4 MHz. *Middle:* Associated τ spectrum for the IM (Cycle 5 data: stars with solid line fit, Commissioning data: dotted line) and for the AM_{1D} (Cycle 5: triangles with solid line fit, Commissioning data: dash-dotted line) with added data points from K15 and Kuzmin & Losovsky (2007). *Right:* Associated flux density spectra, with Cycle 5 data at the top and Commissioning data at lower flux density values. The markers are similar to Fig 5.3.

Table 5.4: The original DM values used to dedisperse the different observations, along with the DM corrections as suggested by both the IM and the AM_{1D}, all in units of pc cm^{-3}. The last column shows how the change in DM values between epochs is impacted by the choice of model.

	Comm.	Cycle 5	Change in DM
Original DM	96.9030	96.9100	0.007
IM correction	96.9000 ± 0.0007	96.9153 ± 0.0006	0.0153 ± 0.0013
AM_{1D} correction	96.9063 ± 0.0005	96.9209 ± 0.0008	0.0146 ± 0.0013

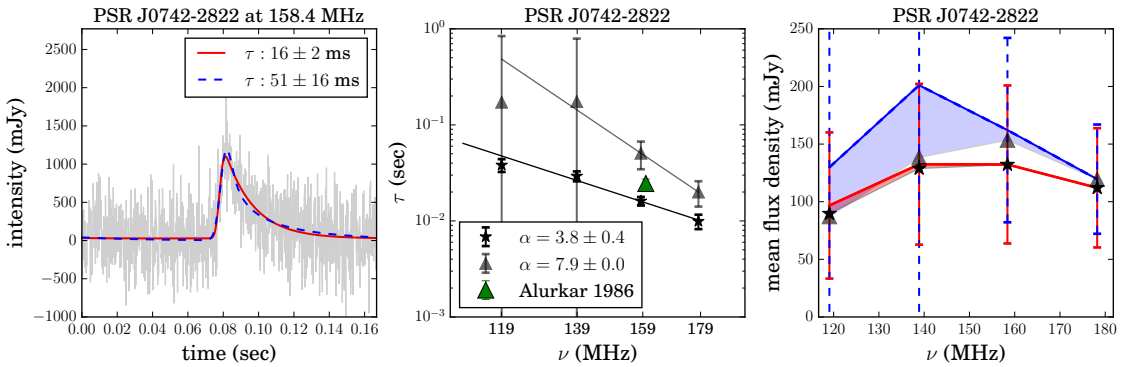

Figure 5.6: *Left:* Low S/N fitted profile from Commissioning data. *Middle:* Associated τ spectrum with an added data point from Alurkar et al. (1986). *Right:* Flux spectrum showing uncorrected and corrected flux density values. All markers and colours as in previous figures.

in Fig. 5.5. The figure also shows α values 1.9 ± 0.1 (IM) and 2.4 ± 0.3 (AM_{1D}) from the Commissioning data, such that especially for the IM the values are in good agreement.

The left panel of Fig. 5.5 shows the comparison of profile fits, between the IM (red, solid line) and the AM_{1D} (blue, dashed line) at 122.1 MHz. The computed τ values differ by a factor of approximately 4, and the AM_{1D} fit follows the tip of the profile peak more closely. The computed χ^2_{red} values are consistently lower for the AM_{1D}, with a mean values quoted in Table 6.1.

This pulsar lies at a distance of 1.74 kpc (previously estimated to be at 4.74 kpc, see Table 5.1) and has a DM value of 96.9 pc cm^{-3}, which is similar to PSR J0040+5716. The α values obtained using the IM for these two pulsars are also comparable.

This pulsar is the first in the source list to overlap with an Ooty Radio Telescope (ORT) dataset at 327 MHz, for which characteristic scattering times were recently published (Krishnakumar et al. 2015, hereafter K15[8]). Their data and methods are different to mine in several ways: (1) The average pulse profiles are far less scatter broadened than my sample set. (2) They follow the method described in Löhmer et al. (2001), in which a high frequency profile is used to estimate and fix the width of a Gaussian template used in the fitting method. (3) Wrap around scattering is not modelled (and not required at this frequency for these pulsars) and (4) for all pulsars marked as 'double component' profiles, only the trailing component of the pulse profile is fitted for.

[8]The K15 data are available at http://rac.ncra.tifr.res.in/da/pulsar/pulsar.html.

The K15 characteristic scattering time for this pulsar is $\tau = 1.74 \pm 0.03$ ms at 327 MHz. Refitting their data with my techniques gives $\tau = 2.80 \pm 0.02$ ms. The main difference seems to come from their choosing a fixed width. A fit with my code, specifying a fixed width as inferred from a high frequency profile, leads to a more similar τ value of 1.80 ms, although I note that the fit to the amplitude of the profile becomes considerably worse. I also note that the pulse profile is not highly scattered at a frequency of 327 MHz, which increases the uncertainty in the obtained τ values. Kuzmin & Losovsky (2007) published a characteristic scattering time of $\tau = 40 \pm 10$ ms at 111 MHz. At 113.2 MHz I find $\tau = 26.7 \pm 1.6$ ms, which translates to 28.1 ± 2.7 ms at 111 MHz when using the obtained IM α value. The literature values are shown in the middle panel of Fig. 5.5. The extrapolation of the IM Cycle 5 τ spectrum to higher frequencies is in good agreement with my fit to the K15 data at 327 MHz. Low frequency scattering time values from the literature for this pulsar and subsequent ones are summarised in Table 5.3.

Table 5.4 shows how the ΔDM correction impacts on the obtained DM value for the two models. The corrections clearly do not favour either model, and as seen in Fig. A.5 in Appendix A, the Commissioning data do not provide well-constrained fits to the ΔDM quantity.

The flux density and spectral index (see Table 5.1) suggest a mean flux density of 237 mJy at 150 MHz, much larger than my measured values of 65 ± 21 mJy (IM) or 80 ± 18 mJy (AM_{1D}). Again, these error bars should be augmented to a minimum value of 50%, such that at 150 MHz they are 65 ± 33 mJy (IM) or 80 ± 40 mJy (AM_{1D}). The flux density spectrum associated with the IM flattens out towards the lowest frequencies, with no obvious turnover. The AM_{1D} shows a more clear turnover towards the lowest frequencies, in agreement with both the raised baseline measurements (represented by the shaded area in the flux density spectrum) and the wrapped scattering tails seen in the AM_{1D} profile fits (Figs. A.5 and A.6).

5.2.5 PSR J0742−2822

P = 0.17 s, $\tau_{150} = 20$ ms, DM = 73.8 pc cm^{-3}, $\delta t = 0.2$ ms, $\delta\nu = 12.2$ kHz

PSR J0742−2822 is a young pulsar associated with an HI shell in Puppis (Stacy & Jackson, 1982). The Commissioning data I have for this pulsar have relatively low peak S/N values. Using 16 frequency channels across the band results in profiles for which all have S/N$>$ 2.7. I therefore use 4 channels, which still yield a maximum

S/N of only 4.5. Using 4 channels I find $\alpha = 3.8 \pm 0.4$ for the IM. This is the first fit for which the theoretical value of $\alpha = 4$ lies within the error bars of the measured α value. Furthermore, the AM_{1D} fails to produce convincing fits, as can be seen in Fig. 5.6, resulting in a large α value with a tight error margin, $\alpha = 7.9 \pm 0.0$. The error bars on τ for the first two channels are large ($> 350\%$), such that the power law fit (weighted by the inverse of the errors squared) is dominated by the two higher frequency τ values only, leading to an inaccurate spectrum.
A scattering measurement of $\tau = 24.5 \pm 2.8$ ms at 160 MHz was obtained by averaging 9 observations using the Culgoora circular array (Alurkar et al., 1986). This data point is shown in Fig. 5.6. I find a τ measurement at 159.6 MHz of 16.1 ± 1.6 ms. Since Alurkar et al. (1986) used a fixed width model (obtained from profiles at 408 MHz) a difference is expected. K15 find $\tau = 0.71 \pm 0.01$ ms at 327 MHz. In comparison, the spectral index of $\alpha = 3.8 \pm 0.4$ implies $\tau = 1.02 \pm 0.25$ ms at 327 MHz. Fitting the K15 data with my code, gives $\tau = 1.5 \pm 0.1$ ms, however, at 327 MHz their data show that the top peak of the pulse profile has split into two components. In these cases they fit only the secondary component (as shown in Fig. 1 in K15), whereas I fit the whole profile. It is worth noting that at 327 MHz the profile is not highly scattered. Lastly, Kuzmin & Losovsky (2007) published a value of 22 ± 5.3 ms at 102 MHz. This is much lower than predicted by my obtained spectral index. A summary of the relevant literature values is given in Table 5.3.

The low S/N data make it hard to make definitive statements about this pulsar. A fit using the AM_{1D} fails, making it an unlikely model. The trend in $\Delta\mu$ versus frequency is very weak, providing a ΔDM value with large error bars (Table 6.2).

The flux spectral index in Table 5.1 suggest a mean flux density of over 2 Jy at 150 MHz. The low S/N data leads to corrected flux density values with large error bars. At 140 MHz the measured values are 133 ± 70 mJy and 201 ± 476 mJy for the IM and AM_{1D}, respectively. For both models the corrections to the flux density values due to scattering are substantial (Fig. 5.6, shaded), and represent a maximum increase in the best-fit flux density of 8% (IM) and 50% (AM_{1D}). The flux density spectrum for this pulsar shows a turnover around 140 MHz, and the profile fits suggest that this could be ascribed to wrap around scattering tails.

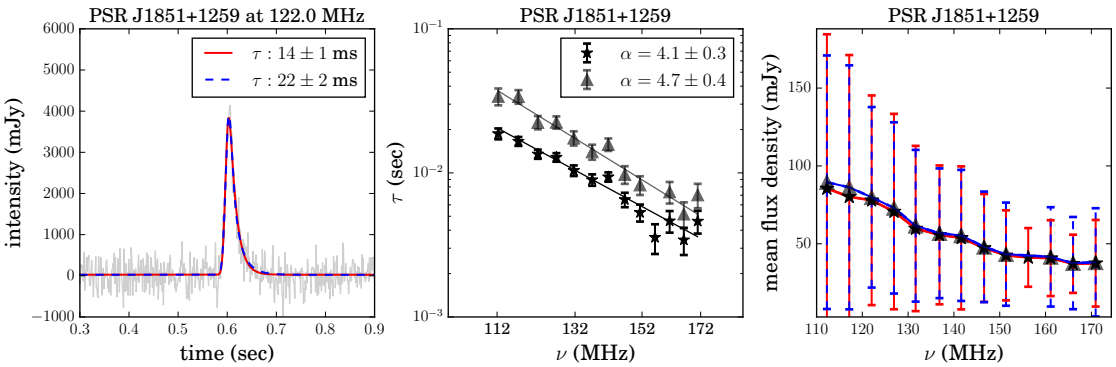

Figure 5.7: PSR J1851+1259. *Left:* Fitted profile from Census data. *Middle:* Associated τ spectrum. *Right:* Flux spectrum. The corrected and uncorrected flux density values are indistinguishable. All markers and colours as in previous figures.

5.2.6 PSR J1851+1259

P = 1.21 s, $\tau_{150} = 6$ ms, DM = 70.6 pc cm^{-3}, $\delta t = 1.2$ ms, $\delta\nu = 3.1$ kHz

This pulsar was discovered in the same survey as PSR J0117+5914 (Stokes et al., 1985). Here I fit Census data of the pulsar. Towards the higher end of the HBA band the profiles appear only marginally scattered. For this reason three of the higher frequency channels were not used. The remaining 13 channels (12 channels using the AM_{1D}) were all fitted with τ values of which the 1σ error bars were less than 23%.

The left-hand panel of Fig. 5.7 shows fits to the data at 122.0 MHz. The plot is zoomed to the on-pulse region, showing half of the pulse period.

The IM fits to the data result in an α value of 4.1 ± 0.3, in agreement with the theoretically predicted value of Eq. (2.27). For the AM_{1D}, $\alpha = 4.7 \pm 0.4$, as shown in Fig. 5.7. This is the second pulsar for which the obtained IM α value matches the theoretically predicted spectral index.

The flux density spectrum is shown in the right-hand side of Fig. 5.7. The flux values are mostly monotonically increasing with decreasing frequency. However, especially the AM_{1D} appears to flatten out at the lowest frequency channels. The mean Census flux density measurement for this pulsar is equal to 37 ± 19 mJy (Bilous et al., 2016). The expected flux density measurement at 150 MHz using the values in Table 5.1 is 48.5 mJy. Both these figures are in good agreement with my results, namely 43 ± 29 mJy (IM) and 43 ± 33 mJy (AM_{1D}) at 151.4 MHz.

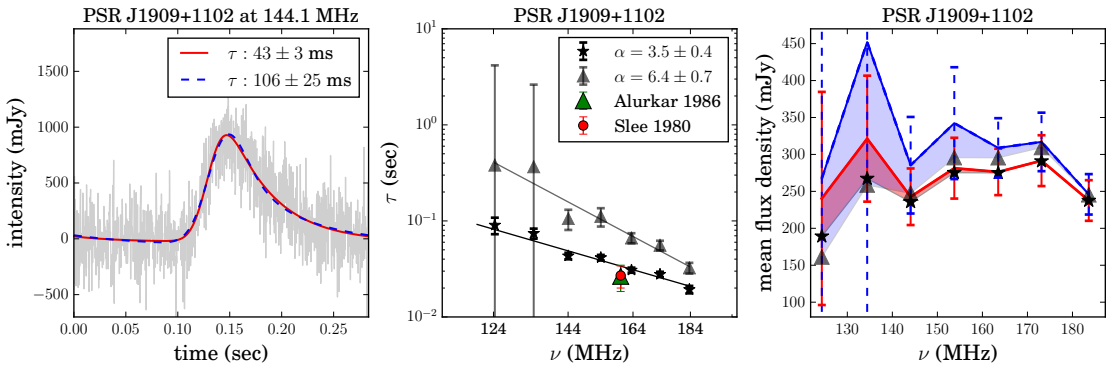

Figure 5.8: *Left:* Scattering fits to the profile of PSR J1909+1102 at 144.1 MHz. IM is shown in red (solid) lines and AM_{1D} is in blue (dashed) lines. *Middle*: The τ spectra associated with the scattering fits. IM in black (stars) and AM_{1D} in grey (triangles). *Right:* The uncorrected flux density values (IM, stars; AM_{1D}, triangles) and corrected flux densities (IM, red line; AM_{1D}, blue line). The flux density corrections shifts the turnover in the spectrum from higher towards lower fequencies.

5.2.7 PSR J1909+1102

P = 0.28 s, τ_{150} = 42 ms, DM = 150.0 pc cm^{-3}, δt = 0.3 ms, $\delta\nu$ = 12.2 kHz

PSR J1909+1102 was discovered in a low latitude pulsar survey with the Lovell Telescope at Jodrell Bank in 1973 (Davies et al., 1973). This pulsar has one of the higher DM values in the observing set and is highly scattered. In Chapter 6, Fig. 6.16, I show the DM versus distance values for the set of sources. PSR J1909+1102 is one of the outliers on this plot.

Since the pulsar is at a low latitude I only have Commissioning data for it. To increase the S/N, I split the HBA band into 8 frequency channels. The peak S/N values for all but the lowest frequency channel (which I exclude from the analysis) range from 3.5 to 9.1. The τ spectrum resulting from these measurements, is shown in Fig. 5.8 (middle panel).

Two similar τ measurements at 160 MHz were obtained by Alurkar et al. (1986) and Slee et al. (1980) using the Culgoora circular array, namely 26.5 ± 8.1 ms and 27 ± 7 ms (Table 5.3). At 163.5 MHz, I obtain 30.7 ± 1.9 ms, within their estimated error at 160 MHz.

Lewandowski et al. (2015, hereafter L15) published a spectral index value of $\alpha = 3.61 \pm 0.03$, based on literature values and a fit to a higher frequency profile from the EPN database. L15 follow the fitting approach as described in Löhmer et al. (2001). L15 do, however, allow for the width of the unscattered profile to

change. Many of the error bars on α values (and some of the α values itself) in L15 were updated in Lewandowski et al. (2015, hereafter L15b). For PSR J1909+1102 the updated value is $\alpha = 3.61^{+0.79}_{-0.74}$. Their α value lies well within the error bars of the spectral index measurement of $\alpha = 3.5 \pm 0.4$ (IM).

K15 published a value of $\tau = 1.35 \pm 0.02$ ms at 327 MHz. Fitting the K15 data myself, I find $\tau = 2.4$ ms at 327 MHz. As with PSR J0614+2229, the main difference seems to be coming from whether or not a model uses a fixed width intrinsic profile. Fitting their data with a fixed width template I find $\tau = 1.10 \pm 0.1$ ms, in closer agreement to their published value.

The flux density value and flux spectral index in Table 5.1 implies a flux density of 610 mJy at 150 MHz (using a simple power law model) which is more than twice the measured IM value of 281 ± 41 mJy at 154 MHz. At this frequency the AM_{1D} predicts 342 ± 76 mJy. To adhere to 50% error margins I change these to 281 ± 141 mJy (IM) and 342 ± 171 mJy (AM_{1D}). The flux density spectrum of PSR J1909+1102 (Fig. 5.8, right-hand side panel), shows significant observed flux density loss due to scattering (shaded areas) that I correct for. The corrected spectrum shows a turnover at around 140 MHz. The pulsar has the largest ratio of τ at 150 MHz to pulse period from the studied set, namely $\tau_{150}/P = 0.15$, and the scattering tails wrap around the full rotational phase.

5.2.8 PSR J1913−0440

P = 0.83 s, τ_{150} = 7ms (Cy) 9ms (Co), DM = 89.4pc cm^{-3}, δt = 0.8 ms (Cy & Co), $\delta\nu$ = 195 kHz (Cy & Co), coherently dedispersed

PSR J1913−0440 features in both the Commissioning and the Cycle 5 datasets. From the latter, I obtain $\alpha = 3.3 \pm 0.1$ (IM) and $\alpha = 4.1 \pm 0.2$ (AM_{1D}). The Commissioning data lead to somewhat lower spectral indices with larger error bars, namely $\alpha = 2.7 \pm 0.2$ (IM) and $\alpha = 3.5 \pm 0.3$ (AM_{1D}).

I concentrate on the Cycle 5 data, which, with 16 frequency channels, have higher S/N values (each profile has peak S/N$>$ 30). In Fig. 5.9 I show the profile fits to 3 frequency channels, along with the τ and flux density spectra and the ΔDM trends. The full set of profiles is shown in Appendix A, Figs. A.10 and A.11.

I note a small flat feature appearing at frequencies above 130 MHz (top middle and right panels of Fig. 5.9). At low frequencies the feature is fit together with the primary component leading to an overestimation in τ. This is visible as a deviation

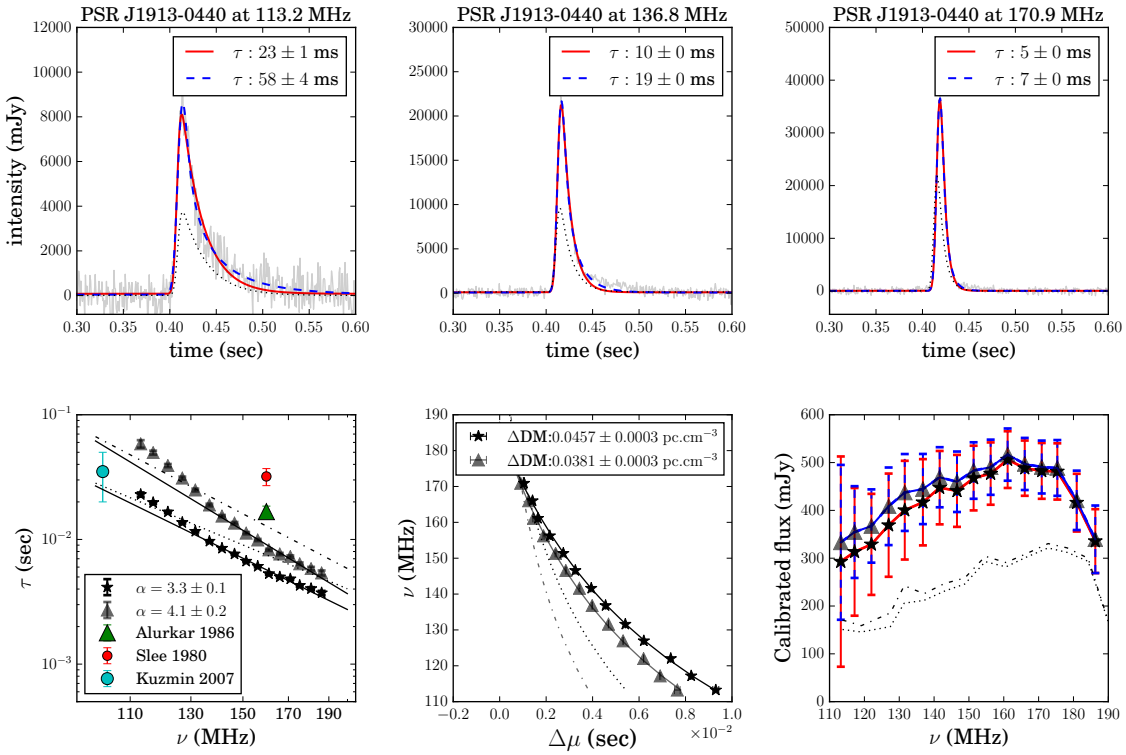

Figure 5.9: *Top:* Scatter broadened profiles of PSR J1913−0440 at three different frequencies in the HBA band (Cycle 5 data: IM fit in solid red and AM_{1D} fit in blue dashed line. Commissioning data: IM fits at similar frequencies to Cycle 5 profiles in dotted lines). A secondary feature can be made out in the middle and right panel. The profiles are enlarged to show 0.3 s of the 0.83 s pulse period. *Bottom, Left:* The τ and flux density spectra for PSR J1913−0440 (IM, stars; AM_{1D} triangles), along with data points from the literature. The Commissioning data fits are also shown as a dotted line (IM, $\alpha = 2.7 \pm 0.2$) and dash-dotted line (AM_{1D}, $\alpha = 3.5 \pm 0.3$). *Bottom, Middle:* Fits to the obtained excess DM values. Markers are as in the previous panel. *Bottom, Right:* The flux density spectra for IM (stars: uncorrected flux density, red solid line: corrected flux density) and AM_{1D} (triangles: uncorrected flux density, blue (top) solid line: corrected flux density). The corrected and uncorrected flux density values are indistinguishable. The AM_{1D} of the lowest 2 frequency channels is associated with large τ error bars (dashed), leading to flux density errors of several 100%. Flux spectra for the Commissioning data are shown as dotted (IM) and dash-dotted (AM_{1D}) lines.

in the fitted τ spectrum. Fitting only components above 130 MHz (IM) would lead to a slightly lower spectral index of $\alpha = 3.2 \pm 0.1$.

Previous scattering measurements for this pulsar exist at 102 MHz (Kuzmin & Losovsky, 2007) and 160 MHz (Alurkar et al. 1986, Slee et al. 1980; see Table 5.3). Using these values as well as their own fits to EPN database profiles at higher frequencies (up to 408 MHz), L15 published an α value equal to 2.62 ± 0.86. I note (from e.g. the K15 data) that the profile is nearly unscattered at 327 MHz, such that I don't value the inclusion of ever higher frequency profiles by L15. The L15 value was changed to $\alpha = 4.18 \pm 0.44$ in L15b, after the inclusion of measurements with the Giant Metrewave Radio Telescope (GMRT, near Pune in India) at 150 and 235 MHz.

Using $\alpha = 3.3 \pm 0.1$, I extrapolate to a τ value of 25 ± 2.2 ms at 102 MHz, which lies within the error bars of the Kuzmin & Losovsky (2007) published value, 35 ± 15 ms. My obtained τ value at 161.1 MHz is 5.3 ± 0.1 ms, much lower than the values at 160 MHz of 16.7 ± 1.8 and 32 ± 5 ms in Alurkar et al. (1986) and Slee et al. (1980), respectively. The difference is likely due to their using lower S/N data, in which the secondary component at these frequencies can not be isolated. K15 find $\tau = 0.19 \pm 0.01$ ms at 327 MHz. Extrapolating my LOFAR results to 327 MHz would lead to a value of $\tau \sim 0.54$ ms. I note that K15 have labelled this pulsar as a double component pulsar, in which case they fit only the secondary component, different from what I do. However, at 327 MHz the pulsar is very weakly scattered.

Due to the presence of the low frequency feature, the fits provide weak average goodness of fit statistics (Table 6.1). The shape of the AM_{1D} profiles fit the secondary feature well, leading to residuals that are much more Gaussian, especially at lower frequencies, than the IM. The deviation from a simple power law in the τ spectrum, seen in Fig. 5.9, therefore also starts at higher frequencies, than for the AM_{1D}. These better fits lead to an α value close to the theoretically expected value of 4. The secondary feature disappears at high frequencies, i.e. at low scattering. If in fact this low frequency feature is due to scattering alone it would provide strong support for an extremely anisotropic scattering mechanism along this line of sight. However, I can not rule out that the feature is intrinsic to the pulsar.

I see a clear ΔDM trend in both the Commissioning and Cycle 5 data for the IM and AM_{1D} fits (Fig. 5.9, lower middle panel). Introducing the ΔDM corrections lead to the improved DM values in Table 5.5. The corrections show that the DM values associated with the two datasets become more equal after the corrections are applied, both for the IM and AM_{1D}. In this respect, the AM_{1D} performs more favourably.

Table 5.5: The original DM values used to dedisperse the different observations of PSR J1913−0440, along with the DM corrections as suggested by both the IM and the AM_{1D}, all in units of pc cm^{-3}. The last column shows how the change in DM values between epochs is impacted by the choice of model.

	Comm.	Cycle 5	Change in DM
Original DM	89.3700	89.3850	0.0150
IM correction	89.3460 ± 0.0009	89.3393 ± 0.0003	0.0067 ± 0.0012
AM correction	89.3500 ± 0.0011	89.3469 ± 0.0003	0.0031 ± 0.0014

The flux density spectrum associated with the scattering fits shows a clear turnover at 160 MHz (Fig. 5.9, lower right panel). This can not be understood through long scattering tails, since the scattering values w.r.t the pulse period are not large enough, and the corrected flux density differs negligibly from the uncorrected flux density.

The flux density and spectral index values from Table 5.1 suggest a flux density of approximately 1590 mJy at 150 MHz. In comparison, the measured values at 151 MHz are 468 ± 68 mJy (IM) and 483 ± 59 mJy (AM_{1D}), which becomes 468 ± 234 mJy (IM) and 483 ± 242 mJy (AM_{1D}) with increased error margins. The Commissioning data for this pulsar result in even lower values of 246 ± 123 mJy (IM) and 259 ± 130 (AM_{1D}) mJy at 149 MHz (with increased error margins).

5.2.9 PSR J1917+1353

P = 0.19 s, $\tau_{150} = 11$ ms, DM = 94.7 pc cm^{-3}, $\delta t = 0.2$ ms, $\delta\nu = 12.2$ kHz

PSR J1917+1353 was discovered by Swarup et al. (1971). It is one of the most distant ($D = 5.00$ kpc) pulsars in the set. The EPN database suggests this pulsar has a single component up to 1.4 GHz and the fits are therefore unlikely to be biased by the presence of secondary components.

I channelise the Commissioning data for this pulsar into 8 frequency channels, which provides peak S/N values between 5.2 and 12.6. The α values obtained are 2.8 ± 0.4 (IM) and 3.6 ± 0.6 (AM_{1D}, see Fig. 5.10 middle panel), the latter of which lies close to theoretical predictions. Scattering values from the literature exist at 102 MHz, 160 MHz and 327 MHz (see Table 5.3).

The K15 data point again underestimates τ according to my measurements, whereas the data point from Kuzmin & Losovsky (2007) seems in good agreement.

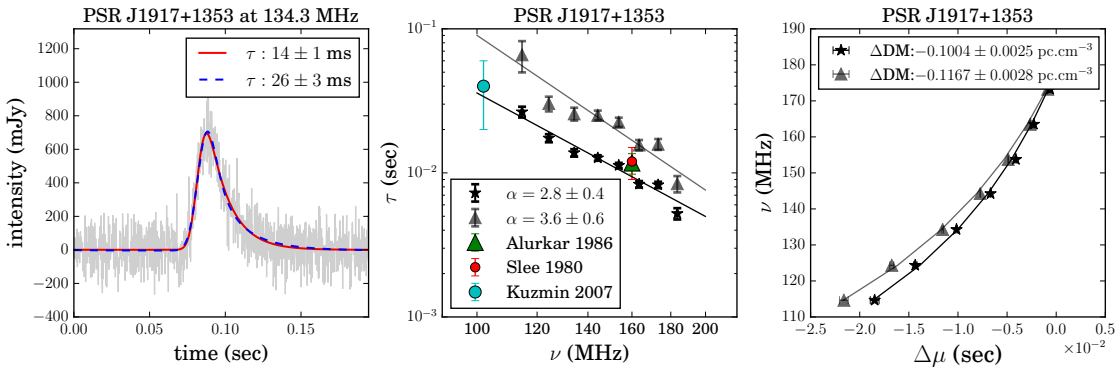

Figure 5.10: *Left:* The scattering fits to a profile shape of PSR J1917+1353 (IM, red solid; AM_{1D}, blue dashed). *Middle:* The associated τ spectra along data points from the literature. *Right:* The obtained ΔDM fits for both models (as before: IM, stars and AM_{1D}, triangles).

Fig. 5.10 shows the obtained ΔDM values for this pulsar in the right-hand panel. The trend is well fit, and the ΔDM values are negative for both the IM and the AM_{1D}. Negative values indicate that the original DM value with which the file was dedispersed was an underestimation. In Appendix A, Fig. A.12 shows that the modelled width evolution of this pulsar follows a clear power law, with spectral indices -2.5 and -2.7 respectively. The trend appears to be anti-correlated to the ΔDM plot.

The expected flux density at 150 MHz using the input of Table 5.1 and a simple power law, is approximately 288 mJy. My fits suggest flux density values that are similar for both models. At 154 MHz, I find 80±11 mJy (IM) and 86±9 mJy (AM_{1D}), or 80 ± 40 mJy (IM) and 86 ± 43 mJy (AM_{1D}) using 50% error margins. Over the HBA band the flux density changes monotonically in the range 48 to 126 mJy. At the lowest frequency channel the profile shows scatter broadening that stretches across the pulse period. This can be seen most clearly for the AM_{1D} (Fig. A.13 in Appendix A, shaded region). The flux density spectrum shows no turnover at low frequencies.

5.2.10 PSR J1922+2110

P = 1.08 s, τ_{150} = 42 ms, DM = 217.0 pc cm^{-3}, δt = 1.1 ms, $\delta\nu$ = 12.2 kHz

PSR J1922+2110 has the highest DM value in the dataset, and is seen to be an outlier in the DM versus distance plot of Fig. 6.16. It was discovered in the same low latitude pulsar survey as PSR J1909+1102 (Davies et al., 1973). I analyse Commissioning data for this pulsar. The high S/N allows me to channelise the band into 16 average

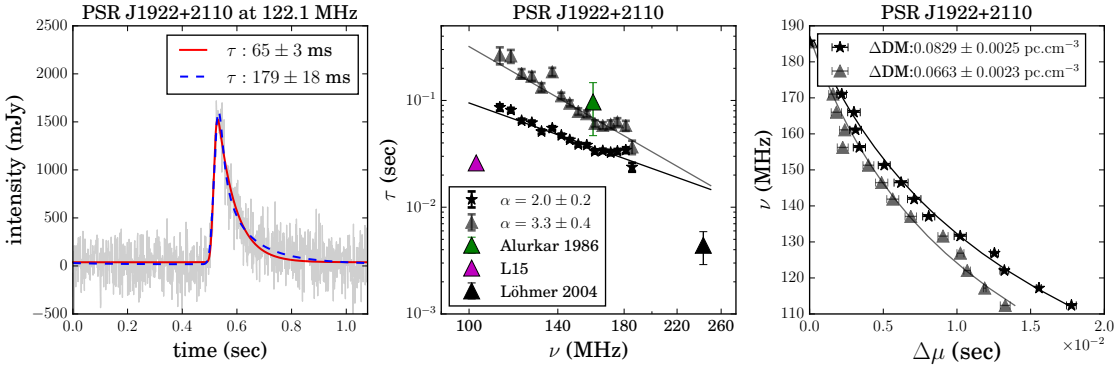

Figure 5.11: Similar to Fig. 5.10, for PSR J1922+2110.

profiles. Fitting the IM leads to $\alpha = 2.0 \pm 0.2$, and $\alpha = 3.3 \pm 0.4$ for the AM_{1D} (Fig. 5.11).

Several scattering measurements are available for this pulsar (Table 5.3). The literature values do not agree well with my estimations. L15 obtained $\alpha = 0.94 \pm 0.88$ for this pulsar, but omitted the value from their subsequent analyses for being "suspiciously low". They measured a τ value at 102.75 MHz of roughly 25 ms, more than three times lower than my data point of 86.1 ± 6 ms at 112.5 MHz. Their value comes from fitting an EPN database profile at 102.75 MHz (Kassim & Lazio, 1999), for which the phase resolution is poor. L15 further claim that PSR J1922+2110 has an asymmetric profile, such that scattering fits to this pulsar could be fitting profile evolution as well. I note that above 410 MHz the pulsar has a secondary component. Löhmer et al. (2004) published a τ value of 4.5 ± 1.5 ms at 243 MHz. This was the only frequency at which the authors present an obtained τ value with a standard error. For the higher frequencies they obtained upper limits on τ only.

I conclude that the LOFAR dataset is likely the best data for measuring the scattering parameters, since it provides high peak S/N values (between 6.8 and 16.4) and good phase resolution (1024 bins per pulse period).

As seen from the profile in the left-hand panel of Fig. 5.11, the IM and AM_{1D} produce very similar fits to the data. This is true for all the frequency channels. The main difference can be seen in the fit of the scattering tail, where the AM_{1D} follows a flatter trend. Clear and well-fit ΔDM trends are shown in the right-hand panel of Fig. 5.11.

The flux density value at 408 MHz and the power law spectral index presented in Table 5.1, leads to an expected flux density of 316 mJy at 150 MHz. The flux density values estimated from the LOFAR scattered profile fits at 151.4 MHz are again much

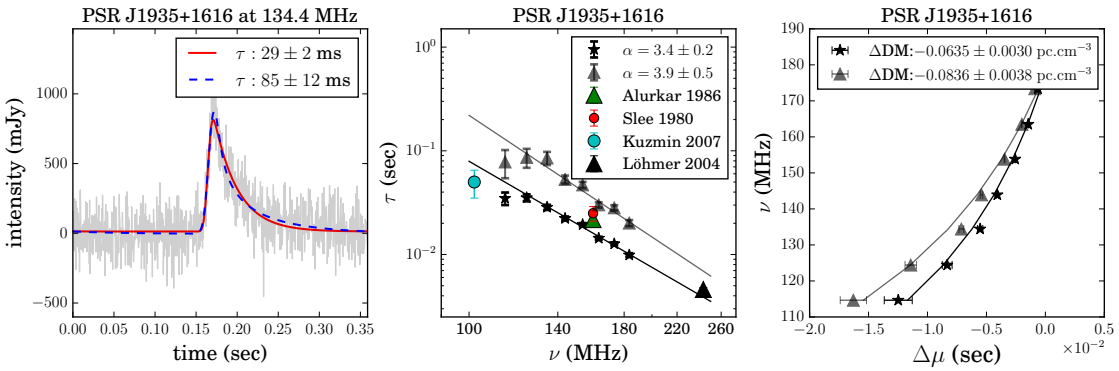

Figure 5.12: Similar to Fig. 5.10, for PSR J1935+1616.

lower: 89±35 mJy (IM) and 96±30 mJy (AM_{1D}), or 89±45 mJy (IM) and 96±48 mJy (AM_{1D}) with increased error margins. The spectra have relatively simple structure, decreasing with frequency. In the AM_{1D} spectrum small contributions due to the corrected flux density calculation can be seen, concurrent with the onset of a wrap around profile shape (Appendix A, Fig. A.13).

5.2.11 PSR J1935+1616

P = 0.36 s, τ_{150} = 20 ms, DM = 158.6 pc cm^{-3}, δt = 0.4 ms, $\delta\nu$ = 12.2 kHz

This pulsar has one of the highest flux density values in the set, having been discovered in a single pulse search using the Lovell Telescope at Jodrell Bank (Davies & Large, 1970). In Fig. 6.16 I see that this pulsar, at a distance of 3.7 kpc, has a higher DM than other pulsars at similar distances.

The Commissioning data for this pulsar are split into 8 frequency channels, leading to peak S/N values between 3.6 and 21.2. I obtain an α value of 3.4 ± 0.2 using the IM (middel panel of Fig. 5.12). This value is in good agreement with the values obtained by Löhmer et al. (2004), $\alpha = 3.4 \pm 0.2$, and L15b, $\alpha = 3.35^{+0.36}_{-0.41}$. Both these literature values of α are determined using other published scattering measurements between 110 and 250 MHz (Rickett, 1977, Slee et al., 1980, Alurkar et al., 1986, Löhmer et al., 2001, Kuzmin & Losovsky, 2007), and therefore serve as an independent comparison to my measurements. My AM_{1D} leads to $\alpha = 3.9 \pm 0.5$, in agreement with theoretical values of 4 or 4.4. The fits for both models look alike, with the AM_{1D} reaching slightly higher into the peaks of the pulse profile and having a different slope in the scattering tail.

The right-hand panel of Fig. 5.12 shows the obtained ΔDM values for this pulsar. The values are negative for both the IM and the AM_{1D}, which indicates that the original DM value with which the file was dedispersed was underestimated. Fig. A.14 shows that the modelled width evolution of this pulsar follows a power law which (similar to what is observed for PSR J1917+1353), is anti-correlated to the ΔDM trend.

Published τ measurements from the literature include 50 ± 15 ms at 111 MHz (Kuzmin & Losovsky, 2007), and two sets of measurements at 160 MHz of 21.7 ± 1.6 ms (Alurkar et al., 1986) and 25 ± 4 ms (Slee et al., 1980), as shown in Fig. 5.12 and Table 5.3. At 327 MHz, K15 published a τ value of 3.21 ± 0.02 ms. My refitting of the data (which also fits for the underlying width of the intrinsic pulse) leads to a value of 1.8 ± 0.1 ms, whereas keeping the value of σ fixed (as obtained from a 600 MHz template taken from the EPN database) I find a value of 3.3 ms, in closer agreement to theirs. I note that the K15 profiles at 327 MHz that overlap with my set of pulsars, are generally, not very scattered, and that a fixed width method often leads to a fit that does not model the peak of the scattered profile well. Extrapolating to 327 MHz using my obtained isotropic spectral index value, leads to a τ of 1.42 ± 0.18 ms instead, in close agreement to my fit of their data at 327 MHz.

The flux density measurements obtained from my scattering fits (IM and AM_{1D}) show a turnover at around 170 MHz, i.e. towards the highest observed frequency (Appendix A). This turnover is not purely associated with a wrap around scattering tail, as scattering corrections to the flux density only become significant below 145 MHz. The calculated flux density values at 154.1 MHz are 95 ± 27 mJy (IM) and 105 ± 22 mJy (AM_{1D}). Again, these errors are increased to 50% to reflect the initial flux calibration uncertainties. However, using a simple power law and the flux parameters of Table 5.1 implies a flux density of approximately 955 mJy at 150 MHz, roughly ten times larger than my values.

Several authors have noted that the line of sight to PSR J1935+1616 is puzzling, e.g Löhmer et al. (2004). In their study of nine pulsars with intermediate DM values (150 – 400 pc cm^{-3}), only PSR J1935+1616 had an α value inconsistent with the expected Kolmogorov prediction. The authors suggested the low α value could be due to multiple scattering screens of finite size or varying scattering strengths. The LOFAR data certainly point towards anomalous scattering, through e.g. an anisotropic scattering mechanism as the discussed AM_{1D}. Alternatively, a truncated scattering screen could provide a basis to interpret the data, as it would lead to both a low α value and a decrease in flux towards low frequencies. A turnover in the flux spectrum

(unrelated to a long scattering tail) is seen for PSR J1935+1616. However, as shown in Geyer & Karastergiou (2016), a scenario involving truncated scattering screens would lead to an observable change in the pulse profile shapes at low frequencies, which is not evident in the data. Soft edges of the screen, multiple screens and low S/N profiles can render these particular effects difficult to discern. The questions, therefore, surrounding the nature of the screen(s) towards this pulsar remain open.

5.2.12 PSR J2257+5909

P = 0.37 s, τ_{150} = 31 ms, DM = 151.1 pc cm^{-3}, δt = 0.4 ms, $\delta\nu$ = 12.2 kHz

PSR J2257+5909 is a bright pulsar discovered in the same survey as PSRs J0543+2329 and J0614+2229 (Davies et al., 1972). Similar to PSR J1935+1616, it is an outlier on the DM versus distance plot (see Fig. 6.16). I could not find previously published scattering times for this pulsar. I split the Commissioning data for this pulsar into 8 frequency channels, and excluded the lowest frequency channel for which the peak S/N is only 2.34. Fitting the remaining seven scattered profiles, I obtain $\alpha = 2.6 \pm 0.4$ (IM) and $\alpha = 3.4 \pm 0.6$ (AM_{1D}), which approaches the theoretical value of $\alpha = 4$.

The profile fits obtained by these models are very similar (Fig. 5.13, left panel). The χ^2_{red} values are near equal, with the AM_{1D} value consistently smaller than the IM value (Table 6.1). The low p-values from the KS test are dominated by two frequency channels. Omitting these 2 (out of 7) channels, increases the p-values to 85.6 % (IM) and 93.8% (AM_{1D}). The ΔDM trends are less well fit for this pulsar and both models show negative ΔDM fits.

The flux density spectra, as calculated from the both models, shows the onset of turning over toward lower frequencies. In the case of the AM_{1D}, the corrected flux density spectrum is straightened out w.r.t the uncorrected flux density spectrum (shaded region, right panel Fig. 5.13). The associated profile fits, of especially the AM_{1D}, show related pulse wrap around at frequencies below 150 MHz (see Appendix A, Fig. A.15). The calculated flux density values are 151 ± 32 mJy (IM) and 173 ± 34 mJy (AM_{1D}) at 153.7 MHz, or 151 ± 76 mJy (IM) and 173 ± 87 mJy (AM_{1D}) with 50% error margins. The Table 5.1 flux parameters, implies a much larger flux density value of approximately 500 mJy at 150 MHz, using a simple power law.

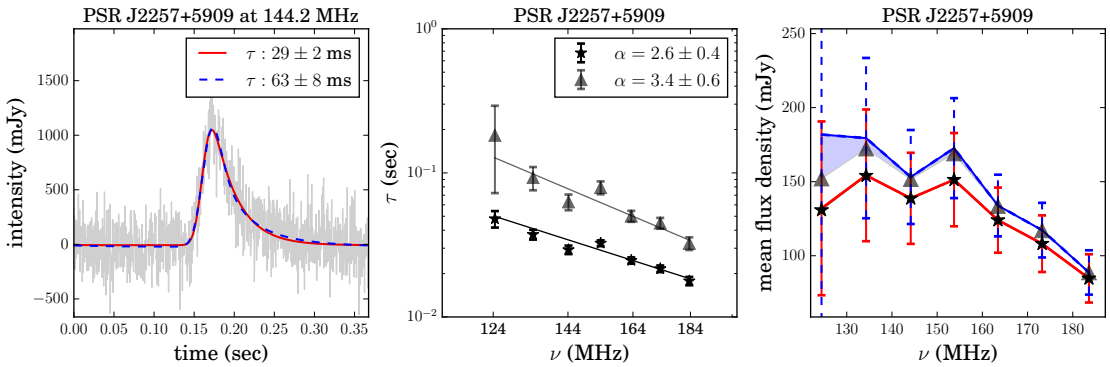

Figure 5.13: *Left:* Scattering fits to the profile of PSR J2257+5909 at 144.2 MHz. IM is shown in red (solid) lines and AM_{1D} is in blue (dashed) lines. *Middle*: The τ spectra associated with the scattering fits. IM in black (stars) and AM_{1D} in grey (triangles). *Right:* The uncorrected flux density values (IM, stars; AM_{1D}, triangles) and corrected flux densities (IM, red line; AM_{1D}, blue line).

5.2.13 PSR J2305+3100

P = 1.58 s, τ_{150} = 9 ms, DM = 49.6 pc cm^{-3}, δt = 1.5 ms, $\delta\nu$ = 3.1 kHz

This pulsar was discovered using Arecibo in 1969 (Lang, 1969). It has one of the lowest DM values in the set, but in contrast its distance is estimated to have a lower limit of 25 kpc (Yao et al., 2017). It is the pulsar with the longest pulse period (1.58 s) in the set. I analyse Census data for this pulsar, split into 16 channels. All across the HBA band the pulse remains only slightly scattered. I find $\alpha = 1.5 \pm 0.1$ (IM) and 2.0 ± 0.1 (AM_{1D}). An example pulse along with the τ and flux density spectra are shown in Fig. 5.12. The pulse shape is enlarged, showing the pulse phase from 0.6 to 1.0 s.

An α value of 3.42 ± 0.26 was recently published by L15. They tabulate their own measurements using the GMRT (at 410 MHz to 1.4 GHz), as well as the results from Kuzmin & Losovsky (2007) (at 44, 63 and 111 MHz) and Alurkar et al. (1986) at 160 MHz (see Table 5.3 for literature values) as sources for their obtained α value. The τ values published by Kuzmin & Losovsky (2007) are $\tau_{44} = 300 \pm 100$ ms, $\tau_{63} = 110 \pm 20$ ms and $\tau_{111} = 13 \pm 3$ ms. A fit across these three values leads to a spectral index of $\alpha = 3.8 \pm 0.1$. Alurkar et al. (1986) published a value of $\tau_{160} = 9.9 \pm 3.6$ ms. The LOFAR frequency channel closest to an observing frequency of Kuzmin & Losovsky (2007) is 112.3 MHz. For this channel I find $\tau_{112.3} = 11.9 \pm 0.5$ ms in good agreement with their value at 111 MHz. Extrapolating the τ values to 44 MHz, leads to a τ value

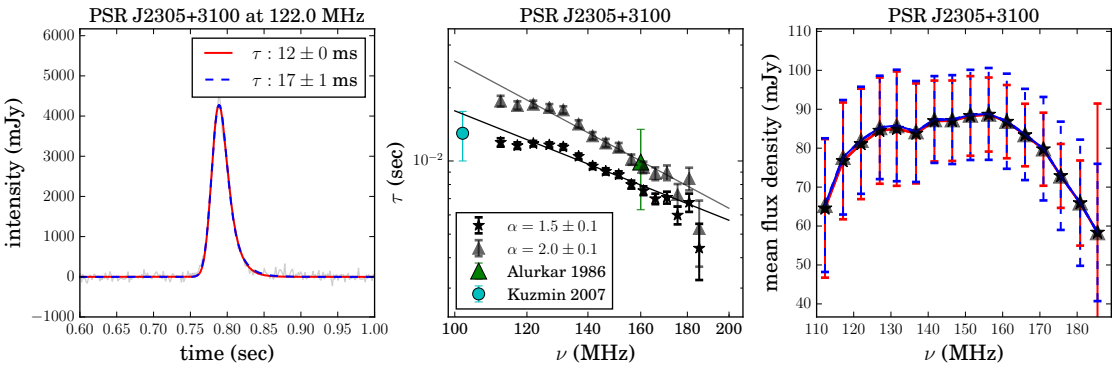

Figure 5.14: Similar to Fig. 5.13 for PSR J2305+3100.

of around 55 ms (using the IM), much lower than calculated by Kuzmin & Losovsky (2007).

The p-values for both models are low (Table 6.1), but significantly increased, to 79.6% (IM) and 80.8% (AM_{1D}), when only the first 5 channels with more notable scattering, are considered.

The near identical scattering fits of the two models and the low levels of scattering, lead to near identical flux density spectra. I compute 88 ± 10 mJy (IM) and 89 ± 12 mJy (AM_{1D}) at 151.3 MHz. These values are amended to have error bars 44 and 45 mJy, respectively, in line with the original flux calibration uncertainties. The mean published Census flux density value is 70 ± 35 mJy (Bilous et al., 2016), which agrees well with my result. I see a turnover in the flux density spectra at around 150 MHz, however, due to the low τ values compared to the pulse period, this is unlikely due to scattering effects.

Having investigated the results for each pulsar independently, I next consider the overall trends of the findings for this dataset in Chapter 6. I examine whether the data favour either fitting model, and discuss cases in which potential evidence for anisotropy is appealing, although it is not conclusive. I discuss the observed profile evolution trends as well as the impacts of truncated scattering screens and the correlations between flux spectra and scattering measurements. These discussions build towards addressing the Open Questions of Chapter 1.

Chapter 6

Discussion of LOFAR Scattering Results

Returning to the Open Questions posed in Chapter 1 (Sec. 1.4), I address them in the view of the results of the previous chapter. In order, I first assess the observed profile shapes at LOFAR frequencies (Sec. 6.1, Question I) and consider whether anisotropic scattering models are required to fit this LOFAR dataset (Sec. 6.2, Question III and Question V). Thereafter, I consider the distributions of spectral indices obtained by the two models (Sec. 6.3, Question III). Next, I investigate what information is gained regarding the profile evolution and dispersion measure from the profile fits. This includes analysing the width evolution of the intrinsic profiles (Sec. 6.4, Question VII). In Section 6.5, I discuss the impact of finite scattering screens, and how this relates to the obtained results (Question IV). Thereafter, I consider correlations between the modelled scattering effects and measured flux spectra (Sec. 6.6, Question VI). Lastly, I return to the well-studied τ versus DM relation and consider how the LOFAR results compare to published trends at 1 GHz (Sec. 6.7, Question II). The majority of this discussion is published in Geyer et al. (2017).

6.1 Profile shapes and τ measurements using two models

As expected from the simulated data in Chapter 4 and the theory of Chapter 2, I find profiles that are scatter broadened with exponential tails at LOFAR HBA frequencies. The shapes of the profiles are highly frequency dependent, such that τ spectra with measurable spectral indices are obtained. The targets are not equally scattered, with PSRs J1851+1259 and J2305+3100 the least discernibly scattered at these frequencies.

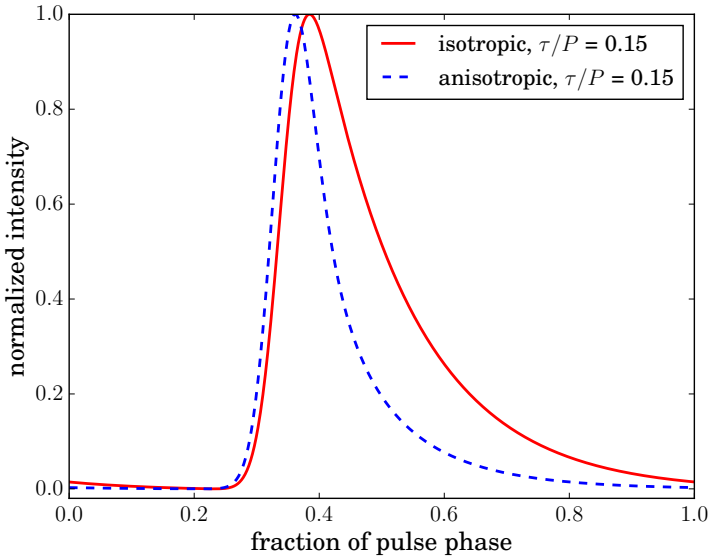

Figure 6.1: A comparison of modelled isotropic and anisotropic pulse shapes with equal characteristic scattering times. The profiles are plotted to have a peak value equal to unity. All other model parameters (σ, μ, A and DC) are equal for both profiles as well.

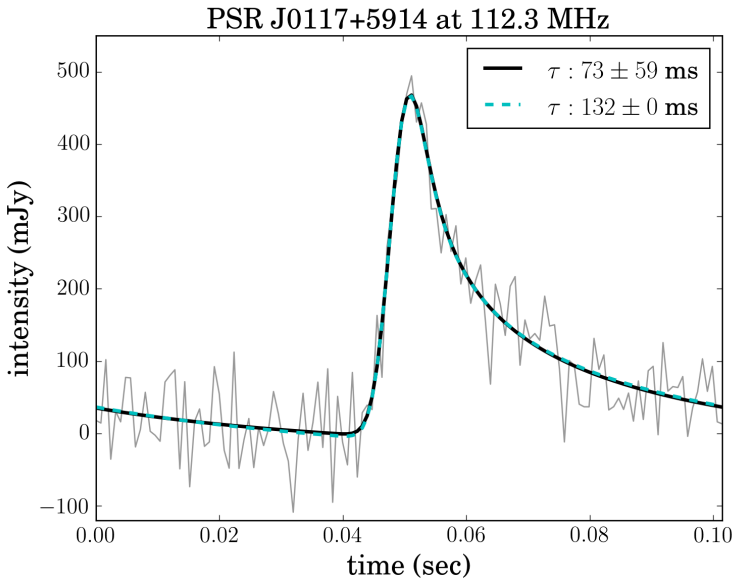

Figure 6.2: Resulting profile shapes for anisotropic model fits of PSR J0117+5914 Census data at the lowest frequency channel of 112.3 MHz. The fits are obtained, (1) by calculating the best-fit τ value (black, solid line), (2) by fixing, $\tau = 0.1322$ s, i.e. equal to the highest τ value within the error range associated with the best-fit value, and refitting for the rest of the parameters (cyan, dashed). These two model fits are indistinguishable.

Table 6.1: Goodness of fits parameters for both the isotropic scattering model (IM) and the extremely anisotropic scattering (AM_{1D}) model. For each model a reduced Chi-squared value (χ^2_{red}) and a p-value of the Kolmogorov–Smirnov test, is given. The quoted values are averaged over the number of frequency channels studied.

Pulsar	IM		AM_{1D}	
	χ^2_{red}	p-value (%)	χ^2_{red}	p-value (%)
J0040+5716	1.73	80	1.74	76.2
J0117+5914 (Co)	1.88	62.2	1.87	70.8
J0117+5914 (Ce)	1.43	81.2	1.33	85.6
J0543+2329	1.69	74.6	1.70	70.8
J0614+2229 (Co)	2.03	87.0	1.94	70.7
J0614+2229 (Cy)	2.05	80.5	1.90	83.7
J0742−2822	1.9	96.7	...	...
J1851+1259	1.85	82.3	1.92	79.23
J1909+1102	2.1	80.2	2.1	77.7
J1913−0440 (Co)	1.95	89.8	1.90	90.0
J1913−0440 (Cy)	2.53	55.8	2.25	71.1
J1917+1353	1.92	76.9	1.94	78.5
J1922+2110	1.9	87.8	1.88	81.9
J1935+1616	2.13	85.2	2.11	85.5
J2257+5909	1.99	68.5	2.00	76.4
J2305+3100	2.24	57.8	2.26	56.4

I find, as expected, that the fitted τ value for a given profile is larger when applying the AM_{1D} compared to the IM. Fig. 6.1 compares the profile shapes modelled with the same τ value. The shapes agree with the intuition that an isotropic scattering medium will scatter more pulsar radiation into the observer's line of sight, than an equivalent extremely anisotropic scatterer. As is seen in the simulated data of Chapter 4 and in some of the profile shapes of Appendix A, the AM_{1D} fit can rise higher into the peak of the profile, and has an elevated scattering tail towards larger times.

I also note that the errors in τ are larger for the AM_{1D} than for the IM, especially at low frequencies. Fig. 6.2 shows that the best-fit profile shape produced by the AM_{1D} fitting code (black, solid line), is indistinguishable from the shape produced when the τ value is fixed at the best-fit value plus a 1σ error, and the remaining parameters are refit (cyan, dashed line). The large error bars in τ stem from the anisotropically scattered shape being closer in shape to the unscattered Gaussian, which makes it more insensitive to changes in τ at low frequencies. Larger errors in τ lead to larger errors in the spectral indices. Table 6.2 contains all the obtained τ values at 150 MHz for the selected target list using the IM or AM_{1D}.

I have used $\chi^2_{\rm red}$ values and the KS test to investigate the goodness of fits of the scattering models. The outcome of these statistics is presented in Table 6.1. Judging from these values, I do not find any pulsar for which the AM_{1D} is an unambiguous requirement. All data are well fitted with the IM. In one case (PSR J0742−2822) the anisotropic result is unreliable, as discussed in Section 5.2.5, producing a spectral index of $\alpha \approx 8$.

6.2 Evidence for anisotropy

For four of the pulsars in the set, there is some evidence for anisotropy, although it is not conclusive. The pulsars are J0117+5914, J0614+2229, J1913−0440 and J2257+5909.

The data of PSRs J0117+5914 (Co and Ce) and J0614+2229 (Co and Cy) are all well fit by the AM_{1D} model. I find that the $\chi^2_{\rm red}$ value at each frequency is closer to 1 for the AM_{1D}, and that similarly the p-values from the KS test are higher for the AM_{1D}. The differences in these values are larger than for most other pulsars in the set. I also find that the α values associated with the two models are well separated for both these pulsars.

In the case of PSR J1913−0440, it could be that a secondary profile feature is well fit by the AM_{1D}, leading to $\chi^2_{\rm red}$ values closer to 1, and higher p-values in the

Pulsar	Isotropic Scattering			Extreme (1D) Anisotropic Scattering		
	τ_{150} (ms)	α	ΔDM (pc cm^{-3})	τ_{150} (ms)	α	ΔDM (pc cm^{-3})
J0040+5716	40 ± 2	2.2 ± 0.2	0.0378 ± 0.0024	86 ± 8	2.7 ± 0.3	0.0143 ± 0.0022
J0117+5914 (Co)	7 ± 0	2.2 ± 0.1	0.0082 ± 0.0009	14 ± 1	3.5 ± 0.4	0.0041 ± 0.0011
J0117+5914 (Ce)	8 ± 1	1.9 ± 0.2	0.0064 ± 0.0006	16 ± 2	2.6 ± 0.2	0.0038 ± 0.0006
J0543+2329	10 ± 1	2.6 ± 0.2	0.0155 ± 0.0020	17 ± 2	2.7 ± 0.3	0.0031 ± 0.0020
J0614+2229 (Co)	15 ± 1	1.9 ± 0.1	0.0030 ± 0.0007	44 ± 4	2.4 ± 0.3	-0.0033 ± 0.0006
J0614+2229 (Cy)	15 ± 0	2.1 ± 0.1	-0.0053 ± 0.0006	44 ± 3	3.1 ± 0.3	-0.0109 ± 0.0008
J0742−2822	20 ± 2	3.8 ± 0.4 ...	0.0013 ± 0.0027		...	...
J1851+1259	6 ± 1	4.1 ± 0.3	0.0271 ± 0.0021	10 ± 1	4.7 ± 0.4	0.0158 ± 0.0017
J1909+1102	42 ± 3	3.5 ± 0.4	0.0351 ± 0.0085	120 ± 27	6.4 ± 0.7	-0.0276 ± 0.0077
J1913−0440 (Co)	9 ± 0	2.7 ± 0.2	0.0240 ± 0.0009	16 ± 1	3.5 ± 0.3	0.0161 ± 0.0011
J1913−0440 (Cy)	7 ± 0	3.3 ± 0.1	0.0457 ± 0.0003	12 ± 0	4.1 ± 0.2	0.0381 ± 0.0003
J1917+1353	11 ± 1	2.8 ± 0.4	-0.1004 ± 0.0025	21 ± 2	3.6 ± 0.6	-0.1167 ± 0.0028
J1922+2110	42 ± 2	2.0 ± 0.2	0.0829 ± 0.0025	85 ± 6	3.3 ± 0.4	0.0663 ± 0.0023
J1935+1616	20 ± 1	3.4 ± 0.2	-0.0635 ± 0.0030	46 ± 4	3.9 ± 0.5	-0.0836 ± 0.0038
J2257+5909	31 ± 2	2.6 ± 0.4	-0.0317 ± 0.0058	68 ± 9	3.4 ± 0.6	-0.0530 ± 0.0050
J2305+3100	9 ± 0	1.5 ± 0.1	0.0184 ± 0.0035	11 ± 0	2.0 ± 0.1	0.0144 ± 0.0023
$\langle\alpha\rangle$		2.7 ± 0.2			3.5 ± 0.4	

Table 6.2: List of obtained τ values, spectral indices, α, and ΔDM values, using two models.

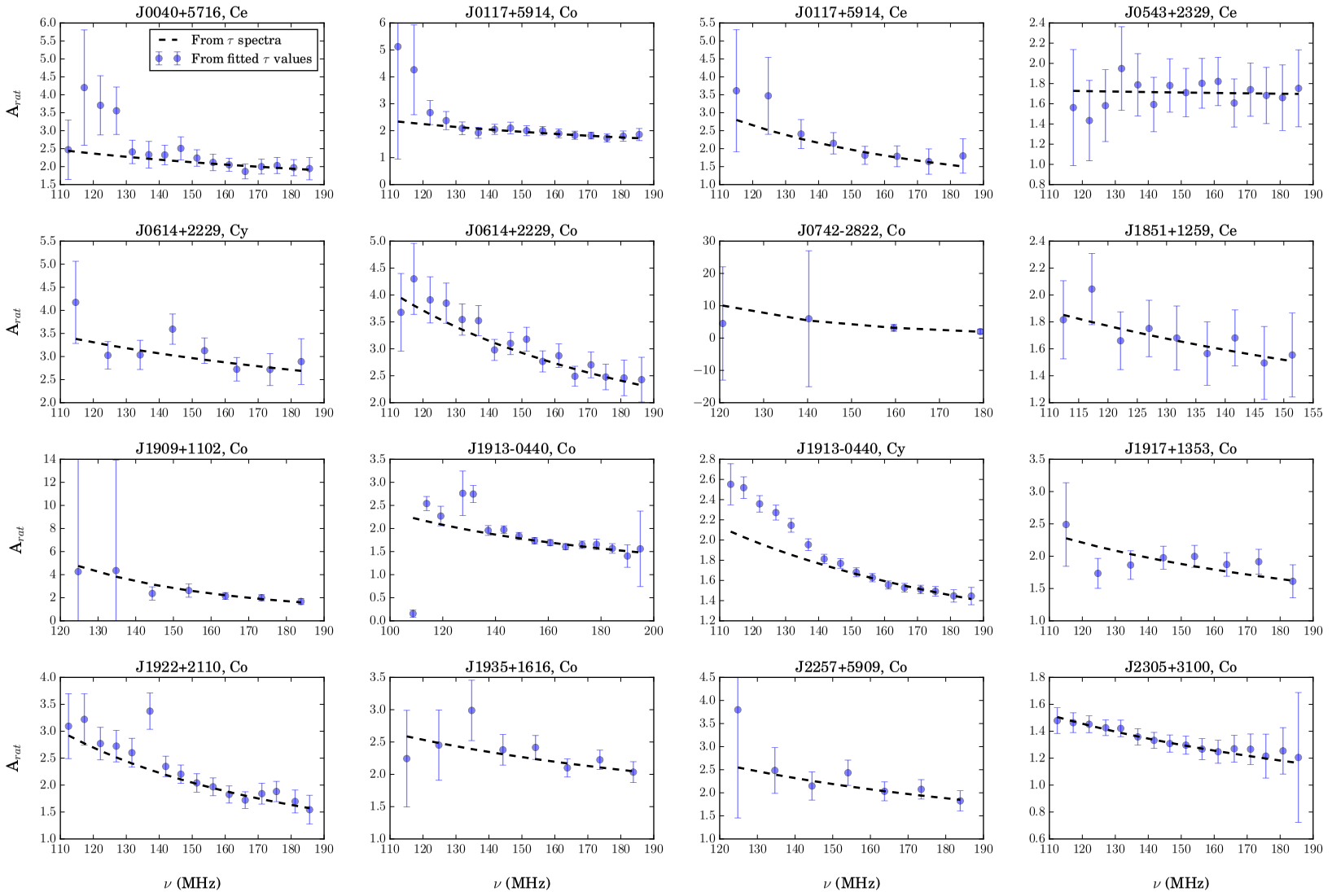

Figure 6.3: The ratio of anisotropy estimated by Eq. (4.10) for each dataset. The purple (circle) data points are computed using the obtained τ values, and the black lines (dashed) are computed using the obtained power law fits to the τ spectra.

KS test, but it is hard to be sure from this data alone. The ΔDM correction also minimises the difference in DM values between the Commissioning and Cycle 5 epochs for this pulsar (as shown in Table 5.5). Again, the α values obtained by the different models are well separated, with the anisotropic case, for which $\alpha = 4.1 \pm 0.2$ (Cy), in agreement with theoretical predictions of $\alpha = 4$.

PSR J2257+5909 shows the widest separation in obtained p-values (85.6% versus 93.8%). The α values for the two models are also well separated and the anisotropic value of $\alpha = 3.4 \pm 0.6$ has an upper limit in agreement with a theoretical value of $\alpha = 4$.

Using the approximation of Eq. (4.10), I calculate estimated ratios of anisotropy for all of the target sources. The results are shown in Fig. 6.3. The plots contain both an estimate of $\tilde{A}_{\rm rat}$ by calculating the ratio of τ values using the two models at different frequencies, as well as the ratio obtained by using the fitted τ spectra of both models. The estimates of the anisotropic ratios all lie between values of 1.4 and 5.5. For a few pulsars I see significant deviations from the power law trend at low frequencies. These include PSRs J0117+5914, J1913−0440, J2257+5909 and less distinctly J0614+2229 – the four pulsars mentioned above.

To compare the trends in Fig. 6.3 to simulations, I simulate scatter broadened data and obtain results in a similar way as was done for Fig. 4.14 in Chapter 4. Here I use a pulse period of 0.6 sec, a duty cycle of 2%, a distance of 3 kpc and observing frequencies between 90 MHz and 180 MHz, all representative of the LOFAR sample in Table 5.1. Fig 6.4 shows the outcomes for a set of simulated ratios of anisotropy, $A_{\rm rat} = (2, 10, 100, 1000)$. The simulated profiles associated with these can be found in Appendix B. The τ spectra in Fig. 6.4, show how an increasing ratio of anisotropy, leads to α values closer to 4.0 for the extreme anisotropic model, as expected, while the α value for the isotropic model is closer to 4.0 for $A_{\rm rat} = 2$. The results for multiple realisations of the noise are shown in Table 6.3. For all the ratios of anisotropy, the α ratios obtained by the two models are well separated. The plots in Fig. 6.4 clearly show that $\tilde{A}_{\rm rat} \sim A_{\rm rat}$ is only a good approximation for $A_{\rm rat} = 2$. For higher degrees of anisotropy the assumption that $\tau_{iso} \sim \tau_{geo}$ breaks down. As such it is difficult to make statements about the ratio of anisotropy using the data in Fig. 6.3.

More detailed tests of anisotropy in the temporal domain would require much higher S/N data, to be able to tell the model profile shapes apart. I have only made use of extreme (1D) anisotropic and isotropic models for fitting profile shapes. For data with high S/N it would be valuable to fit the profile shapes directly using Eq. (2.30) and to obtain the degree of anisotropy in this way. Initial fits using the full

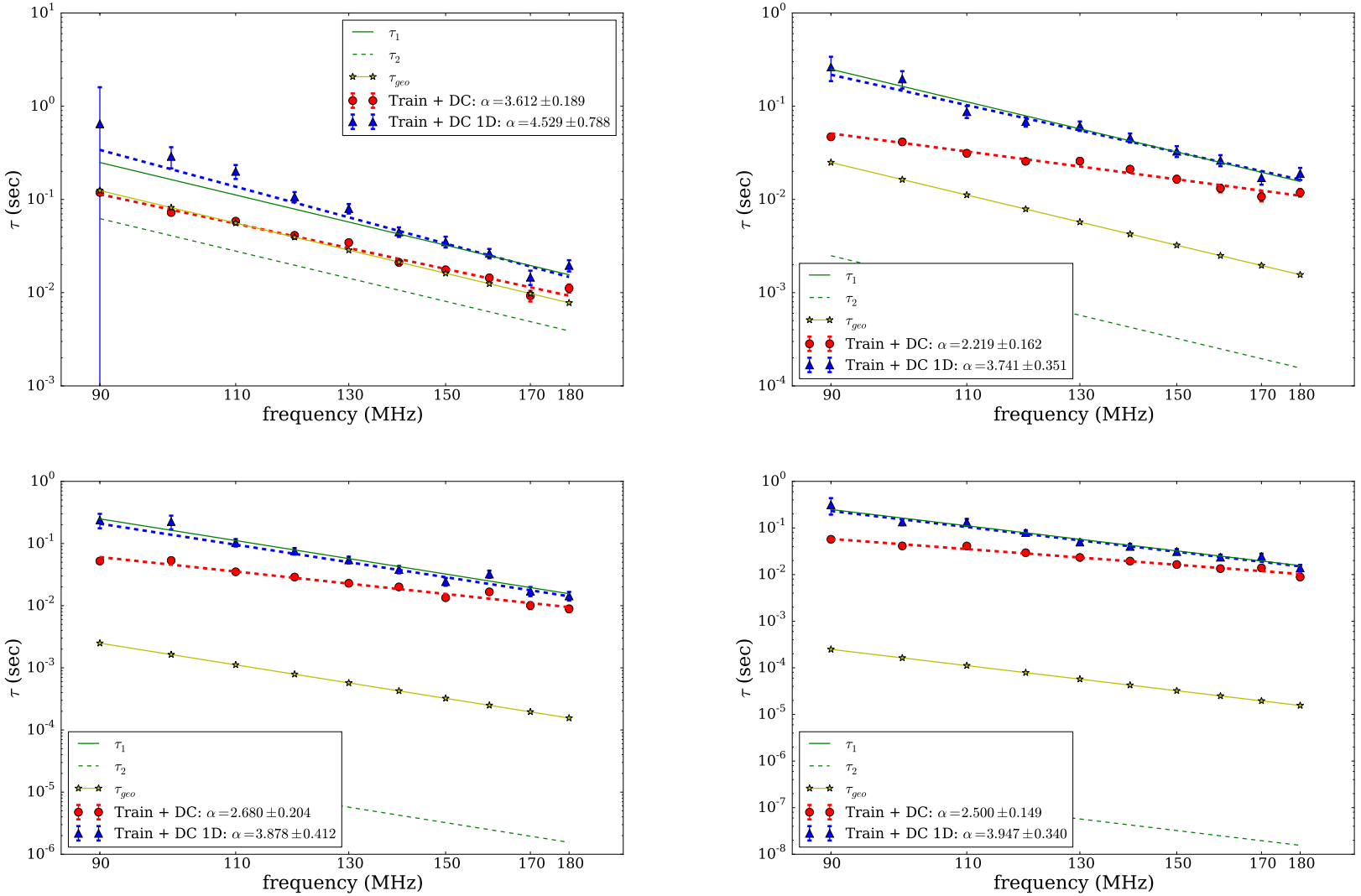

Figure 6.4: Simulated τ spectra for different ratios of anisotropy. *Top:* $A_{\rm rat} = 2$ (left) and $A_{\rm rat} = 10$ (right). *Bottom:* $A_{\rm rat} = 100$ (left) and $A_{\rm rat} = 1000$ (right).

Table 6.3: Table containing the mean and standard deviations of the obtained α values for simulated data of varying degrees of anisotropy. Fits are produced using the IM and AM_{1D} models for 100 Gaussian noise realisations each.

Simulated LOFAR pulsar: 0.6 sec, 2.0% duty cycle, SNR: 10		
Frequency Range: 90 – 180 MHz		
Anisotropic Ratio	$\alpha_{\rm iso}$	$\alpha_{\rm 1D}$
2	3.6 ± 0.2	4.5 ± 0.5
10	2.5 ± 0.6	3.7 ± 0.5
100	2.4 ± 0.2	3.9 ± 0.7
1000	2.8 ± 0.7	4.0 ± 0.5

form of Eq. (2.30) proved difficult to constrain both values of τ well. The fits were also found to be particularly sensitive to the initial guesses of the two τ values.

Combining temporal analysis with secondary (power) spectra analysis (e.g. Stinebring et al. 2001) and the imaging of pulsars where possible, will increase the efficiency of tests for anisotropy. The very-long-baseline interferometry (VLBI) constructed image of PSR B0834+06 (Brisken et al. 2010, as shown in Fig. 2.5) already provides concrete evidence for highly anisotropic scattering surfaces in the ISM.

6.3 Scattering spectral index (α) distribution

In Table 6.2, I summarise the obtained spectral indices for each pulsar for a given scattering model. The average spectral index, using the IM, is $\langle\alpha\rangle = 2.7 \pm 0.2$. This is much lower than the theoretically predicted values of $\alpha = 4$ or 4.4.

Using the IM, the majority of pulsars (11 out of 13) have α values smaller than 3.8. Not a single pulsar is measured to have a best-fit α value larger than 4.0. Only three pulsars have spectral indices in close agreement with the theoretically predicted values (viz. PSRs J0742−2822, J1851+1259 and J1909+1102).

Similar low frequency spectral indices have been reported in L15 and Lewandowski et al. (2013, hereafter L13), although many of the values were dropped from their subsequent analysis in the papers for being "suspiciously low". Four of the pulsars that were excluded in L15 for which I also have measurements, are: PSRs J0614+2229 (L15: $\alpha = 1.73 \pm 0.5$, my $\alpha = 2.1 \pm 0.1$), J0742−2822 (L15: 2.5 ± 0.3, my $\alpha = 3.9 \pm 0.4$), J1917+1353 (L15: 2.11 ± 0.05, my $\alpha = 2.9 \pm 0.4$) and J1922+2110 (L15: 0.98 ± 0.88, my $\alpha = 2.0 \pm 0.2$). In each case I measure a larger α value than L15.

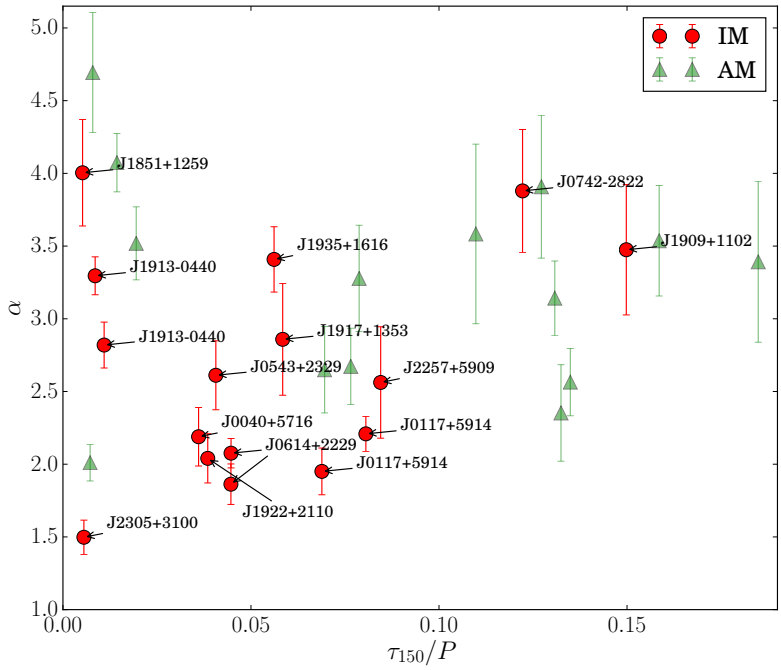

Figure 6.5: Spectral indices α plotted against τ values at 150 MHz in units of the pulse period. These τ values are obtained from the best-fit power law to the τ spectrum of each pulsar. Isotropic values are shown in red (circles), and anisotropic values in green (triangles). Isotropic data points are labelled by the corresponding pulsar names. The larger the τ_{150}/P values, the more the scattering tail of the average pulse profile will wrap around the full rotational phase.

In Chapter 4, using simulated data, I discussed how the accuracy of τ and consequently α measurements, depend on the relative value of τ to the pulse period (P). The *train + DC* method was introduced to improve the accuracy of these measurements. For large τ/P values the scattering tails wrap around the full rotational phase. In extreme cases, as was shown in the left-hand side of Fig. 4.4, the underlying distribution in τ will be skewed by large τ/P values, leading to less accurate estimates of τ values. Fig. 6.5 shows the α values obtained for the set of LOFAR pulsars, as a function of the degree of scattering relative to the pulse period characterised by the fraction τ_{150}/P, with τ_{150} the scattering time value at 150 MHz. I see that for most pulsars $\tau_{150}/P < 0.1$, using the IM, however for two pulsars (PSRs J0742−2822 and J1909+1102) $\tau_{150}/P > 0.1$. While this is a significant scattering fraction (which increases to 0.4 at 110 MHz), an underlying skewed distribution in τ values was only observed for $\tau/P > 1$ in Fig. 4.4. If indeed the low frequency τ values associated with PSRs J0742−2822 and J1909+1102 should have had asymmetric error bars representative of a skewed distribution, it could lead to a slight increase in the measured α values (3.8 ± 0.4 and 3.5 ± 0.4 respectively) bringing them in closer agreement with the theoretical value of 4. Fig. 6.5 shows no clear dependence of α on the τ/P ratio. For a given τ_{150}/P value, I find a range of α values. This is reassuring, as it shows no sign of systematic offsets in α values obtained from my fitting code.

In the previous section I have discussed screen anisotropy. I note that the mean spectral index for the $\mathrm{AM_{1D}}$ is $\langle\alpha\rangle = 3.5 \pm 0.4$, higher than for the IM and closer to the theoretically expected values. In 10 out of the 13 objects the increase in α using an $\mathrm{AM_{1D}}$ is larger than 20%, and for all but one, the increase is larger than 10%. However, for five objects the α values associated with the IM and $\mathrm{AM_{1D}}$ lie within the error bars of each other, making the outcomes of the models less distinct. The anisotropic α value for the majority of pulsars (9/13) has error bars reaching to the theoretically expected values. However, as also noted in the previous section, the error bars on the anisotropic spectral indices are typically larger than for the IM.

In Chapter 4 (Fig. 4.13), I showed that fitting anisotropically simulated pulse profiles with an IM, leads to incorrect τ values and lower spectral indices, while the fits by an $\mathrm{AM_{1D}}$ lead to estimates of the larger τ values. The model-dependent α values obtained here, for which $\alpha_{IM} < \alpha_{AM_{1\mathrm{D}}}$, (while $\alpha_{AM_{1\mathrm{D}}}$ values are often in closer agreement to theoretically predicted values), reflect the simulated trend. Other possibilities for lower α's include screens that are truncated, that have extreme scattering properties or multiple screens along a given line of sight. In Section 6.5, I discuss whether I find evidence for finite scattering screens.

6.4 Profile evolution and DM corrections

6.4.1 Profile evolution

Optimal de-scattering techniques of scatter broadened pulse profiles, would in principle remove the effects of propagation, revealing the intrinsic profile shape. However, as described in Sec. 1.1.4, pulsars also exhibit intrinsic profile evolution with frequency, which has to be disentangled from the scattering frequency dependence. The simplest pulsar model (as shown in Figs. 1.1 and 1.4) predicts, via radius-to-frequency mapping (RFM), an increase in pulse width at low frequencies.

In this study, I have picked the target sources not only based on the scattering tails they exhibit, but also for having simple single component profile shapes that appear to not show dramatic profile evolution, as described in Sec. 3.3.

An exact understanding of the scattering mechanism and its dependence on frequency, would allow for profile shape changes to be disentangled from scattering effects. My results provide evidence for anomalous α values (deviating from expected scattering trends, such as $\tau \propto \nu^{-4}$) making it less straightforward to separate the IISM and intrinsic frequency dependencies.

My fitting techniques (Chapter 4) assume an intrinsic Gaussian-shaped profile, with the obtained standard deviation of the Gaussian (σ) a proxy for pulse width. I analyse the evolution of σ with frequency and compare the obtained σ values at HBA frequencies to the pulsar widths measured at higher frequencies by Lorimer et al. (1995, at 408 MHz) and Hobbs et al. (2004, at 1.4 GHz). The results are shown in Fig. 6.6.

I find that for the majority of the pulsars the widths correspond well to the higher frequency results. In most cases the widths measured at the high frequency end of the HBA band are close to the corresponding widths at higher frequencies, as can be seen for PSR J0040+5716 in the top left panel of Fig. 6.6. The cases for which the high frequency widths are greater than the widths obtained by the IM, include PSRs J0117+5914, J0614+2229, J1913−0440 and J1935+1616. In the case of PSR J0117+5914, as was seen in its flux density spectra as well, outcomes differ significantly between the Commissioning and Census data. PSR J1913−0440 has been discussed as a pulsar with possibly a secondary component, evidence for which is seen not only in the profile shapes, but also in the deviations of the τ spectrum at low frequencies. PSR J1913−0440 has also been considered a candidate for evidence for anisotropy. Here I see that the width evolution of the intrinsic pulse modelled by the IM and $\mathrm{AM_{1D}}$ is significantly different. The $\mathrm{AM_{1D}}$ shows a clear decrease in

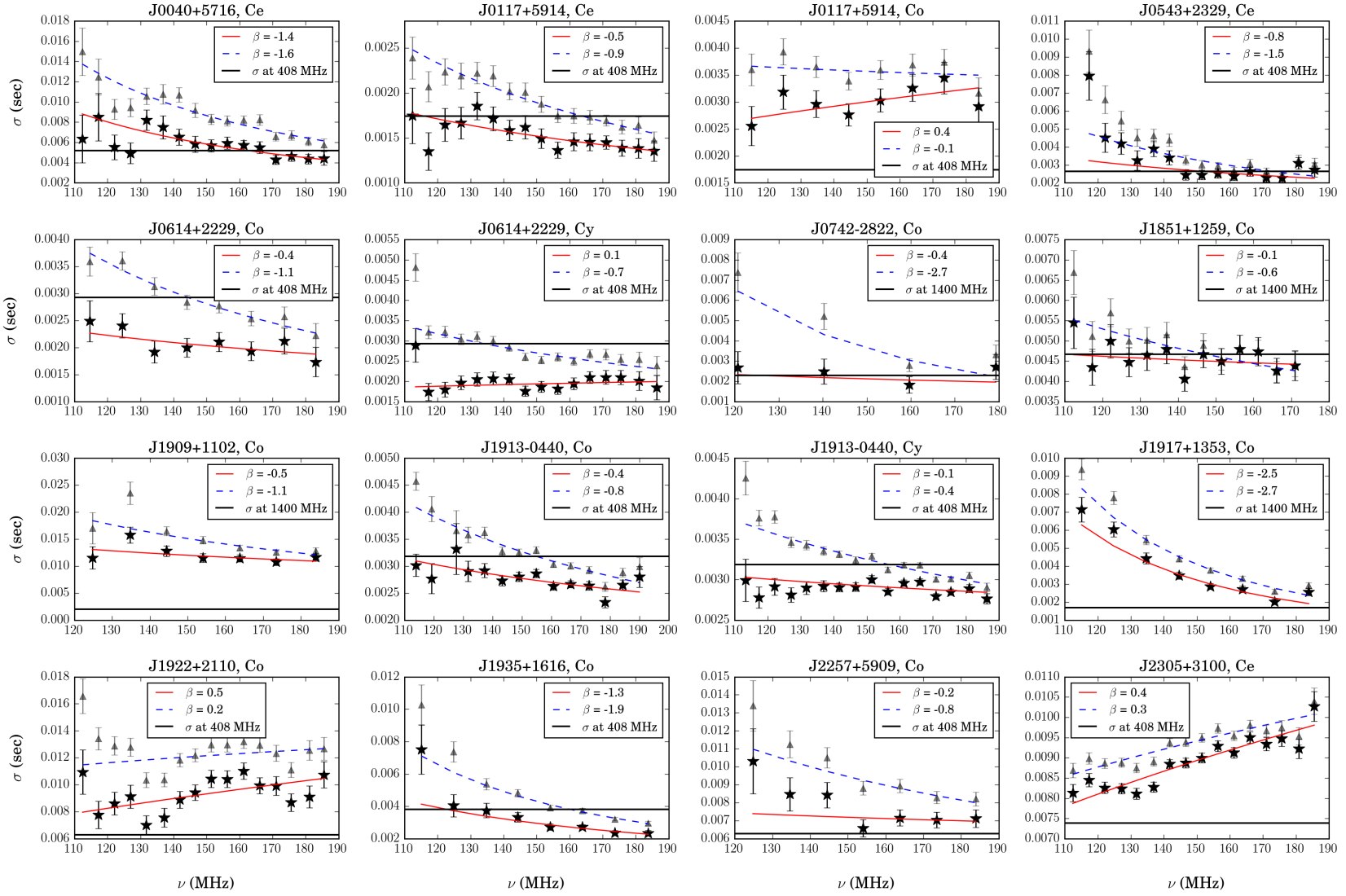

Figure 6.6: The evolution of intrinsic pulsar widths (represented by σ) with frequency for the set of LOFAR pulsars studied. The width evolution is shown for both the isotropic model (stars) and extremely anisotropic model (triangles). The high frequency widths as published in Lorimer et al. (1995, at 408 MHz) or Hobbs et al. (2004, at 1.4 GHz) are shown as horizontal solid lines. I have transformed their full width at half maximum values (w_{50}) to σ values. The spectral indices of a power law fit to the isotropic data ($\sigma \propto \nu^{\beta}$) are shown in the legends.

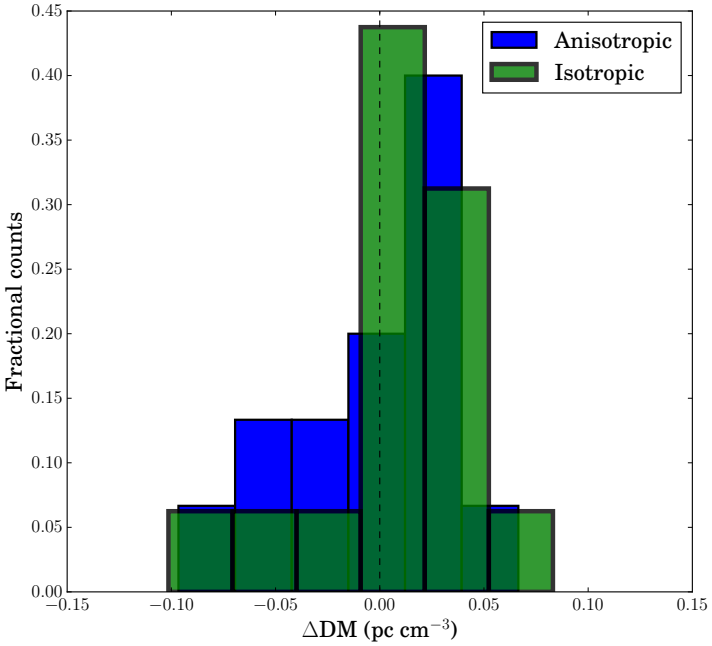

Figure 6.7: Spread in ΔDM values obtained for the set of pulsars.

width with frequency and is in closer agreement to the high frequency width obtained by Lorimer et al. (1995).

PSR J2305+3100 shows an increasing width with frequency. The profile shapes for this pulsar at HBA frequencies are not highly scattered, such that the width evolution likely results from the covariance of σ and τ in the fitting process.

The pulsar which shows the most well-defined width evolution is PSR J1917+1353. The isotropic case is fitted with a power law, $\sigma \propto \nu^{-2.5}$. Hobbs et al. (2004) estimated $w_{50} = 4.0$ ms, which translates to $\sigma = 1.7$ ms. My lowest measured width value for PSR J1917+1353 is 2.0 ± 0.15 ms.

6.4.2 DM corrections

As seen throughout Chapter 5, by fitting for the centroid values (μ) of the intrinsic Gaussian components, I can estimate small corrections to the DM values, that I have labelled as ΔDM. Plots estimating the ΔDM value for each target source can be found in Appendix A. Fig. 6.7 shows the distribution in ΔDM values for both models. Although the histogram represents only a small number of sources, it appears that positive ΔDM values are obtained more frequently than negative values, for both fitting models. A positive value here refers to an overestimation of the original data

DM value by an amount of ΔDM. Rerunning the data reduction with a value set to DM $-$ ΔDM removes this dependence of $\Delta\mu$ on frequency.

I conclude that small errors in DM values are likely introduced by the traditional method in which DM values are obtained from single-epoch datasets. This relies on finding the DM value for which, after the DM delay correction is applied (see Fig. 3.3), the S/N of the sum of the channelised average pulse profiles is maximised. This process is therefore generally sensitive to the location of the pulse peaks of the channelised data. In the case of highly scattered profiles, the true centroid of the intrinsic pulse lies earlier in time than when the peak of the scattered signal is observed. Furthermore, this change is larger at low frequencies and smaller at high frequencies (by Eq. 2.6), such that, typically, the DM value required to maximise the S/N of the sum of the intrinsic pulse profiles is lower than the value required to maximise the S/N of the sum of the scattered pulse profiles.

I have also measured instances in which the obtained ΔDM is negative, and therefore the original DM was an underestimation. For the five pulsars that show negative ΔDM values (PSRs J0614+2229, J1909+1102, J1917+1353, J1935+1616 and J2257+5909), four show negative DM values using both scattering models. As seen from the figures in Appendix A, not all of these are well constrained ΔDM fits. The asymmetric effect of scattering on pulse shapes, tends to drag the profile centroids to larger τ values. However, effects such as the intrinsic profile evolution described previously, can cause shifts in the intrinsic pulse centroid in either direction. It is therefore possible, due to intrinsic pulse evolution and due to the covariance of pulse width and τ, to measure negative ΔDM values. The two pulsars for which the negative ΔDM fits are best constrained (PSRs J1917+1353 and J1935+1616), show width evolution that is well modelled by a power law fit.

Small DM corrections are critical to improve pulsar timing experiments, which as described in Sec. 1.1.5, aim to model the stability of a pulsar rotational periods (P) and period derivatives ($\dot{P}$) over long time scales ($\sim$ 10 yrs) at sub-microsecond to nanosecond scales. These pulsar timing experiments are typically conducted at higher frequencies (around 1.4 GHz). At these higher frequencies, by Eq. (2.19), a smaller angular scale of the IISM is sampled through multipath propagation than at the lower frequencies studied here. This effect is expected to lead to small frequency dependent DM variations ($\sim 4 \times 10^{-5}$ pc cm^{-3}, Cordes et al. 2016). The combination of having small chromatic DM changes along with unmodelled intrinsic pulse evolution, means that small DM corrections obtained at low frequencies can not straightforwardly be extrapolated to improve timing observations.

6.5 Finite scattering screens

As discussed in Secs. 4.1.2 and 4.3.3, and in more detail in Cordes & Lazio (2001) and Geyer & Karastergiou (2016), lower α values can result from finite scattering screens.

If indeed some of the lower α values obtained at low frequencies here, are the result of finite scattering screens in the ISM, I can estimate the scattering screen size for each pulsar at which deviations from theoretical α values (associated with infinite screens) will become observable. For a midway screen, τ can be expressed as

$$\tau = \frac{D\ \sigma_\theta^2}{c}, \tag{6.1}$$

with, as before, D the distance from the pulsar to the observer, σ_θ the standard deviation of the distribution in observing angles and c the speed of light. Using the τ values at 150 MHz for each pulsar (obtained from the power law fits to their τ spectra), I calculate the maximum scattering screen size, for a circular screen, at 150 MHz at which observations become sensitive to the finite nature of the screen. Table 6.4 shows the associated scattering screen sizes for each pulsar as well as the required observing baseline to be able to resolve them. I have chosen σ_θ as a representation of the radial screen size (such that the diameter is $2\sigma_\theta$).

To show conclusively that the observed low α values are correlated with finite scattering screens, would therefore likely require a low frequency interferometer with baselines $\gtrsim$ 2500 km, as given in Table 6.4. The current version of the Low Frequency VLBI Network (LFVN) mostly includes 18 cm and 92 cm receivers (326 MHz to 1.7 GHz) in e.g Russia, India and China, with baselines varying between $\sim$120 km and 5800 km (Molotov et al., 2003). An alternative approach, is to use the space-based observatory *RadioAstron*, jointly with ground-based instruments to form extreme baseline interferometers (Smirnova et al., 2014). This space-ground interferometer, which combines data from the 10-m Space Radio Telescope aboard RadioAstron, the Arecibo telescope and the Westerbork Synthesis Radio Telescope (WSRT), leads to observations with a 220 000 km projected baseline, and unprecedented resolution at meter wavelengths. Studying the scattering towards the nearby pulsar B0950+08 with this interferometer, Smirnova et al. (2014) inferred two independent scattering surfaces along the line of sight, and an α value of 3.00 ± 0.08. As described in Chapter 4, and for example shown in Fig. 4.24, a dependence of τ on frequency that shows a break in its power law spectrum, can be evidence for truncated screens too. This is due to the loss of flux at longer wavelengths where observations become

Pulsar	Screen size ($2\sigma_\theta$, mas)	Baseline (km)
J0040+5716	165	2485
J0117+5914 (Co)	87	4721
J0117+5914 (Ce)	80	5107
J0543+2329	102	4006
J0614+2229 (Cy)	119	3458
J0742-2822	129	3178
J1851+1259	62	6571
J1909+1102	120	3409
J1913−0440 (Cy)	53	7665
J1913−0440	60	6779
J1917+1353	61	6726
J1922+2110	130	3149
J1935+1616	94	4348
J2257+5909	130	3150
J2305+3100	24	17124

Table 6.4: The angular size of midway screens at 150 MHz, for my set of target sources, based on their obtained τ values at 150 MHz and the estimated distance to the source using the YMW16 model, see Table 5.1. The last column provides the required baseline ($B = \lambda/2\sigma_\theta$) to resolve such screens with a low frequency VLBI network, where $\lambda = 2$ m is the wavelength corresponding to 150 MHz.

sensitive to the size of the IISM screen, consequently altering the shape of the observed profiles (Fig. 4.20). The top panel of Fig. 6.8 shows a set of simulated pulses at HBA frequencies, that have been scattered by a circular (disk-shaped) screen of radial size 120 AU. It is simulated to be centred behind a midway disk at a distance of $D_s = D/2 = 1.56/2 = 0.78$ kpc, where D = 1.56 kpc is representative of PSR B0543+2329. The disk-shaped screen means that a loss in flux occurs at a single θ_{max} (and associated t_{max}, cf. Eq. 4.3), different from Fig. 4.20 where the geometry of the rectangular screen leads to continued flux losses at various observing angles.

Bearing in mind that the pulse profiles can have intrinsic shapes different from a single Gaussian, and amidst the noise observed in the average profiles, it is hard to see evidence for pulse shapes altered by the presence of a truncated screen. The middle panel of Fig. 6.8 shows a set of observed pulse profiles of PSR B0543+2329. At the lowest frequency relatively steep profile drops can be seen, whereas at higher frequencies the profile shapes appear more similar to that of Fig. 4.20. Overall the shape evolution of PSR B0543+2329 appears to be well approximated by the simulated data. The corresponding τ-spectra are shown in the bottom panel.

Even though these similarities are interesting, I do not pursue the investigation of the pulsar shapes of the LOFAR dataset in more detail, since there are too many scattering-independent parameters that can affect the details of the profile shape. Higher S/N profile shapes at low frequencies are required to distinguish properly whether imprints of truncated screens are observed.

In Fig. 6.9 I produce τ spectra for the LOFAR dataset using two power laws instead of one. A histogram of the α residuals, $\alpha_{high} - \alpha_{low}$ is shown in Fig. 6.10, where α_{high} is the spectral index associated with the top half of the band, and α_{low} with the lower half. The histogram shows that it is more likely for $\alpha_{high} > \alpha_{low}$, although negative residuals, e.g. for PSR J1913−0440, occur as well. None of the pulsars in the set show clear evidence for sharp broken power law spectra across the HBA band. However, it is likely that small scattering screens will not have physically sharp edges or highly regular shapes, and can therefore feasibly result in increasingly flatter frequency dependencies on τ for a given range of frequencies. This will in turn result in lower estimated α values, as observed here.

A correlation between low α values and high DM values, has been promoted by datasets such as in Löhmer et al. (2001). In Fig. 6.11, I show the dependence of α with DM. This figure includes data points from several other papers, as described in the legend and the caption of the figure. Löhmer et al. (2001) suggested that beyond

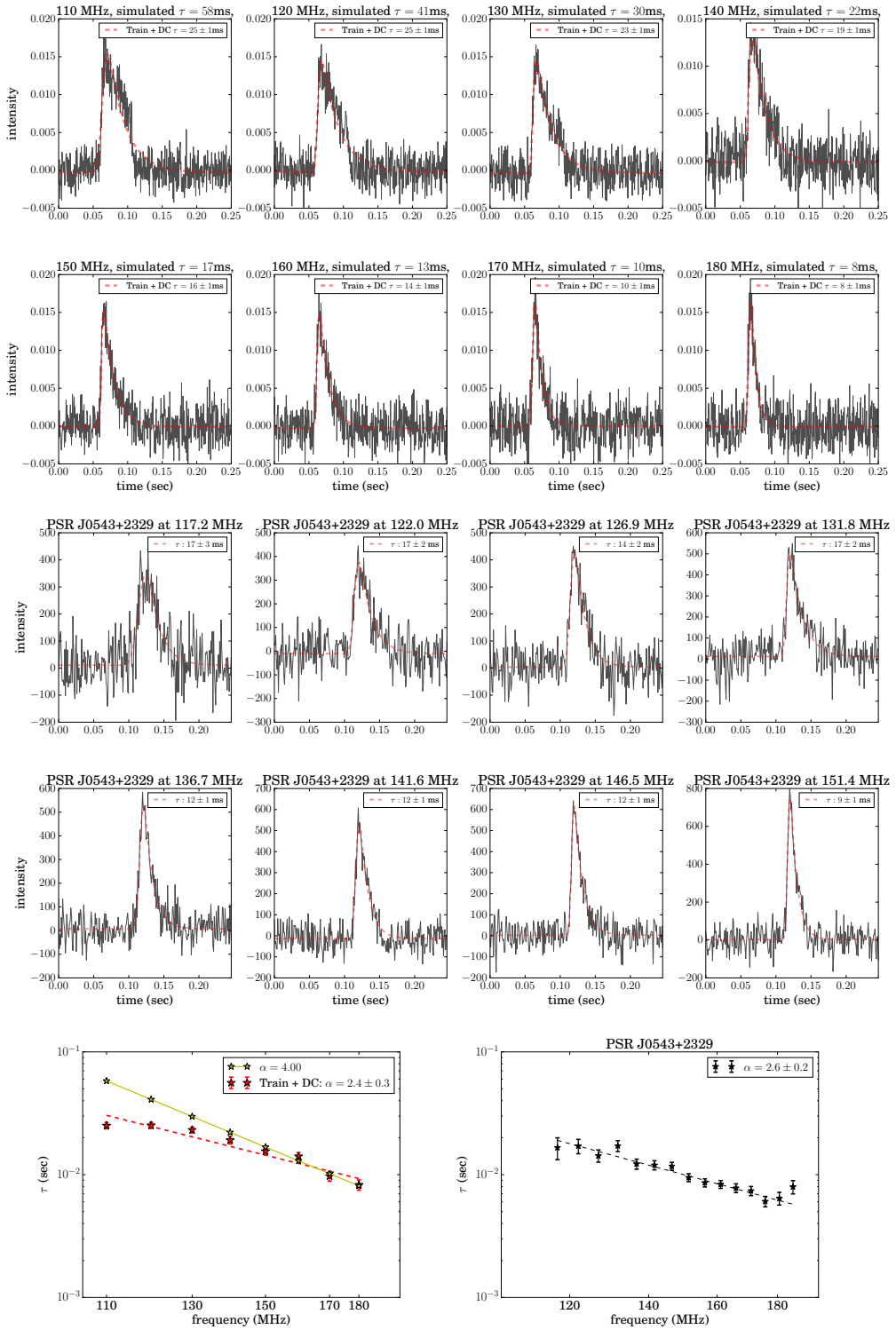

Figure 6.8: *Top, profiles:* Simulated Gaussian profiles at HBA frequencies, representative of a pulsar with $P = 0.25$ s at $D = 1.56$ kpc, consistent with the parameters of PSR B0543+2329. The pulse shapes are scattered by a midway screen of radial size 120 AU centred on the line of sight. *Middle, profiles:* The observed profile shapes of PSR B0543+2329 at HBA frequencies. *Bottom:* The τ spectra associated with the simulated profiles (left) and with PSR B0543+2329 (right). In both cases an isotropic fitting model is used.

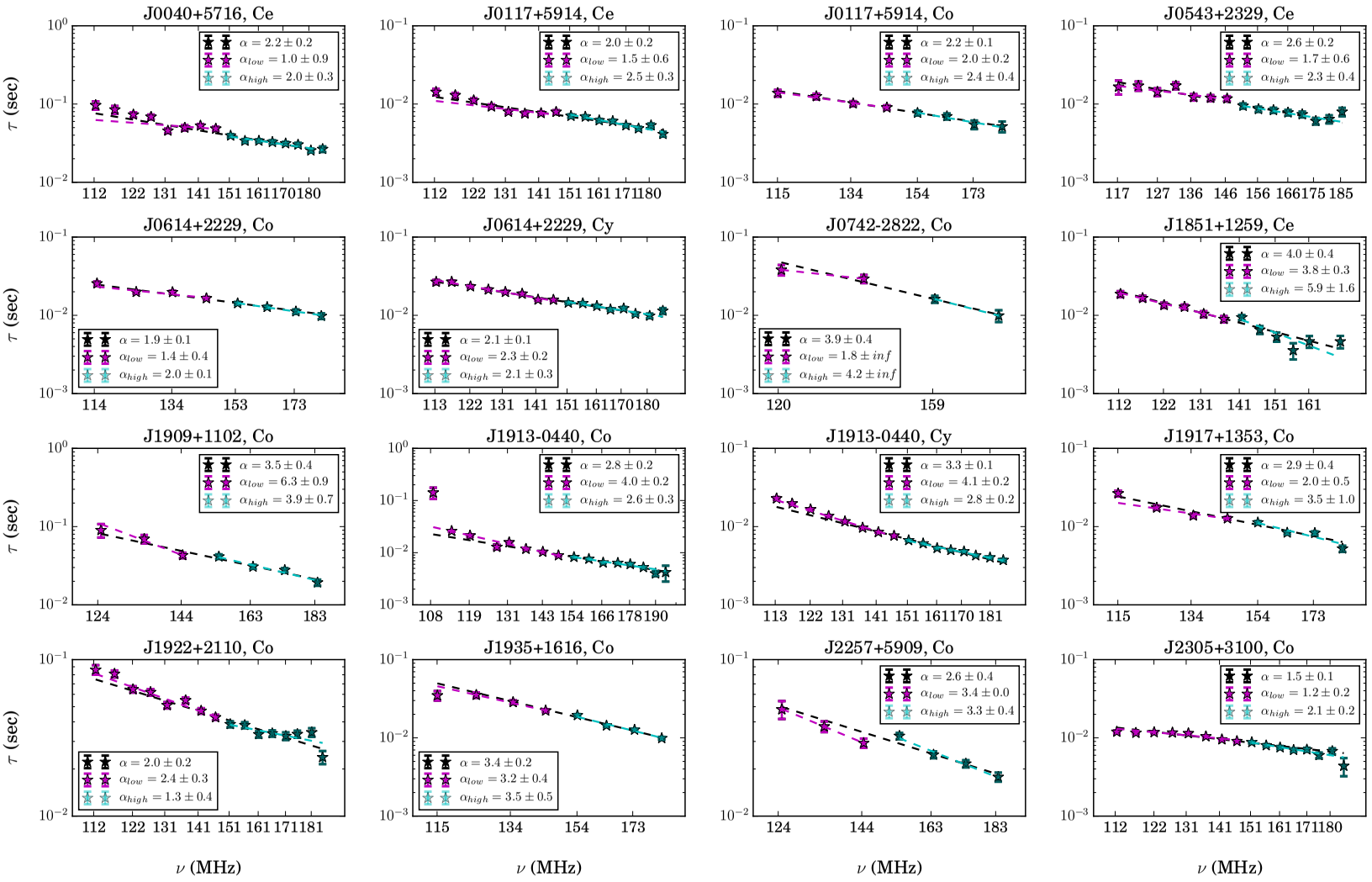

Figure 6.9: The τ-spectra for the LOFAR pulsar dataset, fitted with two power laws instead of one. In each case the HBA band was simply split in the middle.

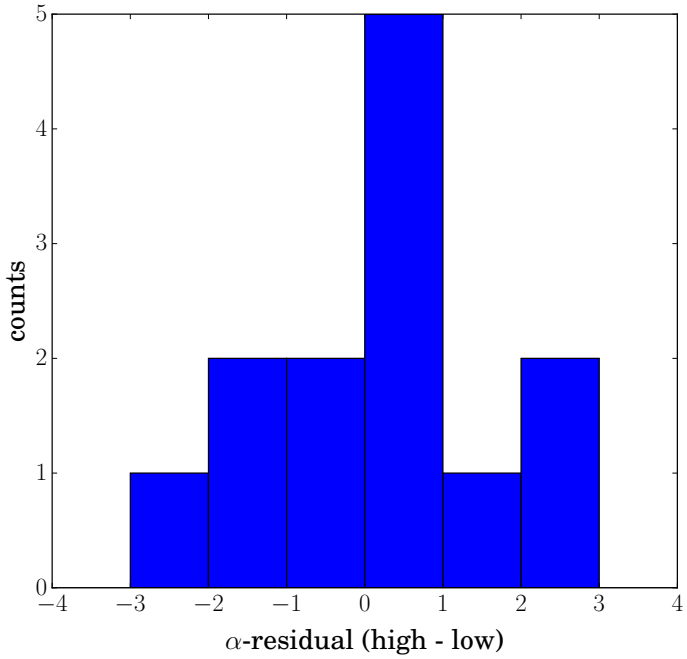

Figure 6.10: A histogram of the change in α values between the upper end and the lower end of the HBA band, i.e. $\alpha_{res} = \alpha_{high} - \alpha_{low}$. It is produced using only one dataset per pulsar, i.e. the total count is 13.

a given DM threshold (DM $>$ 300 pc cm^{-3}) α values deviated from the theoretically expected values. This threshold has been revisited by L13 (amongst others), who suggested that deviations in α start at lower DM values, around DM = 230 to 250 pc cm^{-3}. In their more recent paper (L15), however, additional α measurements have led them to conclude that the previously postulated DM threshold was based on data biased by a small number of τ measurements.

The LOFAR data show low α (< 4) values in the DM range 49 to 217 pc cm^{-3}. I investigate whether the distribution of α values with respect to distance (or DM as a proxy for distance) such as seen in Fig. 6.11 can be produced by a simple picture using truncated scattering screens. As a first step I simulate the observed scattering of a 0.6 s period pulsar, with a Gaussian shape and a duty cycle of 2.5% (chosen to represent the obeserved set of pulsars) behind a circularly truncated screen. I note that the set of LOFAR pulsars all have distances between 1.5 and 5.0 kpc (excluding PSR J2305+3100 at 25 kpc), and an α distribution between 1.5 and 4.0. Fig. 6.12 shows how this distance (D) and α distribution can be modelled using truncated screens. The setup uses a single truncated screen of varying size and scattering strength. The scattering strength is defined by the standard deviation of the Gaussian

distribution in scattering angles, as described in more detail in Sec. 4.1.2. Here I label a scattering strength of $\sigma_a = 3$ mas as ST = 3. For a range of distance values, a screen is placed midway between the pulsar and observer, and the α value over the HBA band calculated. By tweaking the screen size and scattering strength a set of (D, α) pairs are obtained.

In a similar way, low α values, as observed in Löhmer et al. (2001), for more distant pulsars (between 6.3 and 10.2 kpc, and 400 < DM < 1100, in units of pc cm^{-3}) can be produced through truncated scattering screens. This, however, would require screens with higher scattering strengths or multiple scattering screens along a given line of sight. I find it unlikely that this simplistic picture fully describes the scattering in the IISM along different lines of sight. However, evidence for typical sizes and or scattering strengths of screens in the IISM can shed light on the causes of low α values. As discussed in Sec. 2.2.3, evidence for 10–100 AU structures with electron densities as high as tens of cm^{-3}, have come from extreme acattering events (ESEs), often associated with quasars (Fiedler et al., 1987, Walker, 2007). More recently similar type events have been recorded and discussed for pulsars (Lestrade et al., 1998, Walker, 2000, Coles et al., 2015). In Coles et al. (2015) pulsar observations are shown to exhibit enhanced scintillation and changes in DM simultaneously. From these measurements the authors concluded that the observed ESEs in pulsars are caused by similar ∼AU scale over-densities. In Chapter 7, Sec. 7.3, I discuss an ongoing project with Dr. Mark Walker that aims to characterise the small scale gas-structure of the IISM by combining results from Far-infrared spectroscopy and pulsar propagation observations.

6.6 Correlations between scattering and flux density

For each dataset I calculated an average mean flux density spectrum by summing the intensities of the best-fit curve (and dividing it by the number of phase bins across the pulse profile) per frequency channel. This (uncorrected) flux density is corrected for scattering effects through an estimate of the associated raised baseline level (Chapter 4, Sec. 4.3.2.2). Examining the average profile shapes of each pulsar (Appendix A), I find six cases in which profiles with wrap around scattering tails are visible. These are the cases in which I expect to see an associated flux density loss as shown for the simulated data in Figs. 4.15 and 4.16, leading to a discrepancy between the uncorrected and corrected flux density. The six pulsars are PSRs J0117+5914, J0742−2822, J1909+1102, J1917+1353, J1935+1616 and J2257+5909, as discussed

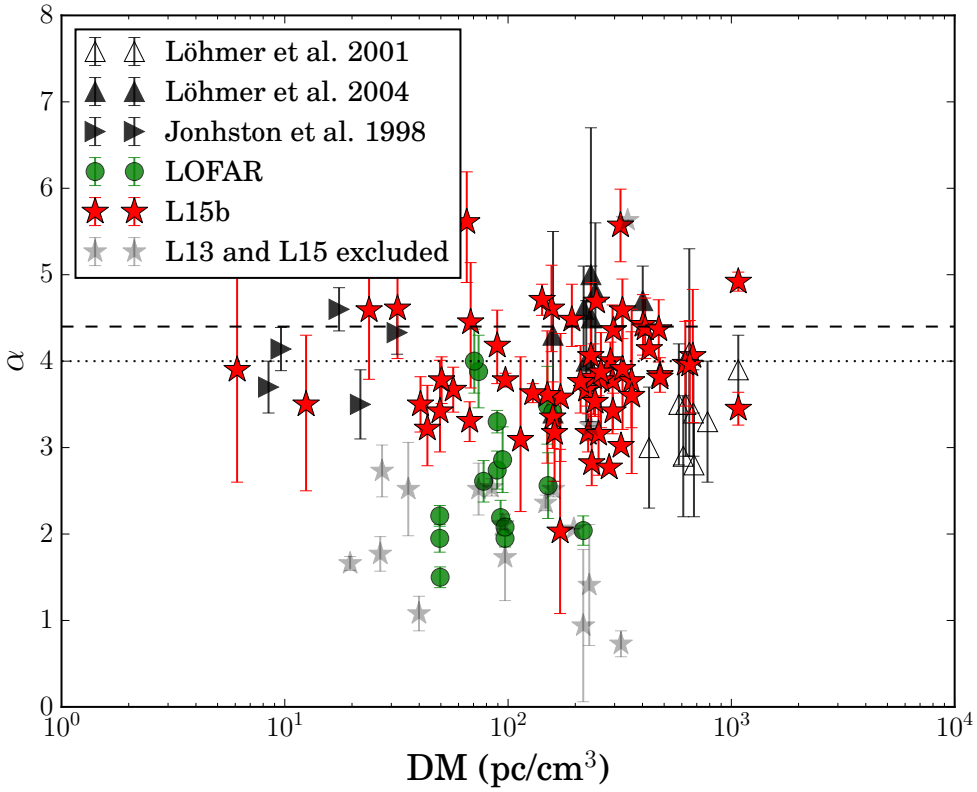

Figure 6.11: Spectral indices (α) are plotted against the corresponding DM values. The LOFAR dataset of this paper is shown in green (circles), with other data points from the literature as indicated in the legend. I show the updated L13 and L15 values as given in L15b (red, dark stars), along with the lower α values from these papers, that were excluded from further analyses (grey, lighter stars).

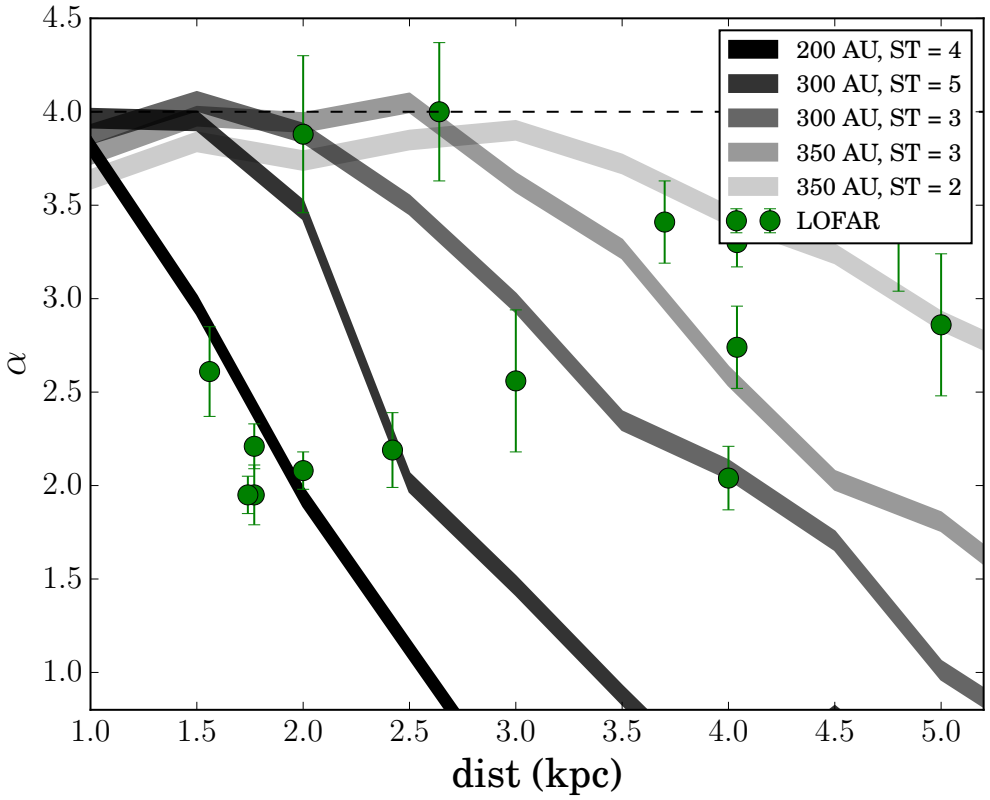

Figure 6.12: The LOFAR data points from this paper (green circles), along with computed α models, that are based on a simple truncated screen model. Circular screens are placed midway along the line of sight, for a set of distances. The screens can differ in size and scattering strength. A simulated pulsar is scattered by the modelled screen and the α value, over the HBA frequency range, estimated. The theoretical value of $\alpha = 4$ is shown as a dashed line. The model with the most extremely deviating values of α (darkest line), is based on a screen with radius 200 AU and scattering strength, ST = 4 (see text for definition). The other model screen sizes and strengths are shown in the legend.

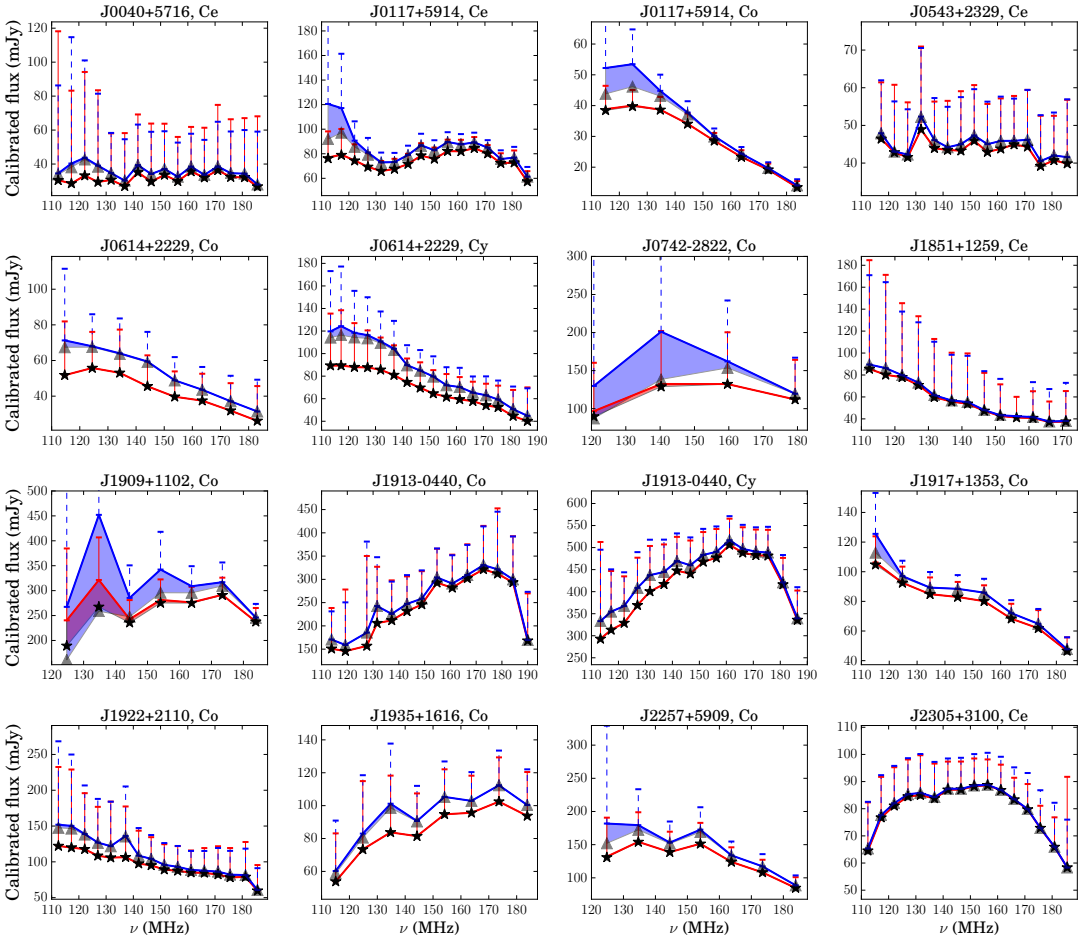

Figure 6.13: The collective mean flux density spectra for the LOFAR dataset. The flux densities are calculated from the integrated scattered profiles. Markers and colours are as in Chapter 5. Indicated error bars are one side of a symmetric error bar.

on a pulsar-by-pulsar basis in Chapter 5 in Sec. 5.2. The collection of flux density spectra for the full dataset are presented in Fig. 6.13.

From this set of six, four show a correlation between the flux density spectrum turnover and the onset of wrap around scattering tails. This includes PSR J1909+1102 which has the highest τ_{150}/P (IM) value of the set, namely 0.15 (see Fig. 6.5) and the joint highest τ_{150} value of 42 ± 3 ms (IM, see Table 6.2). PSRs J1917+1353 and J1935+1616 show wrap around scattering tails that do not correlate with the associated flux density spectra. In the case of PSR J1917+1353 there is no clear turnover in its flux density spectrum, and the turnover in the flux density spectrum of PSR J1935+1616 is at a too high frequency to only be related to long scattering tails. These two pulsars have the lowest τ_{150}/P ratios (0.06) of the six pulsars that show pulse run-in. It is therefore not surprising that their flux density spectra are not dominated by scattering effects. As discussed in more detail in Sec. 5.2.11 (for PSR J1935+1616) such turnovers could potentially be due to scattering by finite screens.

There are three pulsars for which the spectra appear to turnover without the profiles exhibiting extreme scattering tails. These are PSRs J0614+2229 and J1913−0440 for which the flux density spectrum turns over at high frequencies (around 170 MHz), even though $\tau_{150}/P < 0.05$, and PSR J2303+3100 which is only weakly scattered and with $\tau_{150}/P = 0.01$, but has a turnover at around 150 MHz. When the scattering is weak the flux density spectrum shape will be dominated by other effects such as thermal absorption by dense surrounding gaseous environments (e.g. Rajwade et al. 2016) or intrinsic emission properties, or perhaps some form of anomalous scattering. In the cases for which the scattering is large, e.g. PSR J1909+1102 as mentioned above, I do see the expected correlations between scattering and flux density measurements.

My method estimates the degree to which flux is lost due to scattering effects. However, for the correction to hold an understanding of the scattering mechanisms is required (i.e. the correct scattering model has to be used). It will therefore be valuable to compare these corrected values to flux density estimates obtained from interferometric pulsar images. In Chapter 9, I discuss future projects and proposals, which includes analysing joint imagining and beamformed LOFAR data to conduct such a comparison.

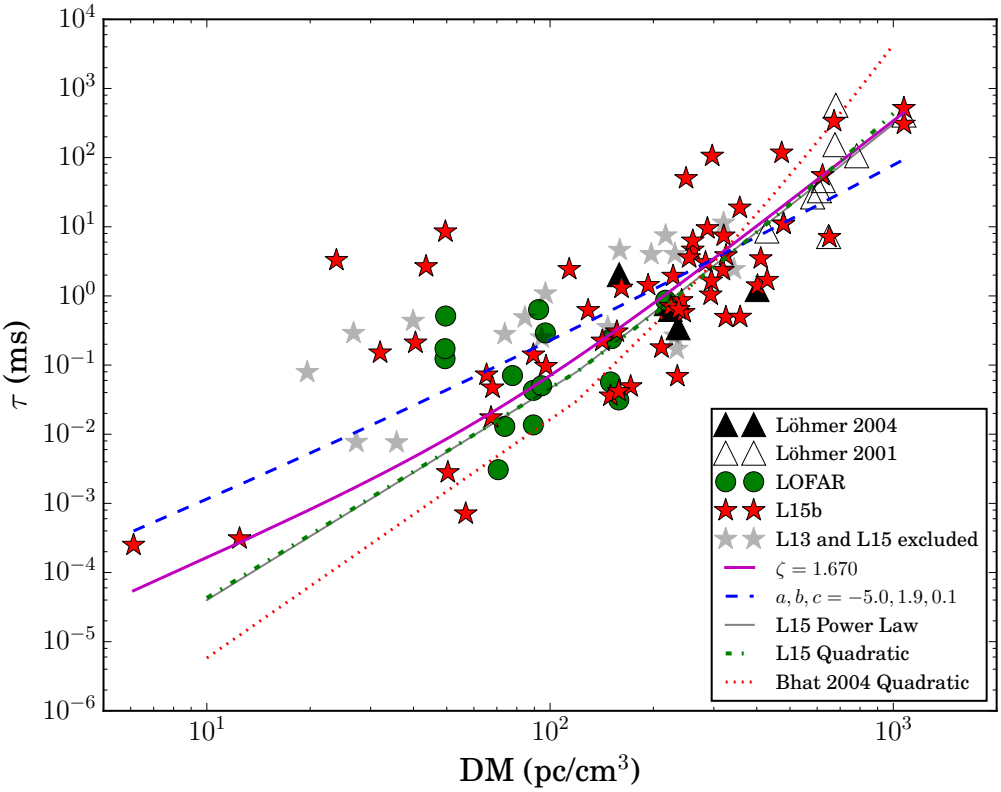

Figure 6.14: Scattering time (τ) at 1 GHz versus DM values, for the LOFAR dataset along with data from Löhmer et al. (2001, 2004) and L15b. L15b contains τ values for most sources in L13 and L15. The data points which were considered erroneous in L13 and L15 are also shown (grey stars). The LOFAR data points from this paper are shown as green circles. To obtain fits all the data, except those marked as *excluded*, were used. The obtained fits are a power law fit (magenta, solid thick line) and a parabolic fit (blue dashed line). The plot also includes the parabolic fit from Bhat et al. (2004) (red, dotted line), as well as the power law and parabolic fits (grey solid, green dash-dotted lines) from L15.

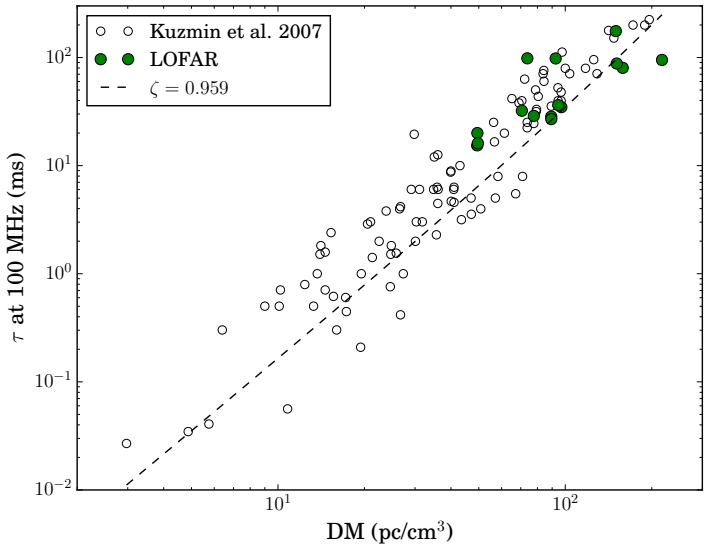

Figure 6.15: The relationship between DM values and τ at 100 MHz, as obtained from the Kuzmin & Losovsky (2007) dataset (empty circles) and the LOFAR dataset in this paper (green circles).

6.7 Scattering time versus DM and distance

I now revisit the scattering time (τ) dependence on DM. An empirical relationship between these quantities, valid for over 10 orders of magnitude in scattering times, and DM values between 1 and 1000 pc cm^{-3}, was published by Bhat et al. (2004). The measurements were based on a dataset of 98 low Galactic latitude sources, using the Arecibo telescope at frequencies between 430 MHz and 2380 MHz. A parabolic function, $\log \tau = a + b \log \mathrm{DM} + \mathrm{c} (\log \mathrm{DM})^2$, is fitted to their data. Alternatively, power laws of the form $\tau \propto \mathrm{DM}^{\gamma}(1 + \kappa\, \mathrm{DM}^{\zeta})$, where γ is fixed at 2.2, as determined from a Kolmogorov spectrum, have been used (Ramachandran et al., 1997, Löhmer et al., 2004).

Fig. 6.14 shows my fits to an ensemble of τ values at 1 GHz versus DM values. I used my obtained IM α values to transform τ values to 1 GHz. The datasets of Löhmer et al. (2001, 2004) and L15b are also shown, along with their obtained fits. The excluded data points from L13 and L15 are shown as grey stars. The LOFAR data points from this work are shown as green (dark) circles.

It is clear that the fitted trends obtained by me, L13 and L15 at low DM values, promote higher τ values than originally proposed by the Bhat et al. (2004) fit. My fit indicates even larger τ values at the low DM values than L13 and L15. My parameter

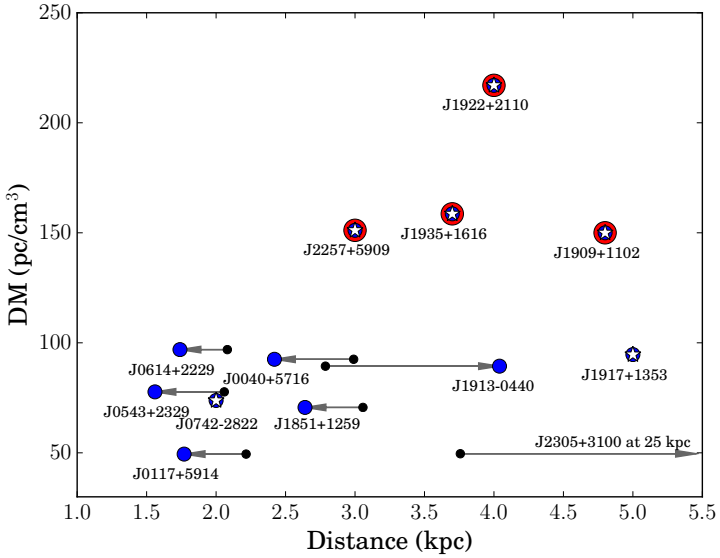

Figure 6.16: The relationship between DM and the distances for the dataset. The DM values of the majority of these pulsars are less than 100 pc cm^{-3}. The blue (small) circles indicate the distances as estimated by the YMW16 model (Yao et al., 2017) or from associated objects (see Table 5.1). Arrows starting from black dots indicate the change in distance estimates from the NE2001 model (Cordes & Lazio, 2002) to the YMW16 model. The data point for PSR J2303+3100 is excluded as it lies far to the right. There are four clear outliers to the typical distance versus DM trend, shown as large circles with red outlines. These high DM values could indicate a more dense and complex ISM along the lines of sight to these sources. Pulsar for which DM-independent distance measurements exist, are marked with white stars.

fits, compared to L15, are $a = -5.0$ (L15, $a = -6.3$), $b = 1.9$ (L15, $b = 1.5$) and $c = 0.1$ (L15, $c = 0.5$). From the power law fits, Ramachandran et al. (1997) and Löhmer et al. (2004) obtained $\zeta = 2.5$ and 2.3, whereas L15 find $\zeta = 1.74$ and I find $\zeta = 1.67$.

If indeed the Bhat et al. (2004) relationship is considered a true reflection of the τ dependence on DM at higher frequencies (e.g. 1 GHz), then my result shows that in order for the relationship to be upheld, the low spectral index values that I have measured at low frequencies, can not persist up to higher frequencies. To reach the Bhat et al. (2004) dependence at higher frequencies with this set of pulsars, their spectral index will need to evolve with frequency. Access to broadband data at higher than LOFAR frequencies for these pulsars, where scattering is still measurable, will allow us to investigate whether spectral indices indeed change.

Fig. 6.15 shows a similar plot of τ versus DM, but for τ at 100 MHz. Here I find $\zeta = 0.96$, much lower than in Fig. 6.14. The plot shows that my obtained values are in good agreement with the Kuzmin & Losovsky (2007) dataset, and again argues for a frequency dependent α.

In Fig. 6.16 the relationship between the distance and DM for the sources in this paper is shown. Arrows indicate the changes in distance estimates from the NE2001 electron density model (Cordes & Lazio, 2002) to the YMW16 model (Yao et al., 2017). The majority of the sources have DM values below 100 pc cm^{-3}. There is no clear increase of DM with distance. Four pulsars are clear outliers on this plot, having higher DM values than the rest of the set. This could point to more complex and dense ISM environments along the lines of sight to these pulsars. In Section 5.2.11 we pointed out that the line of sight to PSR J1935+1616 has been considered anomalous in the literature (Löhmer et al., 2004). Three of the four outliers have been discussed in Section 6.6 as pulsars with wrap around scattering tails. The fourth pulsar is PSR J1922+2110, which together with PSR J1909+1102 has the largest τ_{150} value of 42 ± 2 ms (IM, Table 6.2). Its low frequency profiles along with the flux density spectrum reveal that pulses will likely start overlapping at frequencies just below the lowest observed frequency channel of 112.5 MHz.

Chapter 7

Applications and Ongoing Projects

The pulsar scattering analyses conducted in this thesis, along with the code developed in Chapter 4, have led to several other side projects – the status of which I will describe in this chapter. The projects are summarised as follows. Sec. 7.1 investigates the scattering towards the Galactic Centre magnetar SGR J1745−2900. Sec. 7.2 describes a scattering analysis of the giant pulses of the Crab pulsar. This project formed part of Scott England's MPhil project at Oxford University, under the supervision of Dr. Aris Karastergiou. Lastly, Sec. 7.3 discusses a collaborative project with Dr. Mark Walker from Manly Astrophysics in Sydney, Australia. The project considers joint constraints on the gas structure of the IISM through Far-Infrared spectroscopy and pulsar propagation observations.

7.1 Anomalous Scattering at the Galactic Centre

In Sec. 2.2.3, I reviewed evidence for anomalous scattering in the IISM. The Galactic Centre (GC) environment has produced one of the greatest mysteries in the field of pulsar scattering. Here, I provide a more detailed overview of the GC pulsar scattering anomaly. I propose a simple model of small extreme scattering surfaces, and consider whether this model can reproduce the observed discrepancies in the scattering of the GC magnetar, SGR J1745−2900.

7.1.1 Background and Motivation

Large stellar clusters are found within the GC, with observations of over 100 young massive stars within 1 to 10″ (or 0.04 to 0.4 pc) of Sgr A*, the central supermassive black hole (Paumard et al., 2006, Lu et al., 2009). These clusters host early-type (OB) stars that are considered typical progenitors to neutron stars (Genzel et al., 1997,

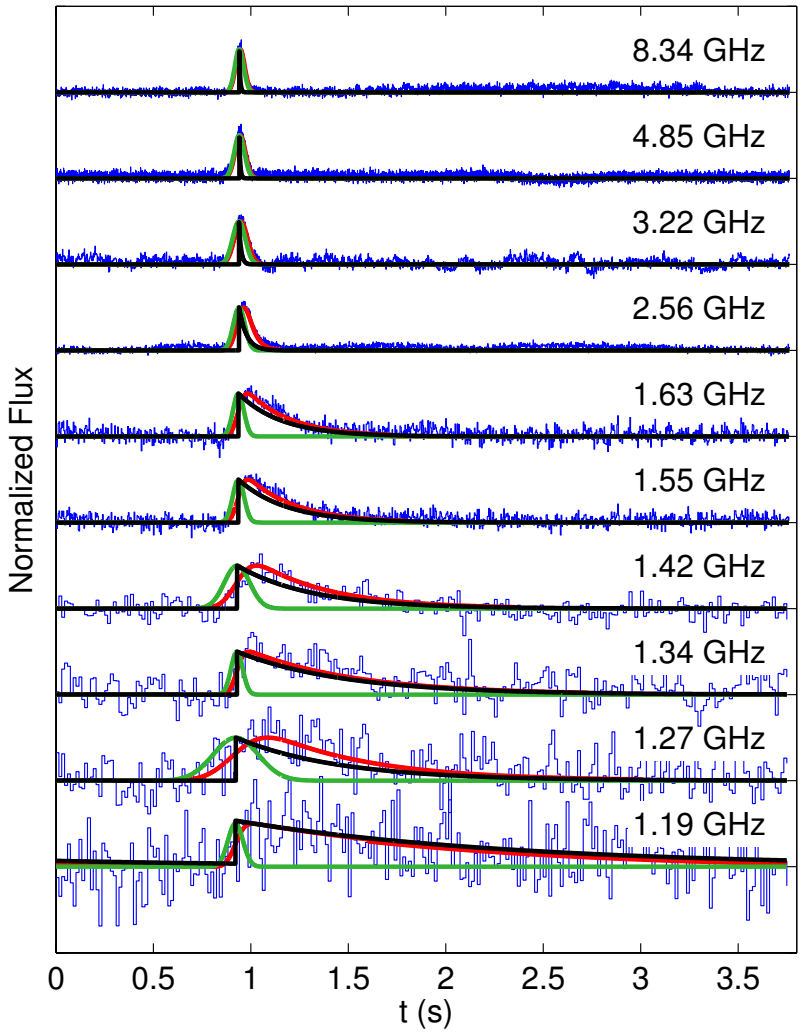

Figure 7.1: Scatter broadened pulse shapes of the GC magnetar, as published in Spitler et al. (2014). The blue curves are the measured profile. The red, green and black lines are the best fitted profile, best-fit Gaussian profile and the scatter broadening function respectively.

Ghez et al., 2003). As described in Sec. 1.1.1, stars of masses 8 to 20 $M_\odot$ have an expected lifetime of approximately 10^7 yrs, after which they collapse to form neutron stars. The presence of these massive star clusters, therefore creates the expectation that a neutron star population, and by extension a pulsar population, should reside in the GC.

Pfahl & Loeb (2004) predicted a pulsar population of 100 to 1000 pulsars in orbits around Sgr A* with orbital periods less than 100 yrs (i.e. at orbital projections < 0.02 pc) and ages less than 10^8 yrs. More recently, Chennamangalam & Lorimer (2014) predicted an upper limit of 200 pulsars in the inner parsec.

Despite these predictions, surveys over the years, as mentioned in Sec. 2.2.3, have not been successful at finding any normal radio pulsar at the GC (e.g. Kramer et al. 2000, Deneva et al. 2010, Macquart et al. 2010, Bates et al. 2011). The failure to find pulsars in the GC, was initially thought to be due to the extremely dense IISM environment surrounding Sgr A*, which has a suggested temperature of $T \sim 10^6$ K and an electron density $n_e \sim 10\text{cm}^{-3}$ (Lo & Claussen, 1983, Lazio & Cordes, 1998, Muno et al., 2004, Genzel et al., 2010). The NE2001 electron density model predicts a scattering time scale of $\tau = 2300$ s at 1 GHz towards the GC (Cordes & Lazio, 2002, Spitler et al., 2014). As such, pulsar signals towards the GC were thought to be scattered out and therefore not observable.

This picture changed significantly in 2013, with the discovery of a radio magnetar, SGR J1745−2900, at a projected distance of 0.1 parsec from the GC in 2013 (Eatough et al., 2013). The source was originally detected as an X-ray flare by the *Swift* observatory (Degenaar et al., 2013, Kennea et al., 2013), and then shown to repeat with a spin period of 3.76 s by NuSTAR (Mori et al., 2013). Radio pulsations of this source were thereafter detected at frequencies ranging from 1.2 to 18.95 GHz (Spitler et al., 2014). The estimated DM value for the source is 1778 ± 3 pc cm^{-3}, and the rotation measure (Sec. 2.1.2), -66960 ± 50 rad m^{-2}, is the highest RM value for any known pulsar. Eatough et al. (2013) suggested the RM is consistent with a large magnetic field pervading the plasma surrounding the supermassive black hole.

Surprisingly however, the observed scattered profiles (shown in Fig. 7.1) were measured to have a scattering time of 1.3 s at 1 GHz, much less than predicted by the scattering models (Spitler et al., 2014). Bower et al. (2014) obtained the first Very Long Baseline Interferometric (VLBI) image of the GC magnetar, and measured an angular size of approximately $\theta = 130$ mas at 8.7 GHz, similar to that of Sgr A* itself.

Combining the measurement of the scattering tail with the scatter broadened image of SGR J1745−2900, and the overall distance to the GC ($D = 8.3 \pm 0.3$ kpc),

uniquely fixes the distance to the scattering screen from the source to $D_s = 5.9 \pm 0.3$ kpc. This large D_s estimate means the scattering surface is not associated with the GC, but speculated to be part of the Scutum spiral arm of the Milky Way (Bower et al., 2014).

Furthermore, considering that magnetars are more rare than both normal and millisecond pulsars (Olausen & Kaspi 2014, Sec. 1.1.3.2), this discovery was thought to increase the statistical chances of discovering GC pulsars.

If indeed the typical pulsar scattering in the GC is as low as measured for the magnetar, and if the discovery argues for the presence of a GC pulsar population, it raises several questions. Firstly, where are all the pulsars (Dexter & O'Leary, 2014) and why were the previous surveys of the GC not successful in discovering them? And secondly, why is the IISM environment around the GC not as dense and scattering inducing as we previously expected(Cordes & Lazio, 2002)?

7.1.2 Two screen scattering model for SGR J1745−2900

I tested a model that would retain the hyper-scattering conditions around the GC, while simultaneously accounting for the measured scattering parameters. The model makes use of finite scattering screens, which can lead to a patchy IISM around the GC. Assuming that magnetars are significantly brighter than typical pulsars at survey frequencies (Camilo et al., 2008, Levin et al., 2010), this model can also explain how magnetar detection is favoured in the GC.

The model adapted consists of two scattering phases: an initial *hyper-scattering* surface close to the GC, followed by a second weaker scattering surface mid-way to the observer, which as suggested by Bower et al. (2014) could be part of the Scutum spiral arm of the Milky Way.

7.1.2.1 The hyper-scattering screen surrounding the GC

The first scattering surface is modelled as a thin screen with a finite size, similar to the scattering discussed in Sec. 2.2.1.1. I find that for a combination of large scattering strength values (κ in $\sigma_a = \kappa\,\nu^{-2}$, Sec. 2.2.1.4), and small screen diameters, IISM scattering can lead to significant observable flux losses but no scattering tail in the pulse profile.

The hyper-scattering screen described by the NE2001 model is located close-in, at a distance of 133 pc from the GC, and predicts $\tau = 2300$ s at 1 GHz (Lazio & Cordes, 1998, Cordes & Lazio, 2002). Using Eq. (2.28), I calculate σ_a at 1 GHz, such

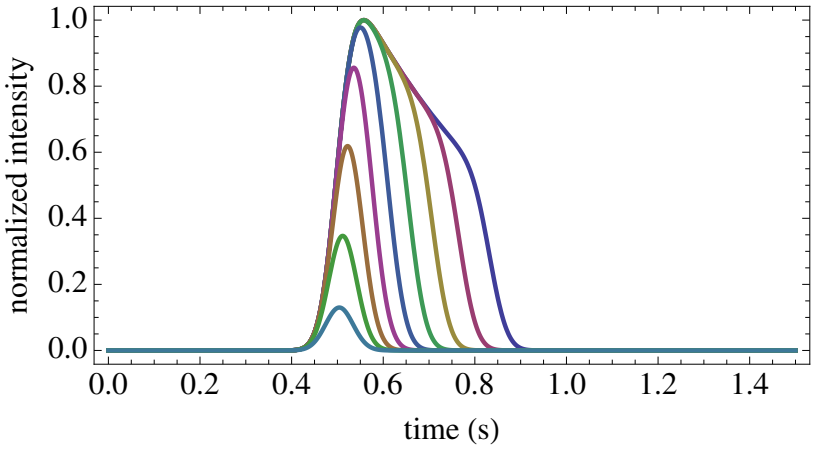

Figure 7.2: Broadened pulse shapes at 8.7 GHz that have been hyper-scattered by truncated screens of varying sizes ranging from 30 AU to 190 AU in increments of 20 AU. The pulse shape escaping the largest screen is plotted here to have an amplitude of 1 with the others normalised accordingly. The flux falls by a factor of approximately 2 (190 AU) to 50 (30 AU) at 8.7 GHz compared to an infinite screen as the size decreases. At lower frequencies the flux loss will be more extreme. At 1.4 GHz the truncated screens will induce a loss of a factor of approximately 1800 to 72 000 for the smallest (30 AU) and largest (190 AU) screens considered here.

that for $D = 8.5$ kpc and $D_s = 133$ pc, $\tau = 2300$ s. I find that $\sigma_a = 85184$ mas, and consequently $\sigma_\theta = 1333$ mas at 1 GHz. These values are similar to angular broadening measurements of GC sources in the literature, namely 700 mas at 1.4 GHz (1372 mas at 1 GHz, Lazio & Cordes 1998) and 525 mas at 1.612 GHz (1364 mas at 1 GHz, van Langevelde et al. 1992).

I obtain broadening functions, using a frequency dependence of $\sigma_a = (85184 \text{ mas})\, \nu^{-2}$, and the functional form of Eq. (2.27). These are turned into broadening functions associated with truncated scattering screens, using Eq. (4.3), with t_{max} the largest temporal delay corresponding to θ_{max}, the angular size of the finite screen (Cordes & Lazio, 2002, Geyer & Karastergiou, 2016). This truncation model describes a circularly truncated screen, with the pulsar aligned with the centre of the (disk-shaped) screen.

Fig. 7.2 shows the average broadened pulse shapes, resulting from the convolution of an intrinsic Gaussian pulse train with the truncated broadening function of Eq. (4.3). The intrinsic pulse has a period of 3.76 s and a pulse width of 0.03 s to match the observations of the GC magnetar (Spitler et al., 2014). The observing frequency is fixed at 8.7 GHz, while the radial extent of the screen is varied from 30 AU to 190 AU. The intrinsic pulse is modelled to have an integrated flux of unity. Similarly, the broadening function is normalised to 1 when integrating over the full

time domain (t = 0 to ∞). Therefore, in the limit where this pulse is convolved with an infinite screen, the flux is conserved and equal to unity. The flux loss associated with these truncated screens ranges from 2 (190 AU) to 50 times (30 AU) at 8.7 GHz, compared to the conserved flux when the signal passes through an infinite screen at this frequency.

Fig. 7.2 shows that it is possible for an intrinsic Gaussian magnetar signal to pass through the truncated screen ($\lesssim$ 110 AU), escaping with roughly Gaussian properties (i.e. with no measurable scattering tail), but with significantly diminished flux. These attenuated pulse shapes will next undergo weaker scattering as they travel through the IISM before being detected terrestrially.

7.1.2.2 Second phase of 'traditional' scattering

The second phase of scattering introduces the characteristic scattering time scale, $\tau = 1.3$ s at 1 GHz, as measured by Spitler et al. (2014). For this purpose, I model an infinite scattering screen which lies halfway between the hyper-scattering screen and the observer, i.e. $D = 8.5 - 0.133$ and $D_s = 5.9 - 0.133$ kpc. This equates to a scattering strength of $\sigma_a = 507$ mas ν^{-2}, approximately 170 times weaker than the close-in hyper-scattering screen.

The result of the second convolution is shown in Fig. 7.3 for the frequencies at which detections were made with the Effelsberg 100-m Radio Telescope, the Nancay Decimetric Radio Telescope and the Jodrell Bank Lovell Telescope. The figure shows how the results from Spitler et al. (2014) can be reproduced using the correct size truncated screen.

7.1.3 The detectable GC pulsar population

Magnetars are a rare class of object, with 29 known sources of which, up to now, only four are observed in the radio spectrum[2] (Olausen & Kaspi, 2014). The flux spectra of the radio emitting magnetars are remarkably flat (Camilo et al., 2007, Levin et al., 2010), different to, as described in Sec. 1.1.4, normal pulsars that typically have steep flux spectra ($S_\nu \propto \nu^{-1.4}$). This means that magnetars can be considerably brighter than pulsars at higher frequencies.

The two phase scattering model described above, can therefore provide a simple explanation for why we detect magnetars rather than more common radio pulsars: the hyper-scattering screens create a patchy IISM structure that attenuates the observed flux of escaping radio emission. At high frequencies this means only the brighter

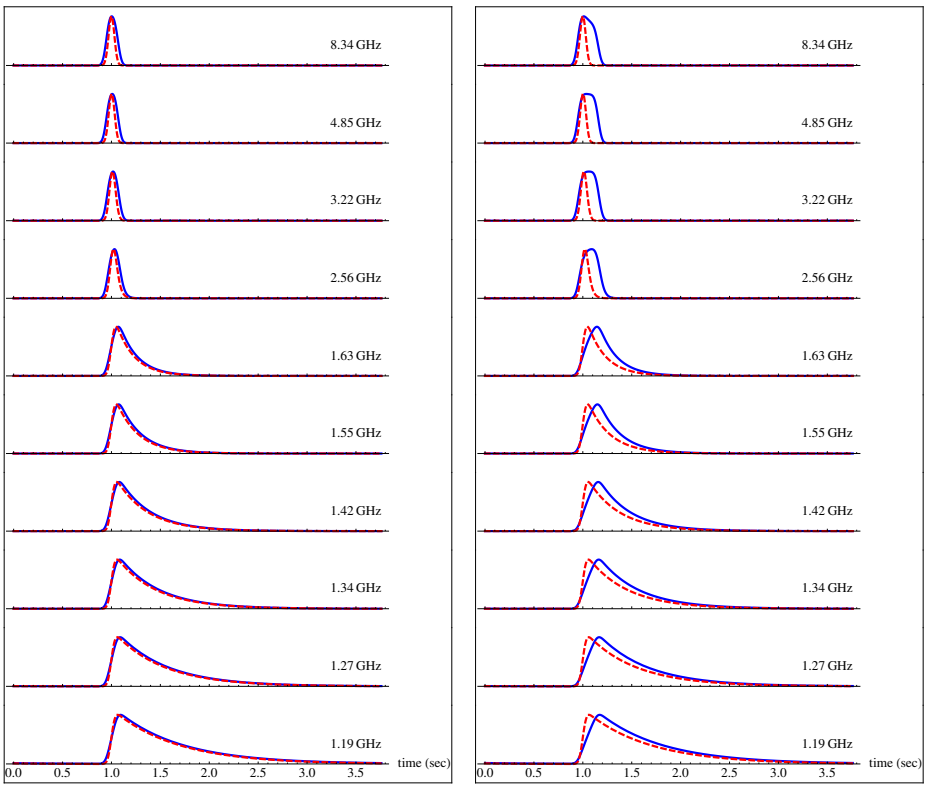

Figure 7.3: Modelled scattered pulse profiles of SGR J1745−2900 at frequesncies that match the Spitler et al. (2014) observing frequencies. Blue curves: Broadened pulse shapes that have first undergone close-in hyper-scattering ($\tau \approx 2300$ s at 1 GHz) by a truncated screen of radial size 110 AU (*left*) or 150 AU (*right*) and thereafter undergo more typical Galactic scattering ($\tau \approx 1.3$ s at 1 GHz) via an isotropic infinite screen. The intrinsic pulse has a period of 3.76 s and a pulse width (σ) of 0.03 s. This corresponds very well to Fig. 2 in Spitler et al. (2014). The red curve shows broadened pulse shapes for a pulse that has only undergone Galactic scattering with a characteristic time scale of $\tau = 1.3$ s at 1 GHz. The y-axis is normalised intensity. All the pulse shapes have been normalised to the same amplitude of unity.

magnetars will be observed. At low frequencies, where pulsars are brighter, the scattering and consequently flux attenuation effects are more severe, making their detection less likely.

Starting with a GC population of a given size ($N_{\rm GC}$), I compute the required flux dilution to obtain the null result of pulsar surveys in the GC. I firstly assume that the luminosity distribution of the Galactic field pulsars is representative of the pulsars in the GC, similar to in Chennamangalam & Lorimer (2014). The radio luminosity distribution of pulsars follows a log-normal distribution as described in Faucher-Giguère & Kaspi (2006).

I pick $N_{\rm GC}$ luminosities from this distribution at 1.4 GHz, and convert them to flux densities at the GC,

$$S_{1.4\,\rm GHz} = \mathcal{L}/D^2, \tag{7.1}$$

where $\mathcal{L}$ is the luminosity value, and D the distance to the GC. Assuming the spectral index distribution of the $N_{\rm GC}$ pulsars is drawn from the normal distribution presented in Bates et al. (2013), I estimate the flux densities of the $N_{\rm GC}$ pulsars at 8.5 GHz and 14.4 GHz, where pulsar surveys of the GC have previously been conducted. The Deneva et al. (2010) survey at 8.5 GHz had a sensitivity of $S_{min} = 23$ μJy and the Macquart et al. (2010) survey at 14.4 GHz a sensitivity of $S_{min} = 31$ μJy. Both found no GC pulsars.

I label pulsars for which the $S_\nu > S_{min}$ as detectable. The aim is to drown out all the detectable pulsars using flux attenuation caused by small scattering screens. Fig. 7.4 shows how the required flux dilution factor scales with GC pulsar population size. The top figure shows the results using the frequency and sensitivities to match the Deneva et al. (2010) survey. The bottom figure shows the results for a study at 14.4 GHz, both matching the sensitivity of the Macquart et al. (2010) survey, and with an increased sensitivity of 10 μJy. A maximum dilution factor of 20 and 60 is respectively required to obscure a population size of 1000 in this way, depending on the sensitivities and frequencies.

The required flux attenuation by a truncated scattering screen can be obtained by a combination of the size of the screen and the scattering strength, κ. Here, I express this scattering strength in terms of the value of τ at 1 GHz for an equivalent infinite screen using Eq. (2.28),

$$\kappa = \sqrt{\tau_{\rm 1GHz}\ c/\ D'_s}, \tag{7.2}$$

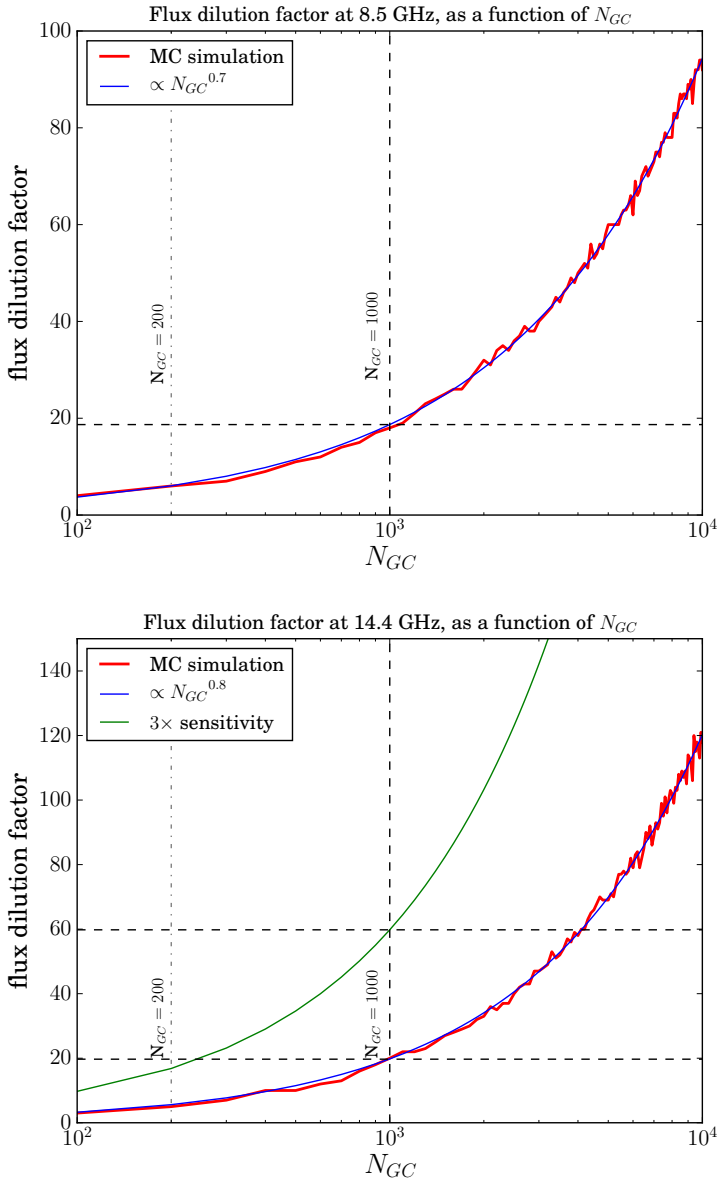

Figure 7.4: *Top:* Flux dilution factor at 8.5 GHz as a function of $N_{\rm GC}$, using the Deneva et al. (2010) sensitivity of 23μJy. The red line is the result of the Monte Carlo (MC) simulation, and the blue line a best fit to the MC result. *Bottom:* Similar to the top panel, but simulated at 14.4 GHz, both with a sensitivity that matches that of the Macquart et al. (2010) survey (31μJy, red and blue) and with an increased sensitivity of 10μJy (green).

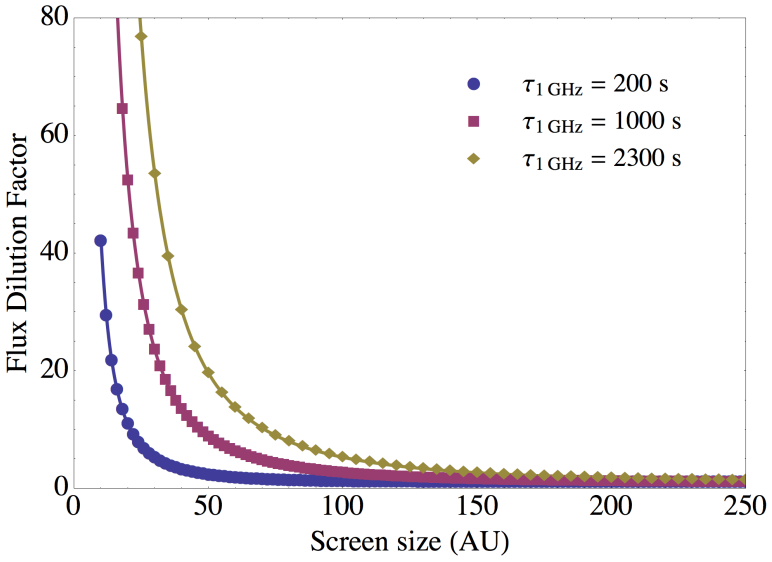

Figure 7.5: The scattering screen flux dilution factor as a function of the screen size (in AU) of the close-in scattering screen, and the scattering strength of the screen, defined in terms of the τ value associated with the broadening function at 1 GHz.

where D'_s depends on $D = 8.25$ kpc and $D_s = 133$ pc as before. Having computed σ_a at 1 GHz in this way, I transform to 8.5 GHz to relate back to (the top panel of) Fig. 7.4. I use three values of expected τ at 1 GHz: $\tau = 2300$ s, based on the NE2001 model, $\tau = 200$ s, an order of magnitude smaller, and an inbetween value of $\tau = 1000$ s. Fig. 7.5 shows the dependence of flux dilution on the radial screen size.

In order to achieve a flux dilution factor of around 20 while maintaining the NE2001 model scattering estimate of $\tau_{1\mathrm{GHz}} = 2300$ s, pulsars in the GC need to be scattered by close-in screens of around 50 AU. For smaller initial pulsar populations in the GC, say of size 200 (Chennamangalam & Lorimer 2014, dash-dotted line Fig. 7.4), the required flux attenuation is only a factor of 5, which can be achieved at these frequencies with larger typical scattering surfaces.

7.1.4 The failures of the model

This two phase scattering model, however, is unable to explain all of the observed phenomena. The biggest conflict comes from the broadening measurements conducted by Bower et al. (2014). The authors measured similar angular broadening measurements for both Sgr A* and the GC magnetar, and concluded that both sources reside behind the same scattering surface. At an estimated projection of 0.1 pc to SgrA* this would require a scattering surface of at least $\sim$ 20,000 AU, much larger than the disk-shaped screens required to attenuate the observed pulsar population.

A recent paper by Bower et al. (2015) published a transverse velocity of 236 km s^{-1} for the magnetar. The direction of the motion is shown to be consistent with a bound orbit in the clockwise disk of massive stars orbiting Sgr A*.

The maximum time the high velocity magnetar can feasibly hide behind a scattering surface of radial size 50 to 100 AU is between 2 and 4 years. Having been discovered in 2013, that means observations of the magnetar should become brighter (by a factor of $\sim$ 20 at 8.5 GHz) by 2017, as it escapes this truncated screen. Unless, of course, the velocity of the finite screen is moving in the same direction as the magnetar. I have not been able to find observations of the source taken in 2017, to test whether significant changes in its luminosity have been observed.

Furthermore, the model needs to address how many screens are required to create a patchy IISM structure around the GC, which causes flux attenuation of the central pulsars while not leading to too many *scatter free* lines of sight, along which we would have observed them by now. A too high concentration of small screens would in principle recreate an average infinite screen, which is in contradiction with the distance estimate to the dominating screen at 5.9 kpc.

7.1.5 Discussion

The GC pulsar population and the possible complex IISM structure in this environment, is an area of ongoing research. Many different theories have been proposed to solve the *missing pulsar* problem and to address the issue of discovering a magnetar first.

The suggestions include that the GC pulsar population is distinct from the Galactic field population and tends to produce magnetars, with young magnetars thought to be the earliest form of pulsars produced in the GC (Dexter & O'Leary, 2014).

Alternatively the GC has been considered to favour millisecond pulsar (MSP) production (Bartels et al., 2016). MSP signals, due to their much smaller intrinsic pulse widths than normal pulsars, will be scattered out completely by the dense IISM in the GC, and are therefore not detected. Bramante & Linden (2014) argued that dark matter interactions with neutron stars would collapse most neutron stars to black holes, such that pulsars are destroyed.

Ultimately, the GC scattering anomaly will only be solved through higher sensitivity surveys that manage to uncover (or refute) a GC neutron star population, and study its peculiarities.

7.2 Scattering of the Crab pulsar's giant pulses

This section of work relates to the MPhys project of Scott England, who completed his project with Dr. Aris Karastergiou in Hilary Term 2017. The project analyses the scattering of giant pulses in the Crab pulsar. To assist with this work, I developed a modified version of the scattering fitting code used in Chapter 4 and 5. I present a brief overview of the motivation, methods and results of this project here.

7.2.1 Background

The Crab pulsar, B0531+21, is the archetypal young pulsar, and the youngest known pulsar. Resulting from a rapid birth spin period, the Crab pulsar has a current period of 33.4 ms and a high spindown rate of $\dot{P} = 4.3 \times 10^{-13}$. These attributes make it an outlier on the P-$\dot{P}$ diagram (Fig. 1.3). Its association with the supernova explosion of 1054, as mentioned in Sec. 1.1.1, provides a direct measurement of its age.

The emission mechanism of this young pulsar, is exceptional in many ways. It has been detected across an extensive frequency range, including radio, optical, X-rays and gamma rays (Moffett & Hankins, 1996). Moreover, its radio emission often gives raise to giant pulses. These are pulses with extreme intensities, between 100 – 1000 times the intensity of a typical pulse, and intrinsic pulse widths of less than a nanosecond (Hankins et al., 2003, Hankins & Eilek, 2007).

The Crab pulsar has a DM of 56.8 pc cm^{-3} and is embedded in its associated supernova remnant at a distance of $D = 2.0$ kpc from Earth. As described in Sec. 1.1.1, the Crab pulsar is measured to have a high proper motion, with a transverse velocity of approximately 120 km s^{-1} (Kaplan et al., 2008). The combination of its high proper motion and the gaseous environment it is embedded in, creates an expectation of complex and dynamic IISM imprints on the observed pulse profiles. It is also suited to a two-phase scattering process, with the first scattering imprint associated with the nebula and the second associated with the integrated IISM along the remaining line of sight (e.g. Rankin & Counselman 1973).

This study considers the profile shapes of the Crab giant pulses at 145 MHz. Access to the pulse shapes of these bright giant pulses, at low frequencies where they appear scatter broadened, provides us with the opportunity to analyse the characteristic scattering times of individual pulses, rather than averaged pulse shapes (as in the case of the LOFAR data in Chapter 5). In this way, instantaneous scattering is measured, such that many measurements over several epochs of observations provide

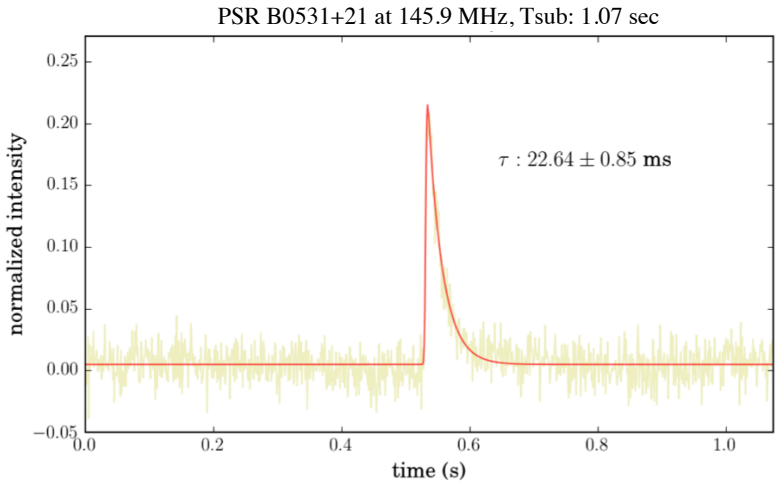

Figure 7.6: An example of a giant pulse from the Crab pulsar and the resulting scattering model fit.

insight into the timescales over which the scattering environment in the Crab nebula is changing.

7.2.2 Data and Methods

Data were collected using the Rawlings Array at the Chilbolton Observatory, one of the LOFAR international stations. The station has 96 tiles of HBA antennas. Data of the Crab pulsar were recorded by Dr. Aris Karastergiou at 145 MHz with a bandwidth of 6 MHz over a period of 4 years (2014 – 2017). The data form part of a radio transient survey that runs most weekends at this station. As such, observations were collected when, during these weekend drift scans, the Crab transitted through a search beam.

At the time of analysis, 20,000 observing files, each representing an observation of just over a second ($T_{sub} = 1.074$ s) with a phase resolution of 1024 bins per T_{sub}, had been recorded. I adapted the scripts used in Chapter 4 and 5 to fit multiple sub-bands with a similar scattering method at a single frequency, producing diagnostic plots for Scott England to analyse. He identified single pulses for which the S/N$>$ 5, while rejecting files containing multiple giant pulses that were not well separated from each other, or high levels of RFI. Fig. 7.6 shows a typical example of a scattered giant pulse, fitted with the scattering model.

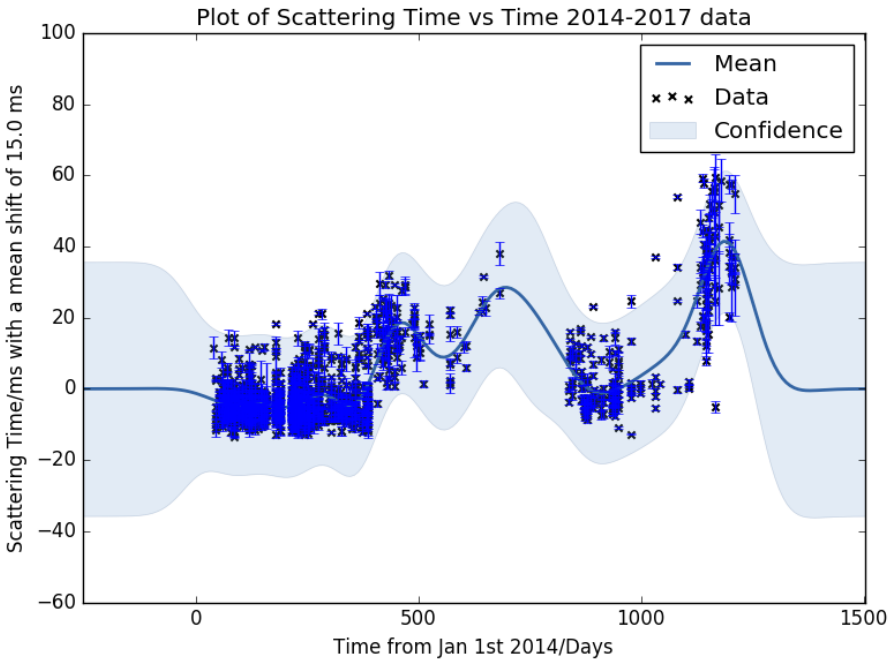

Figure 7.7: Evolution of measured τ values over a period of 4 years, starting on January 1st, 2014. The mean τ value of the sample (15 ms) has been subtracted from the data points, such that the plotted τ values have a mean of zero. Taken from Scott England's MPhys report.

7.2.3 Results

Fig. 7.7 shows the obtained τ values (expressed in relation to the mean τ, as described in the caption) as a function of observing day. The variations in τ are fit with a regression model, similar to the Gaussian Process (GP) regression described in Brook et al. (2016). The main benefit of such models is that they do not take a functional fitting form as an input, but allow the data themselves to inform the fit. For more details on GPs for time series modelling and or the kernel used in this study, refer to Roberts et al. (2012) and Scott England's MPhil report respectively.

The overall mean value of τ is calculated to be 15 ms. For the first 400 days, the fitted τ values are close to this estimated mean, thereafter the τ value increases up to 6 times its mean value from around the start of 2017 (day 1000) to the more recent observations (day 1250). The very last observations seem to show the onset of a decreasing τ value again. The smooth fitted GP model suggests a τ variability scale of 73.3 days.

Scott England estimated, using Eq. (2.28), that for a midway scattering screen, the obtained σ_a lie between 1" and 5". This is larger than, for example, the σ_a values

that range between 1 – 10 mas at 1 GHz, as quoted in Cordes & Lazio (2001) for observations at $D \sim 3$ kpc. Tranformed to an observing frequency of 145 MHz, this gives $\sigma_a = 0.05'' - 0.5''$.

These values suggest that the measured scattering is dominated by the nebula, acting as a close-in scattering screen, and that the variability in the τ measurements is due to overdensities in the nebula and the relative motion between the pulsar and the nebula. To estimate the scale sizes of such overdensities I calculate the average distance covered (transversely) by the pulsar over 70 – 100 days. Kaplan et al. (2008) quoted a transverse velocity of 120 km s^{-1}. Over 70 – 100 days this corresponds to a size scale of 4.9 to 6.9 AU.

7.2.4 Discussion

The results for this Crab dataset show that the τ values associated with its giant pulses, vary on timescales of approximately 70 days. We observe changes in the mean value τ of up to a factor of $\sim$6 over the last several hundred days. If associated with scattering in the nebula, it is likely that the pulsar is passing behind an over-density, with a transverse size of a few AU.

Similar changes in scattering time scales have been observed in the Crab before, specifically related to data taken between 1969 and 1975 at the Arecibo observatory (Rankin & Counselman, 1973, Isaacman & Rankin, 1977). The first 21 months of this dataset were analysed by Rankin & Counselman (1973), who obtained estimates for two scattering timescales associated with the variable nebula and constant IISM contribution respectively. At 100 MHz the authors found a fixed scattering time scale of approximately 6.2 ms and a characterisitc scattering timescale associated with the nebula varying between 0 and 19 ms at 100 MHz. Analysing the full 58 month dataset, Isaacman & Rankin (1977) found a somewhat smaller constant scattering scale of 2.5 ms, and a variable scale ranging from 10 to 25 ms.

If I associate the obtained mean estimate of 15 ms with the average scattering in the IISM and the maximum excess ($\sim$ 60 ms) with the maximum scattering in the nebula, I can translate these time scales to 100 MHz, using a spectral index of $\alpha = 3.5$ (Bhat & Gupta, 2002), to compare our results to the literature results above. This leads to a constant time scale of 4.1 ms and a maximum nebula scattering timescale of 16.3 ms at 100 MHz, similar to the ranges of values given above.

Additional observations by Lyne & Thorne (1975) at frequencies of 408 MHz and 610 MHz revealed an increase of scattering times with up to two orders of magnitude over approximately 4 months, i.e. $\sim$ 100 days.

Continued observations of the Crab at 150 MHz over weekends, with the Rawlings Array at the Chilbolton Observatory, will enable us to analyse the variability of τ in more detail, and will reveal whether the variability timescale of ~ 70 days obtained here, is maintained. Further analysis can improve our detailed understanding of the Crab nebula providing insight into the characteristic size scales and shapes of the over-densities in the nebula.

7.3 The Structure of the WIM and comparisons to pulsar propagation effects

This section describes a project that I am currently working on with Dr. Mark Walker from Manly Astrophysics in Sydney, Australia. A subset of this section will form part of our paper, in preparation. Dr. Walker has developed the theoretical modelling for this project, whereas I have conducted the numerical analysis using the CHIANTI database[9](Dere et al., 1997). For uniformity, I will write using 'we' throughout. As much of this work forms part of current investigations, I describe the motivation and model here, along with only preliminary statements.

7.3.1 Motivation

The project was born from recently published electron density values by the Far Infrared (FIR) community, that were significantly larger ($n_e = 10 - 50$ cm^{-3}, Goldsmith et al. 2015) than the electron densities typically associated with an average line of sight through pulsar dispersion measures ($\langle n_e \rangle \lesssim 0.1$ cm^{-3}, Sec. 1.3).

These new estimates were obtained by a *Herschel* survey of the Galactic plane at FIR frequencies. In particular the Photoconductor Array Camera and Spectrometer (PACS) onboard the *Herschel Space Observatory*, conducted spectroscopic observations of the [NII] 122 μm and 205 μm and the [CII] 158 μm emission lines, across the Galactic plane. The measured intensities of these sets of lines are highly correlated, and allow for estimates of electron densities along a given line of sight, as described in more detail in Sec. 7.3.3.1.

The *Herschel* observations indicate that dense plasma, with $n_e \sim 30$ cm^{-3}, is widespread, motivating us to reconsider the physical conditions in the IISM.

In Chapter 1, Sec. 1.2, I described how an original understanding of the properties of the IISM was developed through studies of optical emission lines (Reynolds et al., 1973). These early studies concluded that the observed optical emission lines were mainly coming from a diffuse warm plasma, with temperatures of T= 8000 K, most often referred to as the warm ionized medium or WIM component of the interstellar medium (Haffner et al., 2009).

By comparing emission measures (EM, Eq. 7.7), with dispersion measures (DM, Eq. 2.2), along particular lines of sight, Reynolds (1991) concluded that the WIM has a low density ($n_e \sim 0.1$ cm^{-3}) and a high filling fraction ($f \gtrsim 0.2$).

[9]http://www.chiantidatabase.org

This conclusion, however, rests on the assumption that both integrals are dominated by the same regions of space, which might not be true if the IISM manifests a broad range in n_e, as suggested by the recent FIR spectroscopy results of Goldsmith et al. (2015). The lower panel of Fig. 7.9 shows their spread in obtained n_e values as a function of Galactic longitude.

This new FIR perspective on the WIM is fundamentally challenging, because the diffuse IISM is characterised, in part, by a typical pressure of

$$P = n_e \times T \sim 3000 \text{ K cm}^{-3}, \tag{7.3}$$

(Jenkins & Tripp, 2011), such that low densities, e.g. $n_e \sim 0.1$ cm^{-3} are expected for a diffuse, fully ionized region. If the WIM densities are actually 100 times larger, as the *Herschel* measurements in Fig. 7.9 suggest for some lines of sight, we immediately face difficult questions about the dynamics – e.g. what confines the gas? Or, if it is not confined, why does it not simply expand until it reaches pressure equilibrium with the ambient medium?

Similar problems have been encountered in studies of pulsar radio-wave propagation in the IISM, where $n_e = 10 - 1000$ cm^{-3} have been inferred from large radio-wave scattering angles and their associated flux modulations (Rickett, 1990, 2011). Various extreme radio-wave scattering (ERS) phenomena have been reported, depending on the nature of the radio source:

- For pulsars: multiple imaging (Cordes & Wolszczan, 1986, Rickett et al., 1997), and parabolic arcs in the secondary spectrum (Stinebring et al., 2001, Cordes et al., 2006), as described in Sec. 2.2.3.

- For quasars: extreme scattering events (Fiedler et al., 1987, 1994, Bannister et al., 2016), and intra-day variability (Kedziora-Chudczer et al., 1997, Dennett-Thorpe & de Bruyn, 2000, Bignall et al., 2003), also described in Sec. 2.2.3.

In most cases the effects are known to be transient, implying that the regions of high plasma density are quite limited in their spatial extent (Kedziora-Chudczer, 2006, de Bruyn & Macquart, 2015). Estimated sizes range from approximately 1 AU to 100 AU (Fiedler et al., 1987, de Bruyn & Macquart, 2015). These are similar size scale as computed in Sec. 6.5 to model LOFAR α distributions from truncated screens, and for the Galactic Centre patchy IISM model in Sec. 7.1.

The incidence of extreme scattering in compact radio quasars is low, around 1 in a 1000 for the most extreme cases of intra-day variability (Lovell et al., 2003), but

the small size of the individual scattering regions means that they must nevertheless be very common – much more numerous than stars, for example. Thus, although the extreme radio scattering phenomena are rare, the plasma structures that cause them are not.

In this work we reconsider conditions in the WIM of the Galaxy. Our aim is to answer basic questions, such as:

Q1: Can the observed emission lines, both optical and FIR, arise from the same gas?

Q2: If so, what are the likely temperatures and densities in that gas?

Q3: Can the same gas also explain the dispersion of radio pulses?

Q4: Can the same gas also explain the ERS phenomena?

Previous studies relating to the properties of the WIM have often assumed that the plasma is energised by UV photons from hot stars (e.g. Mathis 1986). We do not make that assumption, because there are other possibilities both for ionising and for heating the WIM. Low-energy cosmic-rays are, for example, an attractive option (Walker, 2016).

7.3.2 Methods

7.3.2.1 Chianti Database

We use the CHIANTI atomic database to explore emission line characteristics over a range of plasma densities and temperatures, and compare our results to FIR emission line measurements in the literature.

The CHIANTI database was first released in 1997 (Dere et al., 1997). It is a database of atomic energy levels, associated wavelengths and excitation and de-excitation rates for ions abundant in cosmic plasmas. The database provides a computationally easy way of investigating the atomic and spectroscopic properties of optically-thin plasmas. This includes straightfoward calculations of the line emission intensities, ionization rates and level populations of a given species as a function of electron density and temperature. The most recent electron excitation data have been assessed and stored following the method of Burgess & Tully (1992). CHIANTI includes IDL (Interactive Data Language) routines to calculate synthetic spectra, but more recently has also been developed into a PYTHON package, called *ChiantiPy*[10]

[10]http://chiantipy.sourceforge.net

(Landi et al., 2012, Del Zanna et al., 2015). We make use of the *ChiantiPy* implementation.

7.3.2.2 Model for ionized gas distribution

To investigate the constraints from pulsar propagation observations and possibly their combined constraints with spectroscopic results, we construct the following simple model of gas clouds in the IISM. In this model, the electron density is approximately constant, with value $n_e \simeq n_o$, within spherical clouds of radius R, and zero outside them. For simplicity, the space density of those clouds, $\mathcal{N}_c$, is assumed to be uniform within a distance $|z| < Z$ of the Galactic plane, and zero beyond that. For this model the volume filling fraction of the clouds is

$$f = \frac{4}{3}\pi R^3 \mathcal{N}_c \tag{7.4}$$

for $|z| < Z$. In that region, the average electron density is

$$\langle n_e \rangle = f n_o, \tag{7.5}$$

so for a distant target at the Galactic poles we have an electron column $N_e = f n_o Z$, as seen from the midplane. The electron column can be directly related to observations of pulse dispersion, and when expressed in the units $\mathrm{pc\,cm^{-3}}$ is referred to as the dispersion measure (DM), as previously also expressed in Eq. (2.2),

$$\mathrm{DM} = \int n_e \, \mathrm{d}s. \tag{7.6}$$

The emission measure, on the other hand, is

$$\mathrm{EM} = \int n_e^2 \, \mathrm{d}s, \tag{7.7}$$

which for our model is just $\mathrm{EM} = f n_o^2 Z$, when evaluated for a distant target at the Galactic poles, as seen from the midplane. Both EM and DM are expected to vary inversely with $\sin|b|$, for Galactic latitude b, in the case of distant targets. The emission measure can be directly related to observations of the strength of emission lines arising from the WIM, as discussed in Sec 7.3.3. For now we simply note a useful fiducial, that the emission measures observed in optical lines at high Galactic latitudes are typically $\sim 1\,\mathrm{pc\,cm^{-6}}$.

The optical depth of the clouds, τ, is the fraction of the sky that appears covered by their boundaries. (Note the use of τ for optical depth here, different from characteristic scattering time as throughout the rest of the thesis.) For our model it is

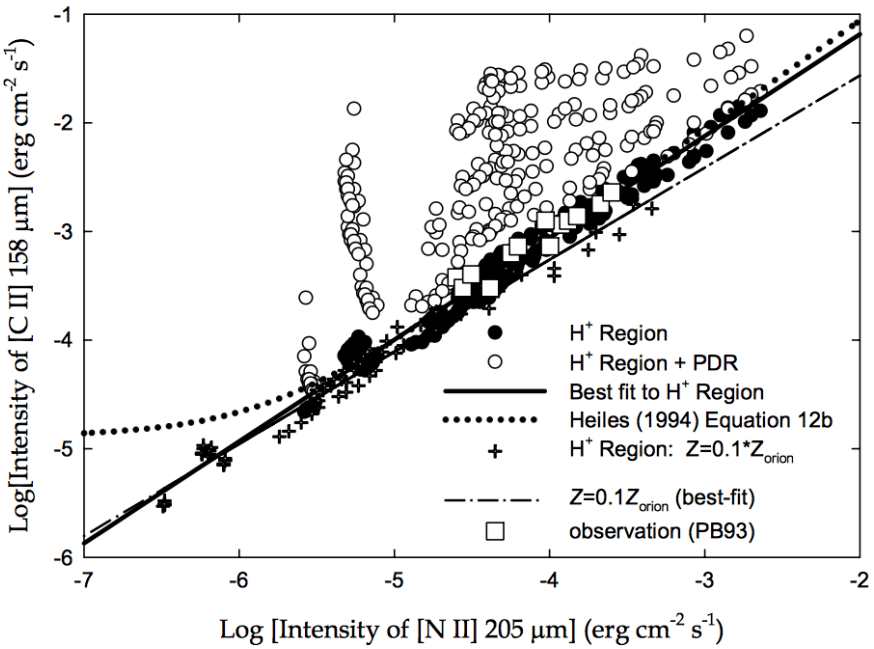

Figure 7.8: Modelled correlation between [NII] 205 μm and [CII] 158 μm lines, taken from Abel (2006).

$$\tau = \mathcal{N}_c \pi R^2 D, \tag{7.8}$$

to distances D that do not extend beyond the cloud distribution. From Eq. (7.4), this can also be written in the form $\tau = (3/4) f D/R$.

In Sec. 7.3.4 we apply the results in two specific cases. First, the case of a uniform distribution of ionized gas, for which we take $f = 1$ and $n_o \to n_u$. Secondly, we consider very dense clouds, such as those inferred by Goldsmith et al. (2015), in which $n_o \to n_g = 30\,\mathrm{cm}^{-3}$, and $f \to f_g$.

7.3.3 Constraints from Spectroscopy

We investigate the possible constraints on the electron density and temperature of the WIM, through FIR and optical spectroscopy results.

7.3.3.1 The [NII] and [CII] FIR emission lines

The ionization potential of nitrogen (14.5 eV) is greater than that of hydrogen (13.6 eV), such that ionized nitrogen lines are expected to be found in highly ionized regions of the WIM only. The nitrogen FIR lines important to this study, are the [NII] 122 μm and 205 μm lines. The [NII] 122 μm line is the transition between energy

levels $^3P_2$ – $^3P_1$, and the [NII] 205 μm is the ground-state transition $^3P_1$ – $^3P_0$. The ratio of the intensities of these two NII lines, provides a direct estimate of the density of the ionized gas and hence the associated electron densities. A low density limit ($n_e \ll 100$ cm^{-3}) with all the nitrogen ions in the ground state produces an intensity ratio of $I([\text{NII}]\ 122\,\mu\text{m})/I([\text{NII}]\ 205\,\mu\text{m}) = 0.7$, whereas in contrast a ratio of approximately 3 is expected for ionized HII regions. The spectrometer on board the *Cosmic Background Explorer* (COBE) measured ratios for these lines ranging from 1.0 to 1.6 (Wright et al., 1991). These ratios were considered evidence for a homogeneous medium of electron densities of ~ 10 cm^{-3} or an inhomogeneous medium with part of the electron density coming from HII regions and part of it from a diffuse WIM with $n_e = 0.2$ cm^{-3}. The latter, was the more accepted theory at the time (Wright et al., 1991, Bennett et al., 1994), and fit with the picture of the WIM having low densities, a scale height of 1500 pc and a filling factor of $f = 0.08$ (Kulkarni & Heilies, 1986).

The ionized carbon line ([CII] 158 μm), is the strongest FIR line observed in the IISM. It is also a key coolant of the gas in the IISM, as discussed in e.g. Bennett et al. 1994, and an important tracer of photodissociation regions (PDRs). Within PDRs low energy photons of 6–13.6 eV dominate the physical processes, such that [CII] 158 μm lines, with an ionization potential of 11.3 eV, are emitted from these regions. (For more details on PDRs, see Tielens & Hollenbach 1985.) The emission line is, however, associated with ionized hydrogen (H^+) regions as well, and can therefore be used as a diagnostic for ionized gas in the IISM. The key is to determine how much a H^+ region, versus a nearby PDR, is contributing to the [CII] emission. Fig. 7.8, taken from modelling by Abel (2006), shows that correlations between [CII] and [NII] emission depend on the origins of the emission, with emission associated with PDR deviating from the obtained linear correlation.

Recent emission line results obtained from *Herschel* across the Galactic plane are presented in Fig. 7.9 (Goldsmith et al., 2015). The top panel shows the measured line intensities of the three observed FIR lines, [NII] 122 μm, [NII] 205 μm and [CII] 158 μm. The bottom panel shows the intensity ratio of the two [NII] lines and the associated electron density values as dashed lines.

The intensity ratios range between 1 and 3, higher than the COBE result mentioned above, and the electron density values are much larger than expected from the conventional picture of the WIM.

The COBE interpretation by which high electron densities are associated with HII regions and low electron densities with the WIM, is challenged by the *Herschel* data. Fig. 7.9 shows remarkably little variation in the line ratio of the two nitrogen lines,

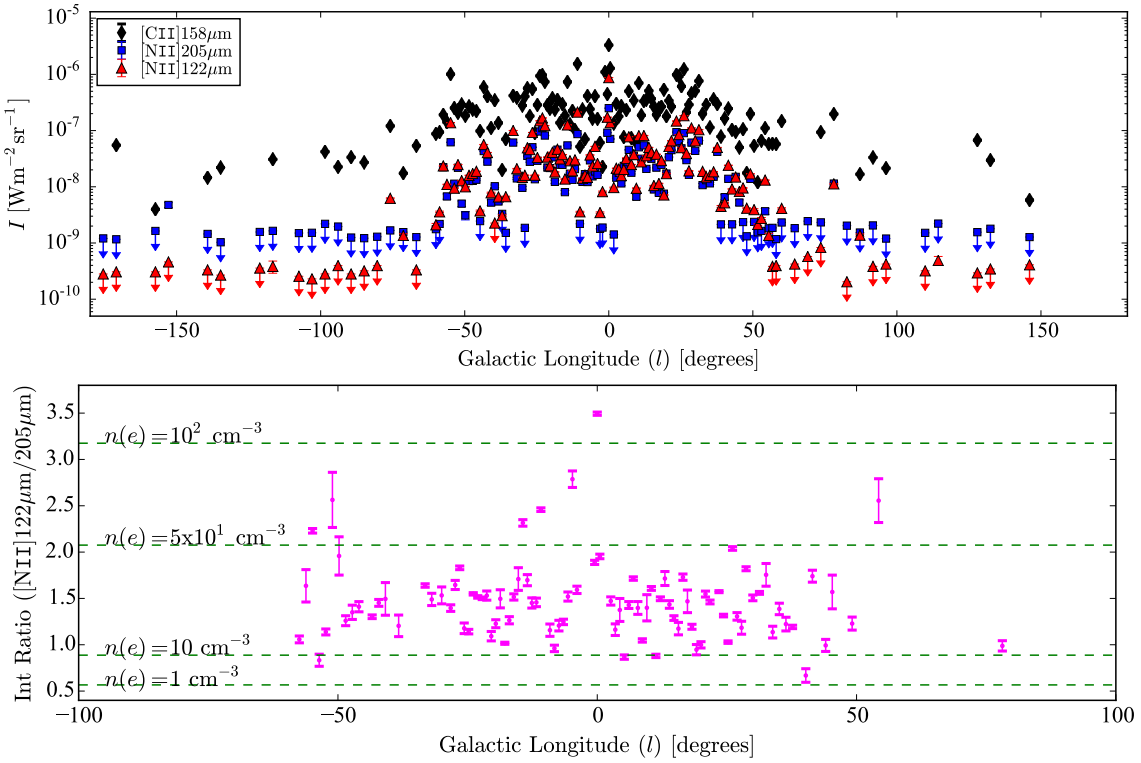

Figure 7.9: FIR line intensity and electron density distributions throughout the Galactic plane. Taken from Goldsmith et al. (2015).

over $\sim$ 150 lines-of-sight in the Galactic plane, which is hard to reconcile with the mixing of two unrelated components.

7.3.3.2 Electron density with CHIANTI

Ratio of the [NII] lines

Goldsmith et al. (2015) demonstrated that the electron density is typically $10 \lesssim n_e(\mathrm{cm}^{-3}) \lesssim 50$, in the regions that are responsible for the bulk of the N^+ FIR line emission in the Galactic plane. Their analysis was undertaken for a single temperature, $T = 8500\,\mathrm{K}$ — a choice that was motivated by photoionization models of the optical emission line ratios observed at high Galactic latitudes (see Haffner et al., 2009).

Although the intensity ratio of the nitrogen lines, $I([\mathrm{NII}]\ 122\,\mu\mathrm{m})/I([\mathrm{NII}]\ 205\,\mu\mathrm{m})$, is not expected to be strongly dependent on temperature, we have investigated the dependence on both electron density and temperature. Our results are shown in Fig 7.10, where it can be seen that the line ratio is indeed insensitive to temperature over a broad range, particularly for the typically measured line ratios in Goldsmith

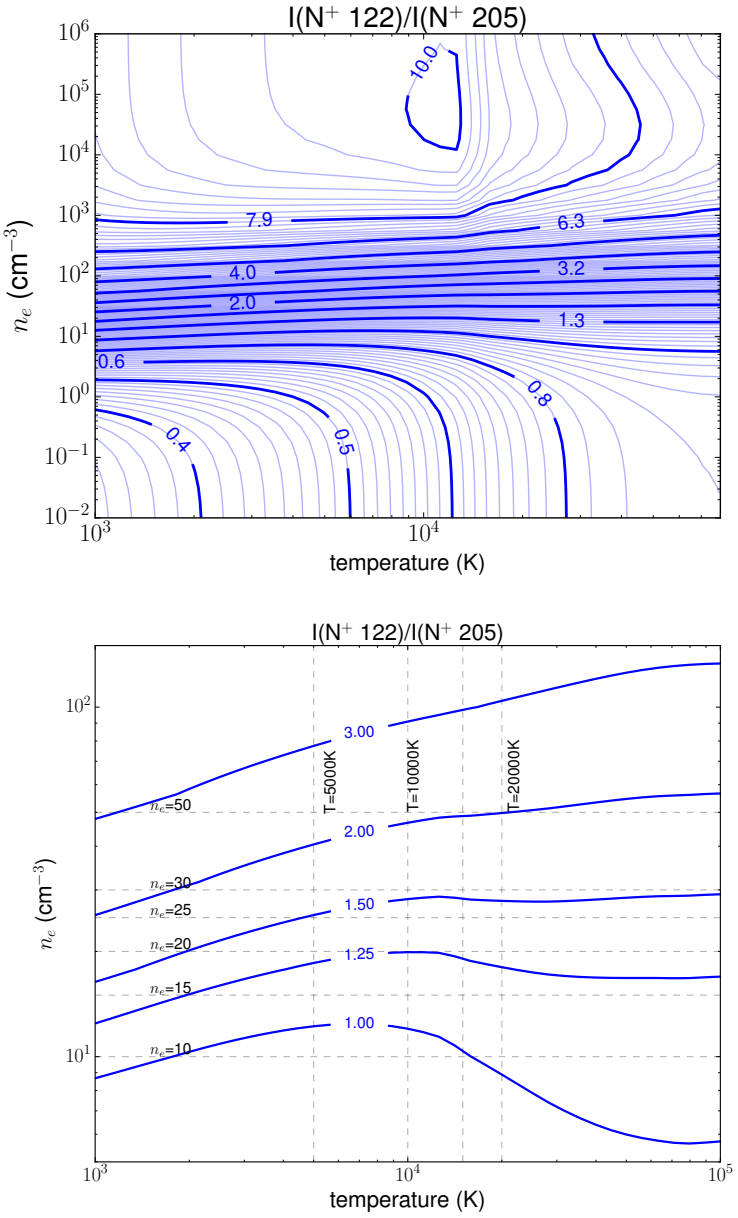

Figure 7.10: *Top:* The intensity ratio $I([\text{N II}]\ 122\,\mu\text{m})/I([\text{N II}]\ 205\,\mu\text{m})$, over a broad range of temperature and electron density values. Bold contour levels are spaced 0.1 in log-space, and fine contour levels 0.01 in log-space. Most of the line ratios measured by Goldsmith et al. (2015) fall in the range $1-3$, for which the inferred value of n_e is seen to be insensitive to the temperature. *Bottom:* An enlargement of the intensity ratios that fall within the range 1 to 3.

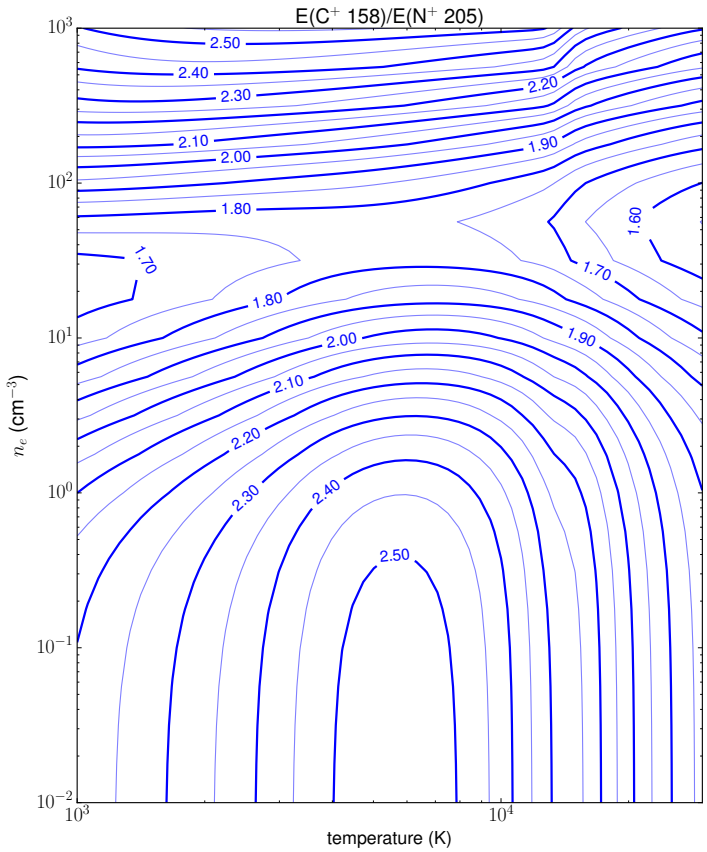

Figure 7.11: The *ChiantiPy* emissivity ratio E([CII] 158 µm)/E([NII] 205 µm), over a range of temperature and electron density values. Bold contour levels are spaced 0.1 in linear space, and fine contour levels 0.05 in linear space. *ChiantiPy* emissivities are intensities per column density, with units erg s^{-1} sr^{-1} per ion.

et al. (2015), that as seen in Fig. 7.10, lie mostly between 1 and 3. The electron density associated with line ratio equal to 1.5 for example, has a minimum of approximately 16 cm^{-3} and a maximum of 28 cm^{-3} over the plotted temperature range (see bottom panel of Fig. 7.10).

Fig. 7.10 further shows that the nitrogen line ratios at conventional WIM electron densities and temperatures ($n_e = 0.2$ cm^{-3} and $T = 8000$ K) as calculated by *ChiantiPy* is 0.55, somewhat lower than the COBE low density limit of 0.7. This is due to updated deexcitation rate coefficients that have become available since the COBE era, see e.g. Tayal (2011).

Ratio of [NII] and [CII]

We also compute the expected ratio of line strengths between the [NII] 205 µm emmission line and [CII] 158 µm, and compare the outcomes to the observed results in Goldsmith et al. (2015), who noted a column density ratio close to 10, for directions in which the NII 205 µm density is of order 10^{16} cm^{-2}, and close to 5 for directions in which the density is higher, 10^{17} cm^{-2}.

The cosmic abundances of carbon and nitrogen, as defined in *ChiantiPy* (using Grevesse & Sauval 1998), are

$$C/H = 3.31 \times 10^{-4} \tag{7.9}$$

$$N/H = 8.32 \times 10^{-5} \tag{7.10}$$

$$C/N = 3.98. \tag{7.11}$$

Furthermore, as described in Sec. 7.3.3, the ionization potential of carbon is significantly lower than that of nitrogen, such that when nitrogen is ionized we expect at least ~ 4 times as many carbon ions as nitrogen ions. It should be noted that a range of cosmic abundances can be found in literature, with the values for the C/N ratio typically lying between 3 and 5 (e.g. Lodders 2010, Nieva & Przybilla 2012).

Using *ChiantiPy* we compute the emissivity (j) of these lines at a given temperature and electron density. Emissivities computed in *ChiantiPy* have cgs units erg s^{-1} sr^{-1} per ion.

For the conventional WIM interpretation, with $T = 8000$ K and $n_e = 0.02$ cm^{-3},

$$\frac{j_{C158}}{j_{N205}} = 2.5, \tag{7.12}$$

and for a higher electron density of $n_e = 30$ cm^{-3}, at the same temperature,

$$\frac{j_{C158}}{j_{N205}} = 1.7. \tag{7.13}$$

Fig. 7.11 shows a contour level plot of the *ChiantiPy* modelled emissivity ratios, for a range of electron densities and temperature values.

This simplistic calculation already creates the expectation that the observed [CII] 158 μm emission associated with the same gas producing the [NII] 205 μm emission, should exhibit a line strength intensity of $\sim 4 \times$ (1.7 to 2.5) $\sim$ 7 to 10 times that of the [NII] 205 μm line strength. This is similar to the observed ratios in Goldsmith et al. (2015), implying that both the [NII] 205 μm and [CII] 158 μm emission are being produced by the same high electron density gas.

7.3.3.3 Optical Emission lines and Temperature

The optical emission lines in the WIM have excitation energies comparable to the thermal energy of the WIM. In contrast FIR lines have much smaller excitation energies. As such, optical emission lines are expected to provide good diagnostics of the temperature of the emitting gas.

Observations of the ratio of optical line strengths relative to Hα in the WIM, are published in e.g. Reynolds (2004). As stated in Sec. 1.2, these line ratio measurements, are however affected by dust scattering which needs to be accounted for. Estimates of the amount of scattered light vary, with literature values ranging from 10% upwards (Witt et al., 2010, Brandt & Draine, 2012). To model the expected ratios of line intensities over a range of electron densities and temperatures, we will again make use of *ChiantiPy*. In particular we aim to investigate the temperature constraints obtained by abundant metals, such as oxygen, carbon, nitrogen and sulfur.

7.3.4 Constraints from radio wave propagation

Because the refractive index contributed by free electrons diverges as ν^{-2} at low frequencies (Eq. 2.4), various aspects of interstellar radio-wave propagation can provide detailed information on the IISM. There are two key diagnostics which we will make use of here: pulse dispersion (Sec. 2.1.1), and the scattering and scintillation that is introduced by small-scale irregularities in the plasma density (Sec. 2.2).

7.3.4.1 Pulse dispersion

As described in Sec. 2.1.1, the group delay of pulsar emission, and hence the observed pulse dispersion measure, is expected to be proportional to the column density of free electrons. At high Galactic latitudes, dispersion measures for pulsars at distances $\gtrsim 1$ kpc are well approximated by the relation

$$\mathrm{DM} \sin|b| = 20 \text{ pc cm}^{-3}, \tag{7.14}$$

and from the DM data alone the scale height is inferred to be $Z \simeq 1\,\mathrm{kpc}$ (Berkhuisen & Müller, 2008).

In the uniform density model, the dispersion measure data imply

$$n_u \simeq 0.02 \text{ cm}^{-3}. \tag{7.15}$$

The corresponding pressure is quite modest: for gas at temperature $T = 10^4$ K, the total pressure would be

$$2 n_u T \sim 400 \text{ K cm}^{-3}. \tag{7.16}$$

This is much less than the typical pressure in the diffuse ISM of $3000\,\mathrm{K\,cm^{-3}}$ (Jenkins & Tripp, 2011).

Interpreting DMs in the framework of dense clouds, with $n_g = 30\,\mathrm{cm^{-3}}$, on the other hand, would imply a volume fraction

$$f_g = \frac{n_u}{n_g} \simeq 7 \times 10^{-4}, \tag{7.17}$$

for those clouds. As noted earlier, such clouds are inevitably over-pressured with respect to the diffuse ISM, with

$$2\, n_g T \simeq 6 \times 10^5 \text{ K cm}^{-3}, \tag{7.18}$$

for $T = 10^4$ K, independent of the volume filling fraction.

As the disk scale-height of the pulse-dispersing gas is observed to be $Z \sim 1\,\mathrm{kpc}$, the implied emission measure is $\mathrm{EM}_u \sim 0.4\,\mathrm{pc\,cm^{-6}}$, for the uniform model, and $\mathrm{EM}_g \sim 600\,\mathrm{pc\,cm^{-6}}$, for the dense clouds. As the latter value is much larger than our fiducial value of unity, at high Galactic latitudes, we can immediately conclude that the dense gas observed by Goldsmith et al. (2015) makes very little contribution to the observed pulse dispersions. There is, in fact, very little room for manoeuvre in interpreting the dispersion measure data, as a uniform gas is the limiting case, and even that case implies an emission measure comparable to what is observed in optical emission lines. In short: if the dispersing electrons are part of the WIM, they must be nearly uniformly distributed.

7.3.4.2 Evolution of dispersion measures

Despite the conclusions of the previous paragraph, the time derivatives of pulsar dispersion measures, conveniently abbreviated as DM-dot, are readily interpreted in terms of dense gas clouds. In a uniform gas distribution, the time derivative is a reflection of the rate at which the overall geometry of the path evolves. That evolution is dominated by the motion of the pulsars themselves, which are typically rapid, as described in Sec. 1.1.2, with

$$v_{psr} \gtrsim 10^2 \text{ km s}^{-1} \simeq 10^{-4} \text{ pc yr}^{-1}, \tag{7.19}$$

so that

$$\left| \frac{\mathrm{d}\,\mathrm{DM}}{\mathrm{d}t} \right| \sim n_u v_{psr} \sim 2 \times 10^{-6} \text{ pc cm}^{-3} \text{ yr}^{-1}. \tag{7.20}$$

That estimate is tiny in comparison with measured values: in a sample of 20 millisecond pulsars (which typically have relatively low speeds), You et al. (2007) reported DM-dot values up to three orders of magnitude larger, while Hobbs et al. (2004) found values up to four orders of magnitude larger, in a sample of 374 pulsars.

It is unsurprising that a strictly uniform gas model, being devoid of structure, does not provide a good description of observed DM-dot values, even though it suffices as a model for DM. Instead, we can consider an approximately uniform gas model, in which the electron density in each cloud is $n_o \simeq n_u$ and the filling fraction is $f \simeq 1$. For an individual gas cloud, the peak electron column-density is $N_e = 2n_o R$, and the transverse gradient of that column is $\sim 2n_o \rightarrow 2n_u$. Assuming that the effective transverse velocity is dominated by the pulsar, and takes the value $v_\perp \sim v_{psr}/2$, then the model leads to a DM-dot that is identical to Eq. (7.20) when a single cloud is present on the line-of-sight. When the line-of-sight passes through many clouds, however, the root-mean-square derivative is (Backer et al., 1993)

$$\left| \frac{\mathrm{d}\,\mathrm{DM}}{\mathrm{d}t} \right| \sim n_o v_{psr} \sqrt{\tau}, \tag{7.21}$$

which is much larger. Following Backer et al. (1993), Hobbs et al. (2004) report that the best fit to their data, for a function of the form $|\mathrm{d}\,\mathrm{DM}/\mathrm{d}t| \propto \sqrt{\mathrm{DM}}$ is given by $|\mathrm{d}\,\mathrm{DM}/\mathrm{d}t| \simeq 2 \times 10^{-4} \sqrt{\mathrm{DM}}$ pc cm^{-3} yr^{-1}. Using the established relationship between DM and distance (Sec. 7.3.4.1) then yields $\tau_u \sim 2 \times 10^5 \, D_{\mathrm{kpc}}$. Thus the DM-dot data may be consistent with an origin in the same, low-density gas responsible for DM, providing that the latter is a space filling population of clouds of size $R \sim 10^3$ AU and electron density $n_u \simeq 0.02$ cm^{-3}.

For the case of dense gas clouds, the calculation proceeds in the same way as we have just described, except that now $n_o \rightarrow n_g$ is three orders of magnitude larger. Thus we expect $|\mathrm{d}\,\mathrm{DM}/\mathrm{d}t| \lesssim 3 \times 10^{-3}$ pc cm^{-3} yr^{-1} in the low optical depth case — i.e. where 0 or 1 dense clouds are present on the line-of-sight. That is large enough that the data of Hobbs et al. (2004) do not require high optical depths except at DM $\gtrsim$ 100 pc cm^{-3}. Hence, for an interpretation of DM-dot in terms of dense gas clouds, we have unit optical depth at a distance of order 5 kpc at low Galactic latitudes.

Because of the very broad spread in DM-dot values that is evident in the pulsar population, even at fixed DM it is currently unclear whether the DM-dot data prefer an interpretation in terms of dense gas clouds over one based on the gas responsible for DMs.

7.3.5 Outlook

This project aims to address the questions posed in the introductory section, Sec. 7.3.1, by analysing the temperature and electron density constraints on the WIM gas coming from both spectroscopy and pulsar propagation techniques. The investigation is conducted using a simple small clouds model for the distribution of gas (Sec 7.3.2.2) and *ChiantiPy*, a powerful atomic emission line database. Dr. Mark Walker is currently investigating the added constraints from extreme pulsar scattering events, while I am continuing the investigation on constraints on temperature that can be obtained from optical emission lines.

Chapter 8

Conclusions

Reflecting, mainly on the results of Chapters 4 to 6, I draw the following conclusions, in terms of new tools developed, new findings and answers to open questions. Thereafter I consider new questions that arise from this work.

8.1 New tools

Chapter 4 describes the development of a robust fitting technique, the *train + DC* method, for extracting scattering parameters, specifically τ values, from scatter broadened pulsar profiles. The method also fits for intrinsic Gaussian profile parameters and produces scatter-corrected flux values, that become important when wrap-around scattering tails are observed. I have shown the importance of introducing a DC offset parameter to obtain accurate values when wrap-around scattering tails are present.

The fitting method can be used with any specified temporal broadening function. In this work I make use of two explicit models, the isotropic and extremely anisotropic (1D) temporal broadening function. I also introduce a new, more general anisotropic broadening function (described by two scattering timescales, τ_x and τ_y) provided in Eq. (2.30). This function is not explicitly used in this work to fit data, mainly because the covariance of the two τ values leads to large uncertainties in their obtained values, and because the obtained fits are sensitive to the initial parameter guesses of the τ values. Ways in which to make use of Eq. (2.28) will be investigated in more detail in the future.

The limitation of this method is that it currently only describes intrinsic Gaussian profile shapes, although it can be extended to include intrinsic profiles made up of several Gaussian components.

The advantage of fitting for Gaussian components, is that it allows me to study the intrinsic changes of Gaussian parameters, e.g. the estimated width evolution of

the pulse profiles. As the understanding of intrinsic evolution mechanisms improve, this will become a more useful diagnostic for testing the accuracy of the scattering fits.

8.2 New findings

I discuss the findings of this work, by considering the Open Questions posed at the end of Chapter 1.

I **How are pulsar profile shapes affected by the IISM at different frequencies?**

Theory and observations in the literature, create the expectation that pulse profiles undergoing IISM scattering will be broadened towards lower frequencies, exhibiting scattering tails. Such shapes were observed in the LOFAR data.

I have shown that thin scattering screens modelled as either isotropic or extremely anisotropic scatterers lead to distinct scattered profile shapes. The extremely anisotropic profile shape typically has a narrower peak and a higher pedestal at delayed times, than the isotropic model. However, these differences are only apparent at very low frequencies, and for data with high S/N (e.g. Fig. 4.12). The data quality of Chapter 5 was typically well fit by both models, without favouring either.

Furthermore, profile shapes can be impacted by scattering screens that are finite in size, such that at long wavelengths, or low frequencies, pulsar emission is no longer scattered back into our line of sight from large angles. Beyond the angular extent of the screen, θ_{max}, no flux is received, which means at times larger than the corresponding t_{max}, no power or scattering tail is observed. This leads to truncated profile shapes at low frequencies, as shown in e.g. Figs. 4.20 and 6.8. The exact shape will be highly dependent on the size and shape of such a scattering cloud or filament, and the alignment of the screen with the pulsar.

II **Does the frequency dependence of pulsar scattering spectra change with frequency?**

The main finding of this thesis is the discovery of anomalously low α values at LOFAR frequencies, where large bandwidths have allowed me to fit many profiles (typically 8 to 16), and hence obtain many τ values across the LOFAR

HBA band. This leads to well constrained α values at these frequencies. From the isotropic method I find an average value of $\langle\alpha\rangle = 2.7 \pm 0.2$.

Using these obtained spectral indices to transform the measured τ values at HBA frequencies to τ values at 1 GHz, I find that my results suggest larger τ than predicted by the τ vs DM trend in Bhat et al. (2004) (Fig. 6.14). This suggests an evolution of the spectral dependence with frequency to maintain the modelled τ vs DM (quadratic on a log-log-scale) trend at higher frequencies.

Figs. 6.9 and 6.10 investigated whether changes in α values are observed when comparing the spectral indices associated with the upper and lower ends of the HBA band. For the small number of samples, 8 out of 13 were found to have higher α indices at the upper end of the frequency band. In the next chapter I propose observations with larger bandwidths by which to investigate whether or not there is a frequency dependence on α in more detail.

III **What temporal broadening functions effectively describe the effect of scattering by the IISM on pulsar data?**

In this thesis I describe three temporal broadening functions: an isotropic, anisotropic and extremely anisotropic broadening function. Using simulated data I find that at low frequencies ($\sim$ 60 MHz) and for data with high S/N, the resulting shapes of the isotropic model and extreme anisotropic model can be distinguished.

However, using LOFAR HBA data, I find that both the isotropic and extremely anisotropic models fit the data equally well, and it is therefore difficult on a pulsar-by-pulsar basis to argue which temporal broadening function is the correct or best description.

Statistical analysis of larger pulsar datasets can improve our understanding of how the outcomes of using these two or three different scattering models change the physical interpretation of the IISM.

IV **Is there evidence in pulsar profile observations for anisotropic scattering?**

As stated in considering the previous question, both isotropic and anisotropic models fit the scatter broadened data equally well. The anisotropic data provided higher α values, with a mean of $\langle\alpha\rangle = 3.5 \pm 0.4$, in closer agreement to theoretically expected values, than the isotropic scattering.

I have also shown that incorrectly fitting anisotropically scattered data with isotropic scattering functions, will lead to lower α values, as is observed in Chapter 5. This, however, is not conclusive evidence for anisotropy.

The most compelling evidence for anisotropy is currently coming from high resolution dynamic spectra and the associated parabolic arcs in secondary spectra. Recent observations with the Green Bank Telescope at 340 MHz and 825 MHz found enhanced parabolic arcs in 13 out of 15 low DM pulsars ($DM < 50$ pc cm^{-3}, Prof. Dan Stinebring, private communication), pointing to anisotropy in the local IISM. Combining the analyses of dynamic spectra and the temporal analyses in this thesis, will improve the diagnostic capabilities of temporal results.

V **Is there evidence in pulsar profile observations for clumpiness in the IISM?**

A clumpy IISM can lead to lower α values at low frequencies, fitting with the results of this thesis. Furthermore, especially for low DM pulsars literature has suggested single dominating scattering surfaces that, if finite in size, will imprint on the observed scattering spectrum. In Fig. 6.12 a set of screens of sizes $\sim$ 100 AU reproduced the observed α values.

As mentioned in answering Question I above, however, we expect to see the effect of a truncated scattering screen in the profile shapes (cf. Figs. 4.20 and 6.8), which is not unambiguously observed in the LOFAR HBA profiles. The simulations used, however, model simple screens with abrupt or sharp edges. More realistic scattering clouds would have a changing electron density (and density gradient) distribution across the cloud, leading to less sharp changes in the profile.

For a given line of sight dominated by a truncated screen (of a few 100 AUs) we expect the τ spectrum to show a break at the frequency at which the observations become sensitive to the edges of the screen. None of our observations show a clear break. However, as mentioned in answering Question II, we do see differences in the α values obtained at the lower and upper end of the HBA band. This assumes a typical midway frequency at which the HBA LOFAR observations become sensitive to finite screens. In reality, however, the frequency at which changes due to a finite scattering cloud occur, will depend on the distance to each pulsar and the size of the screen. Furthermore, physical models of screens with less sharp

edges will lead to less sharp power-law breaks. As such, accurate τ measurements across broader frequency ranges are required to investigate whether breaks in the τ spectra are observed.

We know that in some cases the IISM is certainly clumpy. The observations of the Crab pulsar have confirmed that structures in the nebula have a finite size, allowing the pulsar to pass behind such structures and the observed τ to change significantly. In Sec. 7.3 evidence for high electron densities through Far Infrared spectroscopy, and its potential relation to pulsar propagation effects was also discussed. Future outcomes of this project may lead to additional evidence of a clumpy IISM.

VI **Do we observe IISM effects on pulsar flux spectra at low frequencies?** The extreme scattering of pulsar pulses can smear out the periodicity of the signal. I have shown that these effects can lead to turnovers in flux spectra at low frequencies. The impact of this effect was found to be small in the LOFAR data at HBA frequencies, with only 4 out of 13 pulsars showing a correlation between flux spectral turnover and long scattering tails. The scatter-correction to flux values was estimated to be larger for extremely anisotropic scattering models. The flux analyses in this work is generally handicapped by the large (50%) error bars on the flux density measurements.

Many other causes for flux spectral turnovers, such as thermal absorption by dense surrounding environments, or the possibility that the emission mechanism switches off below some frequency threshold (Secs. 1.1.4.2, 6.6), are discussed in the literature. It is also interesting to note that not many flux spectral turnovers have been observed in milisecond pulsars, where scattering effects can be dominating. The next chapter proposes a new technique by which to distinguish whether low frequency turnovers in LOFAR sources are caused by IISM scattering.

VII **How can we best disentangle intrinsic pulsar effects from IISM propagation effects?**

This question remains unanswered. Fundamentally we hope to distinguish the two effects through their independent frequency dependencies. However, that relies on a complete understanding of the individual frequency dependencies. This work has shown that the frequency dependence of the IISM is far more complex

than a simple power law with a constant spectral index. Until our understanding of IISM frequency dependence for specific lines of sight is improved, disentangling IISM effects from intrinsic profile effects, of which the frequency dependence is even more poorly understood, will remain a difficulty.

Improvements of IISM modelling can come from large baseline (space-ground perhaps) imaging that resolves structures of a few 100 AU at low frequencies, and from high resolution, high sensitivity dynamic spectra.

Improvements to our understanding of the frequency dependence of intrinsic profile shapes, are likely to come from improved theoretical beam modelling, beyond the simple cone-shaped emission model, shown in this work.

8.3 New Questions

In this thesis I have found anomalously low scattering spectral indices for a set of nearby pulsars. These low indices are likely due to either anisotropic scattering mechanisms or finite scattering screens. The main new question is then: Which of these is the more likely scenario? Or is the answer highly dependent on the line of sight and epoch?

If the low α values are largely due to a clumpy IISM with small scattering screens, how prevalent are these clumps? Are they primarily dominating effects towards nearby pulsars? If the clumps have high electron densities as suggested in Sec. 7.3, how are they formed and maintained? Do we see scattering measurements change on the expected time scales, as pulsars pass behind these screens?

If the low α values are mainly due to the anisotropic nature of the IISM, what is the origin of the anisotropy and its typical ratio of anisotropy? Or are these properties highly dependent on the line of sight?

Or, is it generally a combination of the two effects, such as filamentary structures that are both finite in size, and due to their physical shape cause anisotropic scattering of pulsar signals?

Chapter 9

Proposals and Future Work

Following on from the discussion in Chapter 8, I present two future LOFAR projects, that build on the low frequency pulsar scattering investigations in this thesis. The first project, described in Sec. 9.1, aims to investigate whether flux lost due to scattering effects in the time domain, is recovered in pulsar imaging data, or not, with implications for the IISM structure. The second project (Sec. 9.2) proposes to explore the characteristics of scattering screens in the IISM, using datasets with a broader frequency coverage than the data in this thesis.

9.1 Flux spectra in the context of the IISM

9.1.1 The investigation

Pulsar flux spectra typically have steep negative spectral indices, as discussed in Sec. 1.1.4.2, with mean values in the literature ranging from -1.8 to -1.4 (Lorimer et al., 1995, Maron et al., 2000, Bates et al., 2013). However, several studies of slow pulsars, have observed spectral turnovers at low frequencies (e.g. Lorimer et al. 1995). Many physical interpretations, as described in Sec. 1.1.4, that relate to the efficiency of the emission mechanism and the geometry of the beam, have been suggested as causes for such turnovers. These include thermal absorption by dense surrounding environments (Rajwade et al., 2016), or suggestions that the efficiency of the radio emission shuts off at lower frequencies (Malofeev et al., 2000). A specific beam model, such as the cone-shaped beam of Fig. 1.5, would lead to frequency dependent intersections of the line-of-sight with the radio beam. At lower frequencies the line of sight to the pulsar could miss the emitting regions, leading to frequency dependent flux imprints.

Additionally, as I demonstrated in Chapters 4 to 6 (Secs. 4.3.2.2, 4.3.3.3, 5.2 and 6.6), IISM scattering can also imprint on the observed flux density, leading to turnovers in the flux spectra at low frequencies. Such scattering imprints originate in various ways. Figs. 4.15 and 4.16 showed how long scattering tails that wrap around the full rotational phase lowers the observable flux, as intrinsic flux is lost to the raised observing baseline. Since this is an artefact of the temporal domain, the flux lost can in principle be recovered by imaging pulsars directly. Truncated scattering screens also create flux losses toward lower frequencies (e.g. Fig. 4.23) This flux loss is not an artefact of the time domain and will be observed in the image domain as well. Alternatively, a measured flux loss can be associated with scattering screens with inner scale cut-offs Rickett et al. (2009), as briefly described in Sec. 2.2.3.2. The existence of an inner turbulence scale does not reduce the total observed flux, but restricts the IISM scattering to a maximum scattering angle and hence maximum observing angle ($\theta_{\rm max}$). These effects can become observable for large enough inner scales. However, no flux loss will be measured in the image domain.

The effects, alternative to pulsar propagation mentioned above (and in Secs. 1.1.4 and 6.6), that lead to flux spectral turnovers, will all have similar flux measurements in both the image and time domain. Comparing time domain and image domain flux measurements can therefore be helpful in distinguishing whether flux spectral turnovers are caused by propagation effects. Dembska et al. (2015) sucessfully conducted such a comparitive study for six high DM pulsars at 610 MHz, using the GMRT. The pulsars were picked for exhibiting spectral turnovers in the gigahertz regime (GPS pulsars, Sec. 1.1.4). In three of the sources, once the results from the imaging data were added, the original time domain spectral turnovers were shown to be artefacts of IISM propagation, and removed.

9.1.2 Conducting the investigation using LOFAR

To conduct the above investigation, I co-authored a LOFAR observing Cycle 6 proposal with collaboratiors at Manchester University (Project code: LC6_030, PI: Dr. R. Breton). The proposal, requesting simultaneous beamformed and imaging data at HBA frequencies for a set of pulsars, was awarded 60 hrs of observing time, and the data for these projects were taken from the 29 May to 10 October 2016. An outline of my ongoing investigation follows below.

9.1.2.1 Data and Methods

I picked three pulsars that are scattered at HBA frequecies to study. The aim is to test whether the observed flux loss in the temporal domain is recovered in the imaging domain or not. The three pulsars are PSRs J0117+5914, J2113+4644 and J2219+4754, of which J0117+5914 is most prominently scattered at HBA frequencies. The difficulties of this work are to conduct accurate flux calibration in both domains, and consequently obtain accurate flux density values and errors.

Each pulsar in the study was observed with the LOFAR Core, at HBA frequencies for approximately 30 min every two weeks over 5 months. Beamformed and imaging data were conducted simultaneously.

The tools required to conduct analysis of the imaging data include the standard LOFAR imaging pipeline tools, as well as AOFlagger (Offringa, 2010) for RFI mitigation, the Black Board Selfcal System (BBS) for phase calibration (Pandey et al., 2009) and AWImager and the Common Astronomy Software Applications (CASA) for imaging (Tasse et al., 2013, McMullin et al., 2007). The requirements for analysis of the beamformed data is similar to described in Chapter 3.

9.1.2.2 Current Status

I am in the process of analysing the data quality, starting with PSR J0117+5914, since its flux density spectrum in Chapter 5 suggests potential turnovers at low frequencies. Unfortunately, finding the pulsar in the obtained imaging data has proved to be difficult. The LOFAR Image noise calculator[11] estimates an expected noise level for a single sub-band image of 2.44 mJy per beam. However, I find a noise level of approximately 80 mJy per beam.

Fig. 9.1 suggests where this discrepancy comes from. The image of the field clearly contains contamination from a bright off-axis source. Dr. Leah Morabito (Oxford University), helped identify this contaminator as the bright supernova remnant, Cassiopeia A, which, when imaging a larger field becomes visible. In order to obtain results for this pulsar, I will therefore have to mask or remove the effects of this contaminating source first.

An example of the beamformed data for a single observation of PSR J2113+4644 is shown in Fig. 9.2. The data are folded to the pulse period, and split into 16 frequency channels across the HBA band. Currently the scattering code is not fitting for the small leading component, however the obtained models fit the scattered edge of the

[11] https://support.astron.nl/ImageNoiseCalculator/sens.php

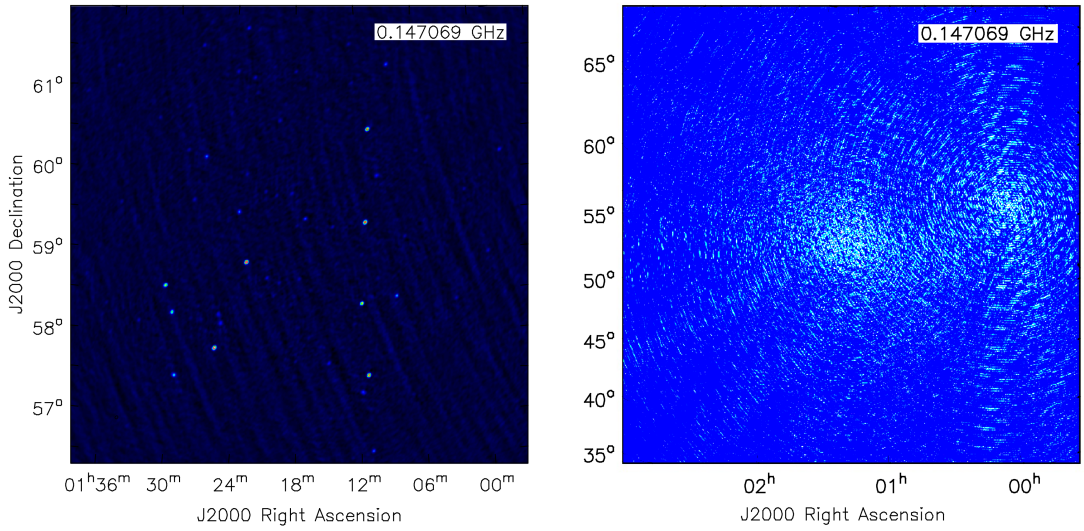

Figure 9.1: Image produced from a single sub-band of the PSR J0117+5914 field. The noise in the image is much higher than expected, and appears to be contaminated by the bright off-axis source, Cassiopeia A, visible in the larger field on the right hand side (where I have artificially enhanced the contrast for ease of view). I will need to mask this contaminating source carefully in order to obtain an image of the pulsar.

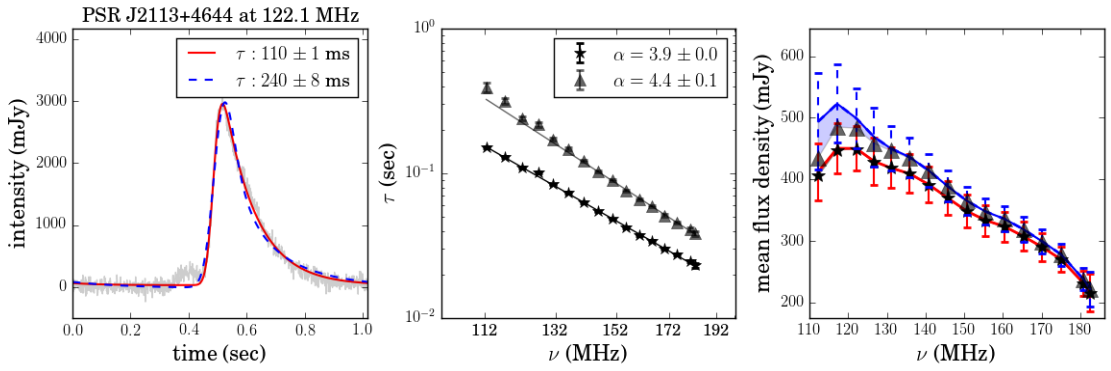

Figure 9.2: Preliminary scattering fits to the beamformed data of PSR J2113+4644, a source not previously analysed in this thesis. Note that the scattering model is currently not fitting the small leading component in any of the frequency bands.

pulsar well, leading to spectral indices $\alpha = 3.9 \pm 0.1$ (IM) and $\alpha = 4.4 \pm 0.1$ (AM). A single observation of PSR J0117+5914 produced $\alpha = 2.3 \pm 0.3$ (IM) similar to the obtained spectral index from the Commissioning and Census data in Chapter 5 of this thesis.

9.2 Characterising the scattering screens

9.2.1 The investigation

The work in this thesis suggests that pulsar τ spectra depend on both the modelled scattering mechanism and the geometry of the scattering screens, each of which has different frequency dependencies. In Chapter 5, using the IM, I found a dependence of τ on frequency with power law indices much smaller (ranging from $\alpha = 2$ to 4) than the theoretically predicted values. I also found that the τ and α values, resulting from the AM fits, differ significantly from the IM values.

In order to understand the anomalous α values, high quality data of the target sources over a larger frequency range will be instructive to distinguish between two scenarios for each source:

- The scenario in which the scattering spectrum is described by a continuous power law with a constant spectral index.
- The scenario in which the scattering spectrum is described by a power law with a higher frequency break in it.

If I find that the first scenario holds, I need to explain the observed spread in α values found in this work. A spread in α values could perhaps be due to varying ratios of anisotropy along different lines of sight in the IISM. If the second scenario holds, I need to investigate at which frequencies the breaks occur, and consider whether these frequencies represent typical size-scales of structures in the IISM. I will also investigate the hypothesis that frequency dependent α values are due to scattering in the IISM being more isotropic at higher frequencies than at low frequencies. Such a result will have implications on our understanding of the physical shape as well as the electron density gradient arrangements of scattering screens, and the distribution of these screens.

Adding results from frequencies of $\sim$250 MHz, will further bridge the gap between the LOFAR HBA frequencies (centred at 150 MHz) used in this thesis and higher frequency results such as those obtained in L15 and Löhmer et al. (2004) (Table

5.3). For sources that do not show changes in α at mid-frequencies, scintillation measurements at even higher frequencies will be required to complete the picture.

9.2.2 Conducting the investigation using LOFAR

The above investigation can be conducted using LOFAR by adding a higher HBA band (210 – 250 MHz, *HBA-high*) to the normal HBA band (110 – 190 MHz) used in this thesis. To be sure that any changes in scattering measurements caused by a variable IISM and proper motions of the pulsar are eliminated, I propose to observe the target sources with a minimum delay between the two bands.

Using the α values obtained in Chapter 5, I calculate the projected τ values at 230 MHz for the sources in this thesis. The set has a minimum value of $\tau = 1.7$ ms. If however α changes significantly with frequency, tending to the theoretically predicted value of 4 at 230 MHz, the minimum τ value is $\sim$ 1.0 ms. I conclude that these effects will be measurable. Assuming errors on τ values at HBA-high similar to what I obtained in the HBA-low analysis, the α value will be estimated with a 1σ error of $\sim 10\%$.

The data analysis methods will be similar to the methods described in Chapter 4 and 5, by which channelised profiles for each pulsar are fitted with two scattering models, the IM and AM.

The technical requirements will also be similar to what was required for the data in this thesis. As before, the observations will be conducted with the HBAs using the LOFAR core. I will propose to record the complex-voltage data for all the sources, which will allow me to perform coherent dedispersion offline, to fully compensate for the dispersion in the IISM.

My suggested source list greatly overlaps with the source list of Chapter 5, with a couple of additional sources that have simple profile shapes and that are expected to exhibit exponential scattering tails. To reach a stable profile shape would require, as before, at least 2000 revolutions per pulsar. I would aim for a minimum observation time of 15 min and a peak S/N ratio of 20.

I will submit a proposal of this nature to the next LOFAR observing cycle.

9.3 Outlook

These proposed projects provide systematic ways in which to investigate the structure of the IISM in more detail. Flux spectral analysis can reveal whether low frequency turnovers are associated with scattering effects or with instrinsic pulse emission and

beam models. In particular, comparing flux spectra obtained from beamformed data and imaging data, will reveal whether turnovers in the beamformed data, as observed in this thesis, are due to physical size-scales within the IISM structure, or artefacts from wrap around scattering tails. The analysis of τ spectra over wider frequency ranges, can reveal the underlying causes of the observed anomalously low scattering spectral indices at low frequencies. Either the low values will be specified by the line of sight and therefore by the anisotropy or particular scattering mechanism associated with the IISM along the line of sight, or it will be specified by the observing frequency, and hence by the typical size-scale of structures within the IISM or the changing frequency dependence of the scattering mechanisms describing the IISM.

Appendix A

Scattering fits and diagnostic plots of LOFAR pulsars

LOFAR HBA profiles fitted with both the isotropic model (IM, red, solid lines) and extremely anisotropic model (AM_{1D}, blue, dashed lines), along with τ spectra, flux spectra, ΔDM and model parameter fits described in Sec. 4.2.

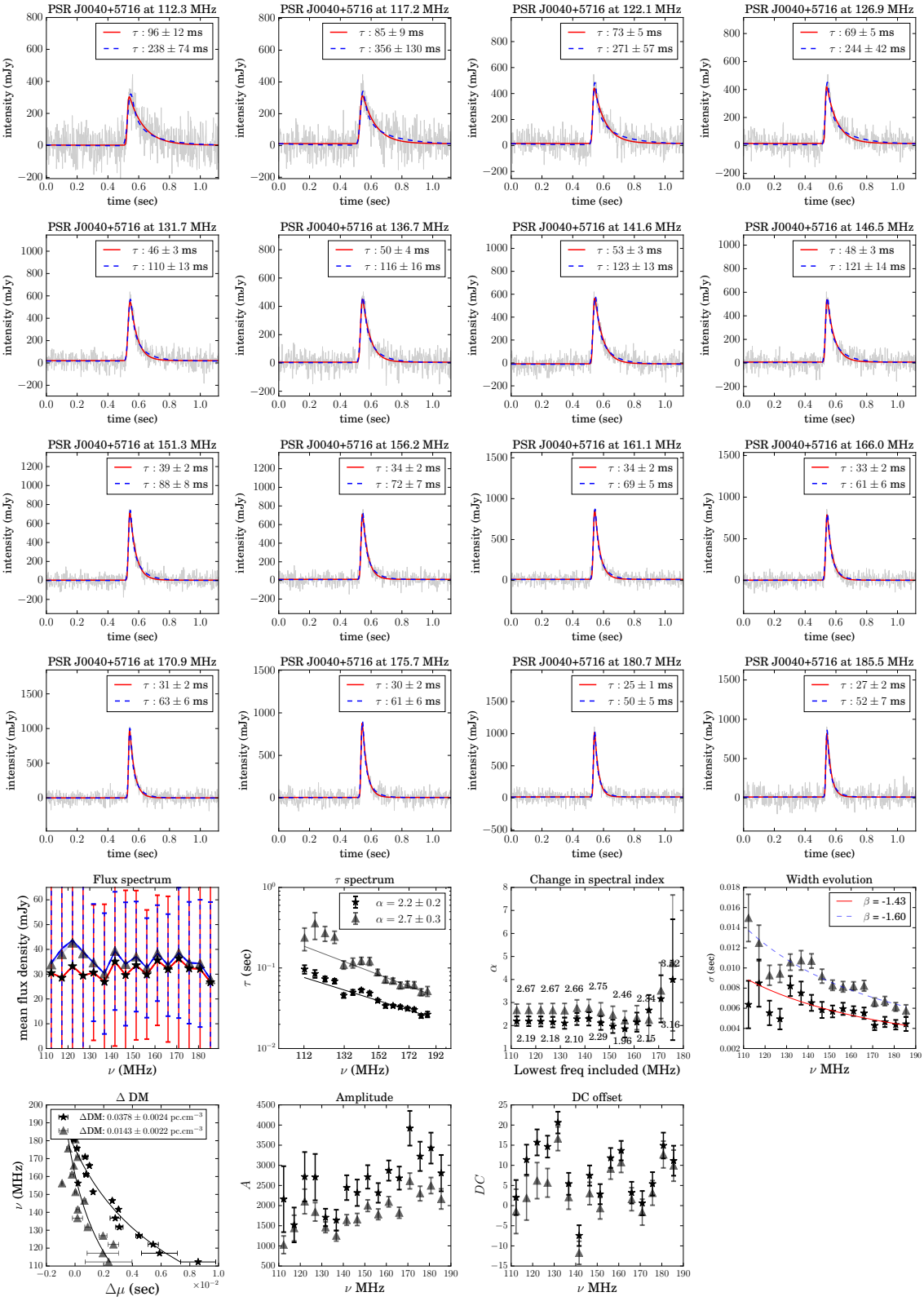

Figure A.1: PSR J0040+5914. Profile fits to the 16 average profiles of Census data, spectra and diagnostic plots.

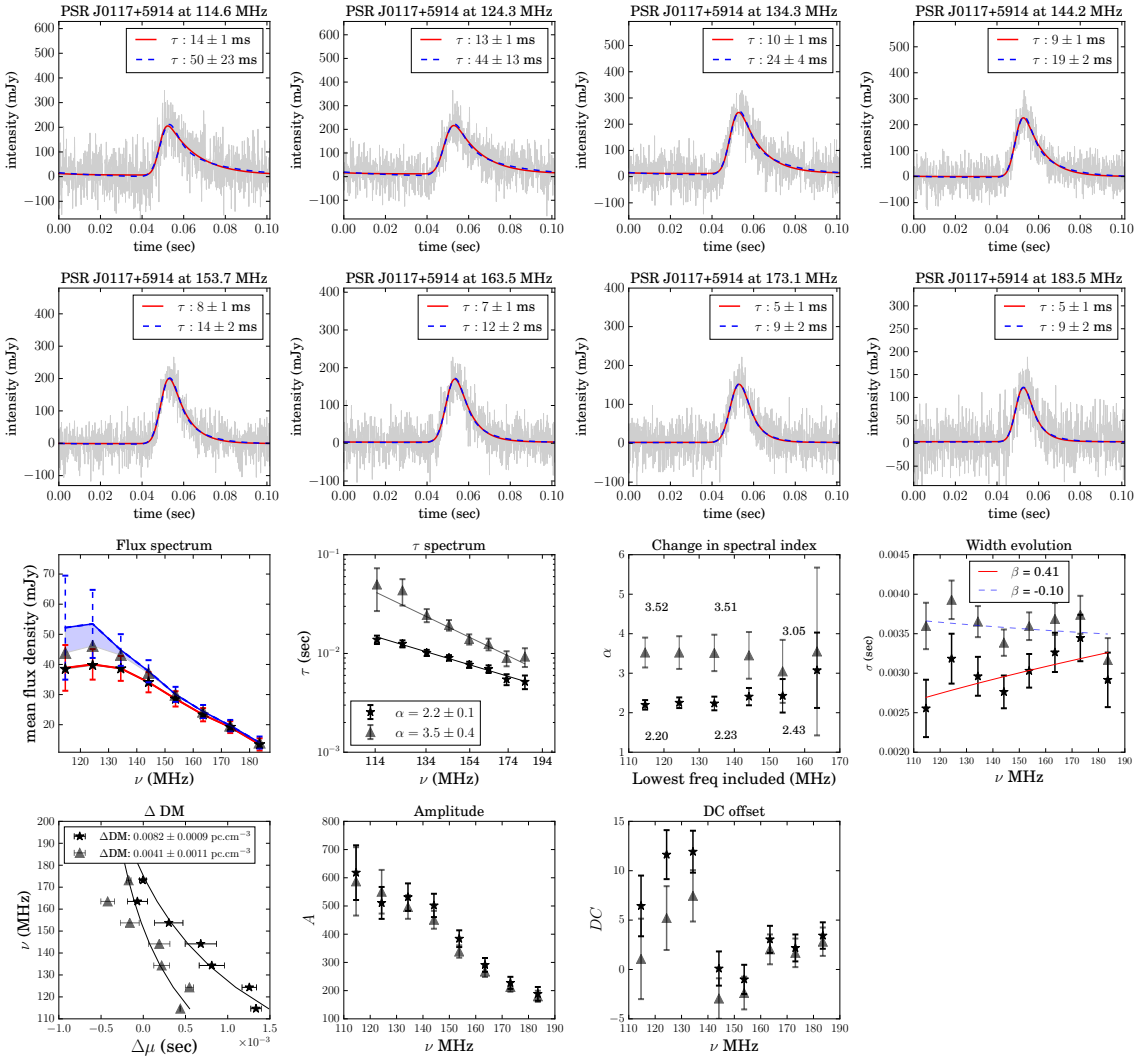

Figure A.2: PSR J0117+5716. Profile fits to 8 average profiles of Commissioning data, spectra and diagnostic plots.

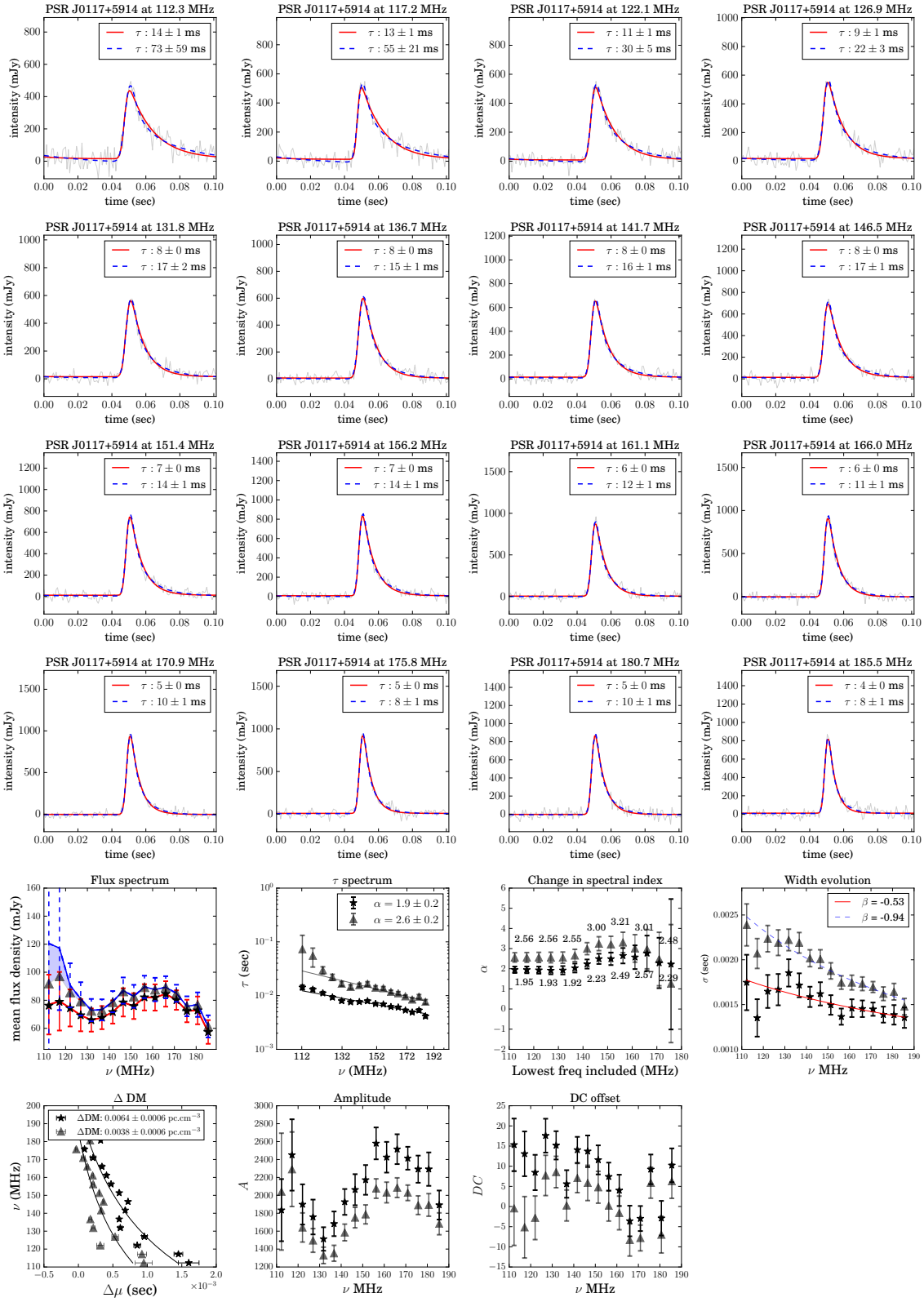

Figure A.3: PSR J0117+5716. Profile fits to 16 average profiles of Census data, spectra and diagnostic plots.

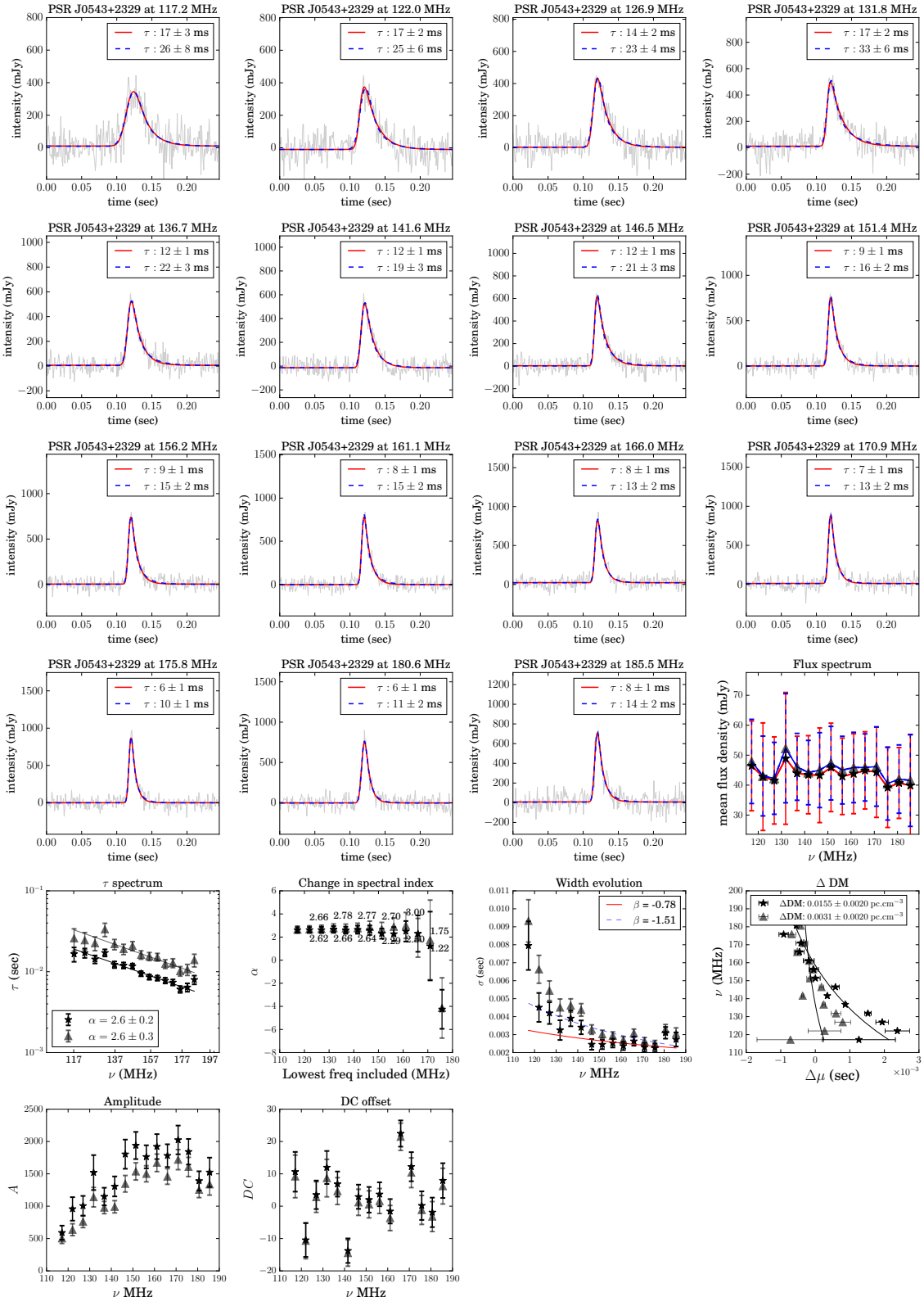

Figure A.4: PSR J0543+2329. Profile fits to 15 average profiles of Census data, spectra and diagnostic plots.

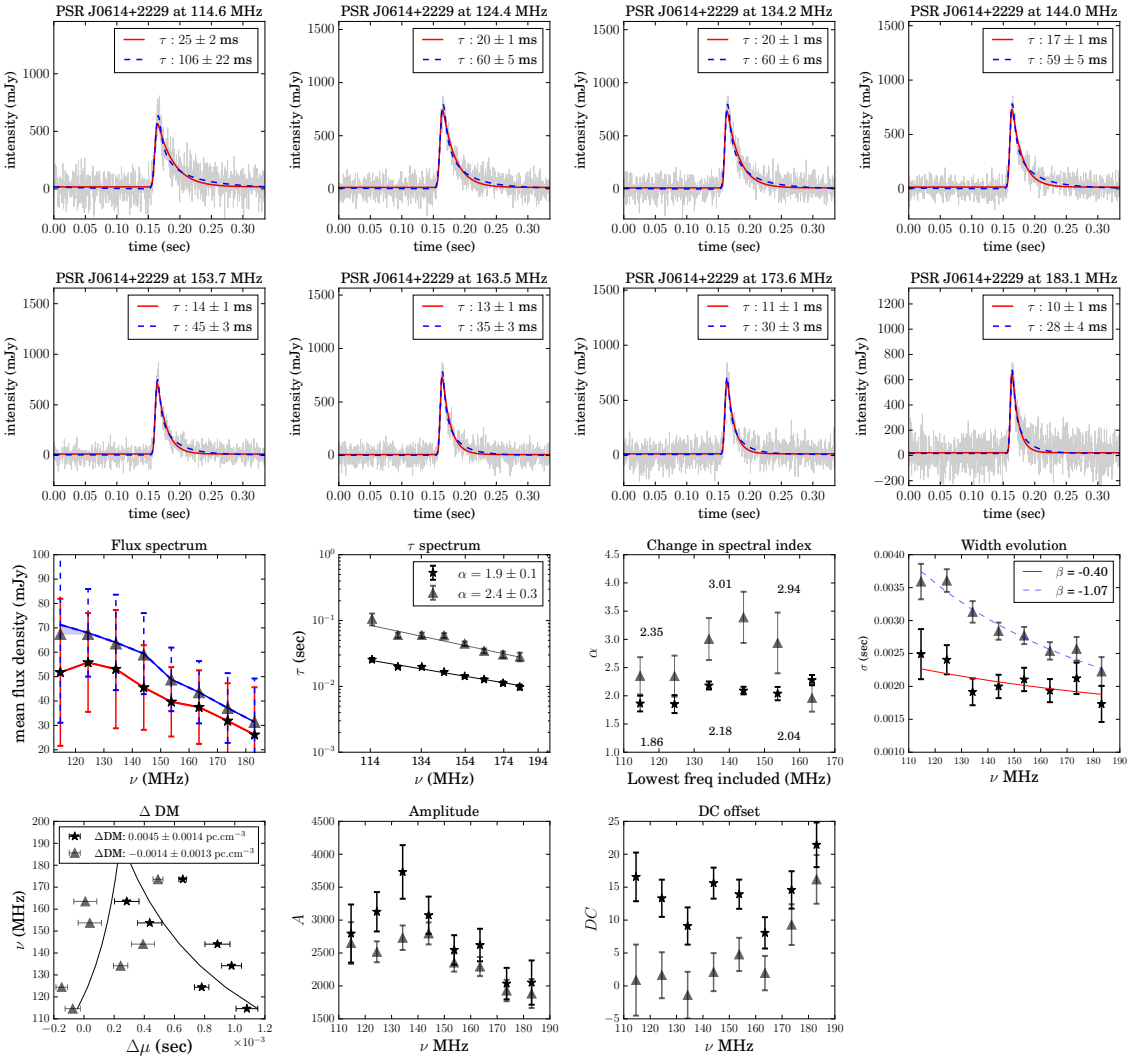

Figure A.5: PSR J0614+2229. Profile fits to 8 average profiles of Commissioning data, spectra and diagnostic plots.

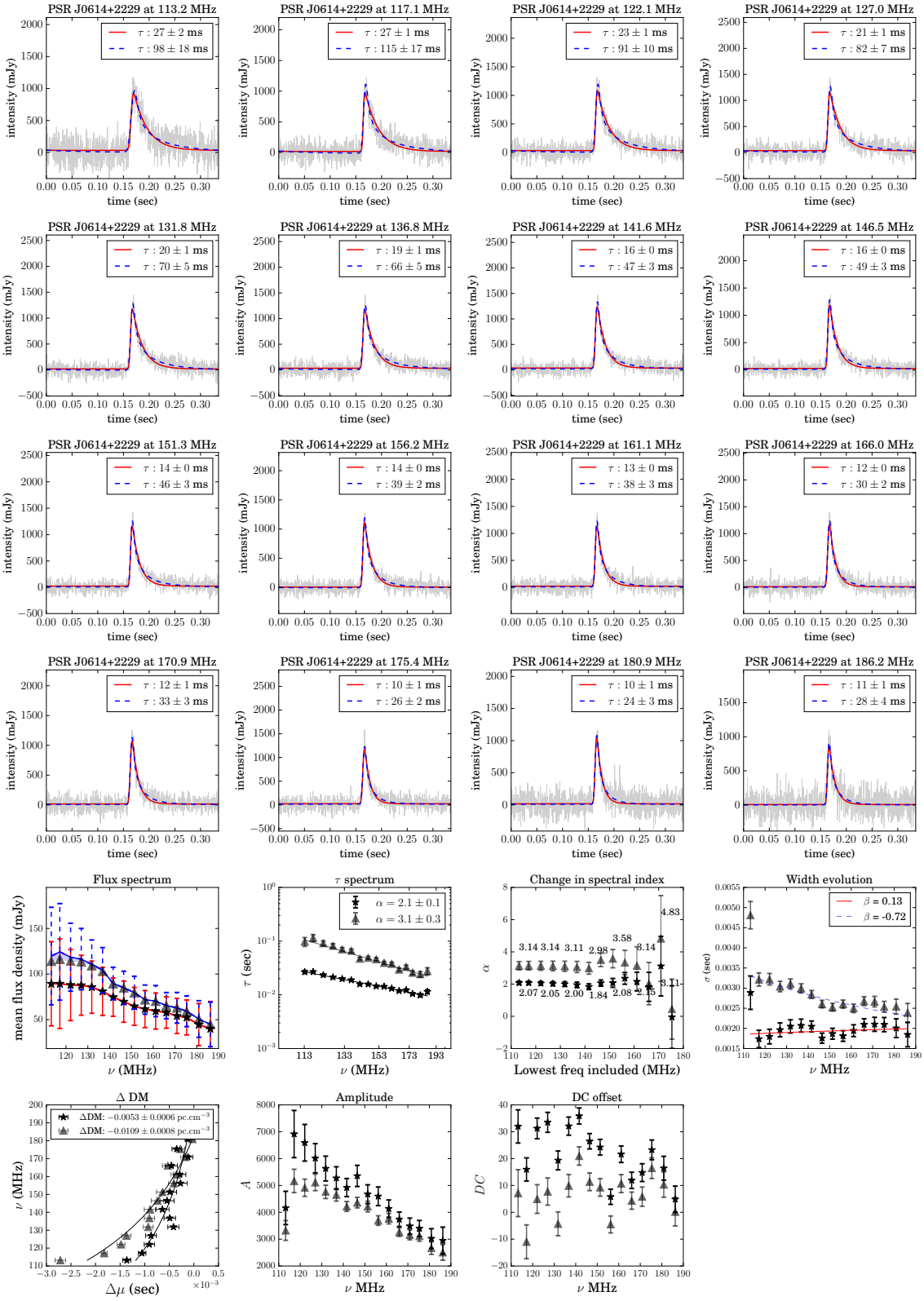

Figure A.6: PSR J0614+2229. Profile fits to 16 average profiles of Cycle 5 data, spectra and diagnostic plots.

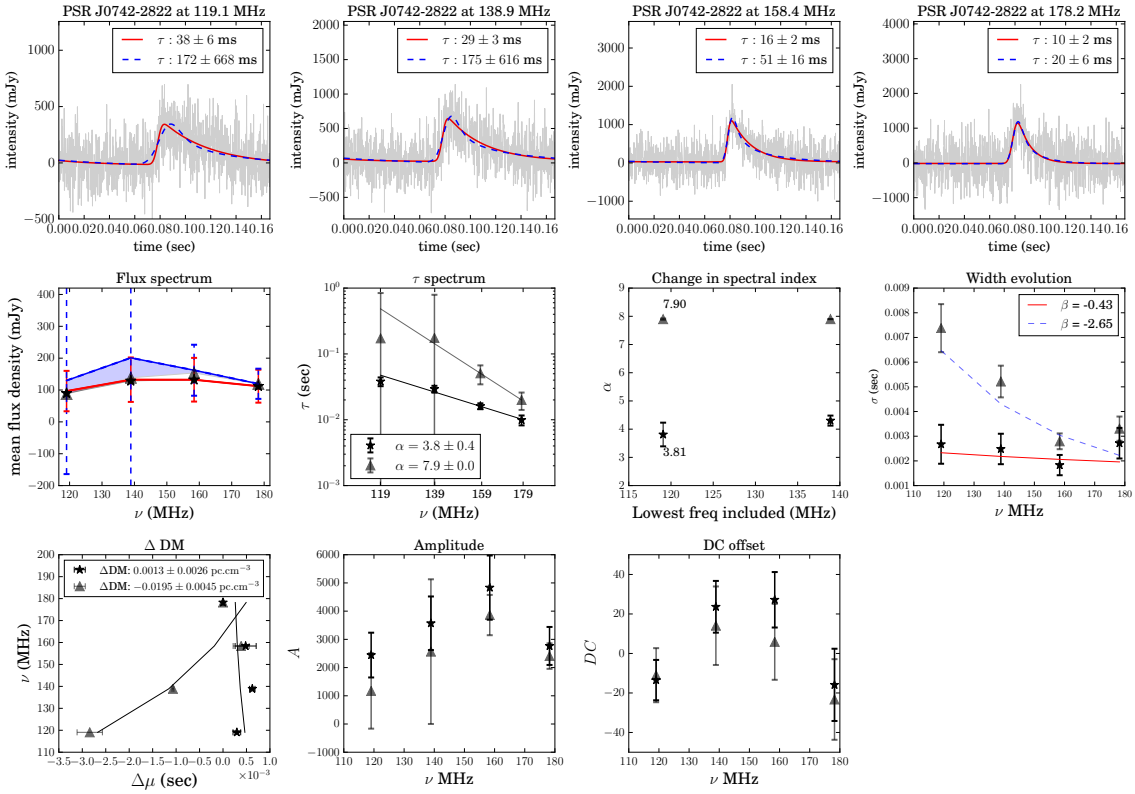

Figure A.7: PSR J0742−2822. Profile fits to the 4 average profiles of Commissioning data, spectra and diagnostic plots.

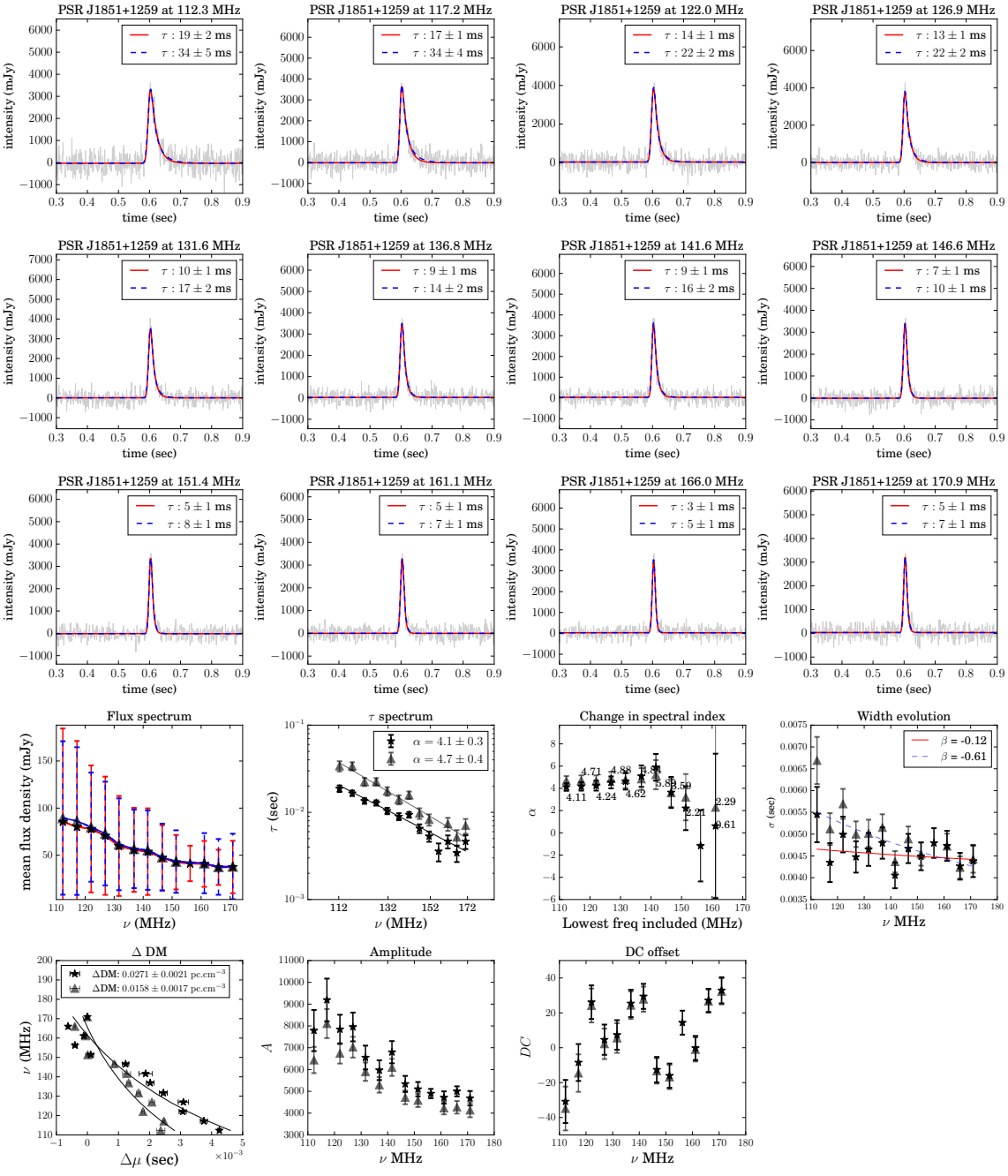

Figure A.8: PSR J1851+1259. Profile fits to 12 average profiles of Census data. Profile plots are zoomed to the on-pulse region.

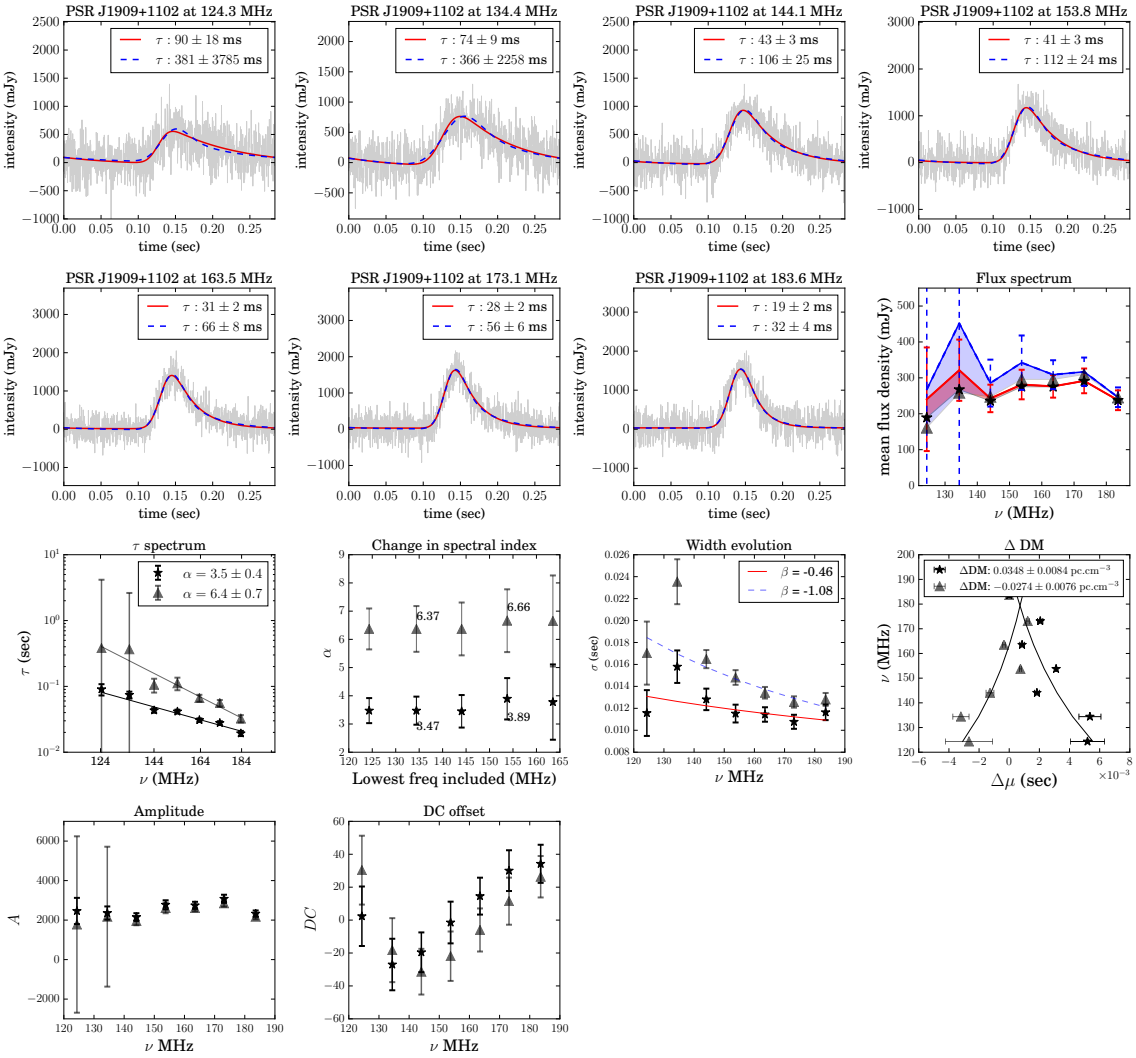

Figure A.9: PSR J1909+1102. Profile fits to the 7 average profiles of Commissioning data, spectra and diagnostic plots.

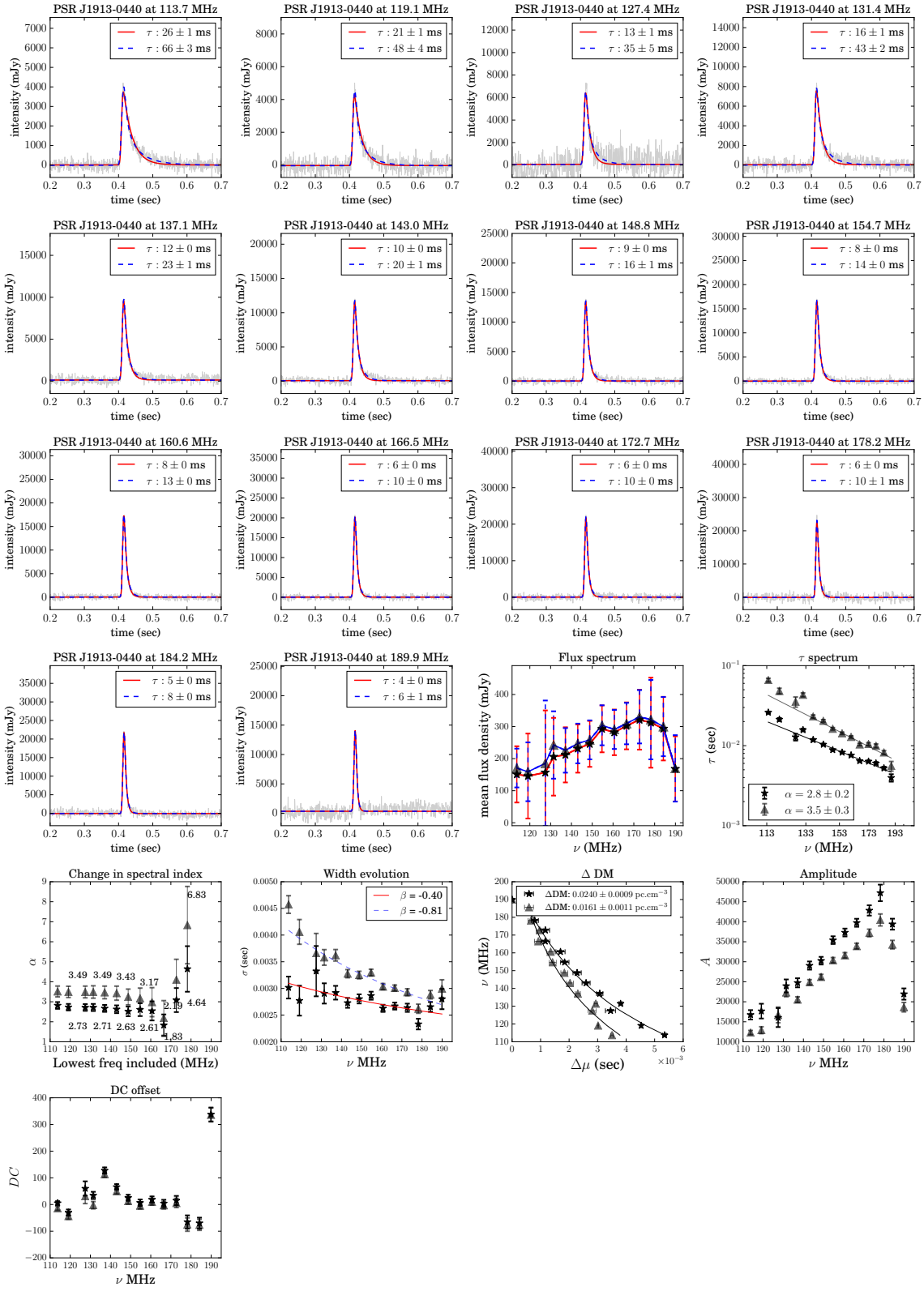

Figure A.10: PSR J1913−0440. Profile fits to 14 average profiles of Commissioning data, spectra and diagnostic plots. Profile plots are zoomed to the on-pulse region.

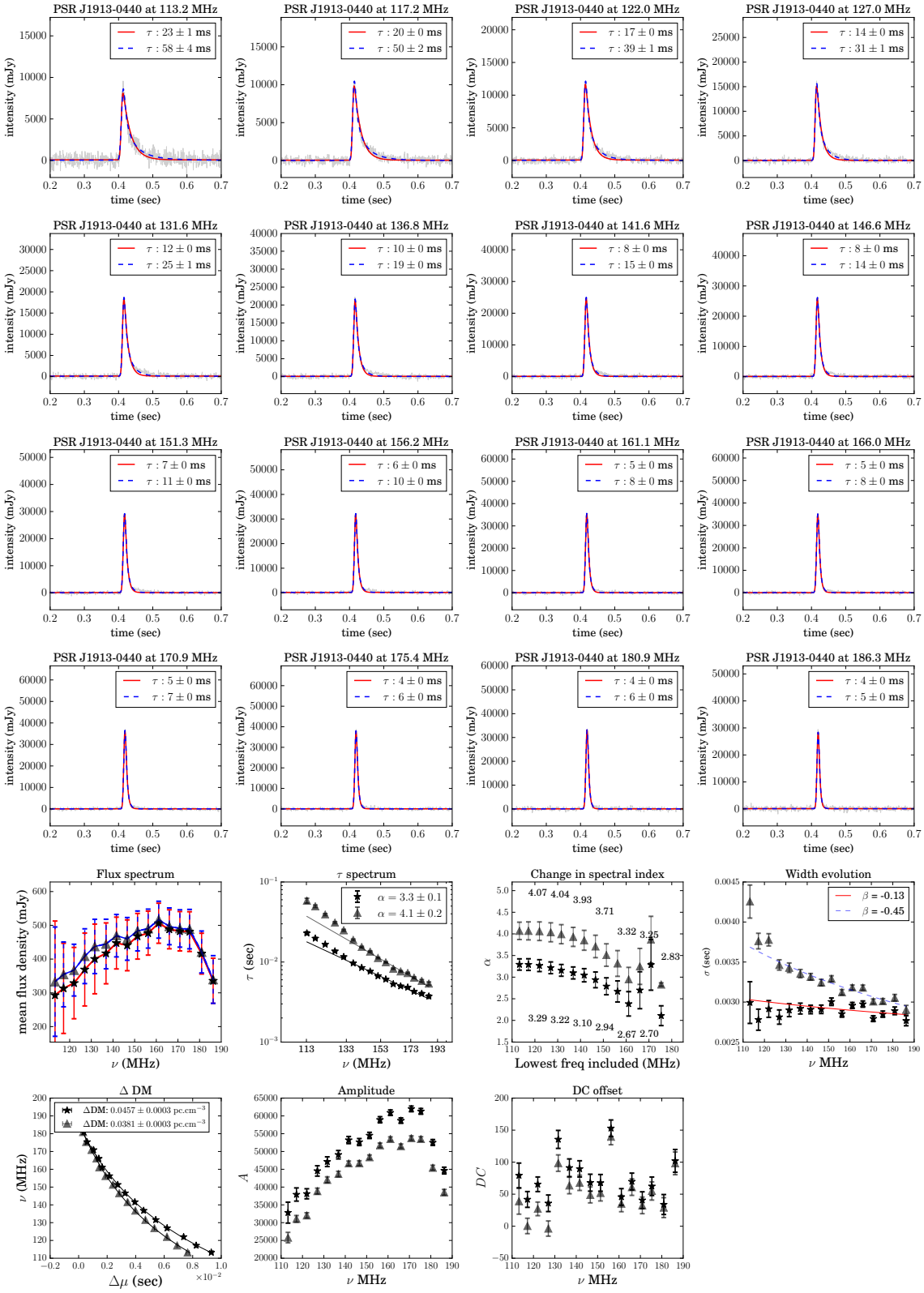

Figure A.11: PSR J1913−0440. Profile fits to 16 average profiles of Cycle 5 data, spectra and diagnostic plots. Profile plots are zoomed to the on-pulse region.

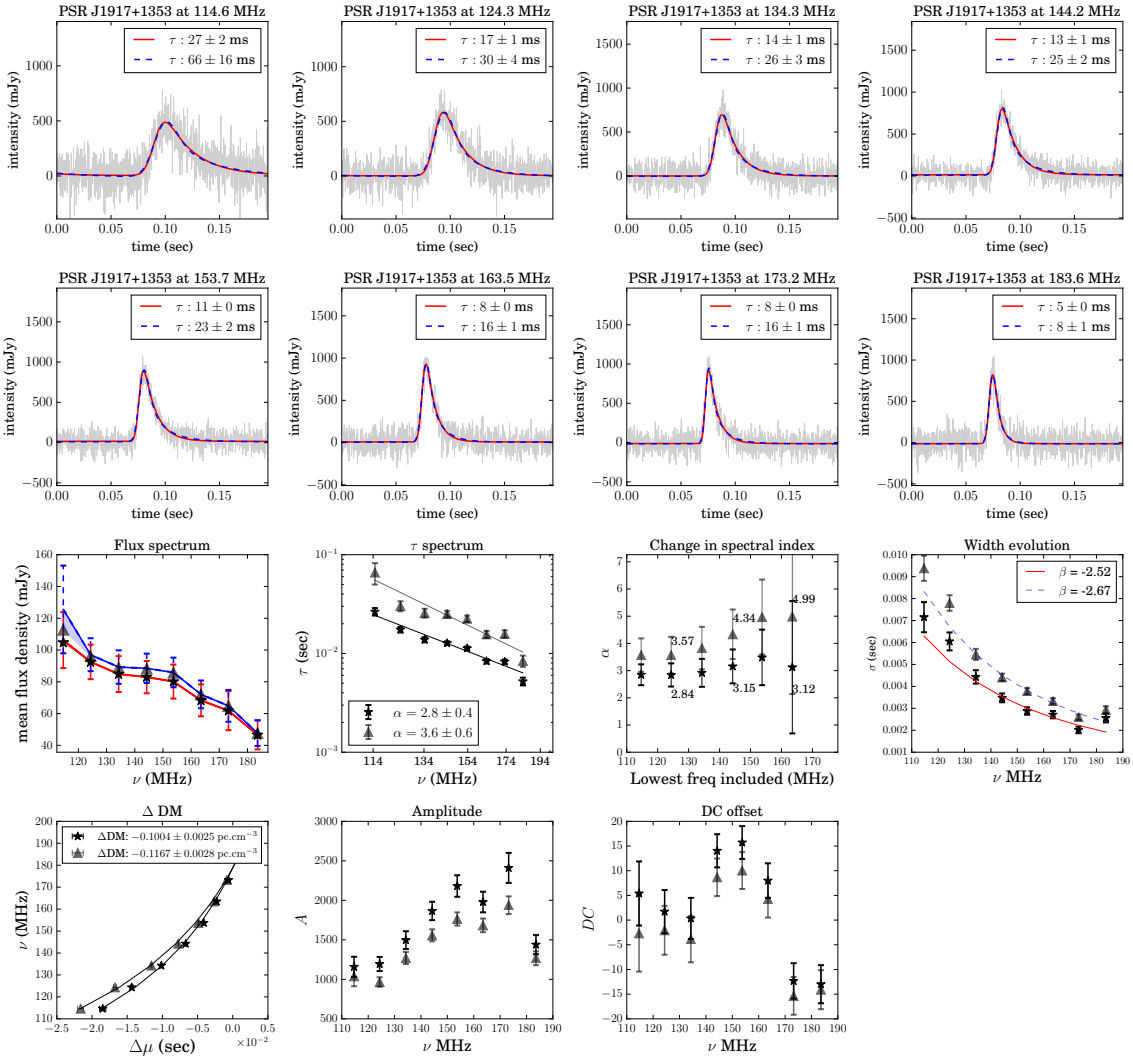

Figure A.12: PSR J1917+1353. Profile fits to the 8 average profiles of Commissioning data, spectra and diagnostic plots.

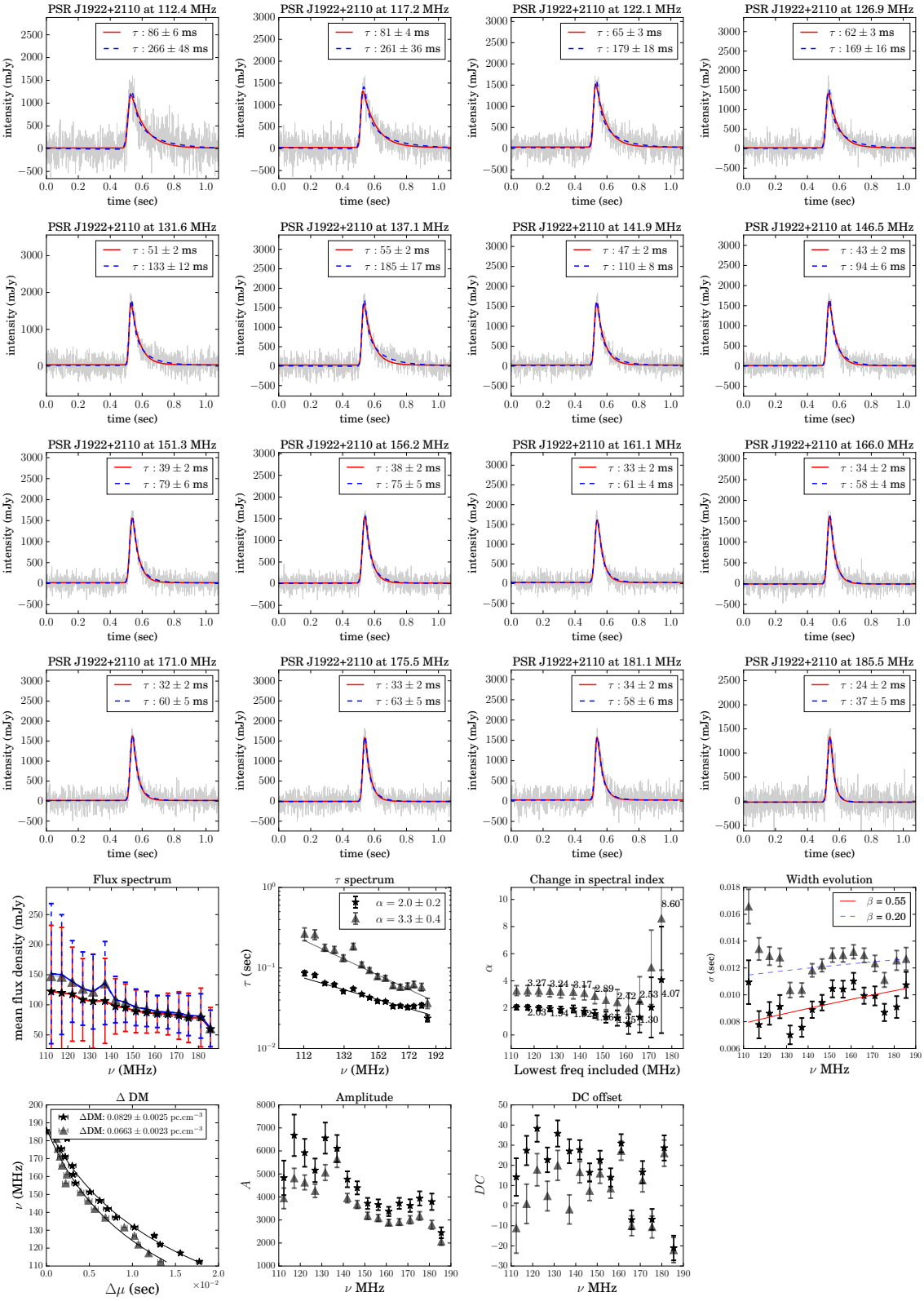

Figure A.13: PSR J1922+2110. Profile fits to 16 average profiles of Commissioning data, spectra and diagnostic plots.

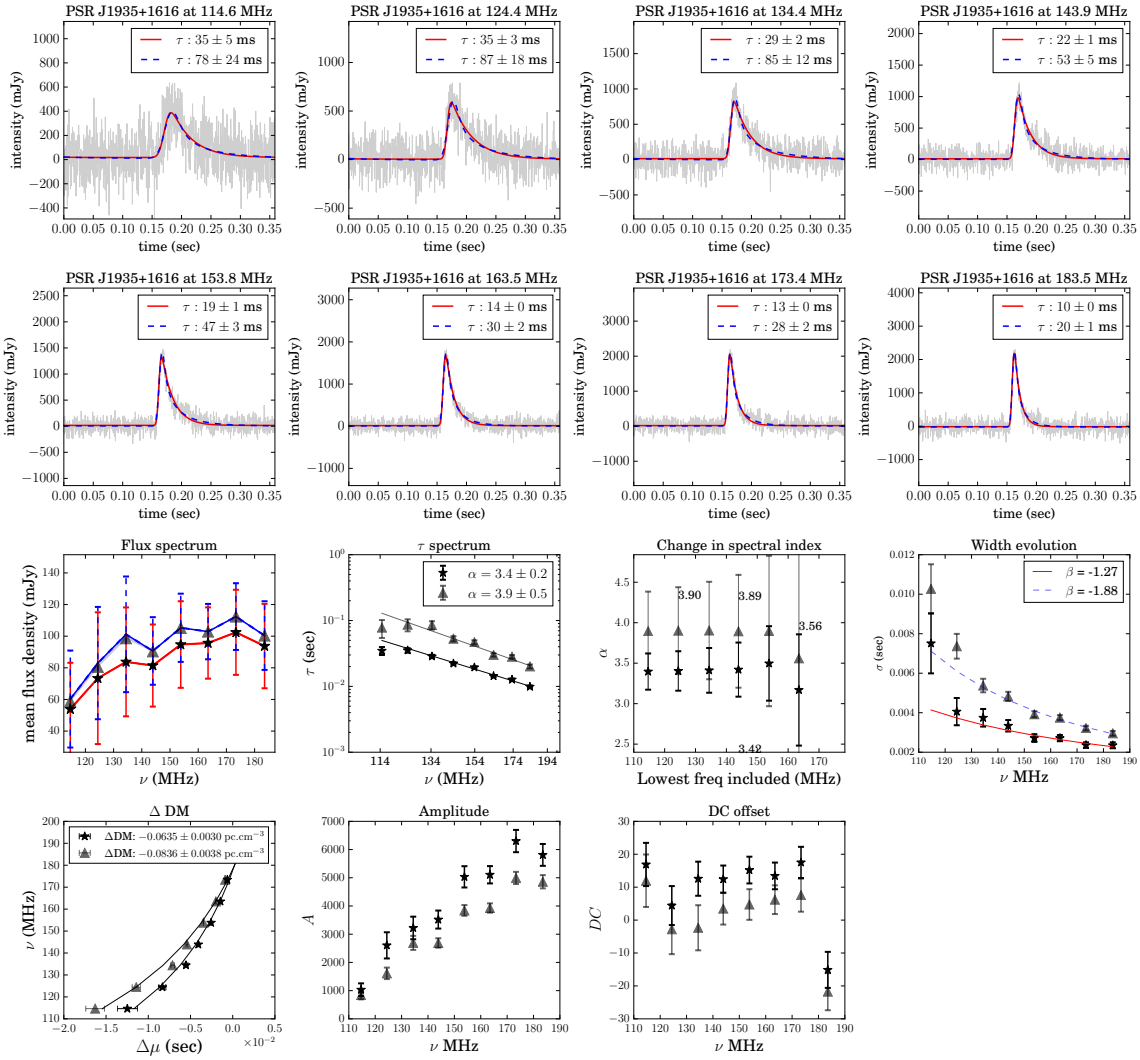

Figure A.14: PSR J1935+1616. Profile fits to the 8 average profiles of Commissioning data, spectra and diagnostic plots.

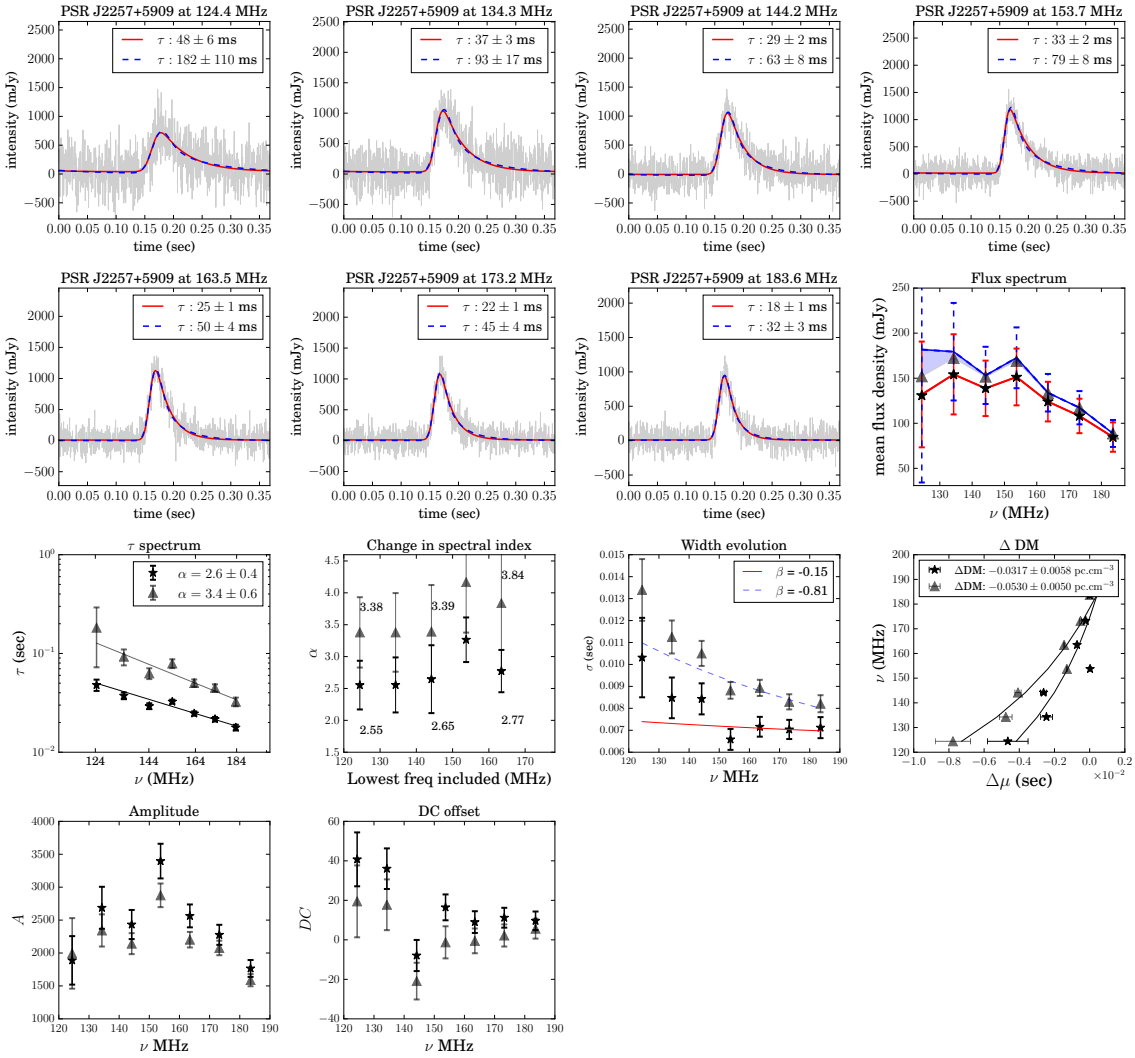

Figure A.15: PSR J2257+5909. Profile fits to the 7 average profiles of Commissioning data, spectra and diagnostic plots.

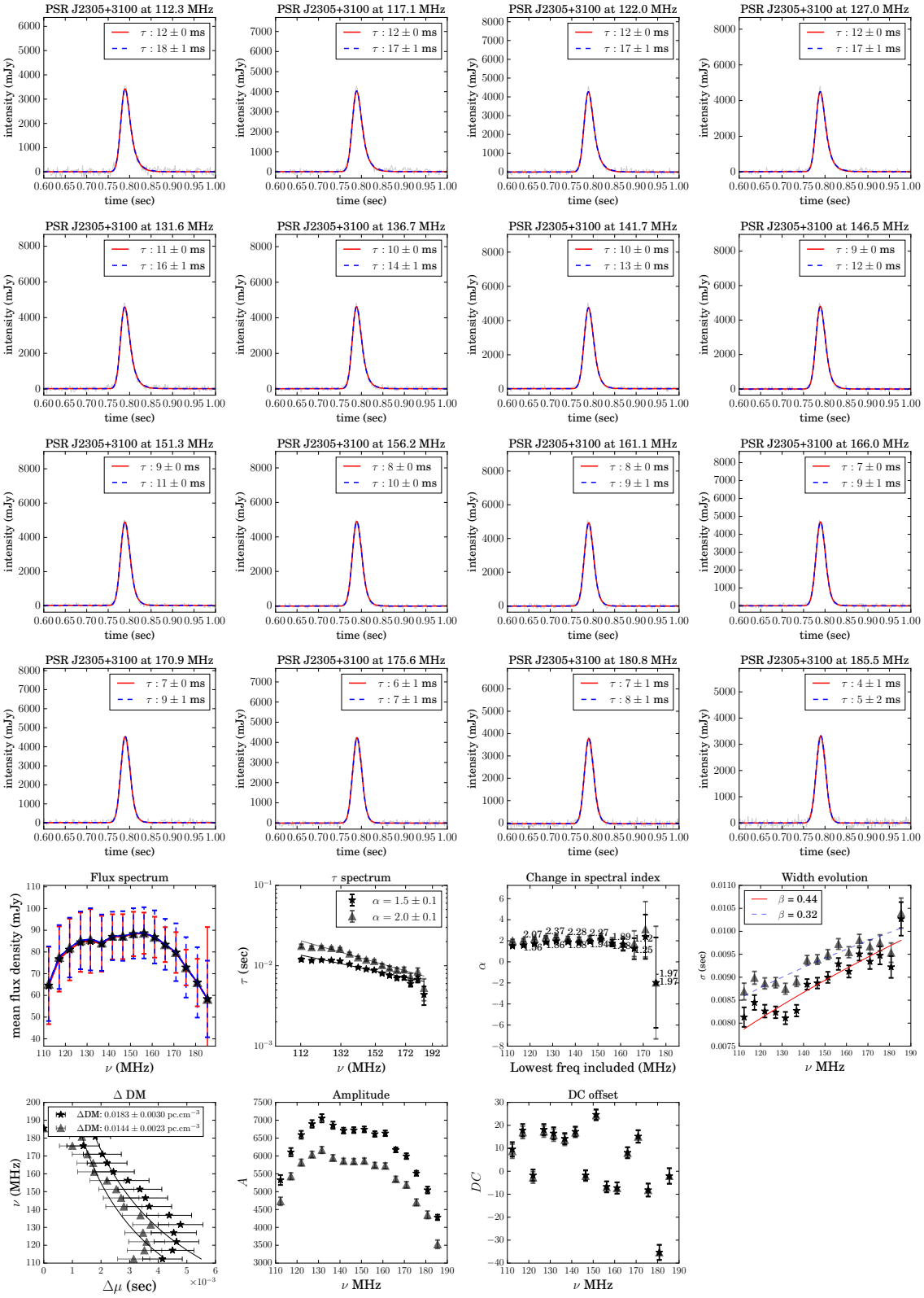

Figure A.16: PSR J2305+3100. Profile fits to 16 average profiles of Census data, spectra and diagnostic plots. Profile plots are zoomed to the on-pulse region.

Appendix B

Simulated Profiles of varying A_{rat}

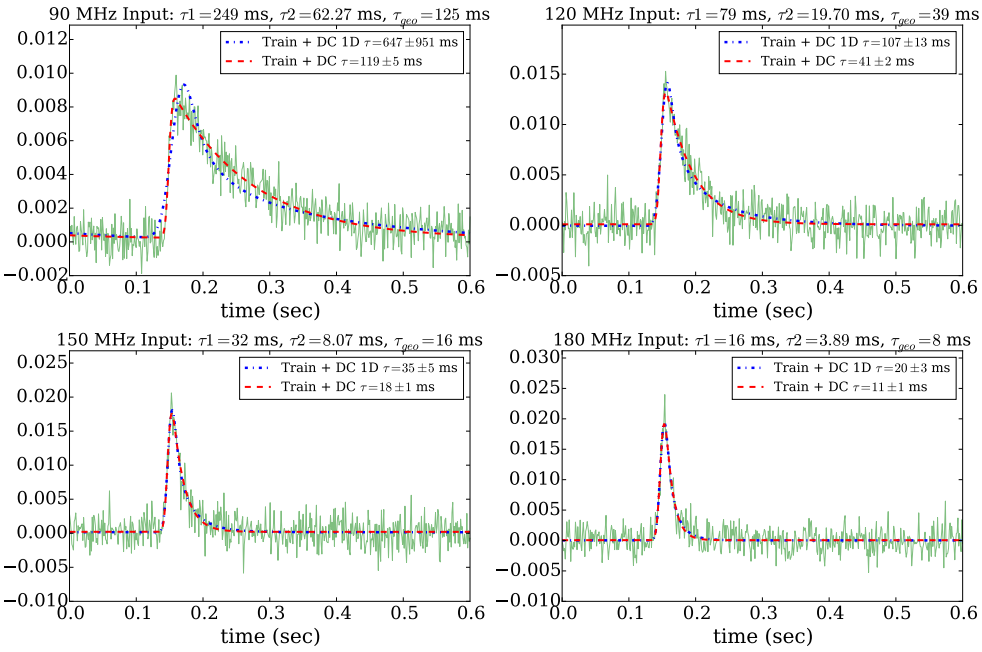

(a) Anisotropy ratio of 2.

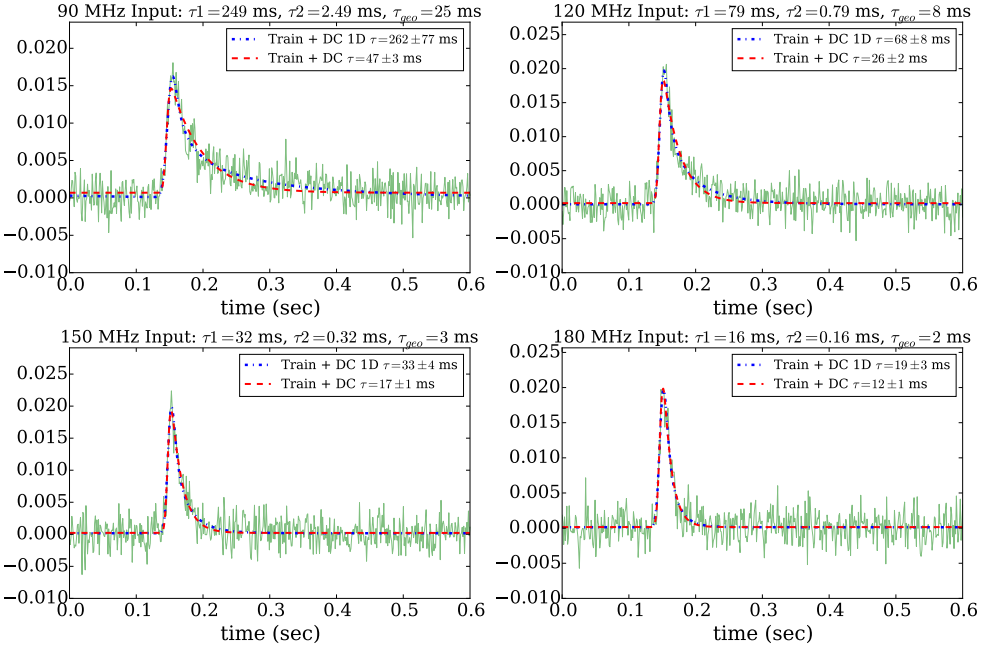

(b) Anisotropy ratio of 10.

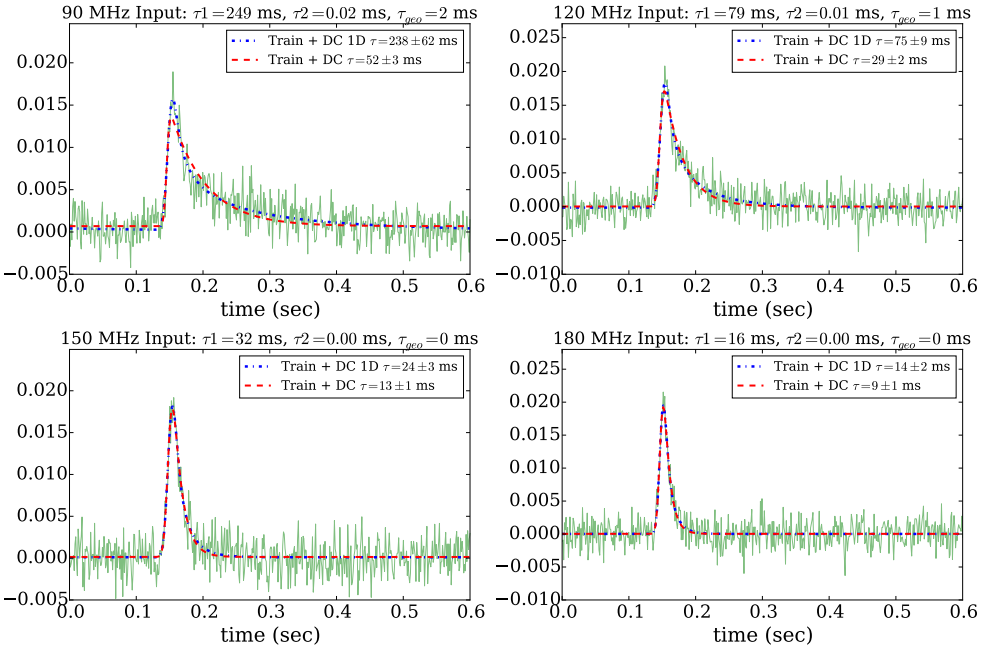

(c) Anisotropy ratio of 100.

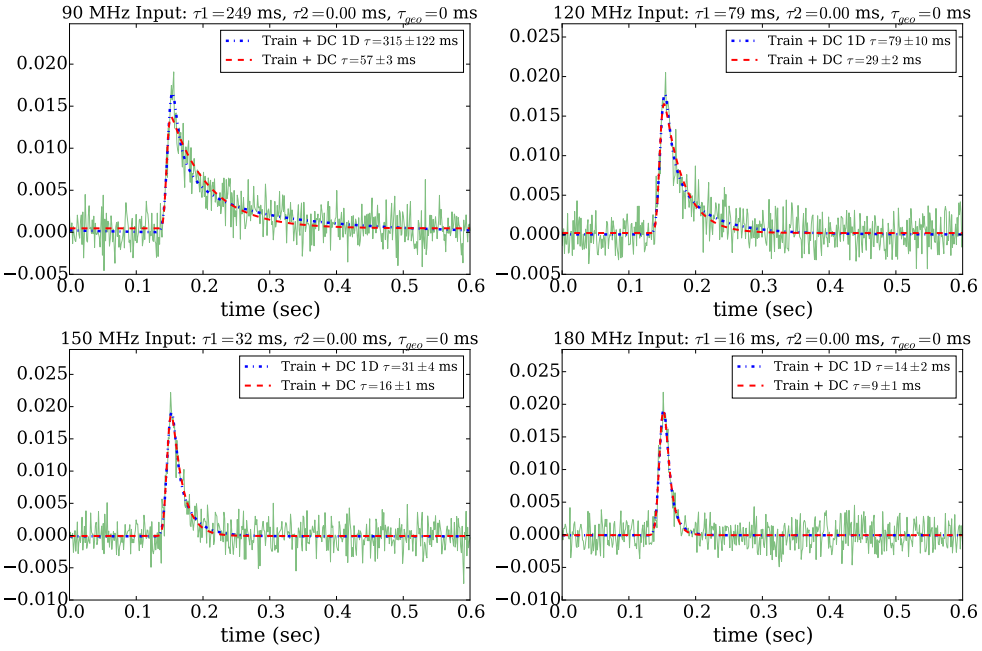

(d) Anisotropy ratio of 1000.

Figure B.1: This set of simulated pulse profiles scattered anisotropically with varying degrees of anisotropy as stated ih the sub-captions (a) to (d). The profiles are associated with the τ spectra of Fig. 6.4. The simulated pulse has a period of 0.6 sec and a duty cycle of 2%. Both the fits of the IM and $\mathrm{AM_{1D}}$ are shown.

Bibliography

Abel N. P., 2006, MNRAS, 368, 1949

Ables J. G., Manchester R. N., 1976, A&A, 50, 177

Alurkar S. K., Slee O. B., Bobra A. D., 1986, Aust. J. Phys., 39, 433

Anderson M., Kaiser H., Neilsen D., Sterling T., Benz A., Mantovani F., 2012, in APS April Meeting Abstracts, *Neutron star evolutions using tabulated equations of state with a new execution model*

Anderson P. W., Itoh N., 1975, Nature, 256, 25

Antoniadis J., Freire P. C. C., Wex N., Tauris T. M., Lynch R. S., van Kerkwijk M. H., et al. 2013, Science, 340, 448

Archibald A. M., Kaspi V. M., Livingstone M. A., McLaughlin M. A., 2008, ApJ, 688, 550

Archibald A. M., Stairs I. H., Ransom S. M., Kaspi V. M., Kondratiev V. I., Lorimer D. R., et al. 2009, Science, 324, 1411

Archibald R. F., Kaspi V. M., Beardmore A. P., Gehrels N., Kennea J. A., 2015, ApJ, 810, 67

Backer D. C., Hama S., van Hook S., Foster R. S., 1993, ApJ, 404, 636

Bannister K. W., Stevens J., Tuntsov A. V., Walker M. A., Johnston S., Reynolds C., et al. 2016, Science, 351, 354

Bartels R., Krishnamurthy S., Weniger C., 2016, Phys. Rev. Lett., 116, 051102

Bates S. D., Johnston S., Lorimer D. R., Kramer M., Possenti A., Burgay M., et al. 2011, MNRAS, 411, 1575

Bates S. D., Lorimer D. R., Verbiest J. P. W., 2013, MNRAS, 431, 1352

Bennett C. L., Fixsen D. J., Hinshaw G., Mather J. C., Moseley S. H., Wright E. L., et al. 1994, ApJ, 434, 587

Berkhuisen E., Müller P., 2008, A&A, 490, 179

Bhat N. D. R., Cordes J. M., Camilo F., Nice D. J., Lorimer D. R., 2004, ApJ, 605, 759

Bhat N. D. R., Cordes J. M., Chatterjee S., 2003, ApJ, 584, 782

Bhat N. D. R., Gupta Y., 2002, ApJ, 567, 342

Bignall H. E., Jauncey D. L., Lovell J. E. J., Tzioumis A. K., Kedziora-Chudczer L., Macquart J.-P., et al. 2003, ApJ, 585, 653

Bilous A. V., Kondratiev V. I., Kramer M., Keane E. F., Hessels J. W. T., Stappers B. W., 2016, A&A, 591, A134

Blaauw A., 1985, in Boland W., van Woerden H., eds, Birth and Evolution of Massive Stars and Stellar Groups Vol. 120 of Astrophysics and Space Science Library, *The progenitors of the local pulsar population*. pp 211–223

Bower G. C., Deller A., Demorest P., Brunthaler A., Eatough R., Falcke H., Kramer M., Lee K. J., Spitler L., 2014, The Astrophysical Journal Letters, 780, L2

Bower G. C., Deller A., Demorest P., Brunthaler A., Falcke H., Moscibrodzka M., et al. 2015, ApJ, 798, 120

Bramante J., Linden T., 2014, Physical Review Letters, 113, 191301

Bramley E. N., 1954, Royal Society of London Proceedings Series A, 225, 515

Brandt T. D., Draine B. T., 2012, ApJ, 744, 129

Brisken W. F., Macquart J.-P., Gao J. J., Rickett B. J., Coles W. A., Deller A. T., et al. 2010, ApJ, 708, 232

Brook P. R., Karastergiou A., Johnston S., Kerr M., Shannon R. M., Roberts S. J., 2016, MNRAS, 456, 1374

Burgess A., Tully J. A., 1992, A&A, 254, 436

Camilo F., Ransom S. M., Peñalver J., Karastergiou A., van Kerkwijk M. H., Durant M., et al. 2007, ApJ, 669, 561

Camilo F., Reynolds J., Johnston S., Halpern J. P., Ransom S. M., 2008, ApJ, 679, 681

Chandrasekhar S., 1931, ApJ, 74, 81

Chennamangalam J., Lorimer D. R., 2014, MNRAS, 440, L86

Cognard I., Bourgois G., Lestrade J.-F., Biraud F., Aubry D., Darchy B., et al. 1993, Nature, 366, 320

Coles W. A., Kerr M., Shannon R. M., Hobbs G. B., Manchester R. N., You X.-P., et al. 2015, ApJ, 808, 113

Coles W. A., Rickett B. J., Codona J. L., Frehlich R. G., 1987, ApJ, 315, 666

Cordes J., Lazio T., 2001, ApJ, 549, 997

Cordes J. M., 1978, ApJ, 222, 1006

Cordes J. M., 1986, ApJ, 311, 183

Cordes J. M., Lazio T. J. W., 2002, arXiv: astro-ph/0207156

Cordes J. M., Pidwerbetsky A., Lovelace R. V. E., 1986, ApJ, 310, 737

Cordes J. M., Rickett B. J., Stinebring D. R., Coles W. A., 2006, ApJ, 637, 346

Cordes J. M., Shannon R. M., Stinebring D. R., 2016, ApJ, 817, 16

Cordes J. M., Weisberg J. M., Boriakoff V., 1985, ApJ, 288, 221

Cordes J. M., Wolszczan A., 1986, ApJ Letters, 307, L27

Davies J. G., Large M. I., 1970, MNRAS, 149, 301

Davies J. G., Lyne A. G., Seiradakis J. H., 1972, Nature, 240, 229

Davies J. G., Lyne A. G., Seiradakis J. H., 1973, Nature, 244, 84

de Bruyn A. G., Macquart J.-P., 2015, A&A, 574, A125

Degenaar N., Reynolds M. T., Miller J. M., Kennea J. A., Wijnands R., 2013, The Astronomer's Telegram, 5006, 1

Del Zanna G., Dere K. P., Young P. R., Landi E., Mason H. E., 2015, A&A, 582, A56

Deller A. T., Moldon J., Miller-Jones J. C. A., Patruno A., Hessels J. W. T., Archibald A. M., et al. 2015, ApJ, 809, 13

Dembska M., Basu R., Kijak J., Lewandowski W., 2015, MNRAS, 449, 1869

Deneva J. S., Cordes J. M., Lazio T. J. W., 2010, in American Astronomical Society Meeting Abstracts Vol. 42 of Bulletin of the American Astronomical Society, *Modeling the Galactic Center Pulsar Population*. p. 464

Dennett-Thorpe J., de Bruyn A. G., 2000, ApJ, 529, L65

Dere K. P., Landi E., Mason H. E., Monsignori Fossi B. C., Young P. R., 1997, A&A Suppl. Series, 125

Desvignes G., Caballero R. N., Lentati L., Verbiest J. P. W., Champion D. J., Stappers B. W., et al. 2016, MNRAS, 458, 3341

Dewey R. J., Taylor J. H., Weisberg J. M., Stokes G. H., 1985, ApJ Letters, 294, L25

Dexter J., O'Leary R. M., 2014, ApJ Letters, 783, L7

Duyvendak J. J. L., 1942, Publications of the Astro. Soc. of the Pacific, 54, 91

Eatough R., Karuppusamy R., Kramer M., Klein B., Champion D., Kraus A. e. a., 2013, The Astronomer's Telegram, 5040

Eatough R. P., Falcke H., Karuppusamy R., Lee K. J., Champion D. J., Keane E. F., et al. 2013, Nature, 501, 391

Espinoza C. M., Guillemot L., Çelik Ö., Desvignes G., Hewitt J. W., Hou X., et al. 2013, MNRAS, 430, 571

Espinoza C. M., Lyne A. G., Kramer M., Manchester R. N., Kaspi V. M., 2011, ApJ Letters, 741, L13

Espinoza C. M., Lyne A. G., Stappers B. W., Kramer M., 2011, MNRAS, 414, 1679

Faucher-Giguère C.-A., Kaspi V. M., 2006, ApJ, 643, 332

Ferrière K. M., 2001, Reviews of Modern Physics, 73, 1031

Fiedler R., Dennison B., Johnston K., Hewish A., 1987, Nature, 326, 675

Fiedler R., Dennison B., Johnston K. J., Waltman E. B., Simon R. S., 1994, ApJ, 430, 581

Genzel R., Eckart A., Ott T., Eisenhauer F., 1997, MNRAS, 291, 219

Genzel R., Eisenhauer F., Gillessen S., 2010, Reviews of Modern Physics, 82, 3121

Geyer M., Karastergiou A., 2016, MNRAS, 462, 2587 (GK16)

Geyer M., Karastergiou A., Kondratiev V. I., Zagkouris K., Kramer M., Stappers B. W., et al. 2017, MNRAS, 470, 2659

Ghez A. M., Duchêne G., Matthews K., Hornstein S. D., Tanner A., Larkin J., et al. 2003, ApJ Letters, 586, L127

Goldsmith P. F., Yıldız U. A., Langer W. D., Pineda J. L., 2015, ApJ, 814, 133

Gómez G. C., Benjamin R. A., Cox D. P., 2001, AJ, 122, 908

Gould D. M., Lyne A. G., 1998, MNRAS, 301, 235

Graham-Smith F., 2003, Reports on Progress in Physics, 66, 173

Grevesse N., Sauval A. J., 1998, Space Science Reviews, 85, 161

Gunn J. E., Ostriker J. P., 1970, ApJ, 160, 979

Gupta Y., Bhat N. D. R., Rao A. P., 1999, ApJ, 520, 173

Gupta Y., Gangadhara R. T., 2003, ApJ, 584, 418

Gupta Y., Rickett B. J., Lyne A. G., 1994, MNRAS, 269, 1035

Haffner L. M., Dettmar R.-J., Beckman J. E., Wood K., Slavin J. D., Giammanco C., et al. 2009, Reviews of Modern Physics, 81, 969

Hamaker J. P., 2006, A&A, 456, 395

Hankins T. H., Eilek J. A., 2007, ApJ, 670, 693

Hankins T. H., Kern J. S., Weatherall J. C., Eilek J. A., 2003, Nature, 422, 141

Hartle J. B., 2003, *Gravity: An Introduction to Einstein's General Relativity*. Benjamin Cummings

Haskell B., Melatos A., 2015, International Journal of Modern Physics D, 24, 1530008

Hassall T. E., Stappers B. W., Hessels J. W. T., Kramer M., Alexov A., Anderson K., et al. 2012, A&A, 543, A66

Helfand D. J., Manchester R. N., Taylor J. H., 1975, ApJ, 198, 661

Hellings R. W., Downs G. S., 1983, ApJ Letters, 265, L39

Hewish A., Bell S. J., Pilkington J. D. H., Scott P. F., Collins R. A., 1968, Nature, 217, 709

Hobbs G., Archibald A., Arzoumanian Z., Backer D., Bailes M., Bhat N. D. R., et al. 2010, Classical and Quantum Gravity, 27, 084013

Hobbs G., Faulkner A., Stairs I. H., Camilo F., Manchester R. N., Lyne A. G., et al. 2004, MNRAS, 352, 1439

Hobbs G., Lorimer D. R., Lyne A. G., Kramer M., 2005, MNRAS, 360, 974

Hobbs G., Lyne A. G., Kramer M., Martin C. E., Jordan C., 2004, MNRAS, 353, 1311

Isaacman R., Rankin J. M., 1977, ApJ, 214, 214

Jenkins E. B., Tripp T. M., 2011, ApJ, 734, 65

Johnston S., Karastergiou A., 2017, MNRAS, 467, 3493

Johnston S., Walker M. A., van Kerkwijk M. H., Lyne A. G., D'Amico N., 1995, MNRAS, 274, L43

Johnston S., Weisberg J. M., 2006, MNRAS, 368, 1856

Jones P. B., 2014, MNRAS, 445, 770

Jones P. B., 2015, MNRAS, 450, 1420

Kaplan D. L., Chatterjee S., Gaensler B. M., Anderson J., 2008, ApJ, 677, 1201

Karastergiou A., Johnston S., 2007, MNRAS, 380, 1678

Kaspi V. M., Beloborodov A., 2017, arXiv: astro-ph/1703.00068

Kassim N. E., Lazio T. J. W., 1999, ApJ Letters, 527, L101

Keane E. F., Kramer M., 2008, MNRAS, 391, 2009

Kedziora-Chudczer L., 2006, MNRAS, 369, 449

Kedziora-Chudczer L., Jauncey D. L., Wieringa M. H., Walker M. A., Nicolson G. D., Reynolds J. E., et al. 1997, ApJ Letters, 490, L9

Kennea J. A., Krimm H., Barthelmy S., Gehrels N., Markwardt C., Cummings J., et al. 2013, The Astronomer's Telegram, 5009, 1

Kijak J., Gil J., 2002, A&A, 392, 189

Kijak J., Gupta Y., Krzeszowski K., 2007, A&A, 462, 699

Kijak J., Lewandowski W., Maron O., Gupta Y., Jessner A., 2011, A&A, 531, A16

Kiziltan B., Kottas A., De Yoreo M., Thorsett S. E., 2013, arXiv: astro-ph/1309.6635

Koekemoer A. M., Fruchter A. S., Hook R. N., Hack W., 2003, in Arribas S., Koekemoer A., Whitmore B., eds, HST Calibration Workshop: Hubble after the Installation of the ACS and the NICMOS Cooling System, *MultiDrizzle: An Integrated Pyraf Script for Registering, Cleaning and Combining Images*. p. 337

Kondratiev V. I., Verbiest J. P. W., Hessels J. W. T., Bilous A. V., Stappers B. W., Kramer M., et al. 2016, A&A, 585, A128

Kramer M., Klein B., Lorimer D., Müller P., Jessner A., Wielebinski R., 2000, in Kramer M., Wex N., Wielebinski R., eds, IAU Colloq. 177: Pulsar Astronomy - 2000 and Beyond Vol. 202 of Astronomical Society of the Pacific Conference Series, *The Effelsberg Search for Pulsars in the Galactic Centre*. p. 37

Kramer M., Stairs I. H., Manchester R. N., McLaughlin M. A., Lyne A. G., Ferdman R. D., et al. 2006, Science, 314, 97

Krishnakumar M. A., Mitra D., Naidu A., Joshi B. C., Manoharan P. K., 2015, ApJ, 804, 23 (K15)

Kulkarni S., Heilies C., 1986, in Hollenbach D., Thronson H., eds, Interstellar Processes, *The Atomic Component*. p. 87

Kuzmin A. D., Losovsky B. Y., 2007, Astronomical and Astrophysical Transactions, 26, 597

Lai D., Chernoff D. F., Cordes J. M., 2001, ApJ, 549, 1111

Lambert H. C., Rickett B. J., 1999, ApJ, 517, 299

Landi E., Del Zanna G., Young P. R., Dere K. P., Mason H. E., 2012, ApJ, 744, 99

Lang K. R., 1969, ApJ Letters, 158, L175

Lang K. R., 1971, ApJ, 164, 249

Lattimer J. M., Prakash M., 2001, ApJ, 550, 426

Lazarus P., Karuppusamy R., Graikou E., 2016, MNRAS, 458, 868

Lazio T. J. W., Cordes J. M., 1998, ApJ, 505, 715

Lee L. C., Jokipii J. R., 1975, ApJ, 201, 532

Lee L. C., Jokipii J. R., 1976, ApJ, 206, 735

Lestrade J.-F., Rickett B. J., Cognard I., 1998, A&A, 334, 1068

Levin L., Bailes M., Bates S., Bhat N. D. R., Burgay M., Burke-Spolaor S., et al. 2010, ApJ Letters, 721, L33

Lewandowski W., Dembska M., Kijak J., Kowalińska M., 2013, MNRAS, 434, 69 (L13)

Lewandowski W., Kowalińska M., Kijak J., 2015, MNRAS, 449, 1570 (L15)

Lewandowski W., Rożko K., Kijak J., Bhattacharyya B., Roy J., 2015, MNRAS, 454, 2517

Liu K., Wex N., Kramer M., Cordes J. M., Lazio T. J. W., 2012, ApJ, 747, 1

Lo K. Y., Claussen M. J., 1983, Nature, 306, 647

Lodders K., 2010, Astrophysics and Space Science Proceedings, 16, 379

Löhmer O., Kramer M., Mitra D., Lorimer D. R., Lyne A. G., 2001, ApJ Letters, 562, L157

Löhmer O., Mitra D., Gupta Y., Kramer M., Ahuja A., 2004, A&A, 425, 569

Lorimer D. R., Bailes M., McLaughlin M. A., Narkevic D. J., Crawford F., 2007, Science, 318, 777

Lorimer D. R., Jessner A., Seiradakis J. H., Lyne A. G., D'Amico N., Athanasopoulos A., et al. 1998, A&A Suppl., 128, 541

Lorimer D. R., Kramer M., 2004, *Handbook of Pulsar Astronomy*. UK: Cambridge University Press

Lorimer D. R., Lyne A. G., McLaughlin M. A., Kramer M., Pavlov G. G., Chang C., 2012, ApJ, 758, 141

Lorimer D. R., Yates J. A., Lyne A. G., Gould D. M., 1995, MNRAS, 273, 411

Lovell J. E. J., Jauncey D. L., Bignall H. E., Kedziora-Chudczer L., Macquart J.-P., Rickett B. J., et al. 2003, AJ, 126, 1699

Lu J. R., Ghez A. M., Hornstein S. D., Morris M. R., Becklin E. E., Matthews K., 2009, ApJ, 690, 1463

Lyne A., Hobbs G., Kramer M., Stairs I., Stappers B., 2010, Science, 329, 408

Lyne A. G., Rickett B. J., 1968, Nature, 218, 326

Lyne A. G., Stappers B. W., Freire P. C. C., Hessels J. W. T., Kaspi V. M., Allen B., et al. 2017, ApJ, 834, 72

Lyne A. G., Thorne D. J., 1975, MNRAS, 172, 97

Macquart J.-P., Kanekar N., Frail D. A., Ransom S. M., 2010, ApJ, 715, 939

Malofeev V. M., Malov O. I., Shchegoleva N. V., 2000, Astronomy Reports, 44, 436

Manchester R. N., 2010, arXiv: astro-ph/1004.3602

Manchester R. N., Hobbs G. B., Teoh A., Hobbs M., 2005, AJ, 129, 1993

Maron O., Kijak J., Kramer M., Wielebinski R., 2000, Astron. Astrophys. Suppl., 147, 195

Mathis J. S., 1986, ApJ, 301, 423

McMullin J. P., Waters B., Schiebel D., Young W., Golap K., 2007, in Shaw R. A., Hill F., Bell D. J., eds, Astronomical Data Analysis Software and Systems XVI Vol. 376 of Astronomical Society of the Pacific Conference Series, *CASA Architecture and Applications*. p. 127

Melrose D. B., Yuen R., 2016, Journal of Plasma Physics, 82, 635820202

Moffett D. A., Hankins T. H., 1996, ApJ, 468, 779

Molotov I., Kovalenko A., Samodurov V., Lipatov B., Dementiev A., Antipenko A., et al. 2003, Astronomical & Astrophysical Transactions, 22, 743

Mori K., Gotthelf E. V., Zhang S., An H., Baganoff F. K., Barrière N. M., et al. 2013, ApJ Letters, 770, L23

Muno M. P., Baganoff F. K., Bautz M. W., Feigelson E. D., Garmire G. P., Morris M. R., et al. 2004, ApJ, 613, 326

Newville M., Stensitzki T., Allen D. B., Ingargiola A., 2014, http://dx.doi.org/10.5281/zenodo.11813

Ng C.-Y., Kaspi V. M., 2011, in Göğüş E., Belloni T., Ertan Ü., eds, American Institute of Physics Conference Series Vol. 1379 of American Institute of Physics Conference Series, *High Magnetic Field Rotation-powered Pulsars*. pp 60–69

Nieva M.-F., Przybilla N., 2012, A&A, 539, A143

Offringa A. R., 2010, in Astrophysics Source Code Library, record ascl:1010.017, AOFlagger: RFI Software

Offringa A. R., de Bruyn A. G., Biehl M., Zaroubi S., Bernardi G., Pandey V. N., 2010, MNRAS, 405, 155

Olausen S. A., Kaspi V. M., 2014, ApJS, 212, 6

Özel F., Freire P., 2016, ARA&A, 54, 401

Pandey V. N., van Zwieten J. E., de Bruyn A. G., Nijboer R., 2009, in Saikia D. J., Green D. A., Gupta Y., Venturi T., eds, The Low-Frequency Radio Universe Vol. 407 of Astronomical Society of the Pacific Conference Series, *Calibrating LOFAR using the Black Board Selfcal System*. p. 384

Papitto A., Hessels J. W. T., Burgay M., Ransom S., Rea N., Possenti A., et al. 2013, The Astronomer's Telegram, 5069

Paumard T., Genzel R., Martins F., Nayakshin S., Beloborodov A. M., Levin Y., et al. 2006, ApJ, 643, 1011

Pen U.-L., King L., 2012, MNRAS, 421, L132

Pfahl E., Loeb A., 2004, ApJ, 615, 253

Philippov A. A., Cerutti B., Tchekhovskoy A., Spitkovsky A., 2015, ApJ Letters, 815, L19

Pilia M., Hessels J. W. T., Stappers B. W., Kondratiev V. I., Kramer M., van Leeuwen J., et al. 2016, A&A, 586, A92

Radhakrishnan V., Cooke D. J., 1969, ApJ Letters, 3, 225

Radhakrishnan V., Manchester R. N., 1969, 222, 228

Rajwade K., Lorimer D. R., Anderson L. D., 2016, MNRAS, 455, 493

Ramachandran R., Mitra D., Deshpande A. A., McConnell D. M., Ables J. G., 1997, MNRAS, 290, 260

Rankin J., Rosen R., 2014, MNRAS, 439, 3860

Rankin J. M., Counselman III C. C., 1973, ApJ, 181, 875

Ransom S. M., Stairs I. H., Archibald A. M., Hessels J. W. T., Kaplan D. L., van Kerkwijk M. H., et al. 2014, Nature, 505, 520

Ravi V., Wyithe J. S. B., Shannon R. M., Hobbs G., 2015, MNRAS, 447, 2772

Reynolds R. J., 1983, ApJ, 268, 698

Reynolds R. J., 1985, ApJ, 294, 256

Reynolds R. J., 1991, ApJ Letters, 372, L17

Reynolds R. J., 2004, Advances in Space Research, 34, 27

Reynolds R. J., Haffner L. M., Tufte S. L., 1999, in Taylor A. R., Landecker T. L., Joncas G., eds, New Perspectives on the Interstellar Medium Vol. 168 of Astronomical Society of the Pacific Conference Series, *The Gaseous ISM: Observations with the Wisconsin Hα Mapper (WHAM)*. p. 149

Reynolds R. J., Scherb F., Roesler F. L., 1973, ApJ, 185, 869

Rickett B., 2011, in Florinski V., Heerikhuisen J., Zank G. P., Gallagher D. L., eds, American Institute of Physics Conference Series Vol. 1366 of American Institute of Physics Conference Series, *Anisotropic and Intermittent Turbulence in the Warm Ionized Interstellar Medium*. pp 107–114

Rickett B., Johnston S., Tomlinson T., Reynolds J., 2009, MNRAS, 395, 1391

Rickett B. J., 1970, MNRAS, 150, 67

Rickett B. J., 1977, ARA&A, 15, 479

Rickett B. J., 1990, ARA&A, 28, 561

Rickett B. J., Coles W. A., Bourgois G., 1984, A&A, 134, 390

Rickett B. J., Lyne A. G., Gupta Y., 1997, MNRAS, 287, 739

Roberts S., Osborne M., Ebden M., Reece S., Gibson N., Aigrain S., 2012, Philosophical Transactions of the Royal Society of London A: Mathematical, Physical and Engineering Sciences, 371

Roy S., 2013, ApJ, 773, 67

Salpeter E. E., 1967, ApJ, 147, 433

Scheuer P. A. G., 1968, Nature, 218, 920

Shao L., 2016, Phys. Rev. D, 93, 084023

Shibazaki N., Murakami T., Shaham J., Nomoto K., 1989, Nature, 342, 656

Sieber W., 1982, A&A, 113, 311

Slee O. B., Otrupcek R. E., Dulk G. A., 1980, Proceedings of the Astronomical Society of Australia, 4, 100

Smirnova T. V., Shishov V. I., Popov M. V., Gwinn C. R., Anderson J. M., Andrianov A. S., et al. 2014, ApJ, 786, 115

Smith F. G., Thompson J. H., 1988, *Optics*. John Wiley and Sons Ltd.

Spitler L. G., Lee K. J., Eatough R. P., Kramer M., Karuppusamy R., Bassa C. G., et al. 2014, ApJ Letters, 780, L3

Spitler L. G., Scholz P., Hessels J. W. T., Bogdanov S., Brazier A., Camilo F., et al. 2016, Nature, 531, 202

Spruit H. C., 2009, in Strassmeier K. G., Kosovichev A. G., Beckman J. E., eds, Cosmic Magnetic Fields: From Planets, to Stars and Galaxies Vol. 259 of IAU Symposium, *The source of magnetic fields in (neutron-) stars*. pp 61–74

Stacy J. G., Jackson P. D., 1982, Nature, 296, 42

Stairs I. H., 2004, Science, 304, 547

Stappers B. W., Hessels J. W. T., Alexov A., Anderson K., Coenen T., Hassall T., et al. 2011, A&A, 530, A80

Stinebring D. R., 2006, Chinese Journal of Astronomy and Astrophysics Supplement, 6, 204

Stinebring D. R., McLaughlin M. A., Cordes J. M., Becker K. M., Goodman J. E. E., Kramer M. A., et al. 2001, ApJ Letters, 549, L97

Stokes G. H., Taylor J. H., Weisberg J. M., Dewey R. J., 1985, Nature, 317, 787

Stovall K., Lynch R. S., Ransom S. M., Archibald A. M., Banaszak S., Biwer C. M., et al. 2014, ApJ, 791, 67

Struve O., Elvey C. T., 1938, ApJ, 88, 364

Sturrock P. A., 1971, ApJ, 164, 529

Sun X. H., Han J. L., 2004, in Uyaniker B., Reich W., Wielebinski R., eds, The Magnetized Interstellar Medium Astrophysics and Space Science Library

Swarup G., Mohanty D. K., Balasubramanian V., 1971, IAU Circ., 2356

Tasse C., van der Tol S., van Zwieten J., van Diepen G., Bhatnagar S., 2013, A&A, 553, A105

Tayal S. S., 2011, ApJS, 195, 12

Taylor J. H., Cordes J. M., 1993, ApJ, 411, 674

Tendulkar S. P., Bassa C. G., Cordes J. M., Bower G. C., Law C. J., Chatterjee S., et al. 2017, ApJ Letters, 834, L7

Teukolsky S., Shapiro S., 1983, *Black holes, white dwarfs, and neutron stars: the physics of compact objects*. New York City: Wiley

Thorsett S. E., 1991, ApJ, 377, 263

Tielens A. G. G. M., Hollenbach D., 1985, ApJ, 291, 722

Trang F. S., Rickett B. J., 2007, ApJ, 661, 1064

Tuntsov A. V., Bignall H. E., Walker M. A., 2012, arXiv: astro-ph/1212.0633

van Haarlem M. P., Wise M. W., Gunst A. W., Heald G., McKean J. P., Hessels J. W. T., et al. 2013, A&A, 556, A2

van Langevelde H. J., Frail D. A., Cordes J. M., Diamond P. J., 1992, ApJ, 396, 686

van Straten W., Demorest P., Oslowski S., 2012, Astronomical Research and Technology, 9, 237

Verbiest J. P. W., Lentati L., Hobbs G., van Haasteren R., Demorest P. B., Janssen G. H., et al. 2016, MNRAS, 458, 1267

Walker M. A., 2000, in Kramer M., Wex N., Wielebinski R., eds, IAU Colloq. 177: Pulsar Astronomy - 2000 and Beyond Vol. 202 of Astronomical Society of the Pacific Conference Series, *Extreme scattering of pulsars*. p. 561

Walker M. A., 2007, in Haverkorn M., Goss W. M., eds, SINS - Small Ionized and Neutral Structures in the Diffuse Interstellar Medium Vol. 365 of Astronomical Society of the Pacific Conference Series, *Extreme Scattering Events: Insights into the Interstellar Medium on AU-Scales*. p. 299

Walker M. A., 2016, ApJ, 818, 23

Walker M. A., Melrose D. B., Stinebring D. R., Zhang C. M., 2004, MNRAS, 354, 43

Walker M. A., Tuntsov A. V., Bignall H., Reynolds C., Bannister K. W., Johnston S., et al. 2017, ApJ, 843, 15

Wang N., Manchester R. N., Johnston S., 2007, MNRAS, 377, 1383

Wijnholds S. J., van Cappellen W. A., 2011, IEEE Transactions on Antennas and Propagation, 59, 1981

Williamson I. P., 1972, MNRAS, 157, 55

Williamson I. P., 1973, MNRAS, 163, 345

Witt A. N., Gold B., Barnes III F. S., DeRoo C. T., Vijh U. P., Madsen G. J., 2010, ApJ, 724, 1551

Wolszczan A., 1983, MNRAS, 204, 591

Wright E. L., Mather J. C., Bennett C. L., Cheng E. S., Shafer R. A., Fixsen D. J., et al. 1991, ApJ, 381, 200

Wucknitz O., 2013, arXiv: astro-ph/1308.3976

Wucknitz O., 2015, in Tarchi A., Giroletti M., Feretti L., eds, Proceedings, 12th European VLBI Network Symposium and Users Meeting (EVN2014), *Probing interstellar scattering towards the Galactic centre with pulsar VLBI*. p. 066

Yao J. M., Manchester R. N., Wang N., 2017, ApJ, 835, 29

You X. P., Hobbs G., Coles W. A., Manchester R. N., Edwards R., Bailes M., et al. 2007, MNRAS, 378, 493